Universitat Autònoma de Barcelona

Vortex Pinning and Creep in YBCO Nanocomposite Films grown by Chemical Solution Deposition

Ferran Vallès Pérez

A dissertation submitted for the degree of

Ph. D. in Materials Science

Vortex Pinning and Creep in YBCO Nanocomposite Films grown by Chemical Solution Deposition

Author:
Ferran Vallès Pérez

Supervisors:
Dr. Anna Palau Masoliver
Prof. Teresa Puig Molina

Institut de Ciència de Materials de Barcelona (ICMAB-CSIC)

DEPARTMENT OF SUPERCONDUCTING MATERIALS AND LARGE SCALE NANOSTRUCTURES

Universitat Autònoma de Barcelona

PHYSICS DEPARTMENT, FACULTY OF SCIENCE

March, 2019

Prof. Teresa Puig Molina, professor of the Superconducting Materials Large Scale Nanostructures Department at the Institut de Ciència de Materials de Barcelona (ICMAB-CSIC); **Dr. Anna Palau Masoliver**, tenured scientist at the Superconducting Materials Large Scale Nanostructures Department at the Institut de Ciència de Materials de Barcelona (ICMAB-CSIC) and **Prof. Àlvar Sànchez Moreno**, professor of the Physics Department at Universitat Autònoma de Barcelona (UAB)

CERTIFY

that the dissertation **"Votex pinning and creep in YBCO nanocomposite films grown by chemical solution deposition "**, submitted by **Ferran Vallès Pérez** to the Science Faculty in fulfilment of the requirements for the degree of Doctor of Philosophy in the Materials Science program has been performed under their supervision.

In witness whereof, they sign this certificate

Author:
Ferran Vallès Pérez

Supervisor:	*Supervisor:*	*Tutor:*
Prof. Teresa Puig Molina	Dr. Anna Palau Masoliver	Prof. Àlvar Sànchez Moreno

Bellaterra, Wednesday 27th March, 2019

Uno de los alumnos aseveró haber completado la lectura
del texto y leyó en voz alta su escueta reseña.
-He aquí una contribución nanométrica a establecer los
límites de un mundo al que no se le conoce fin.
Otro, que admitió no haber dado a basto con ella, añadió
un comentario burlón.
-¡Y con mucha imaginación!

CONTENTS

ACKNOWLEDGEMENTS

The progress of this thesis has relied on many discussions and decisions leaded by my supervisors, who have also contributed with many comments in the writing of this manuscript, which has also been revised by another mate of the group.

The samples have been mainly cooked by other PhD students and technicians from the group and the STEM observations have been performed by other PhD students as well. Some of the figures in this work have not been produced by me but other members of the team, who kindly shared their design expertise.

It has been pleasant to learn many things thanks to the willingness to mentor from former PhD students of the group and to the discussions generated during the group meetings. In general, the people of the superconductors' group at ICMAB (and other people as well), have jointly shared results, slides, graphs, photographs, figures, samples, substrates, furnaces, solutions, problems, joys, coffees, beers, cakes, food, fags, cars, clothes, songs, beds and coaches and in definitive have made this trip much funnier.

The large amount of experiments would have not been possible without the help of the technical staff at ICMAB. In particular, it has been of great importance the help from technicians at the low temperatures lab and at the clean-room facility.

What concerns the experiments at very high magnetic fields, the high temperature superconductors group in LNCMI-Grenoble was very familiar and was engaged to face the many problems we had. In ASC-NHMFL, I received tremendous help not only for running the experiments, but also for the accommodation and bike transportation in the humid atmosphere of Tallahassee.

The contribution to this work is not restricted to the scientific crew but also to the administrative personnel who still take care of the increasing bureaucracy, the maintenance team that where as usual willing to help, the IT guys and the cleaning girls. At the end, everybody has something to do with it, even the receptionists that are always there!

Not to forget the people I forget and the people I do not know of their contribution yet.

It is mandatory to acknowledge the financial support from the Spanish Ministry of Economy and Competitiveness through the "Severo Ochoa" Programme for Centres of Excellence in R&D (SEV-2015-0496), COACHSUPENERGY project (MAT2014-51778-C2-1-R) and FEDER. Also the support from the European Union for EUROTAPES project (FP7-NMP-Large-2011-280432), ULTRASUPERTAPE project (ERC-2014-ADG-669504), COST Action NANOCOHYBRI (CA16218) and from the Catalan Government with 2014-SGR-753 and Xarmae. A portion of this work was performed at the National High Magnetic Field Laboratory, which is supported by National Science Foundation

Cooperative Agreement No. DMR-1157490 and the State of Florida. Also the support of LNCMI-CNRS, a member of the European Magnetic Field Laboratory (EMFL).

It is also convenient to mention the support received from my family, which has been very excited from the first moment and has encouraged me to arrive until the end.

Last, acknowledge the linguistic and scientific education that I have received, the numerous imitations to other published studies that I have used and the continuous familiarisation that I have had with the usual practices in the scientific community.

ABSTRACT

The fabrication of superconducting $YBa_2Cu_3O_{7-x}$ (YBCO) nanocomposite films by the incorporation of nanoparticles in the matrix has demonstrated to strongly enhance the vortex pinning performances under applied magnetic fields and to reduce the effective anisotropy, ensuring great potential for their use in a broad number of applications. Different nanoparticle concentrations, sizes and growth process conditions lead to a rich variety of defects in the films, whose vortex pinning and vortex creep effectiveness depends on temperature and the magnitude and orientation of the magnetic field.

In this thesis, it is presented an extensive research of YBCO nanocomposites grown by the scalable and low-cost chemical solution deposition (CSD) technique, where the incorporation of nanoparticles is obtained following two different approaches: spontaneous segregated nanoparticles and preformed nanoparticles.

By the combination of electrical transport measurements with XRD and STEM microstructural analysis, correlation between superconducting performance and the defect landscape has been possible, allowing us to separate pinning and creep contributions in the regions of the magnetic-field–temperature diagram and therefore foresee the best landscape to operate at certain conditions up to very high magnetic fields (35 T).

It has been demonstrated that the incorporation of nanoparticles induces large densities of stacking faults which strongly affect the pinning and creep contributions in all orientations. Large isotropic pinning forces arise at low-intermediate magnetic fields and at low-intermediate temperatures and anisotropic pinning contributions are strongly altered, especially at high magnetic fields and temperatures.

The arrangement and the typology of the stacking faults induced by the incorporation of nanoparticles is determinant for the final balance of vortex pinning contributions. We demonstrate that the use of preformed small nanoparticles (7 nm) enables a very good control of the stacking-fault-rich microstructure.

A defect landscape characterized by a large density of homogeneously distributed short stacking faults has been identified as the best one to promote huge isotropic pinning contributions, which are ascribed to the nanostrain located at the edges of stacking faults and to atomic defects which may be Cu-O vacancies hosted by stacking faults.

Furthermore, the large density of stacking faults is concomitant with a large density of twin boundaries, both beneficial for the anisotropic pinning when the magnetic field orientation is parallel to the ab-planes (H||ab) and the c-axis (H||c) respectively. However, the coherence breaking of twin boundaries reduces the temperature where anisotropic pinning is effective for H||c. Thick nanocomposites from preformed nanoparticles have shown to significantly avoid this coherence segmentation and be able to afford large critical currents at high magnetic fields and high temperatures.

Stacking faults have been also found to play a decisive role for the preclusion of double kink excitations, which boost magnetic flux creep for H||c and especially H||ab. Furthermore, the isotropic flux creep contribution associated to the nanostrained regions is also reduced in nanocomposites.

In this work, it is shown that nanocomposites provide simultaneously higher flux pinning and lower flux creep especially at low-intermediate temperatures and at low-intermediate magnetic fields. The region of this outstanding performance can be enlarged to larger fields and temperatures by further nanoengineering, since it has been shown that different defect landscapes can be particularly interesting for given operating conditions.

MOTIVATION

A piece of rock floats in the air still but not motionless. When pushed, the rock is capable to follow the path of a curved magnetic rail flying from a distance. This striking image, more typical of a magician than of a scientist, catches the eyes of diverse people no matter who they are.

Beyond this iconic picture and somehow related, superconductors are historically known by another property that is rather revolutionary than emblematic: they exhibit zero electrical resistance. This unique ability of lossless current flow has attracted the attention of many researchers because of its high applicability, especially after the finding of high temperature superconductors (HTS).

Today, superconductors are commercially used, for instance, for magnetic resonance imaging in hospitals, for the generation of very high magnetic fields and for the acquirement of very precise magnetometry in laboratories. Furthermore, the technological development of superconducting conductors based in HTS has enabled to expand the scope of future applications due to their capability to operate at higher temperatures and larger magnetic fields and they are foreseen to play a very relevant role to face the increasing demand of energy.

However, the conditions that limit the zero electrical resistance state (critical current density and irreversibility line) and the difficulty to manufacture cost-effective superconducting wires represent the main scientific and technological-commercial frontier for the application of superconductors in the electrical grid and electric power devices. Besides, $\mathrm{YBa_2Cu_3O_{7-x}}$ (YBCO) is the HTS material that excels in terms of larger irreversibility fields and therefore a broader region of applicability under applied magnetic fields. It is recognized to be the best high field superconducting material and is nowadays being considered for the future case studies of high energy accelerators, fusion reactors, very high magnetic field magnets and NMR systems beyond 1 GHz.

The coated conductor architecture in which current flows through a YBCO HTS film fulfils the requirements for power applications under low external magnetic fields, whereas applications requiring high magnetic fields are still limited by the decay of the critical current density under high external magnetic fields, which has been demonstrated to be controlled by pinning and dynamics of vortex matter in YBCO and other type II superconductors.

Nanometric defects, with a similar size to the coherence length of vortex cores, have been shown to act as vortex pinning centres and considerably increase the critical current density of the material under high magnetic fields.

Chemical solution deposition techniques have a big potential for the development of low cost YBCO films and are scalable to long length coated conductors. The use of chemical solutions, which can be synthesized in large quantities employing inexpensive raw materials, is a very versatile approach that can be also adapted for the acquirement of YBCO nanocomposites by the incorporation of nanosized secondary phases within the YBCO matrix with the purpose of generating artificial vortex pinning centres.

Several nanoengineering methods of superconducting films have allowed to artificially change the defect landscape and improve the electrical performance at different regions of the magnetic-field–temperature diagram. However, the influence of these defects on the superconducting performance is still not fully understood.

The present work, which has been completed in the framework of "European Development of Superconducting Tapes (EUROTAPES)", has been devoted to the study of vortex pinning and vortex creep in CSD YBCO nanocomposites by the combination of electrical transport measurements with nanostructural characterization from scanning transmission electron microscopy and X-ray diffraction techniques. It is intended to depict general correlations between nanostructure and superconducting properties and to elucidate the best pinning landscape for high performance at high magnetic fields.

The main background knowledge and basic experimental methods are described in chapters 1 and 2. Vortex pinning regimes and the strength of pinning centres are identified and discussed in chapters 3 and 4. In chapter 5, vortex creep is analysed by means of the shape of the electrical current-dissipation curves. Finally in chapter 6, the vortex pinning analysis is extended to the properties of novel thin and thick nanocomposite films from preformed nanoparticles and to the region of very high magnetic fields up to 35 T.

CHAPTER 1

INTRODUCTION

1.1 The birth of superconductivity

According to several historical documents[1–4], superconductivity was first observed three years after the first liquefaction of helium, the last permanent gas. It was the culmination of a quest towards lowest temperatures that involved many scientists in Europe during the second half of XIX century until it was accomplished in 1908 when Heike Kamerlingh Onnes, motivated by the study of gas behaviour, attained the first volume of liquid helium with a boiling temperature of 4.2 K at his modern cryogenic laboratory in Leiden.

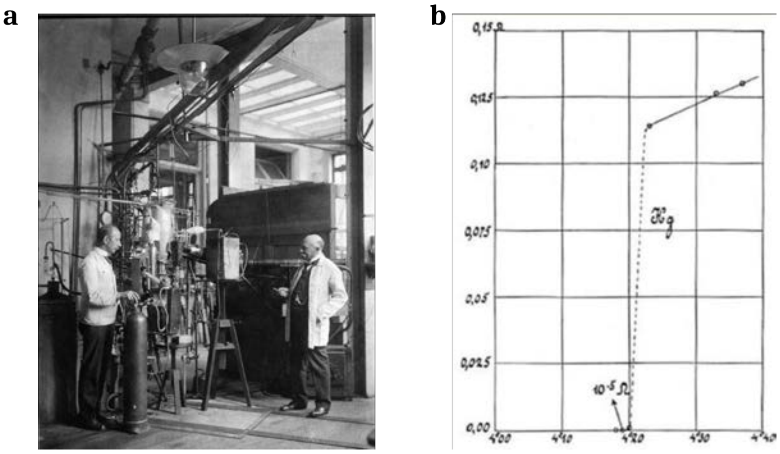

Figure 1.1: historical archive[4]. (**a**) The chief technician (left) and Kammerlingh Onnes (right) in the cryogenic laboratory at Leiden, circa 1911 and (**b**) resistance (in Ω) versus temperature (in K) plot for mercury from one of the experiments performed in 1911.

Onnes' cryogenic laboratory relied on a extensive team of experienced technicians, including glass-blowers and also apprentices from the instrument-maker's school. After the acquirement of liquid helium, Onnes devoted himself with the help of the chief technician (figure 1.1(a)) to the development of a suitable infrastructure for transferring liquid helium to a new cryostat prepared for the study of materials at liquid helium temperature.

At that time, it was a hot question what would happen to the resistance of metals when approaching the absolute zero. Once the new cryostat was ready, Onnes, the chief technician and two apprentices from the school performed the experiments concerning the electrical behaviour of metals. After observing a constant resistance in platinum and gold when decreasing temperature, they chose to measure mercury because it could be made extremely pure by repeated distillation. In 1911, Kammerling Onnes reported to the Dutch academy and at the first Solvay conference the finding of something that was not predictable at all: *zero electrical resistance* (within the experimental accuracy limits) of mercury below 4.2K (figure 1.1(b)).

Third-hand stories explain that liquid helium and superconductivity findings were ruled by moments of serendipity[1,2]. In the case of superconductivity, tales explain that Onnes and his team supposed to have a short-circuit after several observations of zero resistance in the mercury wire. One of the apprentices, appointed to control the helium vapour pressure, nodded off during one of the experiments and let the helium boil. He himself witnessed then that the galvanometer suddenly indicated a jump in resistance. That jump was the evidence of a *critical temperature* (T_c) that separated the normal from the superconducting state of mercury. Regardless of the authorship of that triumph, it signified not only the birth of a new field in the study of materials, which would permit to develop a new technology in the areas of high energy physics, medical imaging or electrical power industry, but also of a novel style of doing science using large scale laboratories.

1.2 Phenomena and theories

By the demonstration of permanent currents in superconducting rings, accomplished by the same Onnes in 1914[3,4] and by other more recent studies using nuclear resonance[5], it is known that the resistance in the superconducting state is zero in a very accurate measure, namely the lower limit of the characteristic current decay time is established to be 10^5 years. Thereby, this phenomena implies *perfect conductivity*.

Although such a property is especially interesting for technological purposes as the generation of permanent high magnetic fields using superconducting coils, Onnes realized very promptly that superconductivity quenches under a *critical magnetic field* (H_c), that was very low for the superconducting materials of that time. In 1917, Silsbee wrote down that the electrical current that generates the critical magnetic field at the surface of the wire is also a critical parameter, named *critical current* (I_c). Temperature, magnetic field and electrical current: the three guards of superconductivity.

In 1933, Meissner and Ochsenfeld published[6] another effect for superconducting materials: the exclusion of magnetic flux from the superconductor at temperatures below T_c: not only the magnetic flux is expelled when applying it to a cold superconductor but also when the magnetic field is already applied in the normal state and the material is cooled down through T_c, confirming that the superconducting state is a thermodynamic state. This state of magnetic exclusion is named *perfect diamagnetism* or *Meissner effect* and also explains why a superconductor quenches at H_c in terms of the energy needed to exclude the magnetic field.

The first successful theoretical models to explain superconductivity were developed in the 1930s with a basic idea of two electrical fluids: one with normal electrons and another with superconducting electrons. Gorter and Casimir proposed a thermodynamic model stating that the free energy F in the superconducting state F_s and in the normal state F_n is different. This difference ΔF is the *condensation energy*, that is reached magnetically when the external field is the *thermodynamic critical field* H_{cth}:

$$\Delta F(T) = F_n(T) - F_s(T) = \frac{\mu_0 H_{cth}(T)^2}{2} \tag{1.1}$$

Where $\mu_0 = 4\pi 10^{-7}\frac{\mathrm{Tm}}{\mathrm{A}}$ is the magnetic permeability of vacuum. On the other hand, the London brothers describe electromagnetism in superconductors starting from Drude's model and Maxwell equations. They arrive to the conclusion, in the called second London equation that the zero magnetic induction observed by Meissner and Ochsenfeld is obtained by the screening of supercurrents J_s flowing at the surface of the superconductor:

$$\vec{\nabla} \times \vec{J_s} + \vec{B} = 0 \tag{1.2}$$

And thereby, the magnetic field induction decays exponentially when entering the superconductor in the form:

$$\vec{\nabla}^2 \vec{B} - \frac{1}{\lambda^2}\vec{B} = 0 \tag{1.3}$$

Where λ is the magnetic field *penetration depth.* An applied exterior magnetic field B_{ext} parallel to the z-axis in the Cartesian coordinate system implies that the magnetic field inside of the superconductor B_z follows a decay along the x-axis as:

$$B_z(x) = B_{ext,z} e^{\left(-\frac{x}{\lambda}\right)} \tag{1.4}$$

In 1950, Ginzburg and Landau used general theory of second order transitions and quantum mechanics and introduced the *order parameter* ψ that describes the local superconducting electrons density n_s ($|\psi|^2 = n_s$).

In a superconductor/normal-metal interface, illustrated in figure 1.2, the result is that the magnetic field decays exponentially with λ, whereas the order parameter decays as:

$$\psi(x) = tanh(\frac{x}{\sqrt{2}\xi}) \tag{1.5}$$

Where the characteristic length ξ is known as the *coherence length.* From the assumptions of this theory, both characteristic lengths λ and ξ increase with increasing temperature and diverge for T → T_c[7] (very similar to empiric observations):

$$\lambda(T) = \frac{\lambda_0}{\sqrt{1 - \frac{T}{T_c}}} \tag{1.6}$$

$$\xi(T) = \frac{\xi_0}{\sqrt{1 - \frac{T}{T_c}}} \tag{1.7}$$

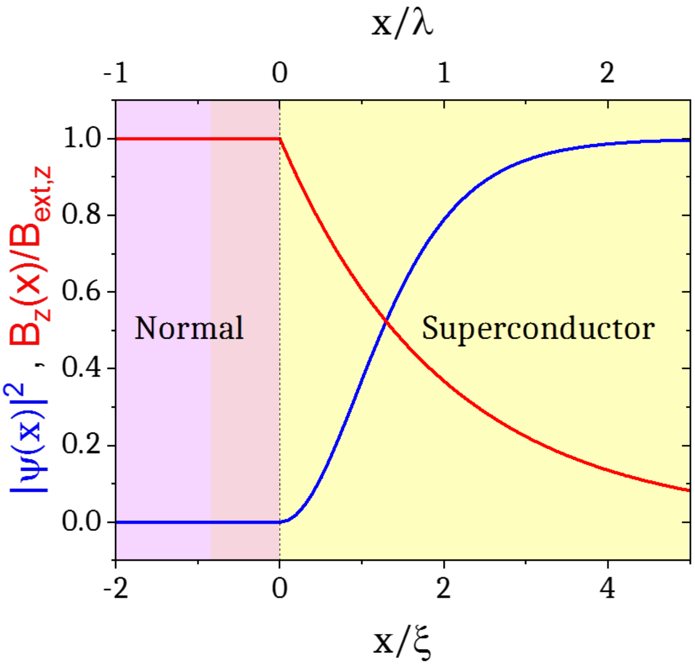

Figure 1.2: spatial dependence of $B_z/B_{ext,z}$ and ψ in the interface between a normal metal and a hypothetical superconductor with $\kappa = \lambda/\xi = 2$.

Only macroscopic theories have been hitherto discussed that do not provide insight into the microscopic origin of superconductivity. However, some experiments showed the *isotope effect*[8–10] reporting a relation between T_c and the mass of the ions M: $T_c \propto 1/\sqrt{M}$, revealing that the crystal lattice plays an important role for superconductivity. In 1957, Bardeen, Cooper and Schiffer developed a microscopic theory of superconductivity, the BCS theory[11]. The key element of this theory is the pairing of the superconducting electrons (*Cooper pairs*) by the presence of a weak attractive interaction mediated by the the lattice vibrations (electron-phonon interaction). Cooper pairs behave as bosons and fall into a coherent ground state forming a Bose condensate. In this condensate, movement of pairs does not involve dissipation. When the kinetic energy of Cooper pairs equals their own binding energy, the Cooper pair breaks at the *depairing critical current density* J_{dp}[7,12]:

$$J_{dp} = \frac{\phi_0}{3\sqrt{3}\pi\mu_0\lambda^2\xi} \tag{1.8}$$

Where $\phi_0 = 2.07 \cdot 10^{-15}$ Wb is the magnetic flux quantum.

1.3 Types of superconductors

After mercury, other metals were found to be superconductors at rather low temperatures, the highest being niobium at 9.25 K. Not only pure elements but also alloys and materials with multiple elements have displayed a superconducting state that just like metals have been explained by the BCS theory, known as *conventional superconductors*.

However, new families of superconductors as heavy-fermion superconductors first observed in the late 70s (see figure 1.3) and oxide cuprates in the 80s displayed a superconducting state that cannot be explained by the BCS electron-phonon coupling, therefore classified as *unconventional superconductors*. Until now, some carbon-based materials like fullerides and also iron pnictides have appeared as new superconductors that are unconventional as well, whereas the recently found hydrogen sulfide (a stinky gas that under the pressure of 155 GPa shows the highest $T_c = 203$ K obtained for any superconductor) belongs to BCS superconductors.

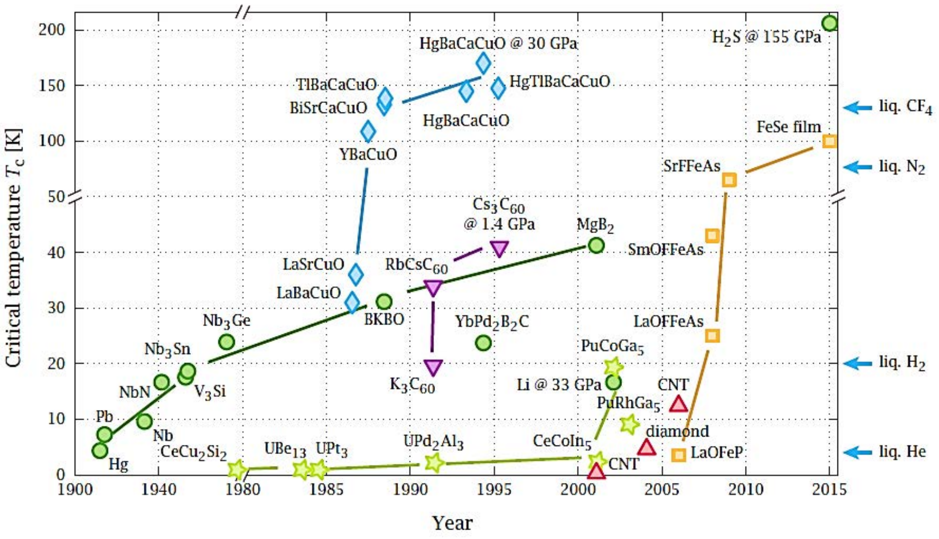

Figure 1.3: timeline of the finding of new superconductors[13]. Conventional superconductors (green circles), heavy fermion (green stars), cuprates (blue diamonds), fullerides (purple triangles), carbon nanotubes (red triangles) and iron-based (yellow squares) superconductors are included.

In a century of history, the variety and complexity of superconductors has expanded to very singular and surprising materials that have been hard to be conformed to an ubiquitous model of superconductivity capable of predicting the finding of new superconductors[14].

Anyhow, theories and experiments led to another interesting separation of superconductors regarding the different response under an applied magnetic field. According to the model developed by Ginzburg and Landau, the energy of the boundary between normal and superconducting regions can be either positive or negative depending on the ratio $\kappa = \lambda/\xi$. When the energy of the boundary is negative, the formation of a normal-superconductor boundary lowers energy and becomes favourable. This differentiates two kinds of superconductors:

$\kappa < 1/\sqrt{2}$	positive boundary energy	Type I (sometimes referred as soft)
$\kappa > 1/\sqrt{2}$	negative boundary energy	Type II (sometimes referred as hard)

In type I (see figure 1.4(a)), there are no boundaries except from the surface and therefore a total exclusion of the magnetic field is given. Meissner state occurs up to H_c, which corresponds to H_{cth}.

In type II (see figure 1.4(b)), the Meissner state occurs only up to the *lower critical field* H_{c1}. Between H_{c1} and the *upper critical field* H_{c2}, the magnetic field penetrates forming normal regions by means of quantized cylindrical flux lines called *vortices* (where $H_{c1} < H_{cth} < H_{c2}$ and $H_{c1} << H_{c2}$). In this phase between H_{c1} and H_{c2}, known as the *mixed state*, the superconductor is not perfect diamagnetic.

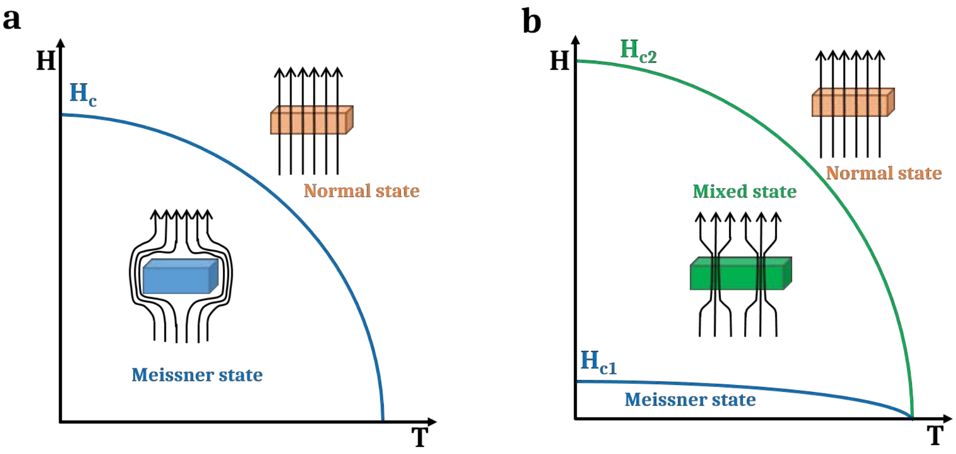

Figure 1.4: H-T magnetic phase diagrams for (**a**) a type I superconductor and (**b**) a type II superconductor.

1.4 Vortex matter in type II superconductors

Before the theoretical development of Ginzburg and Landau, there was already evidence of a new type of superconductors that were not completely diamagnetic. Shubnikov published in 1934 some results on PbTl alloys that showed the gradual penetration of the magnetic field from H_{c1} up to H_{c2}[15]. It took long to attribute this effect to the presence of vortices. Vortices are formed by a core of normal electrons surrounded by the superconducting current J_s with sizes of 2ξ and 2λ respectively (see figure 1.5). The total flux of a vortex is the magnetic flux quantum ϕ_0, that corresponds to the minimum unit of the quantized magnetic flux inside of a superconducting loop.

Vortices interact repulsively to each other leading to the arrangement of a vortex lattice, which was predicted by Abrikosov to be triangular (after some corrections). The first evidence of the existence of vortices was the observation of the triangular arrangement by Essman and Träuble using Bitter magnetic decoration[16]. The lattice proposed by Abrikosov was observed in single crystals. However, in bulk superconductors or thin films, vortices distribute differently due to the existence of structural inhomogeneities in the material called *pinning sites* that yield a local reduction of ψ.

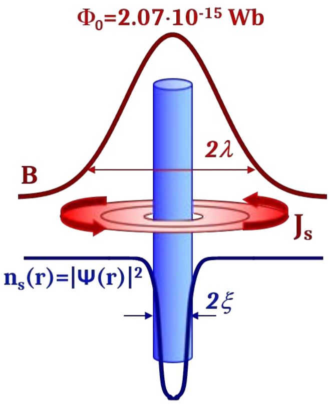

Figure 1.5: schematic view of a vortex. The blue cylinder represents the normal core with radius ξ surrounded by the red superconducting current J_s that generates the magnetic flux quanta ϕ_0 within a surface of $\pi\lambda^2$.

When an electrical current is applied to a type II superconductor, the interaction between the applied current, the magnetic flux in the vortex and the superconducting currents surrounding vortices gives as a result a force acting on the vortices that is equivalent to the Lorentz force that would act on a charge in movement:

$$\vec{F_L} = \vec{J} \times \vec{B} \tag{1.9}$$

Since vortices are formed by a core of normal electrons, any movement of vortices would imply dissipation and type II superconductors would have a null critical current density J_c. However, pinning sites with locally reduced $|\psi|^2$ provide an opposite force to the movement of vortices and therefore J_c is finite (see figure 1.6).

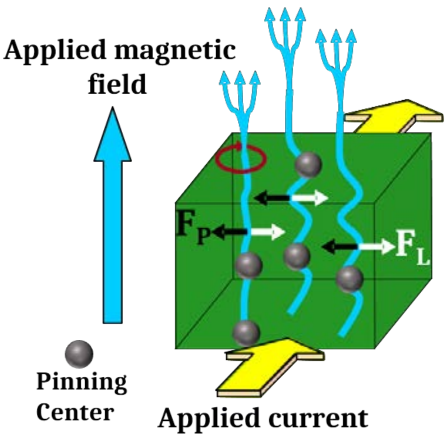

Figure 1.6: schematic view of the competition between the pinning force and the lorentz-like force originated from the local reduction of $|\psi|^2$ and the interaction of the superconducting current and the magnetic field, respectively.

As long as the lorentz-like force do not surpass the pinning force provided by the pinning sites, the current will pass through the material without voltage drop. When the lorentz-like force is equal to the pinning force, vortices start to move and the system starts to dissipate. In the mixed state then, J_c is the *depinning critical current density*, the current density where the lorentz-like force is equal to the pinning force:

$$|\vec{F_P}| = |\vec{F_L}| = |\vec{J_c} \times \vec{B}| \tag{1.10}$$

For $J > J_c$, the mean effective field E_{eff} is locally related to the rate of cutting of flux[17]:

$$\vec{E_{eff}} = \vec{v} \times \vec{B} \tag{1.11}$$

Where v is the local velocity of vortices. Experimentally, J_c is measured by evaluating the dissipation-current characteristics. Figure 1.7(a) displays the expected idealized electric field - current density (E-J) response in a type II superconductor. At current densities below J_c, $F_L < F_P$ and E is zero, whereas above J_c, $F_L > F_P$ and E increases with increasing J. In reality, the E-J relation shows a rounded transition as shown in figure 1.7(b), due to the interaction between vortices and to the thermal activation explained below in section 1.6.2. In the region where $J \sim J_c$, E-J can be approximately fitted to a power law relation $E \propto J^n$, which is linear when plotted in log-log scale in figure 1.7(c). n tells information about the magnetic flux dynamics and the shape of the pinning potentials U(J) in the superconductor, which will be further explained in section 1.6.2.

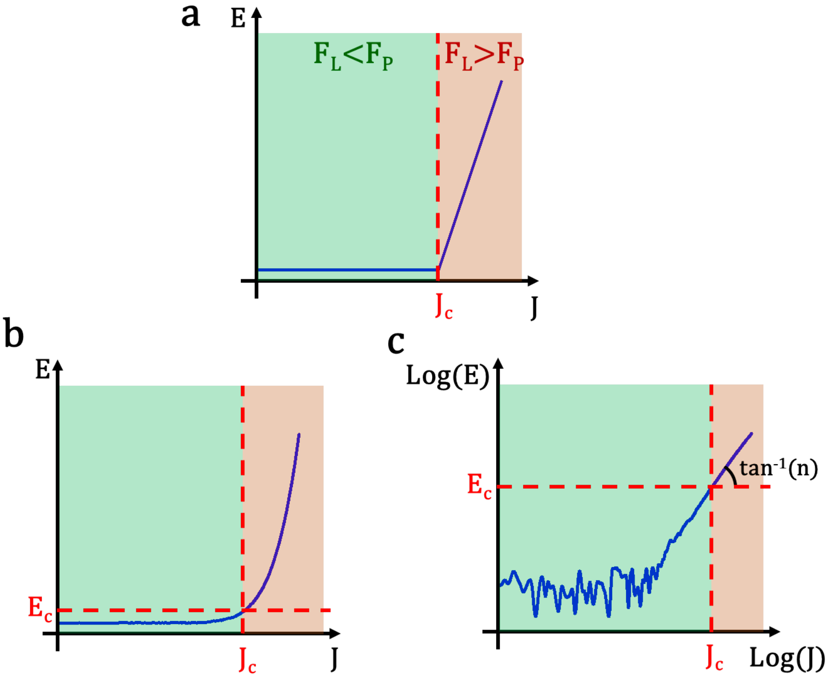

Figure 1.7: (a) idealized and (b-c) experimental response of the electric-field–current-density characteristics in a type II superconductor. The axes scales is linear in (a-b) and logarithmic in (c).

Unlike type I superconductors, type II exhibit a strong magnetic hysteresis. A way to understand such magnetization loops is using the *Bean critical state model*[18]. This model describes the magnetization loops as the consequence of the competition between pinning and lorentz forces, that causes a magnetic field gradient into the superconductor. The gradient of the magnetic field is constant and proportional to the superconducting currents that flow through the gradient with a current density that is J_c. Although this model is based on several approximations, it can be used in thin films to determine the value of J_c from the width of the saturated magnetization hysteresis loop ΔM_{sat} as[19,20]:

$$J_c = \frac{3\Delta M_{sat}}{2R_{eff}} \tag{1.12}$$

Where R_{eff} is the effective radius that would have a cylinder with the same surface as the thin film.

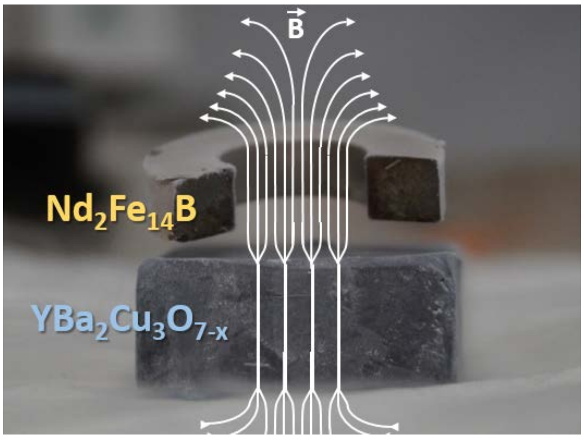

Figure 1.8: stable levitation of a neodimium magnet above a cooled bulk $YBa_2Cu_3O_{7-x}$ ceramic superconductor. Image taken at the Institut de Ciències Materials de Barcelona (ICMAB). White arrows indicate the path of flux lines that get quantized as they penetrate the type II superconductor.

In type II superconductors, *flux pinning* avoids the motion of vortices and resists against any variation of the magnetic field in the material that alterates the vortex and supercurrents configuration. The flux is therefore trapped, and this is believed to be the source of stable levitation in these materials[21], like the levitation of a hard ferromagnet above the type II superconductor $YBa_2Cu_3O_{7-x}$ shown in figure 1.8 (the levitation is also possible the other way round, as long as the superconductor stays cool below T_c).

The measured upper critical fields H_{c2} for type II are much more intense (tenths and even a hundred of T) than H_c for type I (tenths and hundreds of mT). Hence, the original idea of Onnes to use superconductors for electric power and magnetic applications was relaunched again. Large critical current densities could, after all, be supported in superconductors at high magnetic fields and today type II superconductors play a major role in modern science and technology[15].

Magnetic resonance imaging devices in hospitals and the magnetic coils that accelerate particles in the Large Hadron Collider are made from NbTi type II superconductor, with $H_{c2} = 15T$. High magnetic field facilities around the world count on several type II superonducting magnets (made out of NbTi, Nb_3Sn, $Bi_2Sr_2CaCu_2O_{8-x}$, $YBa_2Cu_3O_{7-x}$ or hybrid architectures) that reach permanent magnetic fields up to 45 T in direct current (dc). Furthermore, different type II superconductors have been successfully manufactured as commercial conductors (NbTi, Nb_3Sn, $Bi_2Sr_2CaCu_2O_{8-x}$, $(Bi, Pb)_2Sr_2Ca_2Cu_3O_{10-x}$, $YBa_2Cu_3O_{7-x}$ and MgB_2). Today, such conductors are used for high field magnets and are capable to be used in high-current cables for the transmission of electricity, fault-current limiters, transformers, rotating machines, motors, generators, levitating trains and magnetic separators.

1.5 High temperature superconductors

A remarkable breakthrough came in 1986 when Bednorz and Müller found superconductivity in a ceramic material based on copper oxide[22]. This new family of superconductors, called cuprates, opened the door to high temperature superconductors (HTS), since several cuprates exhibited T_c close to 100 K, far above the boiling point of nitrogen (77 K), which is less costly to find, liquefy and store than helium. After that, other high temperature superconductors have been found (see figure 1.3), but cuprates have still the best chances to substitute metal alloys in high current applications thanks to the very large H_{c2} and large J_c at intense magnetic fields.

Cuprates are type II superconductors and regrettably very anisotropic compounds. In these materials, it is mandatory to obtain a good epitaxy and to keep low angles between grains in order to reach highest superconducting performances. Copper oxide (CuO_2) planes form a common structural element, and they are constituted as the superconducting planes (highest local ψ). The anisotropy is directly related with the distance between these CuO_2 planes.

The layered structure of these materials with a weak inter-planar coupling, their extremely short ξ, the considerably large λ and the increment of thermal fluctuations originated at higher temperatures result in an intricate scheme of different vortex states in the magnetic phase diagram, which has given rise to the vortex physics matter of HTS.

At high temperatures, the thermal energy overcomes the energy involved in the interactions between vortices for the formation of a solid lattice, causing the appearance of a phase transition determined by a melting line. This line is a thermodynamic transition of first order for homogeneous pure crystals and of second order for samples with high amount of disorder, receiving the name of irreversibility line $H_{irr}(T)$. $H_{irr}(T)$ separates the region where vortex matter behaves as a solid (with $J_c \neq 0$) from the region where vortex matter behaves as a liquid (with $J_c = 0$). Even though the material remains in a superconducting state between $H_{irr}(T)$ and $H_{c2}(T)$ with $\psi \neq 0$, vortices cannot be pinned due to their elastic behaviour and have a null J_c. Thus, $H_{irr}(T)$ marks the limit of high-current applicability in type II superconductors.

Figure 1.9 shows $H_{c2}(T)$ and $H_{irr}(T)$ compared for different type II superconductors, among them NbTi, Nb_3Sn, MgB_2, iron based pnictides and cuprate superconductors.

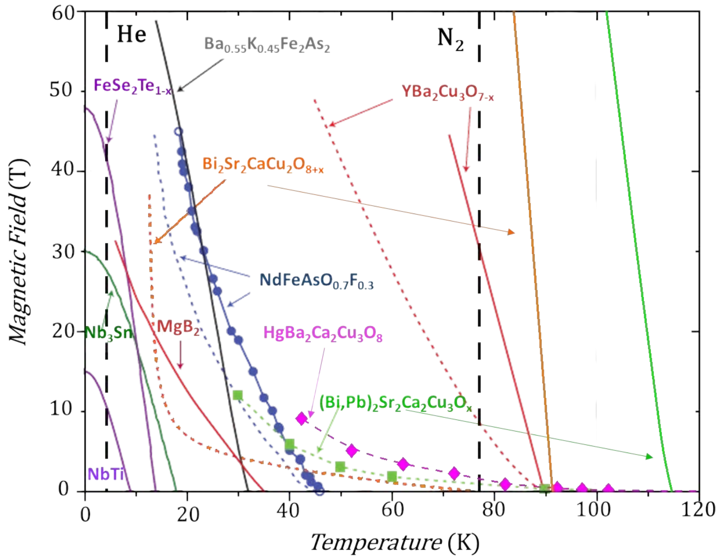

Figure 1.9: comparison of upper critical fields and irreversibility fields in the magnetic phase diagram for different type II superconductors (adapted from[23–25]). Solid curves correspond to $H_{c2}(T)$, dashed curves to $H_{irr}(T)$ and straight dashed lines to the boiling temperatures for helium and nitrogen.

Although $YBa_2Cu_3O_{7-x}$ is the cuprate superconductor with neither highest T_c nor best $H_{c2}(T)$, it provides the highest $H_{irr}(T)$ and therefore, it is the most appealing HTS for the transport of high currents at high magnetic fields.

1.6 YBCO

$YBa_2Cu_3O_{7-x}$, from now on YBCO, is the studied material in this thesis. It is an HTS, unconventional and type II superconductor from the family of cuprates. It crystallizes in a triple perovskite with a unit cell composed by a central YCuO block and two adjacent BaCuO blocks stacked vertically along the c-axis (see figure 1.10). Y can be substitued by other rare earth (RE) elements except by Pr (known as the REBCO family). The planes surrounding the Y^{+3} ion are CuO_2 planes lying normal to the crystallographic c-axis. They are the planes where superconducting current flows[26], separated by charge reservoir blocks which contain oxygen deficient planes between the Ba^{+2} ions, formed of CuO chains. The amount of oxygen vacancies determine the final oxygen content x, which is of prime importance for the superconducting state in cuprates.

The oxygen content determines if the crystal structure is either tetragonal or orthorhombic. It is in the orthorhombic phase that YBCO is superconducting. This superconducting phase appears at a specific doping region between a normal metal at high carrier concentration and an antiferromagnetic insulator at low carrier concentration[27,28], with T_c following an approximately parabolic dependence on the oxygen content x, with a T_c maxima of 92-94 K when it is optimally doped at $x \approx 0.06$[28,29]. The lattice parameters of the YBCO orthorhombic phase are[30]:

a (Å)	b (Å)	c (Å)
3.823	3.886	11.681

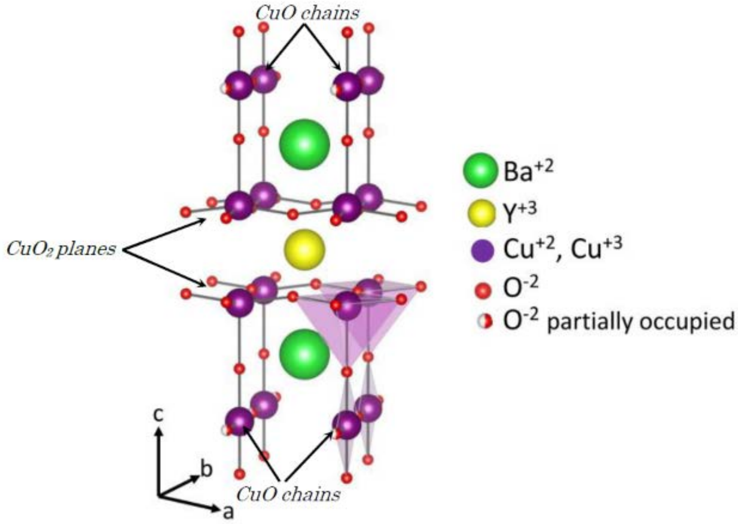

Figure 1.10: crystallographic view of the superconducting $YBa_2Cu_3O_{7-x}$ orthorhombic phase unit cell.

Although the anisotropy in YBCO is not as pronounced as in other cuprate superconductors, YBCO has higher conduction in the ab-plane (carriers are usually localized in the CuO_2 planes) than along the c-axis. This anisotropy, derived from the layered structure of YBCO, affects the effective electron mass and the characteristic lengths of vortices λ and ξ. It means that the nature of vortices change depending on the orientation of the magnetic field with respect to the crystallographic axes. As depicted in figure 1.11(a), λ_{ab} and ξ_{ab} are the characteristic lengths when the magnetic field is applied parallel to the c-axis (H||c). λ and ξ evolve to different values λ_c and ξ_c, when the magnetic field is applied parallel to the ab-planes (H||ab). The extrapolation of these values to the temperature of 0 K yields[17]:

H||c	H||ab
$\lambda_{0,ab}$=135nm	$\lambda_{0,c}$=890nm
$\xi_{0,ab}$=1.6nm	$\xi_{0,c}$=0.24nm

These values, combined with equations 1.6 and 1.7, describe the temperature dependence of the different characteristic lengths, plotted in figure 1.11(b).

The vortex anisotropy parameter γ is the ratio between the characteristic lengths at different orientations, which is equal to the square root of the electronic mass anisotropy m_c/m_{ab}[7]. γ remains constant with temperature:

$$\gamma = \sqrt{\frac{m_c}{m_{ab}}} = \frac{\lambda_c}{\lambda_{ab}} = \frac{\xi_{ab}}{\xi_c} \tag{1.13}$$

γ is an intrinsic parameter that varies for each material. According to the values from literature[17,31,32], YBCO has a $\gamma \sim 5-7$.

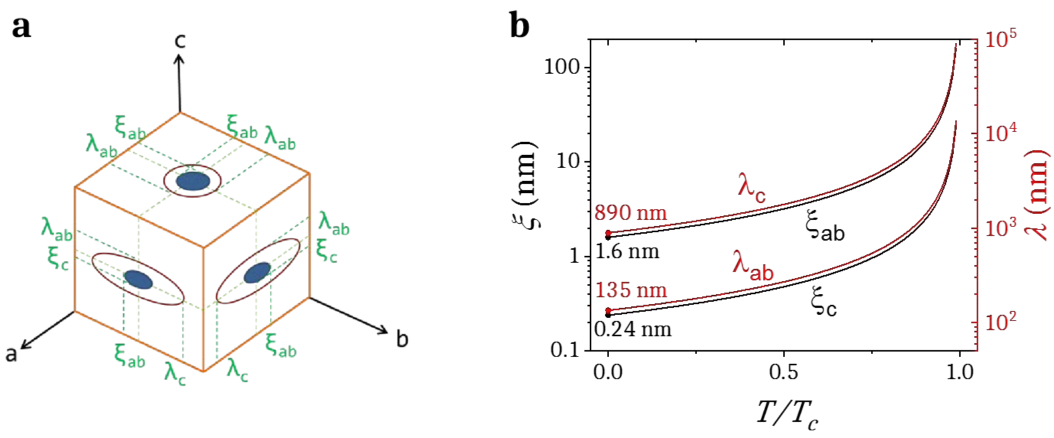

Figure 1.11: coherence length ξ and penetration depth λ in YBCO. (**a**) Sketch of ξ and λ for the different orientations of the magnetic field along the crystallographic axes and (**b**) temperature dependence of ξ and λ, derived from equations 1.6 and 1.7.

1.6.1 Vortex pinning in YBCO

The microstructure of YBCO is very rich in defects. Figure 1.12 shows a schematic representation of typical defects observed in YBCO films. Some of them, such as misoriented grains, high angle grain boundaries or porosity are detrimental to the superconducting properties and must better be avoided. However, stacking faults, partial dislocations, twin boundaries, vacancies, strained nanoregions and small nanoparticles and nanorods (with $\varnothing \lesssim$ 5nm) yield to a local reduction of superconductivity within nanometric sizes of the order of ξ and therefore are considered to be good candidates for vortex pinning.

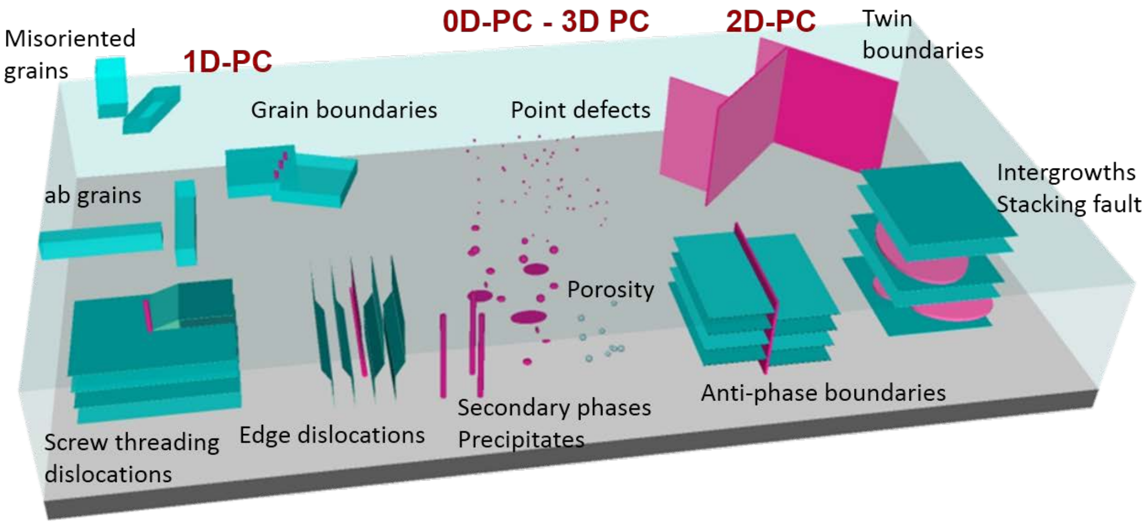

Figure 1.12: schematic view of the most common defects in YBCO films. Pink regions represent nanosized regions able to act as pinning centres. The dimensionality of the pinning centres is also indicated.

Depending on the dimensionality of the defects, they can be differentiated into two kinds of pinning centres: 0D and 3D pinning centres like vacancies, strained nanoregions or nanoparticles (secondary phases) generate *isotropic pinning*, also called random pinning centres, whereas 1D and 2D pinning centres like stacking faults, partial dislocations, twin boundaries or nanorods generate *anisotropic pinning*, also called correlated pinning. Both isotropic and anisotropic pinning centres contribute distinctively to the final J_c for different magnetic field orientations, meaning vortex orientations.

There is an additional source of anisotropic pinning that has the peculiarity of not being originated by a defect, but by the layered structure of cuprates itself. As described in section 1.5, superconductivity is localized in the CuO_2. This effect, called *intrinsic pinning*[33], describes the modulation of ψ along the c-axis with the period of the lattice (maximums at the CuO_2 planes and minimums in between), giving rise to anisotropic pinning for H||ab.

According to the origin of pinning centres, they can be either *natural pinning centres*, when they accidentally appear in the film during growth, or *artificial pinning centres*, when they are intentionally introduced. When the latter is obtained, the films are usually called *nanostructured YBCO* or *YBCO nanocomposites*, consisting in the deliberate introduction of nanosized secondary phases within the structure of YBCO or the inducement of columnar tracks through ion irradiation, accomplished in order to engineer and optimize the pinning landscape of defects[34–40].

The nature of the solid vortex phase in YBCO is determined by the competition between vortex-vortex interactions and vortex-defect interactions. The former promotes the formation of a long-range translational order vortex lattice, whereas the latter, typical in the presence of disorder, favours the appearance of a glass with short range order[41].

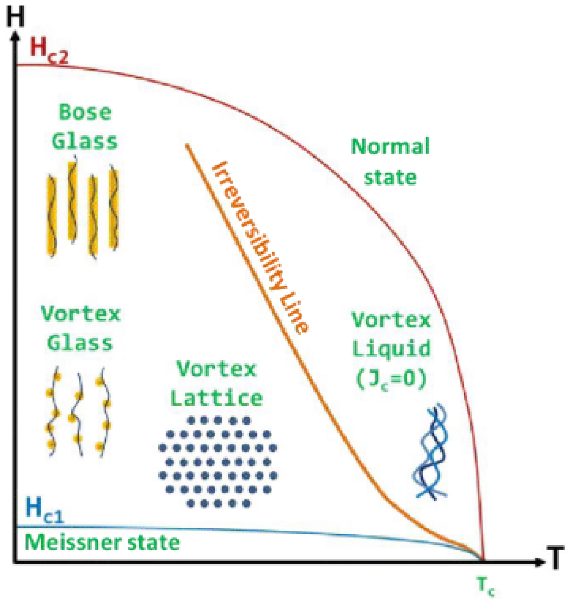

Figure 1.13: representation of the magnetic phase diagram of YBCO in presence of disorder.

Under pinning dominated by isotropic point disorder, the vortex glass phase[42,43] is expected, characterized by line wandering[7]. When the dominating disorder is anisotropic, vortices are very localized in the region of the correlated defects, giving rise to the Bose glass phase[44,45]. Figure 1.13 displays the schematic representation of the typical magnetic phases of defect-rich YBCO that ultimately determine the dependence of J_c with temperature and magnetic field.

1.6.2 Thermally activated flux creep in YBCO

In HTS, operating temperatures can be high, the coherence length is small and the anisotropy is large, leading to thermal fluctuations that strongly influence vortex dynamics. Some of the manifestations of thermal activated flux creep is the decay of persistent currents with time, the relaxation of trapped magnetic fields and the rounded shape of the electric-field–current dependence E(J).

The standard flux creep model is a theory developed by Anderson and Kim to give explanation to these effects, especially that one of the E(J) dependence, introducing the concept of thermal activation and predicting a relaxation process that consists of a slow redistribution of flux lines, causing a change in the magnetic moment with time, generally referred as magnetic flux creep[46–48].

At non-zero applied current, flux creep is possible with the help of thermal activation even if $F_L < F_P$. In this model, flux lines originated by z-oriented magnetic field B are assumed to jump pinning barriers as a unit (encouraging cooperative motion) because λ (indicative of the repulsive interaction range) is typically larger than the distance between lines. Therefore, the force on the flux line and the thermal activation act together against the pinning barrier U_P.

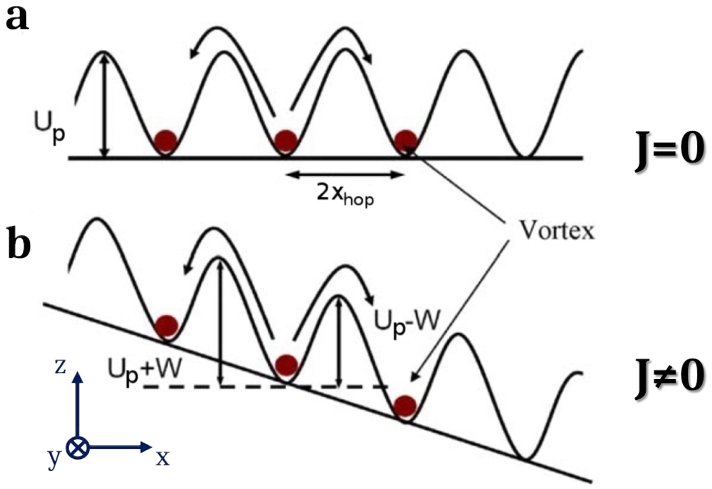

Figure 1.14: sketch of the spatial potential energy (a) for no applied current and (b) for an applied current.

The model considers a linear spatial dependence of the pinning barriers U(x) with the form of a sawtooth sketched in figure 1.14(a), where U(x) maximums reach U_P, representing a system with homogeneous pinning centres. Then, the rate R of hopping through a particular barrier due to thermal activation is[17,49]:

$$R = R_0 e^{-U_P/k_B T} \tag{1.14}$$

Where R_0 is the attempt hopping frequency of the flux lines lying in the z direction and k_B is the Boltzmann constant. In the case that a current is applied along the y direction (see figure 1.14(b)) the potential barriers become tilted along the x direction by an extra potential W associated to the lorentz-like force f acting on a given flux line derived from equation 1.9:

$$-\frac{\mathrm{d}W}{\mathrm{d}x} = f = JBV_d \tag{1.15}$$

Where V_d is the volume of the moving flux line. As a result, the energy necessary to overcome the potential barrier changes at each sense of the x direction: to the right it is reduced to $U_P - fx$ and to the left it is increased to $U_P + fx$. Then, the net rate R of hopping to the right is:

$$R = 2R_0 e^{-\frac{U_P}{k_B T}} \sinh\left(\frac{f x_{hop}}{k_B T}\right) \tag{1.16}$$

Where x_{hop} is the distance from the minima to the maxima of the sawtooth potential (hopping distance). The mean flux-line velocity comes as a result $2x_{hop}R$ and the dissipated electric field E, applying equation 1.11, becomes $E = 2x_{hop}RB$. From equation 1.15, W should be a decreasing function of J. As a first approximation, the net barrier is reduced linearly with J:

$$W = -U_P \frac{J}{J_0} \tag{1.17}$$

Where J_0 corresponds to the critical current density required to tilt the barrier pinning potential to zero: $J_0 = U_P/BV_d x_{hop}$. Then, the electric-field–current-density relation E(J):

$$E = 4x_{hop} R_0 B e^{-\frac{U_p}{k_B T}} \sinh\left(\frac{U_P J}{k_B T J_0}\right) \tag{1.18}$$

From this expression, three regimes are expected for different ranges of J:

- when $J << J_0$, then $\sinh(U_P J/k_B T J_0) \approx U_P J/k_B T J_0$, the electric field becomes proportional to J and the system develops a small resistivity. This regime is called thermally activated flux flow (TAFF).
- when $J \approx J_0$, and also taking into account the general case that $U_P >> k_B T$, then the hyperbolic sinus can be simplified as $\sinh(U_P J/k_B T J_0) \approx \frac{1}{2} e^{U_P J/k_B T J_0}$. This is the flux creep regime, where the electric field increases exponentially with the current.

- when J >> J_0, the pinning barriers stop mattering and the flux flows steadily with a resistivity $\rho = \rho_n B/B_{c2}$, due to the damping of the medium and total absence of pinning, where ρ_n is the resistivity at the normal state. This is the flux flow regime, where the electric field increases linearly with the current.

Zeldov et al[50] introduced the description of a barrier potential that decays logarithmically with the current density instead of linearly, determined from the experimental data acquired by analysing the V-I characteristics:

$$W = -U_P \ln\left(\frac{J}{J_0}\right) \tag{1.19}$$

Thus, the electric field in the flux creep regime with a logarithmic potential can be approximated to:

$$E \approx \frac{2x_{hop} R_0 B e^{-\frac{U_p}{k_B T}}}{J_0^{U_P/k_B T}} J^{U_P/k_B T} \tag{1.20}$$

In this regime then, E(J) can be fairly well fitted to a power law $E = AJ^n$ (as illustrated in figure 1.7(c)), where A and n are constants. The power index n is equivalent to the logarithmic derivative of the E(J) relation:

$$n = \frac{\mathrm{d}\left[\ln(E)\right]}{\mathrm{d}\left[\ln(J)\right]} \approx \frac{U_P}{k_B T} \tag{1.21}$$

Hence, n is directly proportional to the pinning energy in the system and provides information on the vortex dynamics in the region of flux creep.

1.6.3 YBCO nanocomposite coated conductors

Vortex pinning and flux creep depend on the magnetic field orientation, causing a magnetic field orientation dependency of J_c and n as well. Even at the orientation of the magnetic field where critical currents are lowest (in general, H||c), YBCO enhances remarkably the three critical parameters J_c, T_c and H_{c2} in comparison to the workhorse of low temperature magnets NbTi as depicted in the J-T-H 3D graph in figure 1.15(a). Thus, YBCO is an ideal candidate for high magnetic field applications.

As explained in section 1.6.1, a proper change in the microstructure of $YBa_2Cu_3O_{7-x}$ can be performed by the growth of nanocomposites (that combine superconducting $YBa_2Cu_3O_{7-x}$ with nanometric non-superconducting regions) in order to enhance the pinning sites and therefore enlarge even more J_c or H_{c2}.

Furthermore, the successful development of suitable methods to grow epitaxial YBCO films on top of bi-axially textured substrates following a multilayered architecture, named *coated conductors* (CCs, see figure 1.15(b)), has raised new opportunities to promote

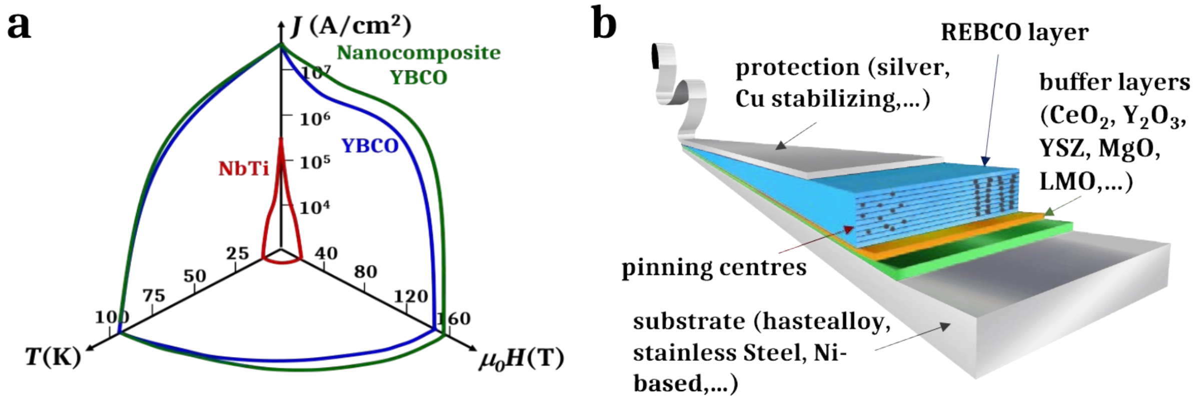

Figure 1.15: (**a**) 3D plot of the critical parameters J_c, T_c and H_{c2} for NbTi, pristine $YBa_2Cu_3O_{7-x}$ and $YBa_2Cu_3O_{7-x}$ nanocomposite for H||c and (**b**) sketch of the typical architecture of a CC.

practical and scalable conductors for power applications at high magnetic fields and temperatures[51–56].

The magnetic field-temperature ranges which should be attainable now with YBCO CCs are much wider than with any other found superconducting material and many research programs have been established in USA, Japan, Europe, Korea and China to follow up the development of such conductors. In the framework of the European consortium Eurotapes (European Development of Superconducting Tapes)[56], composed of 21 European partners including industries and leaded by ICMAB, one of the main issues has been the optimization of the superconducting performance of REBCO films that are grown by pulsed laser deposition (PLD) or chemical solution deposition (CSD).

This thesis is focused on the analysis of the interplay between microstructure and the electrical performance of YBCO films grown by CSD, in particular YBCO nanocomposites with the inclusion of nanoparticles, in order to understand and determine the range for improvement in vortex pinning and flux creep when adding secondary phases in the YBCO matrix.

CHAPTER 2

EXPERIMENTAL METHODOLOGY

2.1 Sample growth from chemical solution deposition

There are several methods that can be used to grow highly textured YBCO films and avoid the presence of high angle grain boundaries that would imply a decrease of the superconducting properties[57]. Most of CC fabrication techniques require a highly pure environment and sophisticated vacuum control as sputtering[58], pulsed laser deposition[59,60], pulsed electron deposition[61], liquid phase epitaxy[62] or chemical vapor deposition[63].

Chemical solution deposition (CSD) emerged as a low cost long length scalable technique for the fabrication of high performance CCs at atmospheric pressure (no vacuum in any step of the process). It is a very different approach where the solution composition and the deposition parameters determine the final thickness while the film epitaxy is achieved during a separate growth process[64–66].

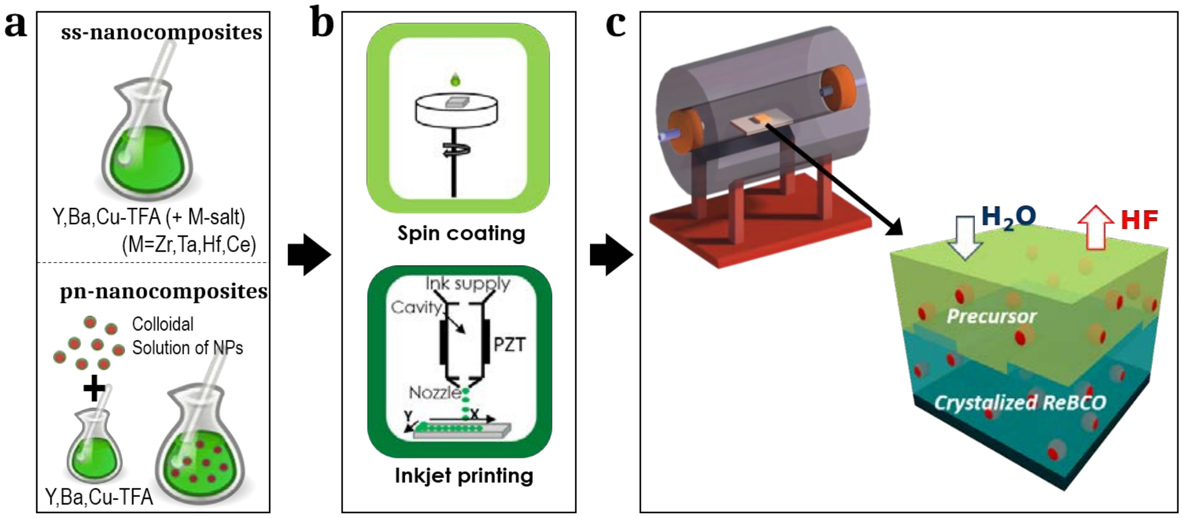

Figure 2.1: sketch of the steps for the CSD-TFA growth route of YBCO nanocomposite films. (a) Solution preparation, (b) deposition technique and (c) heating steps.

The films studied in this work have been grown by CSD from the metal-organic decomposition of trifuoracetate (TFA) salts in solution[67,68], which is the most widely used solution-based route to achieve epitaxial YBCO. Recently, the interest of decreasing the amount of fluorine has increased and several groups (ours among them) has devoted special effort to work with the so-called low fluorine solutions[69–72] (where only 70% or 80% or the metallorganic salts contain fluor), or even with fluorine free carboxylate salts in which case the growth mechanism changes completely[73].

The steps of the CSD-TFA route are depicted in figure 2.1. First, a precursor solution of adequate stoichiometry, purity and rheological parameters needs to be prepared. Secondly, the solution is deposited on the substrate, which is a decisive step for the final thickness of the film. Finally, the film is heated according to the following steps: first, a pyrolysis for the elimination of the organic material and generation of solid nanophases and then a heating process at higher temperatures where the film crystallizes in the YBCO phase and is oxygenated to get into the superconducting phase with optimal doping.

2.1.1 Solution synthesis

The preparation of the metal-organic TFA YBCO precursor solution consists of the dissolution of YBCO powder in an excess of trifluoroacetic anhydride, a small quantity of trifluoroacetic acid (Aldrich 99%) and distilled acetone, stirred and heated at 55° for 60 h, subsequently filtered and evaporated through vacuum[65,68,74].

Afterwards, the mixture of TFA salts ($Ba(TFA)_2$, $Cu(TFA)_2$ and $Y(TFA)_3$) is redissolved in anhydrous methanol or dry acetone. This solution is finally stored in sealed vials in an inert atmosphere.

The molar concentration of the metal salts in the solution has been typically 1.5 M or 0.75 M (M = mols/l), yielding to a final molar concentration of Y in the solution of 0.25 M and 0.125 M (given the fact that there is 1 mol of Y for each 6 mols of metal-salts) and to a final as-grown films thickness of 250 ± 20 nm and 150 ± 20 nm respectively.

The use of fluorine in the TFA approach to form YBCO layers is justified by two main reasons: the avoidance of moisture and carbon contamination by the formation of barium fluoride BaF_2 instead of barium carbonate $BaCO_3$ and the control of the growth process by the hydrofluoric acid (HF) evolving rate[67,71].

In order to promote the formation of secondary phases in the YBCO matrix, the components of the initial formulation can be modified. In this work, the acquirement of epitaxial superconducting nanocomposites has been achieved by the proper addition in the preparation of the (Y,Ba,Cu)-TFA solution with two different approaches (see figure 2.1(a)):

- *Spontaneously segregated nanocomposites (ss-nanocomposites)*, including additional metal salts (Zr, Ta, Y, Cu,...) directly to the precursor solution that leads, after deposition and growth, to the spontaneous segregation of two different phases, where the superconducting phase is epitaxial YBCO and the non-superconducting phase crystallizes in the form of nanoparticles. In this work, $BaZrO_3$, Ba_2YTaO_6 and mixed Ba_2YTaO_6-$BaZrO_3$, Ba_2YTaO_6-CuO, Ba_2YTaO_6-Y_2O_3 and $BaZrO_3$-Y_2O_3 spontaneous segregated nanoparticles have been used, whose growth details are explained elsewhere[75–77].

- *Preformed nanoparticles nanocomposites (pn-nanocomposites)*, based in the mixing of a previously stabilized colloidal solution containing preformed nanoparticles (in this work, CeO_2, ZrO_2, HfO_2, $BaZrO_3$ and $BaHfO_3$ nanoparticles) in the TFA precursor solution used for YBCO film growth. Nanoparticles are synthesized by solvothermal methods, whether via microwave-assisted method or via thermal activation. The specific approaches used for the stabilization of the nanoparticles are explained in detail for each kind of nanoparticle in several reported works[66,74,78,79].

Nanoparticle concentrations are expressed in this work by the percentage of the molar concentration of nanoparticles with respect to the YBCO molar concentration. For example, for the nanocomposite YBCO + 10%M $BaZrO_3$ (usually simply expressed as 10% $BaZrO_3$ in this manuscript), there is 1 mol of $BaZrO_3$ for 10 mols of YBCO, which means a $BaZrO_3$ molar concentration of 25 mM for a typical YBCO molar concentration of 0.25 M.

2.1.2 Deposition technique

TFA-YBCO precursor solutions were deposited on $5 \cdot 5$ mm^2 $LaAlO_3$ (LAO) single crystal substrates previously cleaned and thermal treated in oxygen flow with the process depicted in figure 2.2(a), in order to remove all possible remaining organic content and induce a surface reorganization that creates terraces, favouring the nucleation of new phases[80].

The deposition technique strongly affects the required rheological parameters of the solution. Two deposition methods were used in this work, performed in a glove box with clean atmosphere, controlled temperature ($18 - 23$°C) and low humidity (< 3g/cm^3) provided by flowing N_2:

- *Spin coating*, where a volume of 15μL of precursor solution is deposited on the substrate that is placed on a spinner and is accelerated to 6000 rpm in 1 s and spinned during 2 min[74]. With this technique, the thickness of as-grown films is typically 50-300 nm obtained with varying molar concentrations. Spin coating multideposition can be also used for the acquirement of thicker layers.

- *Inkjet printing*, where the solution is deposited in droplets generated in a single nozzle with a piezoelectric of lead zirconate titanate drop-on-demand actuator[81,82]. With this technique, by controlling the rheology and concentration of the solution and determining the drop volume and spacing, it is feasible to obtain thick ($\sim 1\mu$m) films in one single coating. In order to reach thicker films than 500 nm, organic additives had to be included in the solution to avoid liquid movements during the deposition and also film cracking during the pyrolysis process.

After the deposition, as-deposited films that are homogeneous in thickness are annealed at 70°C for 5 min in the dry atmosphere of the glove box, before being transferred to the pyrolysis furnace.

2.1.3 Pyrolysis process

The pyrolysis is a low temperature process (300 – 500°C) that is followed in order to decompose the organic matter. During this process, the film shrinks, becomes denser and liberates gaseous phases, releasing the generated stress. It is crucial to control the processing parameters to avoid detrimental effects as film cracking, buckling, blistering or porosity and achieve homogeneous solid precursor films.

The conventional pyrolysis process for spin coated films is illustrated in figure 2.2(b), performed in a tubular furnace in a quartz tube with an oxygen flow of 0.07 l/min. During this thermal process, water vapour is introduced into the gas flow at ∼ 110°C during the heating ramp and closed at ∼ 150 – 200°C during the cooling ramp, necessary for the hydro stabilization of the $Cu(TFA)_2$ salt and for the prevention of its sublimation that would imply Cu deficiency[65,83].

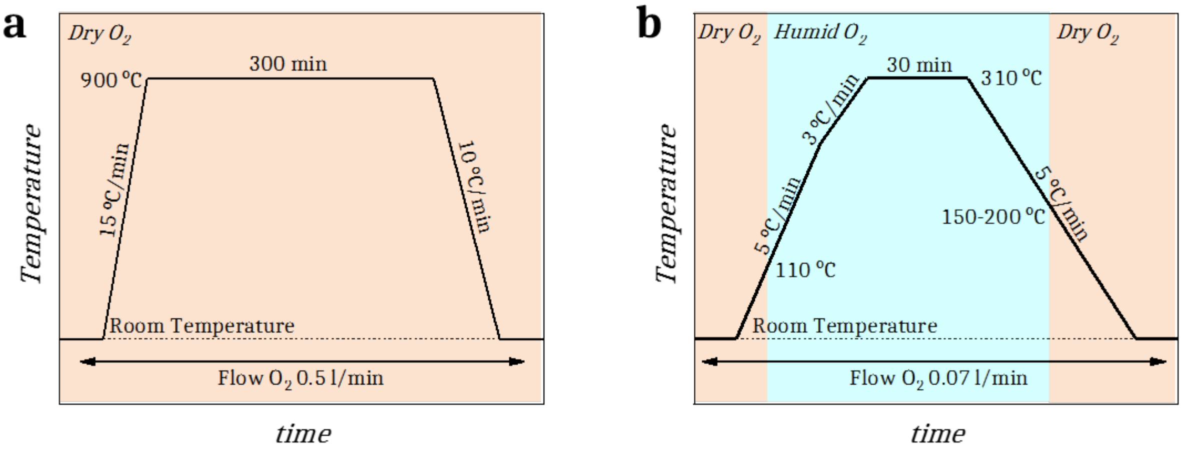

Figure 2.2: schematic thermal profile of (a) the substrate treatment and (b) the conventional pyrolysis process.

The pyrolisis process strongly depends on the mechanical properties of the gel film. In the case of thick films deposited by inkjet printing, a thorough study of the heating ramps has been carried out[82], revealing that up to 160°C the heating rate can be as high as 50°/min, whereas in the range 180 – 280°C, the heating rate should be maintained below 5°/min to avoid film buckling and cracking.

After the pyrolysis in oxygen atmosphere, the film is composed by intermediate phases of $Ba_{1-x}Y_xF_{2+x}$ and CuO, identified with analytical studies of decomposition reaction[83]. The not adjusted reaction of the pyrolysis process is illustrated in the scheme of figure 2.3.

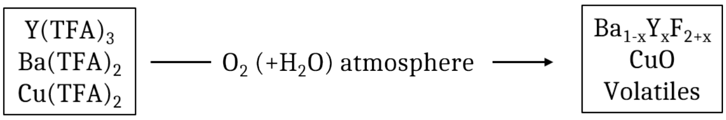

Figure 2.3: scheme of the decomposition reaction of the TFA metal trifluoroacetate precursors during the pyrolysis process.

2.1.4 Growth process

The growth process is a second thermal process that includes the nucleation, crystallization and oxygenation steps of the YBCO phase. This process is conducted in a tubular furnace as well. The thermal profile of this process is shown in figure 2.4(a).

Firstly, as-pyrolysed films are heated up to the growth temperature T_{growth} (typically 700-800 °C) in a dry mixed atmosphere of O_2 and N_2 with a total pressure of 1 bar and a partial pressure of 0.2 mbar of oxygen. During the heating ramp, the water vapour is introduced at T_{H_2O} obtaining a humid atmosphere for BaF_2 decomposition, necessary for the removal of fluorine through evaporation of HF. The partial pressure of water vapour in the humid atmosphere is 23 mbar. The respective flow rates are controlled with mass flow controllers.

Then, an annealing stage is followed for the YBCO crystallization, characterised by a dwell at the growth temperature in the humid atmosphere.

Subsequently, again in a dry atmosphere of O_2 and N_2, the film is cooled down, changing at 600 °C to an atmosphere of only O_2 and following a second dwell at the oxygenation temperature $T_{oxygenation}$ (typically 450-550 °C). In this oxygenation process, oxygen is inserted in the YBCO structure, that is transformed from the tetragonal to the orthorhombic superconducting phase[84,85]. Finally, the film is cooled down to room temperature.

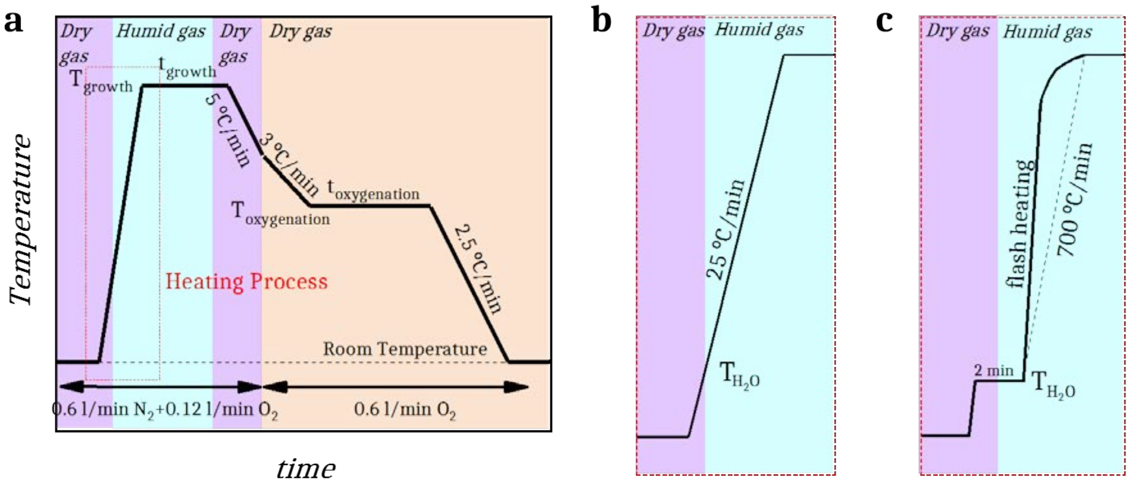

Figure 2.4: (a) schematic thermal profile of the general YBCO growth process and the specific (b) conventional and (c) flash heating processes.

Most of the samples in this work were grown with a conventional heating process, but some of them were heated with a flash heating ramp.

In the case of the conventional heating mode, the sample is placed in the centre of the furnace and heated up with a constant heating ramp of 25°/min (see figure 2.4(a)).

In contrast, in the case of flash heating mode, the furnace is pre-heated and the sample is pushed into the centre of the furnace suddenly acquiring the growth temperature T_{growth}

(see figure 2.4(b)) with an average heating ramp of ~ 700°C/min[74], providing high kinetics for YBCO nucleation and growth and thus leading to a fast formation of c-axis YBCO films.

According to phase identification results[86], the primary YBCO formation reaction is firstly the decomposition of $Ba_{1-x}Y_xF_{2+x}$ into $Ba(O_xF_y)_2$ and Y_2O_3, followed by a decomposition of $Ba(O_xF_y)_2$ in the humid atmosphere, releasing HF and reacting with Y_2O_3 and CuO, which leads to the formation of the YBCO film (the schematic not adjusted reaction is shown in figure 2.5). The film is finally oxygenated under a high oxygen flow rate up to an optimal doping state, being ready for the superconducting performance.

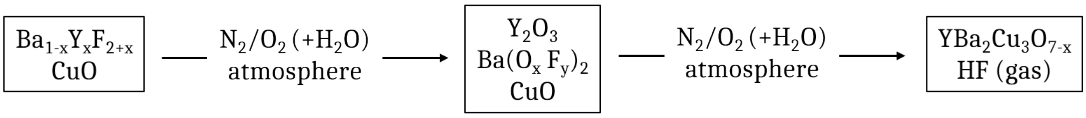

Figure 2.5: scheme of the YBCO formation reaction from the pyrolysed film during the growth process.

2.2 Microfabrication

Critical current densities are so high in YBCO films, that it would be necessary to apply currents of hundreds of A to evaluate the critical values for 5 mm wide and ~ 300 nm thick films. In lab scale, it is interesting to evaluate the critical superconducting properties without need of applying such power consuming current intensities. Besides, the measurement of zero dissipation implies to avoid resistance coming from the current leads and warming effects generated by some resistance in the electrical contacts. Therefore, the sample is lithographed and a superconducting circuit is designed with a 4 point configuration around thin bridges in order to evaluate critical currents in the range of $\sim 0.00001 - 2$ A, using electrical contacts with very low contact interface resistivity.

2.2.1 Electrical contacts

In order to avoid unusual effects as Joule heating and possible sample destruction or wrong J_c determination, the quality of the electrical contacts is of prime importance for the electrical transport measurements and also for magnet applications[87]. The contact interface resistivity ρ_c is defined as:

$$\rho_c \equiv \ R_c A_c \tag{2.1}$$

Where R_c and A_c are the contact resistance and the contact area respectively. Following the method developed by Ekin et al[88], low resistivity contacts ($\rho_c \sim 10\mu\Omega cm^2$) can be obtained by sputtering a noble metal layer (Au or Ag) on top of the superconductor surface where the external equipment wires will be connected.

The deposition process is depicted in figure 2.6(a-e). A brass shadow mask with designed gaps (obtained after brass photolithography) is placed on top of the YBCO film. After-

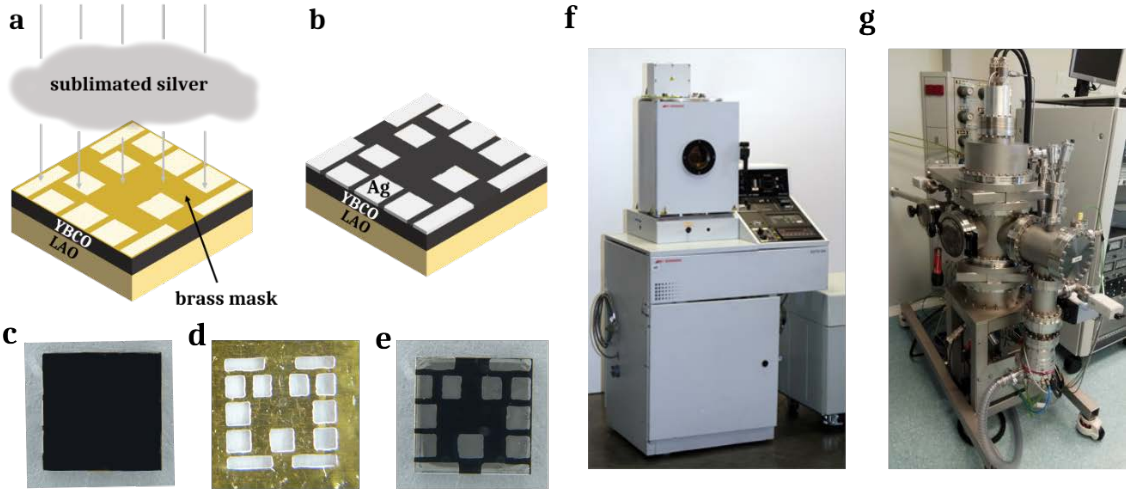

Figure 2.6: scheme and equipment of the electrical contact deposition process. (a-b) show the schematic view of the sublimated Ag contact deposition, optical photographs show (c) the YBCO film before contact deposition, (d) the lithographed brass mask, (e) the YBCO film after contact deposition, (f) the thermal evaporator from Boc Edwards and (g) the sputtering/ion-milling system from TSST.

wards, the sublimation and deposition of $\sim 300 - 500$ nm of Ag is carried out. In this work, silver has been deposited in the ISO 7 cleanroom at ICMAB whether by a thermal evaporator in a vacuum chamber of $\sim 10^{-6}$ mbar (Evaporation System Auto 306 from Boc Edwards, see figure 2.6(f)) or by plasma-assisted sputtering in an argon atmosphere at a pressure of 0.1 mbar (Sputtering/Ion-Milling System from TSST, see figure 2.6(g)).

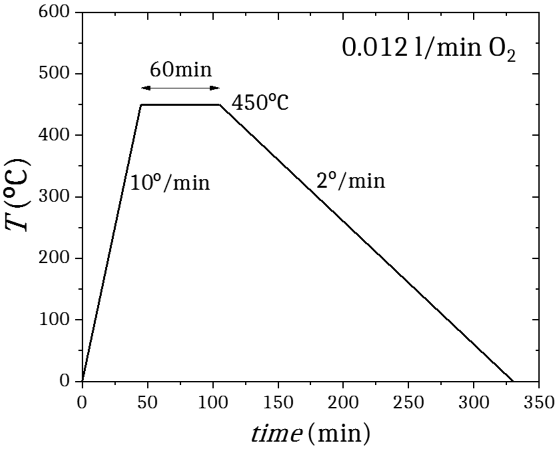

Figure 2.7: schematic thermal profile of the post-annealing process for the achievement of high quality silver contacts.

In order to obtain high quality electrical coupling between the metal contacts and the film, a post-annealing treatment is needed consisting of a 1 hour dwell at 450 °C with a 0.012 l/min O_2 flow. The annealing is conducted in a quartz tube inside of a tubular furnace, whose thermal profiled is illustrated in figure 2.7. At this annealing temperature and dwell time, small modifications of the microstructure are expected[89].

2.2.2 Photolithography

Photolithography allows to design YBCO bridges in the range of μm that accomplish the needed cross-section to reach the critical currents with relative low applied currents.

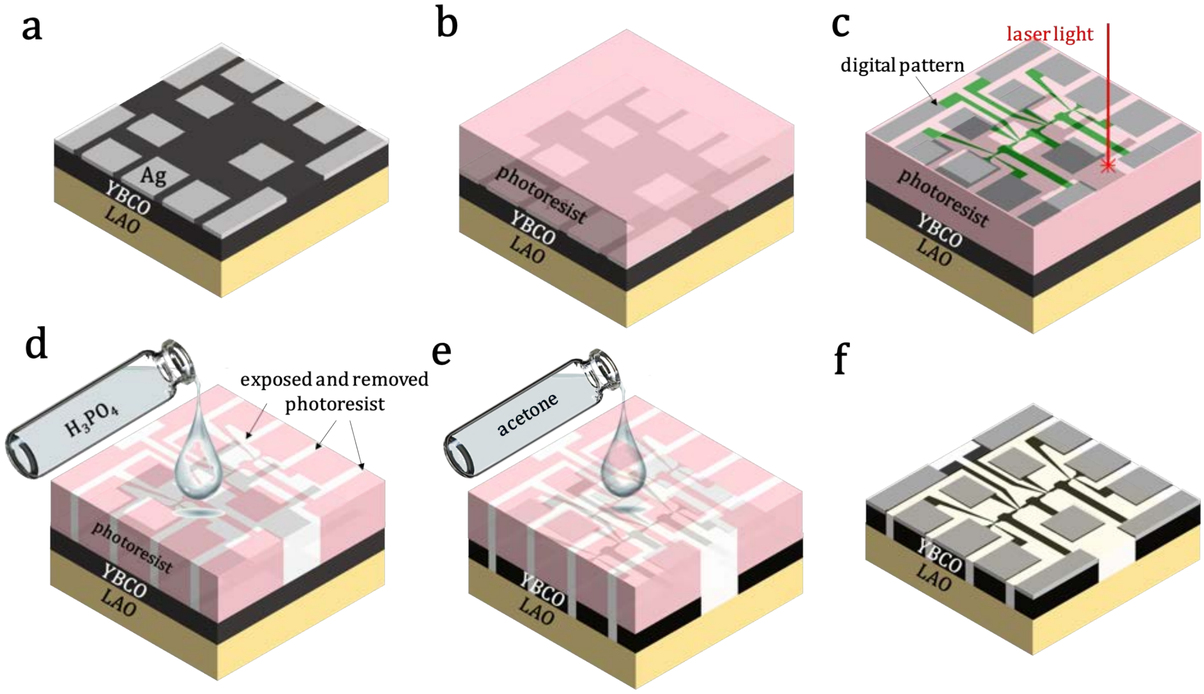

Figure 2.8: schematic view of the steps in the photolithography process of YBCO using a positive photoresist and laser exposure.

Performed in a cleanroom environment, the consecutive steps of this process are depicted in figure 2.8:

a The film surface with deposited Ag contacts is cleaned with acetone and methanol, photographed in figure 2.9(a).

b A layer of positive photoresist (MICROPOSIT(TM) S1813(TM)) is spin coated (5000 rpm during 25 s) on top of the YBCO film and subsequently cured at 70 °C during 1 min.

c The photoresist is exposed to laser light in the gaps of a designed digital pattern with the help of a Micro-Writer from Durham Magneto Optics LTD (photographed in figure 2.9(c)), which is a direct-write photolithography device that uses a software mask to define the exposed patterns. After the exposure with combination of 5μm and 1μm lasers, the activated photoresist is removed by stirring the sample inside of a developer (Microposit MF 319) during 2 min.

d After examining that the generated pattern in the photoresist coincides with the Ag contacts, the sample is stirred in a 1:100 or 1:10 acid solution of $H_3PO_4 : H_2O$ for 10-20 s (depending on the thickness of the sample and acid concentration). Wet etching of YBCO is accomplished when H_3PO_4 soaks through the gaps of the photoresist pattern, removing the unwanted YBCO.

e The remaining photoresist on the YBCO layer is wiped out by the agency of an acetone ultrasonic bath.

f The final sample is a YBCO electrical circuit with the metal contacts, as photographed in figure 2.9(b). The edges of the film may be short circuited due to spin coating edge effects. They can be manually removed with a tooth stick soaked in 1:10 $H_3PO_4 : H_2O$ solution.

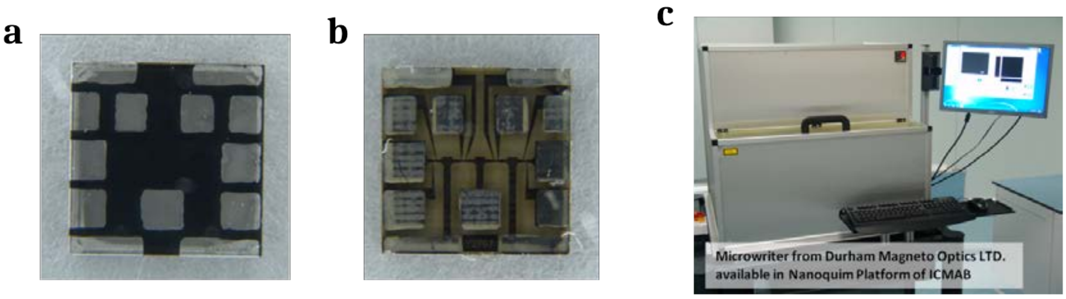

Figure 2.9: YBCO film (a) before and (b) after the photolithography process. (c) Micro-Writer from Durham Magneto Optics LTD in the cleanroom at ICMAB.

The process here described has been the main procedure for the preparation of the films for electrical transport measurements. However, another procedure has been seldom used where samples have been fully covered with silver followed by a physical etching of the gaps with ion milling. Different patterns have been used in this thesis for entire samples of 5 mm by 5 mm (see figures 2.10(a-b)) and half cut samples (see figures 2.10(c-d)).

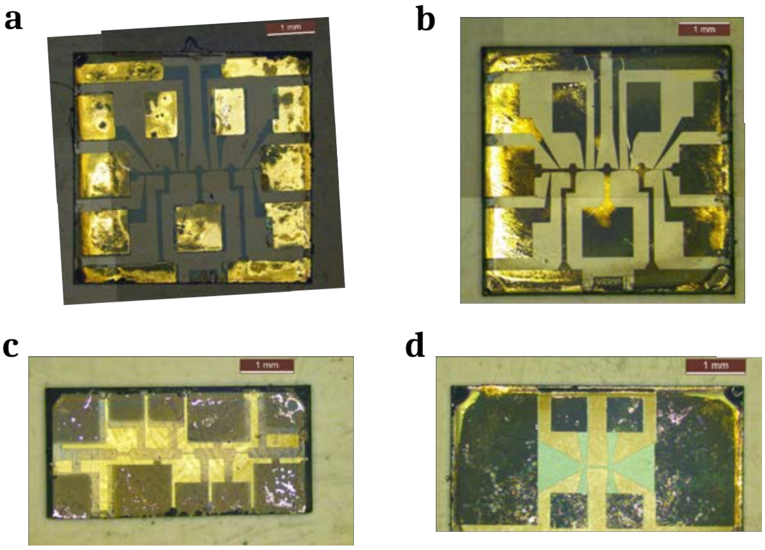

Figure 2.10: optical microscope images of different photo-lithographed patterns. Scale bars correspond to 1 mm.

With these patterns, it has been possible to measure bridges with different cross-sections and characteristics. Bridge widths range from 5 μm to 150 μm and the standard length has been 200 μm although 400 μm has been also used.

Patterns from figure 2.10(a,b,d) allow to measure the direct resistivity of the bridge apart from critical currents. T the one from figure 2.10(c) is less sharp and more resistant to the burning of the bridge at high currents and the one from figure 2.10(b) is protected with a silver layer on top of the entire superconducting circuit.

2.3 Sample characterization

Before the microfabrication process is implemented in order to measure the electrical properties, films are characterized with non-invasive techniques as X-ray diffraction and dc-magnetometry. When samples are patterned, bridge thicknesses have been currently measured with profilometry for an accurate calculation of J_c.

Seeking for correlation between microstructure and electrical properties, the principal samples have been not only electrically characterized but also studied in parallel by scanning transmission electron microscopy, whether studying a lamella directly from the same characterized bridge or studying a part of the second half of a cut sample like in figure 2.10(c).

2.3.1 X-ray diffraction

X-ray diffraction (XRD) is a structural characterization technique whose theoretical basis lies in the Bragg law[90]. The wavelength of X-rays radiation is of the order of ∼ Å, the same order of magnitude as inter-atomic distances. Therefore, the study of XRD allows to identify the internal crystal structure of matter in the atomic and inter-atomic scale.

Any kind of inter-planar spacing fluctuations in the crystal lattice will affect the X-ray reflection and can be detected by analysing the Bragg peak characteristics such as position (2Θ) or the full width half maximum (FWHM). The usual configuration for X-ray diffraction measurement is the conventional $\Theta - 2\Theta$ scan configuration, shown in figure 2.11(a).

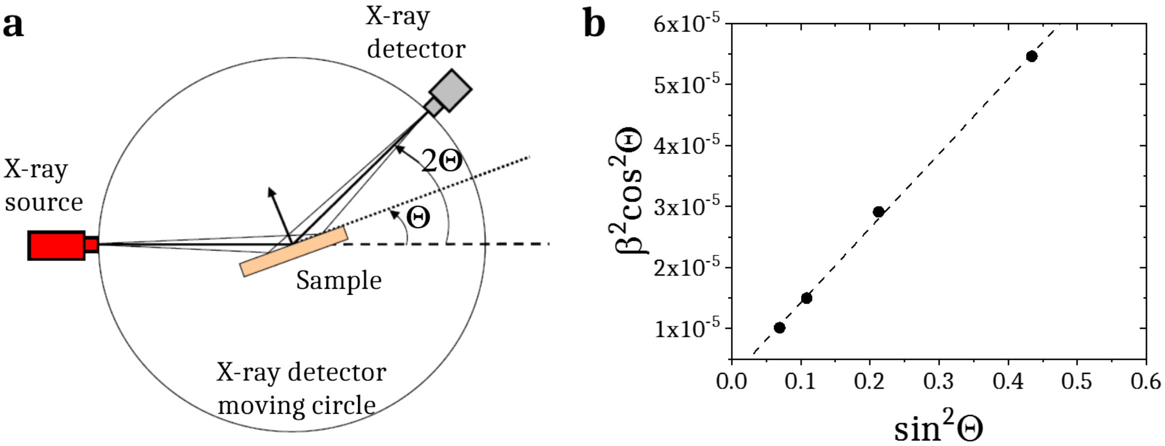

Figure 2.11: (a) aketch of the conventional $\Theta - 2\Theta$ scan configuration (adapted from[91]) and (b) Williamson-Hall plot of the (00l) peaks for a YBCO nanocomposite. Nanostrain ε can be extracted from the slope of the linear fit (dashed line).

As later explained in section 3.1.2, nanoscale strain is very common in YBCO nanocomposites. Following the Williamson-Hall method[92], it is possible to measure the *nanostrain* ε along the c-axis by the analysis of the $\Theta - 2\Theta$ scans with long acquisition time, following the equation:

$$\beta^2 \cos^2(\Theta) = \frac{\lambda_{\alpha 1}}{L_\perp} + 16\varepsilon^2 \sin^2(\Theta) \tag{2.2}$$

Where β is the integrated breadth of the (00l) YBCO Bragg peaks after the subtraction of the contribution from the instrument, $\lambda_{\alpha 1}$ is the wavelength of the Cu $K_{\alpha 1}$ radiation and $L_\perp$ is the coherent volume size perpendicular to the scattering vector.

The $\Theta - 2\Theta$ scans have been performed by the technical staff at ICMAB with a step size of 0.02° every 2 s by a Siemens D5000 diffractometer, using a Cu K_α radiation with wavelength $\lambda_{\alpha 1} = 1.540560$ Å. A typical plot $\beta^2 \cos^2(\Theta)$ vs $\sin^2(\Theta)$ is shown for a nanocomposite in figure 2.11(b), where ε can be extracted from the slope of the linear fit.

2.3.2 SQUID dc-magnetometry

The magnetization of YBCO films has been inductively measured by the technician in the low temperature laboratory at ICMAB with a dc-magnetometer consisting of a Quantum Design superconducting quantum interference device (SQUID, see figure 2.12), with a vacuum pump, a 7 T superconducting coil for applied magnetic fields and temperature control between 1.8 K and 400 K. The SQUID detection system consists of a group of pick-up coils placed at the middle of the superconducting magnet. The sample is moved along the pick-up coils, inducing a current on them proportional to the magnetic flux variation. The SQUID detector, by the application of Josephson junctions[93], has a magnetic moment accuracy of 10^{-9} Am^2 (10^{-6} emu).

Figure 2.12: SQUID dc-magnetometer in the low temperatures lab at ICMAB.

According to the critical state model, J_c is directly related to the saturated magnetization as expressed by equation 1.12. Hence, this inductive method can be used to obtain the temperature and magnetic field dependence of J_c. Although the results shown in this thesis manuscript are mainly electrical transport measurements, SQUID measurements have been used to evaluate T_c and J_c of as-grown films before deciding to perform invasive electrical transport measurements and have been also useful for the optimization of the preparation of films during the microfabrication process, controlling any alteration of the superconducting properties. Furthermore, some inductive J_c results (denoted as J_c (SQUID)) are used in this manuscript for completeness of the different studies.

2.3.3 Profilometry

For the calculation of the current density J in electrical measurements, it is necessary to determine the size of the cross-section of the bridge where the current flows:

$$J = \frac{I}{wt} \tag{2.3}$$

Where w is the width of the bridge, that can be easily calculated from optical microscope images with resolution of $\sim \mu$m, and t is the thickness. Although thickness can be deduced from the molar concentration of the precursor solution, it is convenient to measure the thickness directly of the bridge for a proper calculation of the J_c value, especially in inkjet printed and multi-layered thick films. This can be done with the surface profiler P16+ from KLA Tencor located in the cleanroom at ICMAB (see figure 2.13(a)).

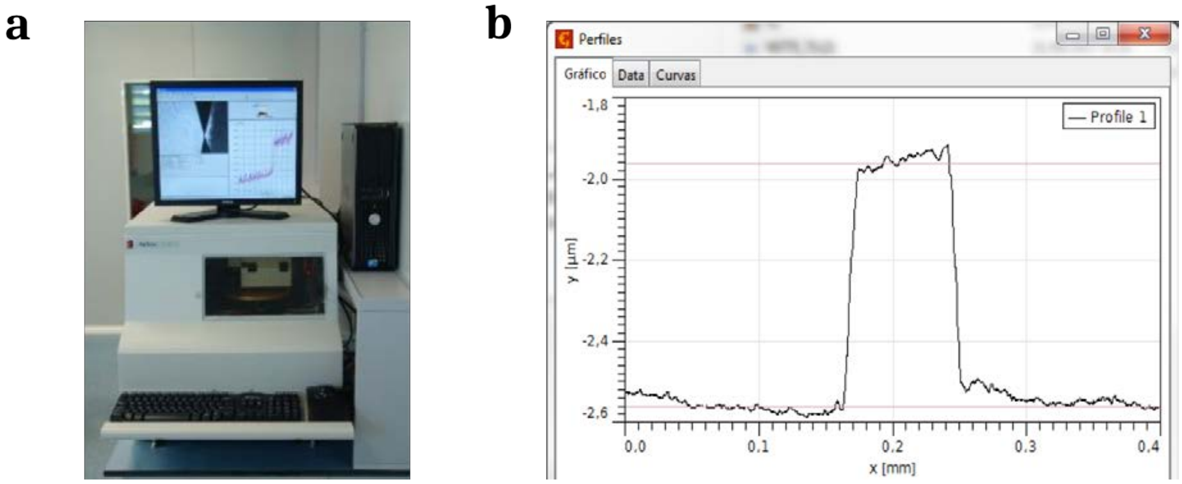

Figure 2.13: (a) surface profiler P16+ from KLA Tencor in the cleanroom at ICMAB and (b) surface profile of a 600 nm thick and 70 μm wide YBCO bridge.

This tool uses a diamond stylus that stays in contact with the sample at a constant applied force as low as 0.5 mg. This lowest force has been usually the applied one for the bridge analysis of the patterned YBCO films in this work. A profile example is shown in figure 2.13(b), where a bridge of an inkjet printed sample is analysed.

2.3.4 Electrical transport measurements

Electrical transport measurements were carried out by the standard 4-points method, depicted in figure 2.14(a), ensuring that the voltage drop is strictly measured in the length of the bridge. The current was applied parallel to the ab-plane, always perpendicularly to the applied magnetic field which was rotated with angle θ from the c-axis (0°) to the ab-plane (90°), ensuring maximum Lorentz force configuration ($J \perp H$). Figure 2.14(b) shows a typical example of logarithmic E-J characteristics. J_c was determined for a critical electric field $E_c = 10\ \mu V/cm$ criterion. The n value was calculated by fitting the power law $E \propto J^n$ over a range extending from a minimum electric field $E_{min} = 50\ \mu V/cm$ to a maximum electric field $E_{max} \sim 300\ \mu V/cm$ where the measurement stops, ensuring that the measurement is close to J_c in the region of flux creep (see section 1.6.2) and that there is enough smooth data for a proper fit.

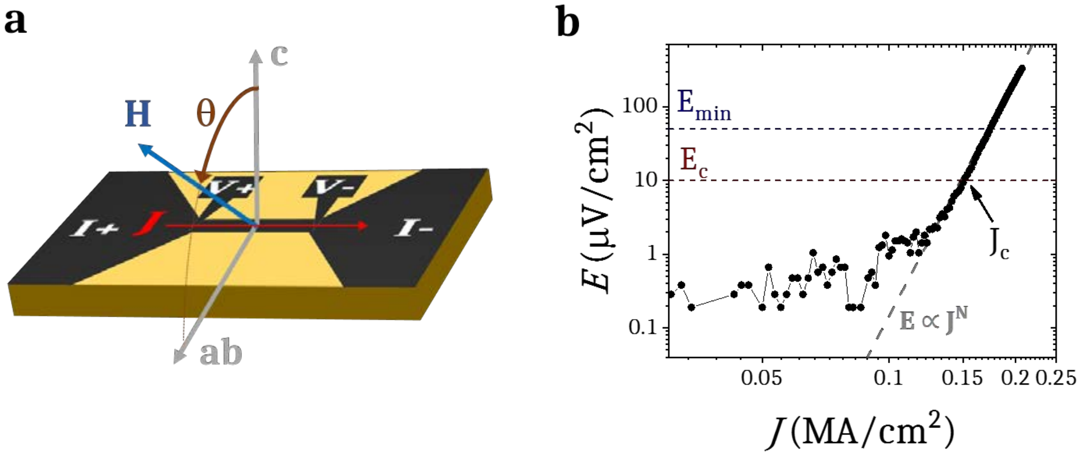

Figure 2.14: (a) scheme of the 4 point configuration with maximum Lorentz force and (b) logarithmic plot of the E-J experimental data for a pristine YBCO film at 77 K, 1 T. E_c, E_{min} and $E \propto J^n$ fitting are indicated with dashed lines.

The resistance R has been also measured using the 4-point configuration. It is given by the ratio between the measured voltage and the applied current V/I, using a low frequency ac-current of 0.01 mA at 33 Hz. The resistivity ρ is calculated from the expression 2.4, where L is the length of the bridge.

$$R = \frac{\rho L}{wt} \tag{2.4}$$

$\rho(T)$ curves have been obtained by ramping down the temperature with a 5 K/min rate and reading voltage every 2 K, whereas near T_c the used rate was 0.5 K/min and voltage was read every 0.1 K. T_c was determined using a mid-point criterion[94]. Thus, T_c corresponds to $T_{c0.5}$ and the width of the transition $\Delta T_c = T_{c0.9} - T_{c0.1}$, where T_{cx} is the temperature at which $\rho(T_{cx}) = x\rho_n(T_{cx})$ being $\rho_n(T)$ the linear fit of the metallic normal resistivity at the normal state.

The irreversibility line $H_{irr}(T)$ has been obtained by inverting the $T_{irr}(H)$ line, acquired from the ρ(T) curves at different magnetic fields, following the criteria $\rho(T_{irr})/\rho(100K) = 10^{-3}$.

2.3.4.1 Physical property measurement system

Except the results obtained up to very intense magnetic fields (> 9T), electrical transport measurements have been performed in a physical property measurement system (PPMS) from Quantum Design, shown in figure 2.15. This vacuum system includes a 9 T superconducting magnet and temperature is controlled in a helium cryostat from 1.9 K to 400 K. It counts with a rotating motor to change sample orientation θ with respect to the applied magnetic field with an angular range of 370° and an accuracy of 0.1°, enabling to measure E-J curves for different T, H and θ.

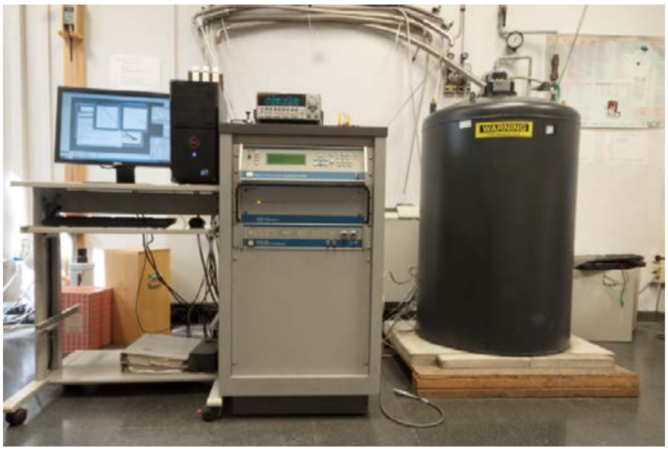

Figure 2.15: PPMS in the low temperatures lab at ICMAB.

Voltage-current characteristics were obtained in the PPMS by measuring 256 points separated by a regular current step size, ramping the current up to a maximum value I_{max}, determined by voltage and power dissipation limits V_{max} and $P_{max} = V_{max}I_{max}$ in a feedback loop. If any measurement surpasses any of both limits, the current is immediately cut off to avoid bridge damaging.

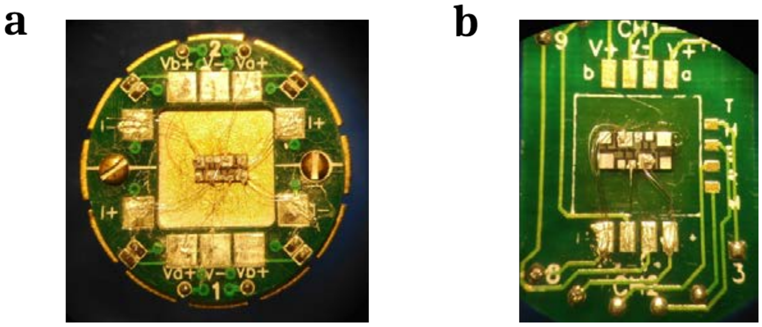

Figure 2.16: YBCO sample mounted and contacted on top of (a) a round puck and (b) a rotating puck.

The PPMS includes a nanovoltmeter and a dc/ac current source which provides currents down to 10 μA and up to 2 A when using a round puck (see figure 2.16(a)) and up to

0.5 A when using a rotating puck (see figure 2.16(b)). Unless the sample is wedged, the round puck is limited to measurements when the applied magnetic field is parallel to the c-axis.

The sample is mounted and glued on the puck with GE varnish and contacted with a 0.05 mm diameter silver wire attached to the contact pads of both sample and puck with silver conductive paint. The use of various silver wires in the same pad has been perceived as favourable for avoiding contact heating.

2.3.4.2 High magnetic field measurements

The study of the electrical performance of CSD YBCO films, with special focus on the nanocomposites, has been extended to very intense magnetic fields in the facilities of the Laboratoire National des Champs Magnétiques Intenses (LNCMI, in Grenoble) and of the National High Magnetic Field Laboratory (MagLab, in Tallahassee). First, the proof of concept of measuring lab scale CSD YBCO films on LAO substrates was developed in LNCMI, achieving the first results and understanding the main difficulties related to:

- Sample mounting in a handmade probe and set-up.
- Sample damaging because of high pressure from pressure electrical contacts, moisture during warming of the probe and/or too high applied currents.
- Sample burning due to transient current peaks from the current source.
- Sample detachment due to the large induced Lorentz forces.
- Electrical ground and noise control.
- Liquid He bubble in the cryostat during cooling.

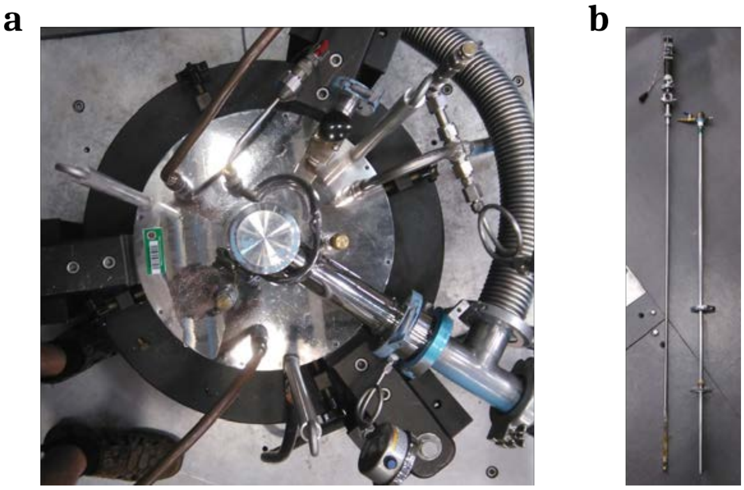

Figure 2.17: (a) top of the 35 T 32 mm magnet at Maglab with a cryostat inside and (b) tight-vacuum probe and its cover.

High field results presented in this manuscript belong to the later experiments in the Maglab, where most of the difficulties were solved. 4-points electrical transport measurements were conducted in a 35 T 32 mm bore resistive magnet, shown in figure 2.17(a).

A tight-vacuum ∼ 1.6 m long probe has been used (see figure 2.17(b)) provided with a rotating handle on the top and a cover that seals the purged atmosphere inside.

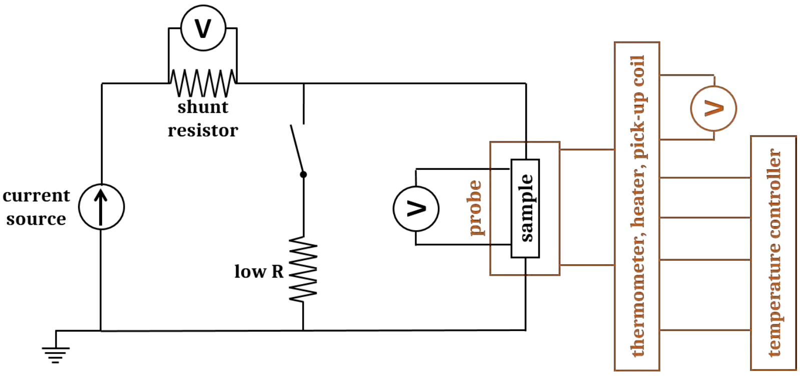

Figure 2.18: Electrical circuit of the set-up for electrical transport measurements at very high magnetic fields.

The electrical circuit of the set-up is represented in figure 2.18. Current is generated in a current source and flows through a shunt resistor of known resistance in order to deduce the current intensity. The sample is generally short-circuited except when the measurement runs. On the other side, the probe counts with a Cernox thermometer and a heater consisting of copper wire wounded around the probe. Temperature is controlled in the range of 4.2-60 K with a temperature controller.

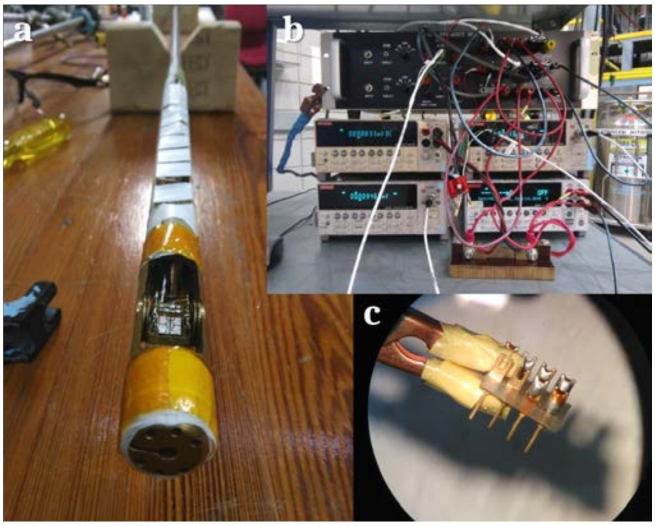

Figure 2.19: experimental set-up. (a) Sample mounting on the probe, (b) electronic devices and (c) pins soldering of the G10 support.

Samples were mounted on G10 supports fabricated in the workshop, which are pinned to a rotating platform inside of the probe (see figure 2.19(a,c)). Pick-up coils are wounded around the rotating platform for the estimation of the orientation of the magnetic field θ with respect to te sample. The electronic set-up out of the probe is partially shown in figure 2.19(b). It consists of a current source limited to 5A (Kethley 2440 Sourcemeter), various Kethley nanovoltmeters to monitor voltage drops in the sample, in the shunt and in the pick-up coil, a breakout box, a shunt resistor and a Lakeshore temperature controller (model 336).

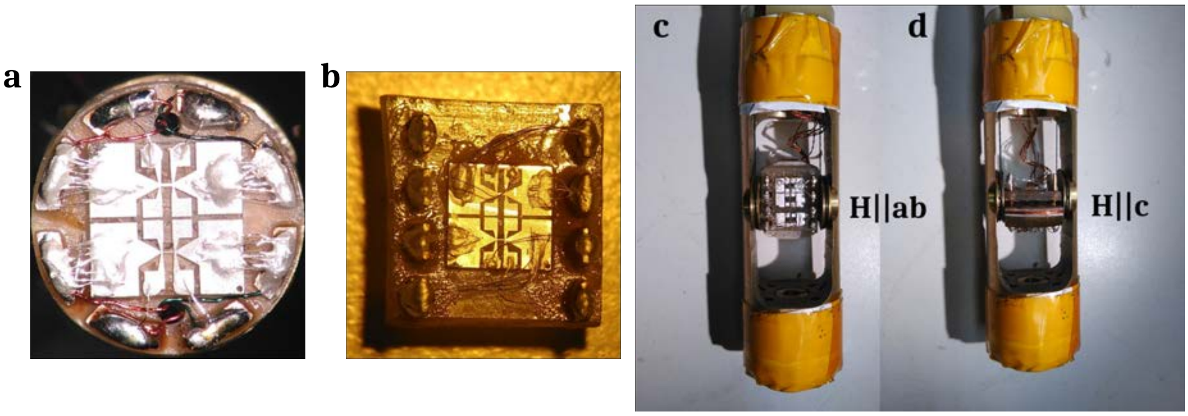

Figure 2.20: (a-b) YBCO sample placed on G10 supports for respective rotating platforms, that can be oriented at (c) H||ab and (d) H||c among other orientations.

Samples are contacted through 0.05 mm diameter silver wires with conductive silver paint. The wires are afterwards soldered to the pins of the support with Sn60Pb40 solder (see figures 2.19(c) and 2.20(a-b)). The support is able to rotate a range of $\sim 200°$, limited by the stress of the wires. The orientation of the support in the probe cavity is shown in figures 2.20(c-d) for 90° (H||ab) and 0° (H||c).

2.3.5 Scanning transmission electron microscopy

The analysis of aberration corrected scanning transmission electron microscopy (STEM) images has been crucial for some of the main outcomes of this thesis. STEM allows the visualization of the atomic structure of crystals in the real space with sub-atomic resolution. An electron beam is extracted from an electron gun, which is then focused into the crystal sample by the use of electromagnetic coils. The transmitted electrons are gathered by either the use of diverse annular detectors, each one providing complementary information. Different imaging modes and analytical techniques were used for the observations carried out by other members of the group:

- High-angle annular dark-field (HAADF), also referred as Z-contrast, achieved by using an annular detector with very large inner and outer angles, which collect those electrons undergoing Rutherford scattering with the atomic nuclei of the crystal. The brightness of each atomic column approximately scales with the atomic number as $\sim Z^2$.
- Low-angle annular dark-field (LAADF), achieved by using an annular detector with lower inner and outer angles, which enables to collect those electrons deviated at lower angles due to the dechannelling effects generated by the distortions of the crystal lattice. It allows then to better identify nanoscale strained regions.
- Annular bright field (ABF), where diffracted beams are excluded by placing an aperture in the back focal plane which only let the electrons from the direct beam

to go through. It permits to image all the atomic sub-lattices that are present within the crystal structure, also light elements that can not be imaged by Z-contrast.

- Geometrical Phase Analysis (GPA) is a specific software that maps how two specific Bragg reflections, selected from the Fast-Fourier Transform pattern associated to a high resolution lattice image, varies through the image, giving information on local displacements and rotations of atomic planes[95].
- STEM is suitable for the spectroscopic mapping by energy-dispersive X-ray (EDX) spectroscopy, which is a technique used for the chemical composition analysis that relies on the interaction of an X-ray excitation (induced by an electron or x-ray beam) and a sample, allowing a unique set of peaks in the spectrum for a particular atomic structure.

The nanoparticle distribution, size and atomic scale defect landscape of the films were studied mainly with a FEI Titan (60-300 kV) microscope equipped with a third order probe-aberration corrector, a monochromator and an X-field emission gun. A thorough analysis of the microstructure of CSD-TFA YBCO nanocomposites is carried out in two other PhD theses[96,97].

CHAPTER 3

VORTEX PINNING REGIMES IN CSD NANOCOMPOSITES

The defect landscape in YBCO films has been demonstrated to strongly affect the critical current density dependences in the magnetic-field–temperature diagram due to particular vortex pinning properties associated to different kind of defects. In this chapter, the dependence of J_c with T, H and θ is studied in CSD ss-nanocomposites in order to identify vortex pinning regimes where the critical current performance can be boosted when particular pinning sites are dominant.

3.1 Previous background

3.1.1 Critical current density dependences

As described in section 1.6.1, vortex pinning depends on temperature T, magnetic field intensity H and orientation θ. Hence, J_c and other superconducting parameters related to pinning as the pinning force F_P depend on these physical magnitudes. Several vortex pinning theoretical models try to give explanation to the critical current density dependences.

3.1.1.1 Temperature dependence of J_c

Two different theoretical models have been proposed for the temperature dependence $J_c(T)$ regarding the pinning strength of pinning centres: *weak* and *strong* pinning centres. On one side, the weak collective pinning model[7] predicts a fast decay of $J_c(T)$ following the expression of the weak critical current density $J_c^{wk}(T)$ in presence of weak defects:

$$J_c^{wk}(T) = J_c^{wk}(0)exp\left(-\frac{T}{T_0}\right) \tag{3.1}$$

where $J_c^{wk}(0)$ is the weak pinning contribution at 0 K and T_0 is the temperature associated to the characteristic vortex pinning energy of weak defects. 0D point defects with sizes smaller than ξ are thought to be responsible of weak pinning.

On the other side, for strong defects (as correlated defects, for example), the Bose glass theory[44] accounts for a smoother $J_c(T)$ dependence following the expression of the strong critical current density $J_c^{str}(T)$:

$$J_c^{str}(T) = J_c^{str}(0) exp\left[-3\left(\frac{T}{T^*}\right)^2\right] \tag{3.2}$$

where $J_c^{str}(0)$ is the strong pinning contribution at 0 K and T^* is the temperature associated to the characteristic vortex pinning energy of strong defects. Thus, strong pinning centres (1D, 2D and some 3D pinning centres) are more effective than weak pinning centres at higher temperatures.

Pristine and nanocomposite YBCO films studied in this thesis include defects of different nature. Therefore, their simultaneous contribution will be responsible for the final pinning performance[98].

The fitting of experimental results to these temperature dependent expressions is a useful tool for discerning the domination of certain pinning centres in the magnetic phase diagram. However, it is important to remark that the validity of these models in YBCO is stronger at low magnetic fields and strictly restricted to temperatures up to $\sim 60 - 70$ K[7,98].

3.1.1.2 Magnetic field intensity dependence of J_c

The density per unit area of vortices n_v is proportional to the total magnetic flux in the superconducting material divided by the vortex flux quantum ($n_v = \mu_0 H/\phi_0$). Assuming an homogeneous square lattice of vortices ($n_v = 1/a_0^2$), the vortex lattice parameter a_0 yields:

$$a_0 = \sqrt{\frac{\phi_0}{\mu_0 H}} \tag{3.3}$$

For disordered YBCO, a_0 is rather an approximation of the spacing between vortices. When the magnetic field H increases, the amount of vortices increase and the distance between them diminishes, involving three different regimes of depinning that can be observed in the $J_c(H)$ dependence, evaluated in figure 3.1.

At very low magnetic fields, up to a certain magnetic field H^*, vortices lay at very large distances and interact slightly one with another but strongly with defects. In this region, named single-vortex pinning regime, J_c is nearly independent of the magnetic field, being $J_c(H) \sim J_c^{sf}$, where J_c^{sf} is the critical current density at self-field (sf), the magnetic field arising from the current itself[99,100]. In thin films, a $J_c(H)$ plateau is observed at this region in a logarithmic scale, as observed in figure 3.1.

In the case of correlated pinning[44,101–103], H^* is associated to the matching magnetic field H_Φ at which the density of vortices n_v is equal to the density of defects n_d ($n_d = \mu_0 H_\Phi/\phi_0/$). In this case, the spacing between pinning centres d_{PC} coincides with

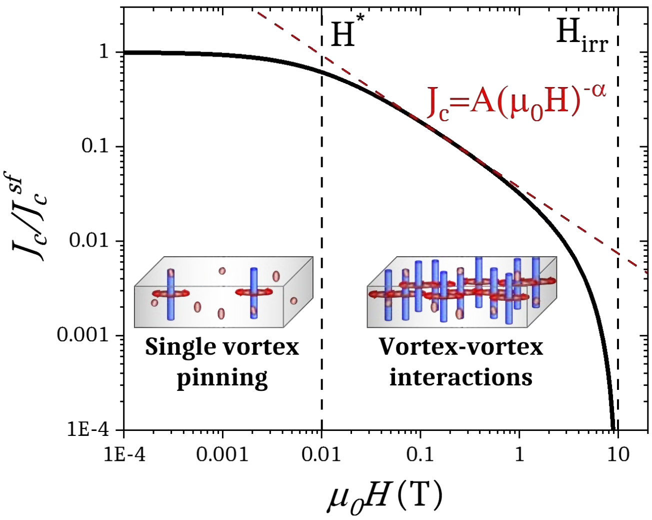

Figure 3.1: magnetic field dependence of the normalized critical current density J_c/J_c^{sf} for a pristine YBCO film at 77 K. Single vortex pinning and vortex-vortex interactions regimes are indicated.

the vortex lattice parameter $d_{PC} = a_0 = \sqrt{\phi_0/\mu_0 H_\Phi}$. The association $H^* \sim H_\Phi$ is more valid at low temperatures, where thermal excitations are less prominent[44,102].

At intermediate and high fields above H^*, called vortex-vortex interactions or collective pinning regime, the electromagnetic interaction between vortices becomes more relevant than interactions of vortices with defects, implying a $J_c(H)$ decay that generally follows a power law regime relation:

$$J_c(H) = A(\mu_0 H)^{-\alpha} \tag{3.4}$$

where A and α are constants. The power law exponent α is typically in the range of 0.5-1[104], in agreement with several theoretical approaches that deal with vortex-vortex interactions (1 for collective pinning, 1/2 for plastic pinning and for the flux line share model, 5/8 for strong pinning in large point pins,...)[44,105–108].

Both, enhancement and reduction of α have been observed in multiple nanostructured YBCO thin films with the introduction of nanoinclusions in comparison with pristine films[31,37,104,108–117], reaching α values as large as 1.1 and as low as 0.2.

Finally, when the magnetic field approaches the irreversibility field H_{irr}, $J_c(H)$ drops very fast to zero. The entire $J_c(H)$ can be fitted by a single phenomenological equation that uses the parameters that define these regions[118,119]:

$$J_c(H) = J_c^{sf}\left[1 + \frac{H}{H^*}\right]^{-\alpha}\left[1 - \frac{H}{H_{irr}}\right]^2 \tag{3.5}$$

3.1.1.3 Magnetic field orientation dependence of J_c

Isotropic pinning centres reduce superconductivity equally in any orientation of the magnetic field θ with respect to the crystallographic c-axis, depicted in figure 3.2. However, as explained in section 1.6, vortex characteristic lengths ξ and λ change with the orientation of the magnetic field. Blatter et al[7] introduced an angular dependent scaling factor $\epsilon(\theta)$ that depends on θ as:

$$\epsilon(\theta) = \sqrt{\frac{1}{\gamma^2}\sin^2(\theta) + \cos^2(\theta)} \tag{3.6}$$

where γ is the anisotropic constant from equation 1.13, leading to an angular dependence of the characteristics lengths: $\lambda(\theta) = \lambda_{\mathrm{ab}}/\epsilon(\theta)$ and $\xi(\theta) = \epsilon(\theta)\xi_{\mathrm{ab}}$.

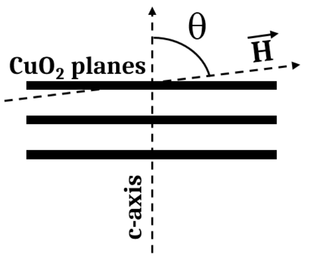

Figure 3.2: sketch of the magnetic field orientation θ with respect to the crystallographic c-axis

By applying the scaling rule[120] to the magnetic field, an applied magnetic field H can be scaled in an anisotropic layered superconductor into $H_{\mathrm{scaled}}(\theta)$, that follows the same angular dependence as $\xi(\theta)$:

$$H_{scaled}(\theta) = \epsilon(\theta)H \tag{3.7}$$

When isotropic pinning dominates pinning at some conditions in a layered superconductor, the magnetic field dependence of $J_c(\theta)$ curves collapse onto one curve when H is replaced by $H_{\mathrm{scaled}}(\theta)$[98,121–124]. Also in this case, $H_{\mathrm{irr}}(T)$ and $H_{c2}(T)$ curves superpose for different angles θ when they are replaced by $\epsilon(\theta)H_{\mathrm{irr}}(T)$ and $\epsilon(\theta)H_{c2}(T)$ respectively.

In pristine CSD YBCO films, the isotropic collapse of $H_{\mathrm{irr}}(T,\theta)$ or $J_c(H,\theta)$ with the scaled magnetic field is successful for $\gamma = 5 - 6$, in agreement with the intrinsic anisotropy of YBCO. However, in nanocomposite films like in figure 3.6, the same analysis leads to an effective scaling factor $\epsilon_{\mathrm{eff}}(\theta)$ composed of an effective anisotropy parameter γ_{eff} that is lower than γ, ranging from 1.5 to 4.

In particular, the intrinsic anisotropy γ of these nanocomposites can be determined from the study of the angular dependence of the upper critical field curve $H_{c2}(T)$[7]. Some experiments at very high fields confirmed that the intrinsic anisotropy γ, associated to the electrical mass anisotropy of the YBCO crystal, remains being the same for YBCO films with nanoparticles ($\gamma \sim 5$)[32,123,125]. However, the collapse of $H_{\mathrm{irr}}(T,\theta)$ and $J_c(H,\theta)$

in diverse nanostructured films with nanoparticles[32,75,123,126–128] elucidate the presence of a different effective anisotropy γ_{eff} for the scaling under pinning conditions when they are plotted versus an effective magnetic field H_{eff}:

$$H_{eff}(\theta) = \epsilon_{eff}(\theta)H = \sqrt{\frac{1}{\gamma_{eff}^2}\sin^2(\theta) + \cos^2(\theta)} \tag{3.8}$$

Hence, while the effective anisotropy γ_{eff} is modified through the incorporation of nanoscale isotropic defects, the intrinsic electron mass anisotropy remains unaltered.

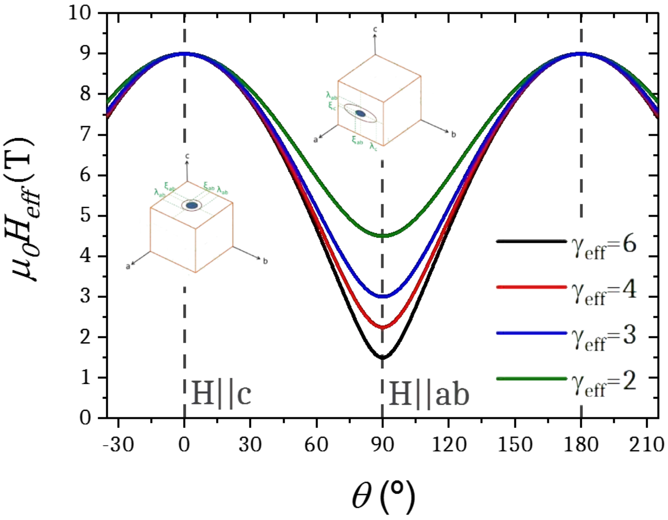

Figure 3.3: angular dependence of H_{eff} when H=9T for different γ_{eff}. Insets for H||c and H||ab recall the vortex configurations from figure 1.11(a).

In figure 3.3, the θ dependence of H_{eff} is plotted for different γ_{eff} when the applied magnetic field is 9 T. At H||c, $H_{\mathrm{eff}} = H$ for any γ_{eff}, whereas at H||ab, each γ_{eff} leads to a different H_{eff}, being the largest the one with smallest γ_{eff}. Although superconducting properties in nanocomposites (low γ_{eff}) decrease at H||ab due to a higher H_{eff}, the magnetic field dependent superconducting properties are less anisotropic and can be homogeneously enhanced in all orientations.

Anisotropic pinning centres generate strong pinning at specific orientations of the magnetic field and their contribution falls out of the isotropic collapse of $H_{\mathrm{irr}}(T,\theta)$ or $J_c(H,\theta)$. The J_c values that deviate from the collapsed line, have an extra anisotropic contribution J_c^{aniso}, that can be calculated by considering:

$$J_c = J_c^{iso} + J_c^{aniso} \tag{3.9}$$

Which is a rough approximation since it does not consider interaction between defects, but it is an appropriate approximation whenever one of the two kinds of defects is dominant. As it is shown in the following section, the most common correlated pinning centres in CSD YBCO films are planar defects: twin boundaries at H||c and stacking faults and intrinsic pinning at H||ab.

These planar defects provide a positive J_c^{aniso} contribution with the exception of twin boundaries, that depending on the magnetic field, temperature or vortex motion direction may act either as strong pinning centres or channels for easy vortex flow. In the latter case, a suppression of J_c is observed when H is parallel to the c-axis of YBCO ($\theta = 0°$ or $\theta = 180°$)[129,130].

In a strong anisotropic pinning potential, the vortex lattice can gain energy by aligning vortices parallel to the pinning centres, leading to three different angular regimes[7] depicted in figure 3.4 for the case of intrinsic pinning. For small misalignments of θ, up to the lock-in critical angle θ_L, vortices are locked and remain parallel to the planes, named lock-in regime (fig. 3.4(a)). At larger angles, up to the trapping critical angle θ_T, vortices accommodate with kinks and parallel segments where the magnetic lines recall to the shape of a staircase, called staircase regime (fig. 3.4(b)). When surpassing θ_T, vortices do not accommodate and keep straight at the orientation of the magnetic field (fig. 3.4(c)).

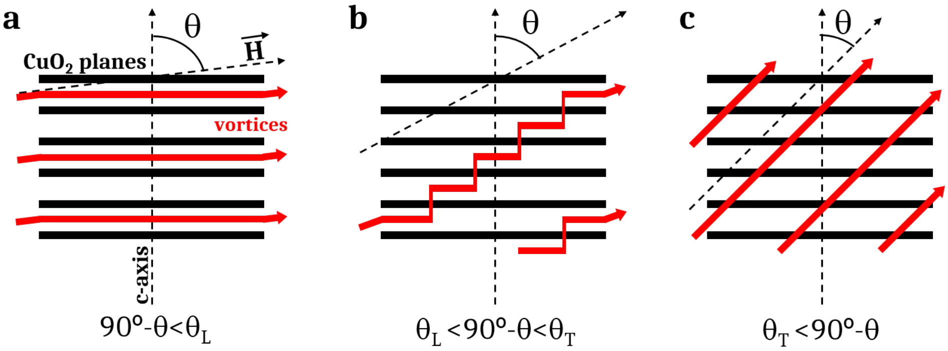

Figure 3.4: schematic view of vortices in (a) lock-in, (b) staircase and (c) straight-vortices regimes for orientations θ close to H||ab.

The pinning energy provided by anisotropic pinning centres at these angular regimes enhances $J_c(\theta)$ gradually as vortices are turned towards the direction of the pinning centre, interacting with the additional isotropic pinning centres that scale with the effective magnetic field H_{eff}.

The theoretical calculation for θ_T for magnetic fields $H \ll H_\Phi$ is independent of the magnetic field: $\theta_T = (2\varepsilon_p/\varepsilon_l)^{1/2}$, where ε_p is the pinning energy per unit length and ε_l is the vortex line tension, that corresponds to $\varepsilon_l = (\phi_0^2/(4\pi\mu_0\lambda^2))\ln(a_0/\xi)$. For $H \gg H_\Phi$, θ_T decays with the magnetic field as $H^{3/2}$ and $H^{3/4}$ for linear and planar defects respectively[7,131].

3.1.2 Nanostructural defects in CSD YBCO films

Epitaxial YBCO films usually display a great variety of nanoscale structural defects that can be observed by experimental techniques as XRD or STEM. Depending on the YBCO precursors and the growth method used to synthesize films, different crystallographic defects have been found as oxygen vacancies, cation disorder, threading, screw or edge dislocations, grain boundaries, twin boundaries, antiphase boundaries, ab-grains, stacking faults, intergrowths, nanoscale strain, etc.

As explained in section 1.6, the orthorhombic phase is characterized by the presence of oxygen vacancies, which in turn, control superconducting properties as T_c or J_c. Besides, a very common defect appear in CSD YBCO during the growth-oxygenation process: the *stacking fault*, also called *Y124 intergrowth* and illustrated in figure 3.5(a), that consists of an ab planar defect caused by the interruption in the vertical stacking sequence of YBCO, precisely the addition of an extra layer of CuO chains.

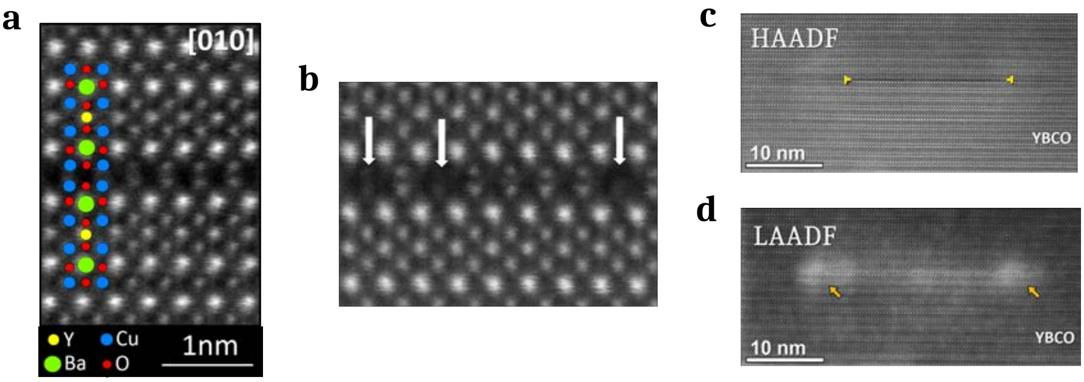

Figure 3.5: STEM images of high-magnification and defect identification. (a) Z-contrast image of a YBCO film with a stacking fault (dark stripe) where the ionic structure of YBCO is projected, (b) Z-contrast image indicating with white arrows the O-decorated Cu vacancies found inside of stacking faults and (c) Z-contrast image (d) and LAADF of an isolated stacking fault, where the partial dislocations and the associated strain are indicated by marks and arrows, respectively.

The generation of stacking faults can be interpreted as a mechanism to relieve accumulated stress generated at the grain boundaries or interfaces between different phases[132,133]. When stacking faults form an homogeneous ordered array, they result in the $YBa_2Cu_4O_y$ phase (Y124), which in turn, is a superconducting phase with lower $T_c = 80K$[134].

Stacking faults have been recently observed to host defect clusters consisting of 2 copper vacancies surrounded by 3 oxygen vacancies (O-decorated Cu vacancies)[135]. These clusters, indicated in figure 3.5(b), are expected to gain a ferromagnetic moment in the vicinity of the superconducting CuO_2 planes. Another relevant defect concomitant with the formation of stacking faults is the partial dislocation that appears at the edges of the planar defect, shown in figures 3.5(c-d). In the low angle mode of STEM, the higher contrast regions located on the dislocations indicate the strain associated to the atomic displacements and therefore regions of increased *nanostrain*.

The amount of stacking faults can be tuned by the change of different parameters during the oxygenation process (temperature, annealing time, cooling rate, oxygen partial pressure)[89,136]. In pristine films, stacking faults tend to accumulate near the surface of the film and at the interface with the substrate. An alternative very efficient way of strongly increase the density of stacking faults and modify their length is the insertion of *nanoparticles* in the YBCO matrix. In this case, stacking faults are generated during the growth process before the oxygenation step[75].

CSD is a very versatile technique that allows the incorporation of secondary phases by adding them to the precursor solution. Nanoparticles of $BaZrO_3$, Ba_2YTaO_6, $BaCeO_3$ or Y_2O_3 with diameters ranging from 5 nm up to 50 nm have been successfully incorporated and homogeneously distributed in the YBCO matrix, showing no decrease of the superconducting properties of the final YBCO nanocomposite but improved in field J_c behaviour[75,123,137]. Figure 3.6(a) illustrates the homogeneous distribution of $BaZrO_3$ nanoparticles along $\sim 1\ \mu$m wide cross-section.

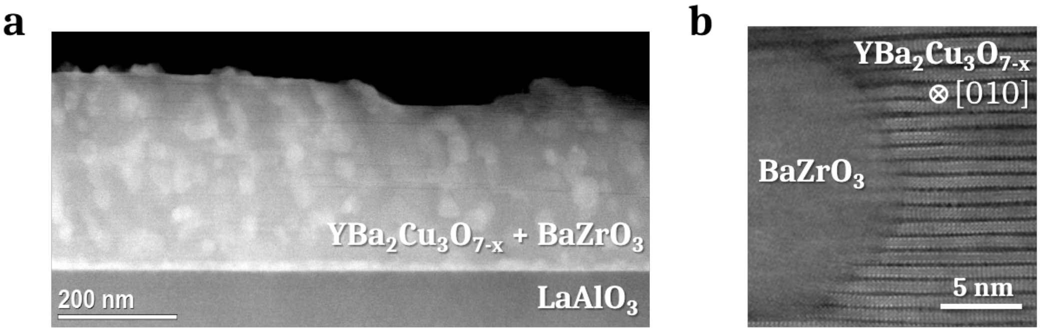

Figure 3.6: STEM images of YBCO-$BaZrO_3$ nanocomposites. (a) Low magnification LAADF image that shows the homogeneous distribution of nanoparticles (brighter spots) and (b) high-resolution Z-contrast image of the interface between a $BaZrO_3$ nanoparticle and YBCO.

The incoherent interface between nanoparticles and the YBCO matrix, originated by the lattice mismatch and the random orientation of the nanoparticle, induce a high concentration of stacking faults as observed in figure 3.6(b).

Another relevant defect in CSD YBCO films are the *twin boundaries*, the boundaries that separate the formation of a-axis and b-axis twin domains, formed to relieve spontaneous strains associated to the tetragonal-to-orthorhombic structural phase transformation during the oxygenation process of YBCO[84,85,132]. They consist of thin c-oriented planes with disordered and oxygen deficient regions[138]. In pristine CSD-TFA films, twin boundaries are coherent and separate twin domains with a typical spacing of the order of $\sim$ 45 nm, whereas in a CSD-TFA nanocomposite the domain spacing is reduced below 10 nm[139]. Moreover, the formation of domain walls is blurred by the already present high amount of stacking faults and hence this c-oriented planar defect losses its coherence along the c-axis[139].

Figure 3.7 shows the twin domains in the case of a YBCO-Ba_2TYaO_6 nanocomposite. It is possible to distinguish the domains through the observation of a stacking fault, since it involves a shift of half unit cell along the b axis[139]. Thus, there is a displacement of one CuO chain layer with respect to the other when viewed along the [100] zone axis, whereas the layers lay head-to-head when viewed along the [101] zone axis. As observed in the image, the structure of twin domains is strongly segmented in the presence of a high density of stacking faults[96,130].

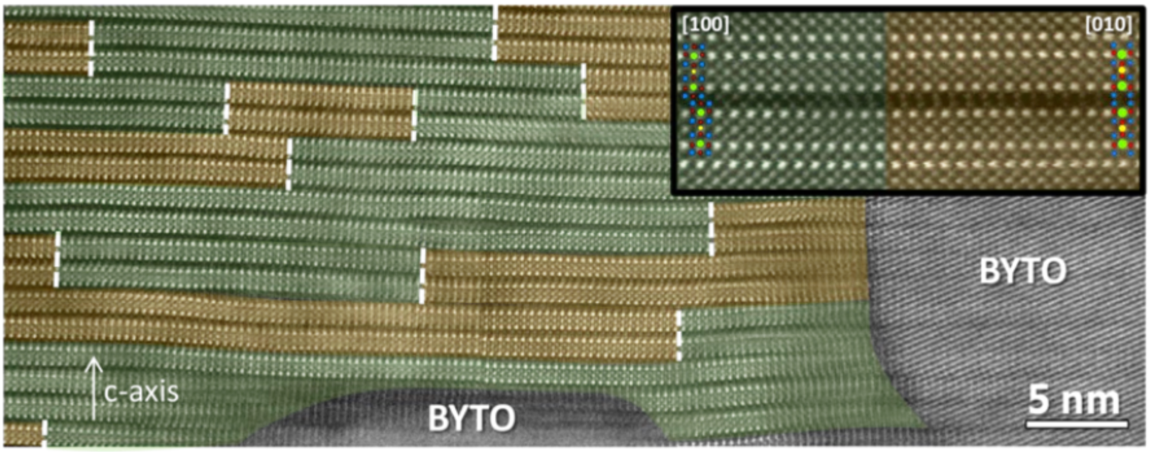

Figure 3.7: STEM image of a YBCO-Ba_2TYaO_6 nanocomposite. Green and brown colored regions mark different twin domains, corresponding to [100] and [010] YBCO zone axis orientations respectively. White dashed lines represent the twin boundaries. The inset shows the determination of each orientation according to the shift of half unit cell along the b-axis.

3.1.3 Previous work in CSD YBCO nanocomposites

In the last decades, the seek for an adequate microstructure that favours vortex pinning has been widely discussed and has certainly incited to search for new nanoengineering approaches able to tune the YBCO defect landscape with artificial pinning centres[35,56,57,104,110,112,140,141].

The study of vortex pinning roles played by defects as nanoparticles[75,117,126,142–146], nanorods[38,114,117,144,147,148], twin boundaries[129], dislocations[105,114] or natural and irradiated columnar defects[108,140] has been based on the correlation between growth processing parameters, electrical transport or magnetic properties and microstructural visualization techniques as atomic force microscopy, XRD, scanning electron microscopy or especially transmission electron microscopy.

Studies in CSD YBCO nanocomposites[75,76,122,126,149–151] revealed the generation of quasi-isotropic pinning coming from local scale inhomogeneous strains around the included non-coherent nanoparticles, associated to the distortion of the YBCO matrix. The nanostrain ε raises and correlates with the decrease of the effective mass anisotropy γ_{eff} (see figure 3.8(a)) and the increase of the isotropic contribution of the pinning force F_P^{iso} (see figure 3.8(b)).

This correlation between local strain and superconductivity has been explained in terms of the bond contraction pairing model[75,150,152,153], which is a 2D model assuming that hole pairing in adjacent Cu positions is made possible by the contraction of the in-plane Cu-O-Cu bond length d_{CuO} (see figure 3.9(a)). The elongation of d_{CuO} would quench Cooper pair formation just with a 1% of tensile strain, that turns the pair-breaking energy 2Δ into negative values, defined by:

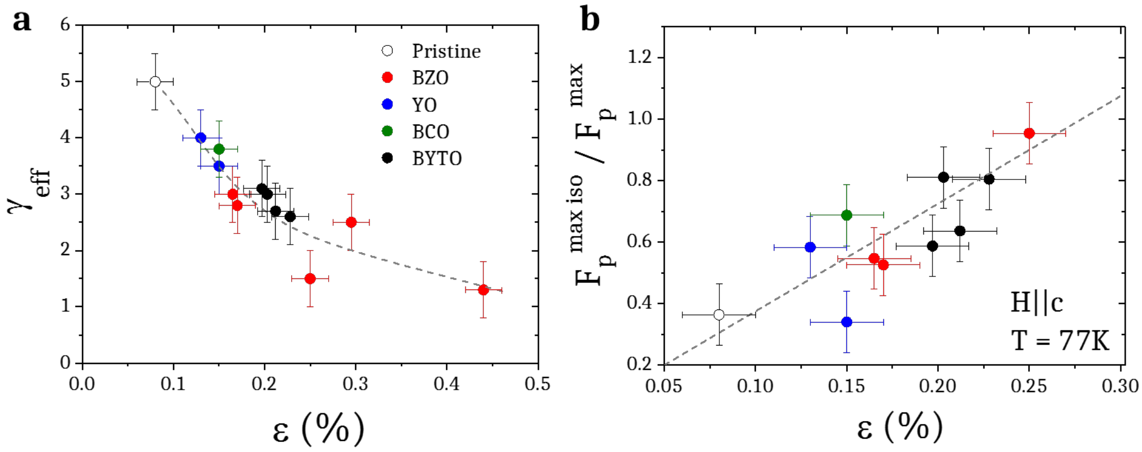

Figure 3.8: dependence of (a) γ_{eff} and (b) $\mathrm{F_P^{iso-max}/F_P^{max}}$(77K,H||c) versus nanostrain for pristine and ss-nanocomposite films with different nanoparticle compositions and concentrations[75].

$$2\Delta = 4\frac{(t_{CuO})^2}{U} - 8t_0 \tag{3.10}$$

Where $\mathrm{t_{CuO}}$ is the transfer integral between the Cu d and O p orbitals of neighbouring atoms that depends inversely with the bond length as $\mathrm{t_{CuO}} \propto 1/\mathrm{d_{CuO}}^5$, U is the on-site Coulomb repulsion and $8\mathrm{t_0}$ is the energy gained by releasing two electrons at the bottom of the conduction band, that is, the band width.

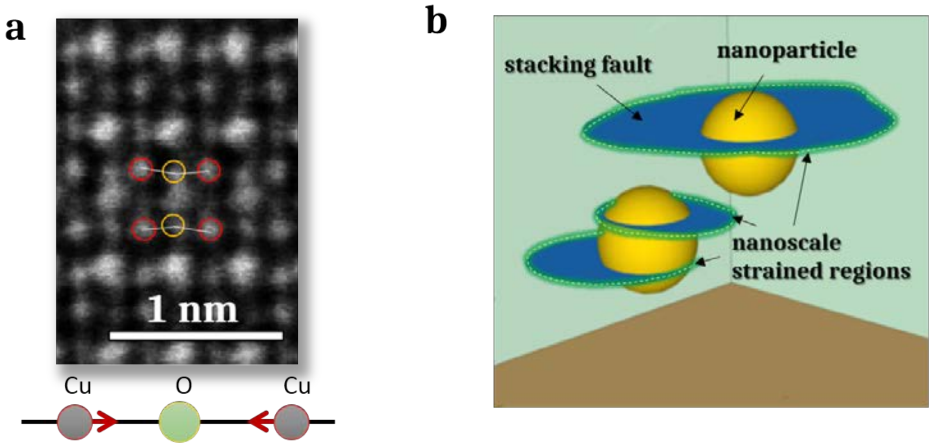

Figure 3.9: (a) ABF image of YBCO, where one Cu-O-Cu bond is marked. (b) Schematic view of the generated nanoscale strained regions, bounding the planar stacking faults.

The combination of high-resolution HAADF and LAADF STEM images as in figure 3.5 (c-d), showing an isolated stacking fault, reveals the localization of nanoscale strain at the edges of the stacking fault which is enclosed by a partial dislocation[133]. As described in section 3.1.2, the incoherent interface between the nanoparticles and the YBCO matrix induce a high concentration of stacking faults. Hence, the incorporation of nanoparticles strongly transforms the inhomogeneous nanostrain landscape, mediated by the planar Y124 intergrowths that induce a lattice deformation on the surrounding YBCO (sketched in figure 3.9(b)).

Most of pinning studies are limited to the properties when H is applied parallel to the c-axis of the crystal structure. A rotating device is necessary in order to explore orientations towards H||ab, and technical problems or sample burning are more usual for H||ab due to the application of higher critical currents. However, several vortex pinning studies have been focused on the correlated pinning when H is applied parallel to the CuO_2 planes of YBCO[28,131,154–157] and also to other ab-planes in layered iron based pnictides[158,159]. These works describe the observation of the $J_c(\theta)$ sharp peak attributed to intrinsic pinning and how the electric properties change all over the orientations when extrinsic pinning appears at H||ab coming from extended disorder such as for example Y124 intergrowths.

Y124 intergrowths are the most common defect in Y123 ($YBa_2Cu_3O_y$ phase) thin films and the density dramatically increases with disorder[132,135]. In order to obtain a deeper understanding on the role that stacking faults play in the generation of nanostrain and the reduction of γ_{eff}, this chapter is devoted to the identification of regimes of pinning domination coming from stacking faults in order to confirm or disprove their importance in the advanced pinning landscape in CSD YBCO nanocomposites.

3.2 Enlargement of the single-vortex pinning regime

This and the following two chapters show the results obtained for pristine and CSD-TFA ss-nanocomposites containing $BaZrO_3$, Ba_2YTaO_6, and mixed Ba_2YTaO_6-$BaZrO_3$, Ba_2YTaO_6-CuO, Ba_2YTaO_6-Y_2O_3 and $BaZrO_3$-Y_2O_3 spontaneous segregated nanoparticles, sometimes referred in this thesis as BZO, BYTO, and mixed BYTO-BZO, BYTO-CuO, BYTO-YO, and BZO-YO nanocomposites respectively. All these films have an approximated thickness of 250 ± 20 nm. The investigation of the growth, processing and oxygenation of these films is explained in detail in another PhD thesis[77].

Different nanoparticle compositions and concentrations are used in order to generate different landscape of stacking faults, leading to different nanostrain and pinning regimes. The aim of mixing distinct nanoparticles that nucleate in a different way is to explore other kind of nanocomposites and to count with a broader scope of stacking fault arrangements (density, length, shape,...).

The nanostrain and main electrical transport properties from the principal samples are shown in table 3.1. The main remark is that neither T_c nor ΔT_c show any sort of degradation for nanocomposites. The dramatic increase of stacking fault density and the incorporation of insulating nanoparticles do not drastically modify the superconducting YBCO phase structure or the oxygen doping. Both pristine and nanocomposite films are perfectly epitaxial showing $J_c^{sf,77K}$ values in the range of 1 to 4 MA/cm^2 and T_c values in the range of 91 to 93 K. Therefore, the study is performed with good quality and optimally doped samples with comparable critical current densities.

Figure 3.10(a) shows the $J_c(H)$ curves for several samples at 77 K for H||c, where nanocom-

NAME	COMPOSITION	T_c (K)	ΔT_c (K)	$J_c^{sf,77K}$ (MA/cm^2)	ε (%)
Pristine-1	$YBa_2Cu_3O_{7-\delta}$	90.0	1.4	4.2	0.13*
Pristine-2	$YBa_2Cu_3O_{7-\delta}$	92.4	6.4	2.8	0.13*
Pristine-3	$YBa_2Cu_3O_{7-\delta}$	91.7	2.3	3.1	0.13*
Pristine-4	$YBa_2Cu_3O_{7-\delta}$	92.7	3.1	4.3	0.13*
8BYTO	$YBa_2Cu_3O_{7-\delta}+$ 8%M Ba_2YTaO_6	90.2	1.0	3.5	0.20
8BYTOmod$^+$	$YBa_2Cu_3O_{7-\delta}+$ 8%M Ba_2YTaO_6	91.0	4.5	1.2	0.27
10BYTO	$YBa_2Cu_3O_{7-\delta}+$ 10%M Ba_2YTaO_6	92.3	3.1	1.3	0.27
6BYTO-5BZO	$YBa_2Cu_3O_{7-\delta}+$ 6%Ba_2YTaO_6/5%$BaZrO_3$	90.6	4.3	2.0	0.25
6BYTO-5YO	$YBa_2Cu_3O_{7-\delta}+$ 6%M Ba_2YTaO_6/5%M Y_2O_3	90.6	2.6	1.8	0.24
6BYTO-10CuO	$YBa_2Cu_3O_{7-\delta}+$ 6%M Ba_2YTaO_6/10%M CuO	91.0	2.5	2.9	0.25
10BZO-5YO	$YBa_2Cu_3O_{7-\delta}+$ 10%M $BaZrO_3$/5%M Y_2O_3	91.7	1.8	3.0	-
10BZO-5YOmod$^+$	$YBa_2Cu_3O_{7-\delta}+$ 10%M $BaZrO_3$/5%M Y_2O_3	91.8	2.2	1.9	0.26
5BZO-5YO	$YBa_2Cu_3O_{7-\delta}+$ 5%M $BaZrO_3$/5%M Y_2O_3	91.0	1.7	4.0	0.20

Table 3.1: pristines and ss-nanocomposites. Main electrical properties and nanostrain for pristine and ss-nanocomposite films studied in chapters 3, 4 and 5. The name of ss-nanocomposites is preceded by SS when needed for comparison. *: 0.13 is the nanostrain measured in a very similar pristine film. $^+$: mod stands for modified initial solution.

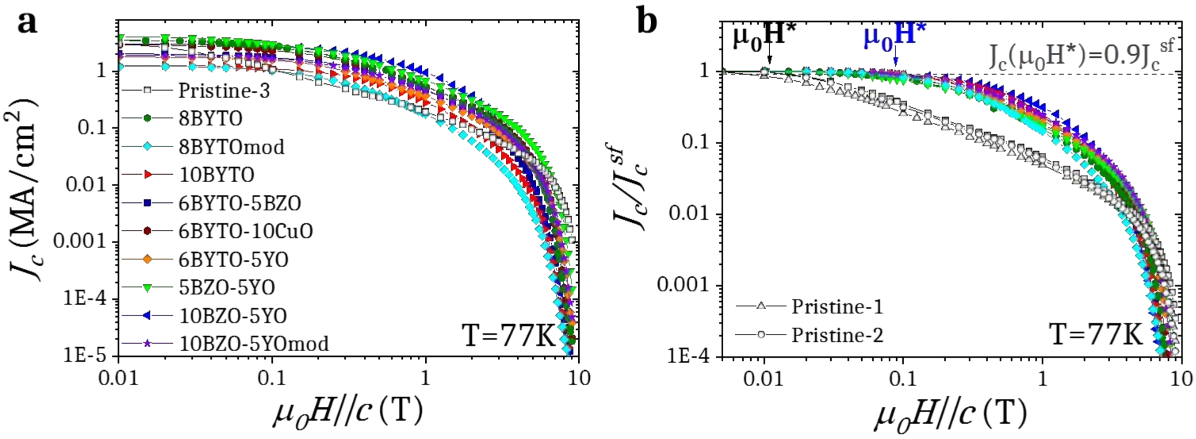

Figure 3.10: magnetic field dependence of (a) J_c and (b) normalized J_c/J_c^{sf} for pristine and ss-nanocomposite thin films at 77K for H||c.

posites provide higher J_c in an intermediate magnetic field range of $\sim 0.05-5$ T. However, the strong decay of J_c at high magnetic fields, usually ascribed to the irreversibility line, occurs at lower magnetic fields for nanocomposites than for the pristine sample, what suggests a reduction of H_{irr} for nanocomposites. This downward shift of the irreversibility line for H||c is commonly attributed to the loss of c-axis correlated pinning[98,125,140,160–162], twin boundary pinning in this case.

The smoother magnetic field dependence appreciated for nanocomposites in the normalized critical current density J_c/J_c^{sf} in figure 3.10(b) foresees a completely different pinning scenario as compared with pristine samples. An evidence of the presence of a higher density of defects is the enlargement for nanocomposites of the single-vortex pinning regime limited by the so called crossover or accommodation magnetic field H^*[7,44,101,103,118], previously introduced in section 3.1.1.2. This characteristic field H^* can be phenomenologically defined for the $J_c(H)$ dependence either by the crossing of the individual fittings of the single-vortex pinning and vortex-vortex interactions regimes[105,108,163], the onset field of the $J_c(H) \sim H^{-1}$ dependence[102] or the field at which the critical current reaches 90% of the self-field value[164,165]. In this work, the latter definition is used:

$$J_c(\mu_0 H^*) = 0.9 J_c^{sf} \tag{3.11}$$

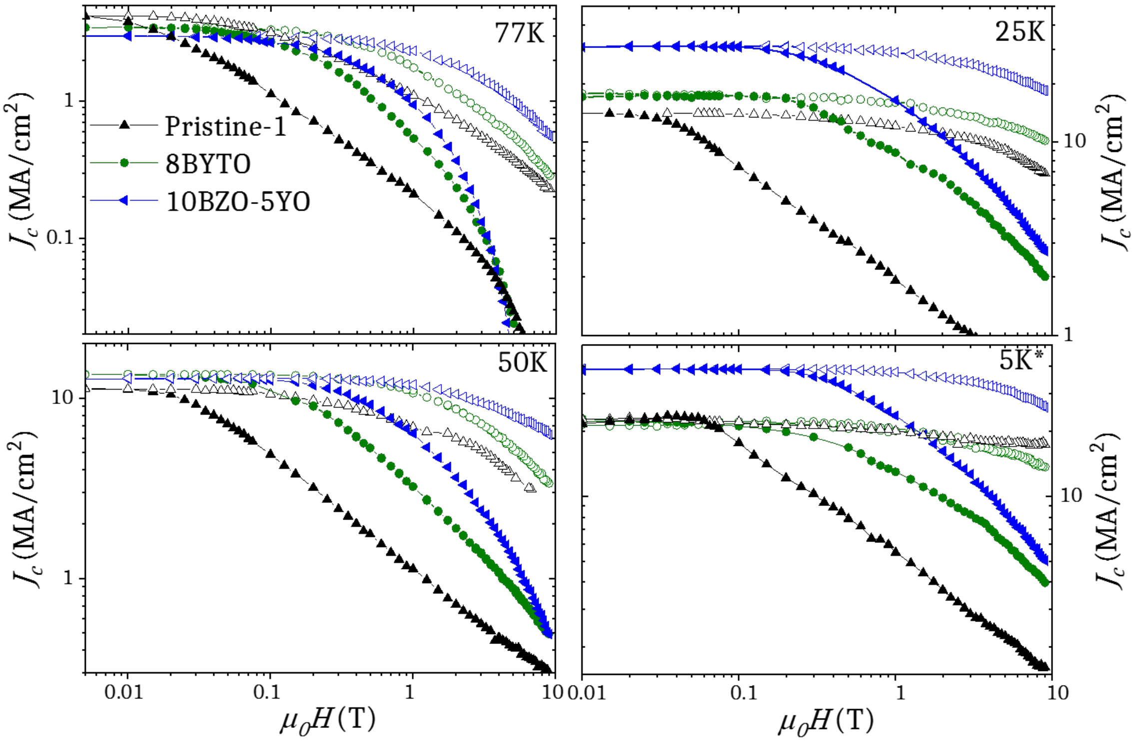

Figure 3.11: magnetic field dependence of J_c at temperatures of 77, 50, 25, and 5 K for a pristine sample, 8BYTO and mixed 10BZO-5YO, for H||c (closed symbols) and H||ab (open symbols). *:at 10 K for 10BZO-5YO.

The study of the magnetic field dependence is extended to lower temperatures and to the H||ab orientation for three samples, for comparison: Pristine-1 and nanocomposites 8BYTO and 10BZO-5YO (see figure 3.11). A first observation is that the strong decay related to the irreversibility line is shifted to higher fields at lower temperatures (in agreement with the $H_{irr}(T)$ dependence) so that J_c is always higher for nanocomposites up to 9T for temperatures below 50K. It is also remarkable that the critical current densities for H||ab are higher for nanocomposites. Only the 8BYTO sample is surpassed by the pristine at 5 K and high fields, where $J_c(H)$ is almost flat for the pristine sample.

Although the strong $J_c(H)$ decay is shifted to higher fields at lower temperatures, a crossover of $J_c(H)$ is foreseen between pristine and nanocomposite films if a linear extrapolation is performed, due to higher α values in nanocomposites in comparison to the pristine, further discussed in section 3.3.2.

Pristine, 8BYTO nanocomposite and mixed nanocomposite 10BZO-5YO exhibit respectively from smallest to largest H*, for both H||c and H||ab, what suggests that the enlargement of the single vortex pinning regime is related to the generation of a defect that pins at different orientations of the magnetic field.

The temperature dependence of H* is plotted in figure 3.12 for different samples. No matter the composition or the concentration, every nanocomposite has in common the enlargement of the single vortex pinning regime in comparison to the pristine sample, for both H||c and H||ab.

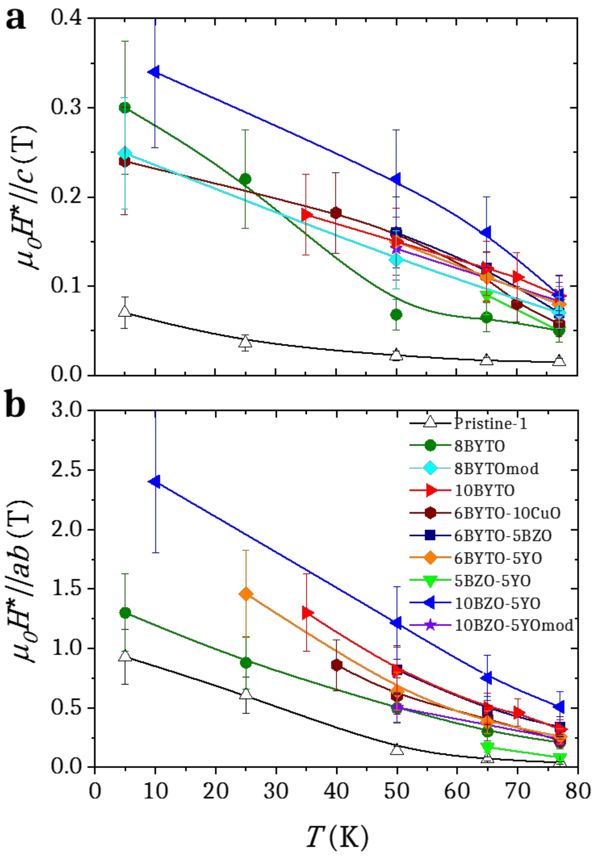

Figure 3.12: temperature dependence of μ_0H* for (a) H||c and (b) H||ab for pristine and ss-nanocomposites.

At very low temperatures, some nanocomposites exhibit μ_0H* as high as 0.35 T for H||c and 2.5 T for H||ab. The average ratio of $H^*_{\mathrm{nanocomposite}}/H^*_{\mathrm{pristine}}$ is ∼ 5 for H||c. However, for H||ab, the ratio changes from ∼ 5 at high temperatures to ∼ 2 at lower temperatures.

When interpolating the $J_c(H)$ data shown in figure 3.11 along the magnetic field axis, and fitting the obtained interpolated curves transversely through the $J_c(T)$ dependence, one obtains a 3D matrix that corresponds to the 3D surface of $J_c(H, T)$, shown in figure 3.13 for the same samples and orientations (H||c & H||ab). The temperature fitting equation is a combination of mainly the sum of equations 3.1 and 3.2 and secondary a B-spline interpolation explained in detail in appendix A.

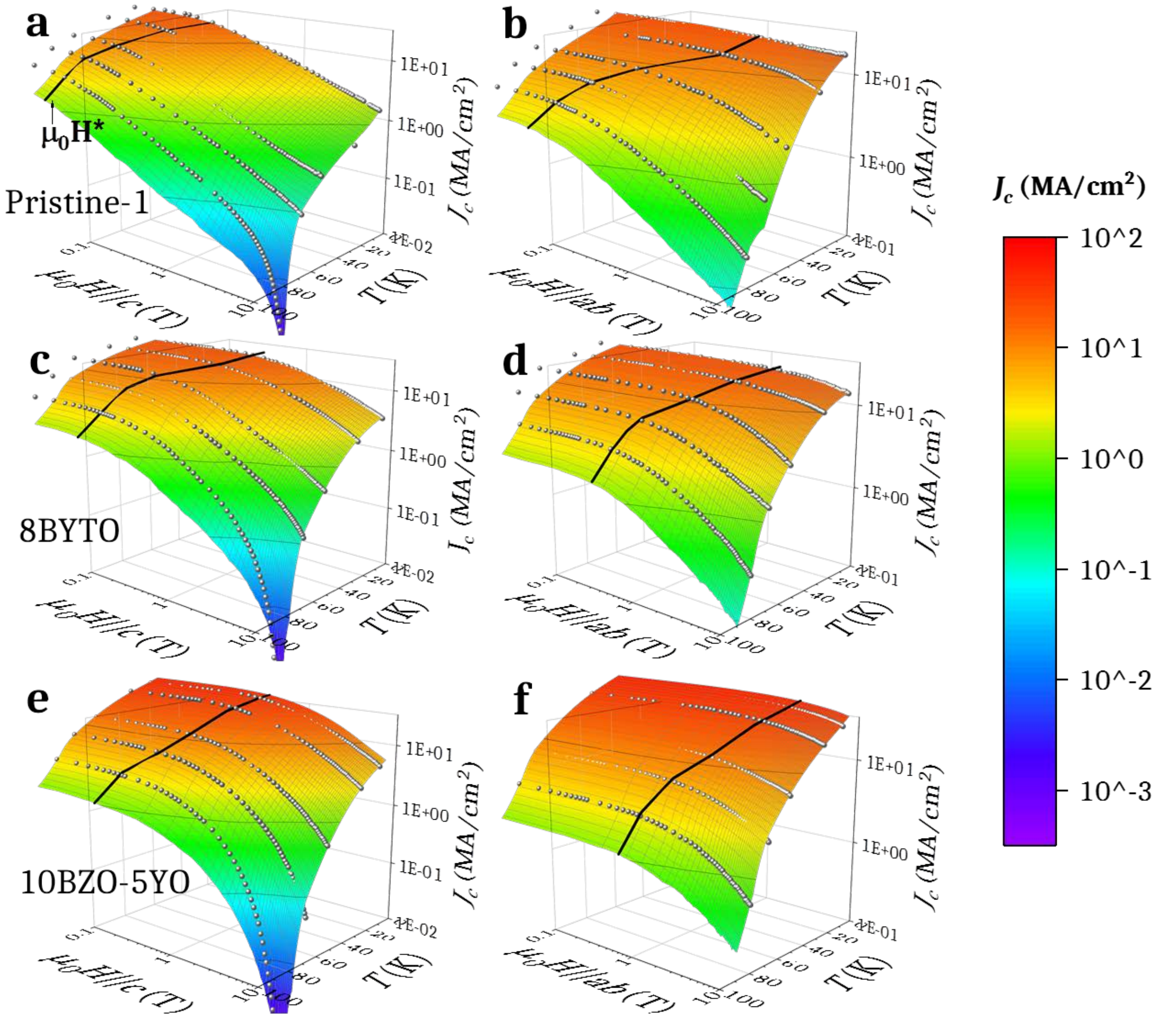

Figure 3.13: 3D $J_c(H, T)$ surfaces for (a-b) Pristine1, (c-d) 8BYTO and (e-f) 10BZO-5YO films for H||c (left) and H||ab (right). Open symbols are the measured $J_c(H)$ curves and solid lines correspond to the $\mu_0H^*(T)$ lines from figure 3.12.

At low temperatures and low magnetic fields, concurrent with the enlargement of the $\mu_0H^*(T)$ line, the 3D $J_c(H, T)$ representation illustrates the enlargement of the reddish high density current region (> 10 MA/cm^2) for nanocomposites, the appealing region for high-current applications. On the other hand, the rapid decay of J_c related to the irreversibility line is visible at an earlier stage for nanocomposites for H||c but not so evident for H||ab.

In order to study how the enlargement of the single vortex pinning regime is related to the new pinning landscape arising in CSD-TFA YBCO nanocomposites, characterised by the presence of many stacking faults, both isotropic and anisotropic pinning contributions need to be evaluated.

3.3 Isotropic pinning

3.3.1 Irreversibility line and isotropic collapse

The irreversibility line $H_{irr}(T)$ that separates solid from liquid vortices, and hence the region of finite J_c, has been obtained through $\rho(T)$ measurements at 0.5 T, 1 T, 3 T, 5 T and 9 T for different orientations in the same bridges were the I-V curves measurements have been carried out.

The comparison of nanocomposites versus a pristine sample is shown in figure 3.14 and reveals a decrease of $H_{irr}(T/T_c)$ for nanocomposites, particularly pronounced for H||c but less obvious for $\theta = 60°$ and especially for H||ab, where the 10BZO5YO nanocomposite reveals no decrease.

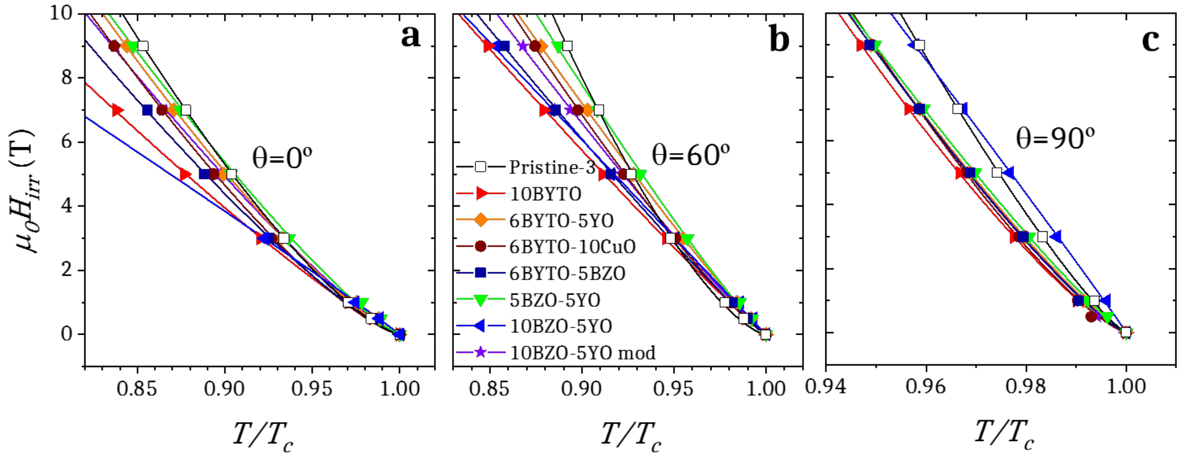

Figure 3.14: normalized temperature dependence of the irreversibility line $H_{irr}(T/T_c)$ for pristine and ss-nanocomposites for the magnetic field orientations: (a) H||c (b) $\theta = 60°$ and (c) H||ab.

Note that the insertion of defects in nanocomposites can change the dominating pinning and therefore work out well for the performance at some H-T conditions but at the same time weaken sources of pinning that are dominant at other regions of the H-T diagram.

As explained in section 3.1.1.3, $H_{irr}(T,\theta)$ curves collapse into the same curve for different θ belonging to an angular range with absence of correlated defects $(40° - 70°)$ when it is replaced by the scaled irreversibility line $\epsilon(\theta)H_{irr}(T,\theta) = H_{eff}(T_{irr})$. Figure 3.15 shows the collapse for a pristine and the 6BYTO-5BZO nanocomposite where different γ_{eff} are tested. $\gamma_{eff} = 6$ and $\gamma_{eff} = 2.5$ show the best superposition for the pristine and the nanocomposite respectively. γ_{eff} of all samples have been obtained following this procedure.

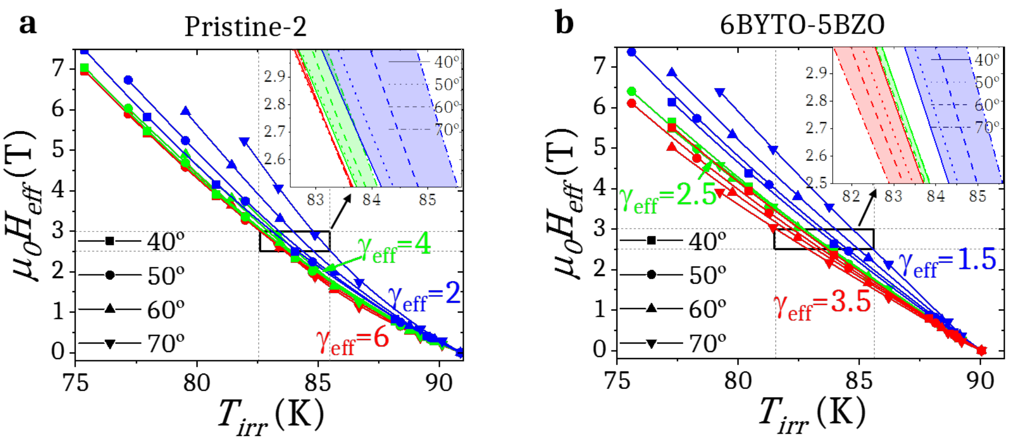

Figure 3.15: collapse of the scaled irreversibility line $H_{eff}(T_{irr})$ for (a) Pristine2 and (b) 6BYTO-5BZO. The different colors correspond to different tested γ_{eff}. Insets are zooms of the selected regions (dashed lines).

$J_c(\theta)$ curves can be plotted versus the scaled magnetic field H_{eff} as shown in figure 3.16 for the same pristine and 6BYTO-5BZO samples, where γ_{eff} values obtained in figure 3.15 are used. The collapsed curves (dashed lines) represent the lines coinciding with the J_c values that are essentially coming from isotropic pinning contributions ($J_c^{iso}(H_{eff})$).

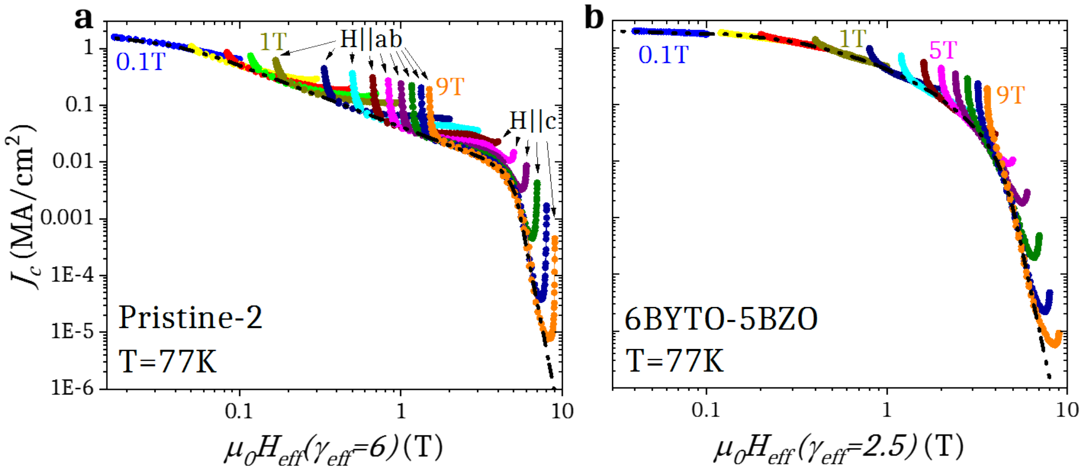

Figure 3.16: $J_c(\theta)$ as a function of $\mu_0 H_{eff}$ with corresponding γ_{eff} for (a) Pristine-2 and (b) 6BYTO-5BZO films at 77 K. The dashed line is the identification of the collapsed $J_c^{iso}(H_{eff})$ line. Deviations from the collapsed values are identified for orientations close to H||ab and H||c for the pristine film.

The J_c values that surpass the collapsed line, have an extra anisotropic contribution J_c^{aniso}, that can be calculated by using equation 3.9.

At 77 K, the pristine film exhibits strong anisotropic contributions for orientations close to H||ab and H||c whereas the nanocomposite exhibits less anisotropic contribution for H||c and a wider collapsed isotropic angular range.

The isotropic collapse line $J_c^{iso}(H_{eff}(\theta))$ can be transferred to $J_c^{iso}(H)$ for each orientation of the magnetic field and to $J_c^{iso}(\theta)$ for each magnetic field. Figure 3.17 shows the $J_c(\theta)$ dependence at 77 K for the same pristine and 6BYTO-5BZO samples where the collapsed

$J_c^{iso}(\theta)$ is also indicated. This plot illustrates that not only isotropic contributions are altered by a change of γ_{eff} but also anisotropic contributions suffer a change for both H||ab and H||c from pristine to nanocomposite film: a widening of the ab-peak, related to the increase of stacking faults (further developed in section 3.4.1) and the reduction of the c-peak, quantified by very different $J_c^{aniso}(9T, H||c, 77K)$ values: $4.5 \cdot 10^{-4}$ MA/cm^2 for the pristine and $9 \cdot 10^{-6}$ MA/cm^2 for the nanocomposite. This latter alteration for H||c is related to the twin boundary coherence break (further developed in section 3.4.3).

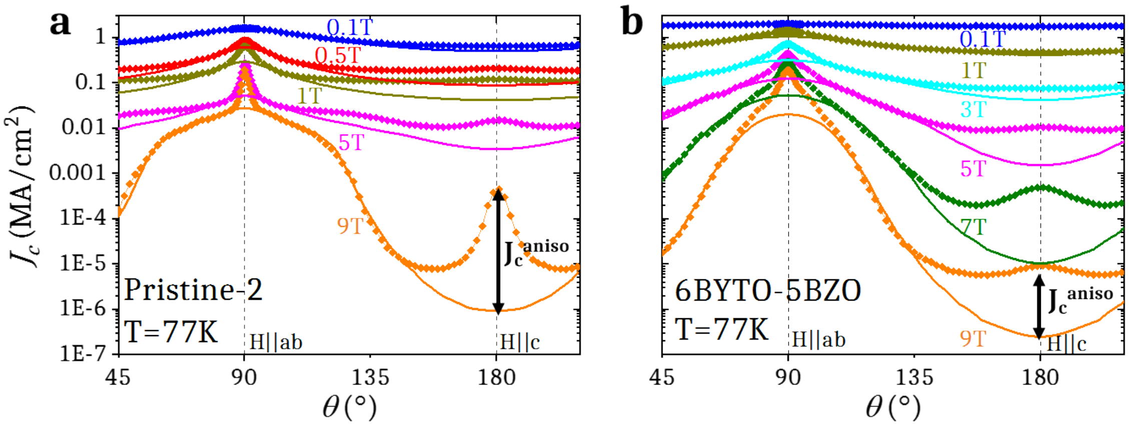

Figure 3.17: $J_c(\theta)$ dependence at 77 K for (a) Pristine-2 and (b) 6BYTO-5BZO samples. The solid lines correspond to the isotropic contribution $J_c^{iso}(\theta)$ obtained from the collapse in figure 3.16. Double-headed arrows indicate $J_c^{aniso}(9T, H||c, 77K)$.

3.3.2 Isotropic contributions in the H-T diagram

Using the approximation proposed in equation 3.9 for the in-field $J_c(H)$ dependence at different temperatures, it is possible to disentangle isotropic and anisotropic pinning centres active at different temperatures and magnetic fields, providing a unique tool to evaluate and look for the most adequate vortex pinning landscape under different operating conditions.

In this section, $J_c(H)$ curves for the three samples introduced in figure 3.11 are extensively analysed at a wide range of temperatures for both H||c and H||ab. The critical current density is separated into isotropic and anisotropic in-field contributions and the origin of changes in nanocomposites, as the change in $\mu_0 H^*$ or α values, is discussed.

First, the pristine film results shown in figure 3.18 confirm that pinning for H||c is dominated by isotropic pinning centres at low magnetic fields, up to 0.1-0.2 T at high temperatures (65-77 K) and up to 9 T at very low temperatures. H^* is much lower than these magnetic fields and thus coincides with H^*_{iso}, corresponding to the limit of the single vortex pinning regime restricted to the isotropic contribution and calculated by $J_c^{iso}(H^*_{iso}) = 0.9 J_c^{iso}(sf)$. Only in the power-law regime at higher temperatures, the contribution of anisotropic defects start to be visible and therefore α is product of hybrid pinning composed by isotropic and anisotropic defects. Anisotropic pinning clearly dominates at high temperatures and fields, suggesting that twin boundaries are important at these conditions and are responsible of preserving a high H_{irr} for H||c.

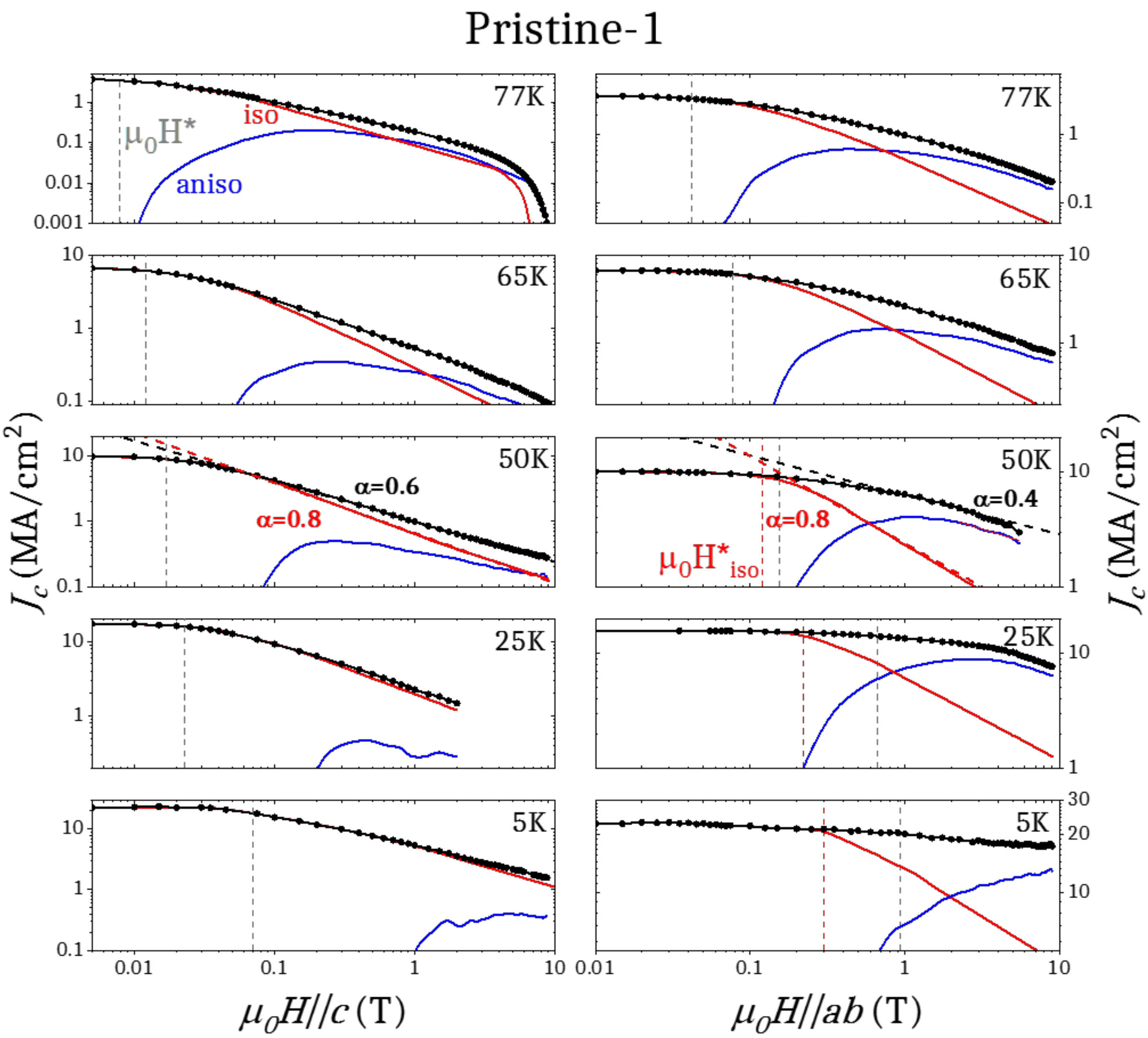

Figure 3.18: $J_c(H)$ separation into $J_c^{iso}(H)$ and $J_c^{aniso}(H)$ for Pristine-1 at 77 K, 65 K, 50 K, 25 K and 5 K for H||c (left) and H||ab (right) orientations. Dashed vertical lines indicate μ_0H^* and $\mu_0H^*_{iso}$ magnetic fields. Dashed inclined lines are examples of linear fittings to the power-law equation $J_c(H) = A(\mu_0H)^{-\alpha}$.

For H||ab, anisotropic pinning is more prominent. Below 50 K, anisotropic defects take part in the single vortex pinning regime as well, enhancing H^* up to almost an order of magnitude larger than H^*_{iso}. The correlated pinning coming from intrinsic pinning and stacking faults dominate at intermediate and high fields. However, at very low temperatures, isotropic defects do compete with anisotropic defects up to intermediate magnetic fields. Therefore, α is related to the presence of both anisotropic and isotropic components.

α values at different temperatures for the pristine film are in the range $0.5 - 0.7$ for H||c, which are typical values for standard samples without nanoengineering. α_{iso} is slightly higher: $0.6 - 1$. It is then the influence of anisotropic pinning centres that reduce α to lower values. For H||ab, the reduction promoted by anisotropic pinning is even clearer, where $\alpha \sim 0.1 - 0.6$ whereas $\alpha_{iso} \sim 0.6 - 1$.

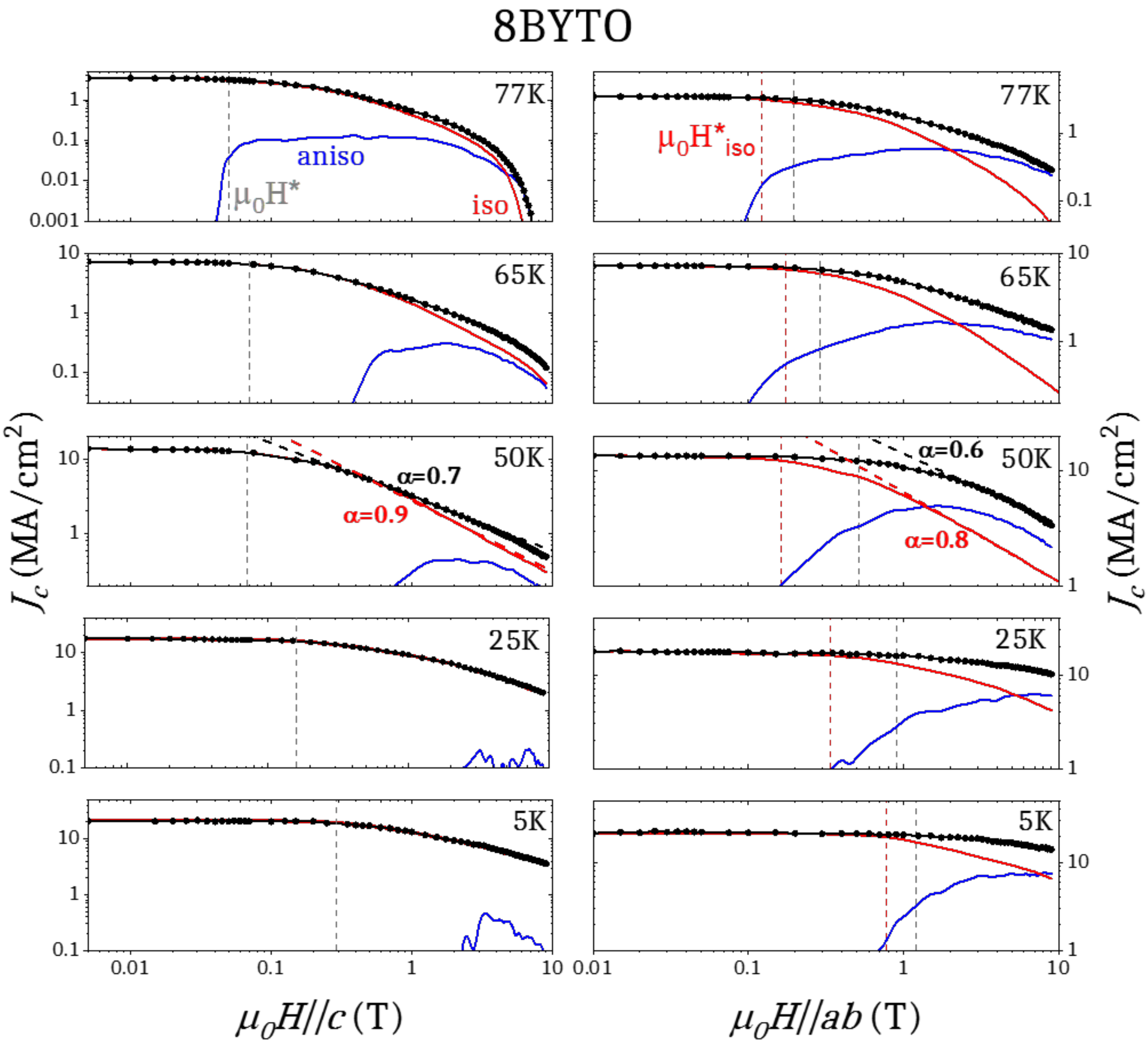

Figure 3.19: $J_c(H)$ separation into $J_c^{iso}(H)$ and $J_c^{aniso}(H)$ for 8BYTO at 77 K, 65 K, 50 K, 25 K and 5 K for H||c (left) and H||a (right) orientations. Dashed vertical lines indicate $\mu_0 H^*$ and $\mu_0 H^*_{iso}$ magnetic fields. Dashed inclined lines are examples of linear fittings to the power-law equation $J_c(H) = A(\mu_0 H)^{-\alpha}$.

Secondly, in the case of the 8BYTO nanocomposite shown in figure 3.19, the separation of $J_c(H)$ curves for H||c reproduces similar features to that ones from the pristine film, except for two important differences: the greater enlargement of H^*, related to an increase of isotropic pinning centres, and the less appreciable anisotropic pinning contribution attributed to the twin boundaries. In fact, below 25 K, it is hard to appreciate any contribution of anisotropic pinning centres, so that the entire $J_c(H)$ is dominated by isotropic pinning.

For H||ab, apart from the enlargement of H^*_{iso}, the magnetic field difference between H^* and H^*_{iso} is observable already at high temperatures in contrast to the pristine sample. It is reasonable to observe for nanocomposites an additional anisotropic contribution at high temperatures since stacking faults are characterized by a wider pinning well than intrinsic pinning and therefore are still effective to pin vortices with larger coherence length ξ at higher temperatures. At high fields, pinning is shared by isotropic and anisotropic defects, that are more dominant at low temperatures and high temperatures respectively.

The α decrease promoted by anisotropic pinning centres is lower in this sample. For H||c, α goes from $\alpha^{\mathrm{iso}} \sim 0.6 - 1.2$ to $\alpha \sim 0.6 - 0.8$, in agreement with vanishing of the twin boundary contribution. The same occurs for H||ab, where an already low $\alpha^{\mathrm{iso}} \sim 0.4 - 1$ is only reduced to $\alpha \sim 0.3 - 0.6$. This means that the new configuration of planar defects originated due to the incorporation of nanoparticles act differently in the collective pinning regime than the usual intrinsic pinning dominant configuration in pristine samples.

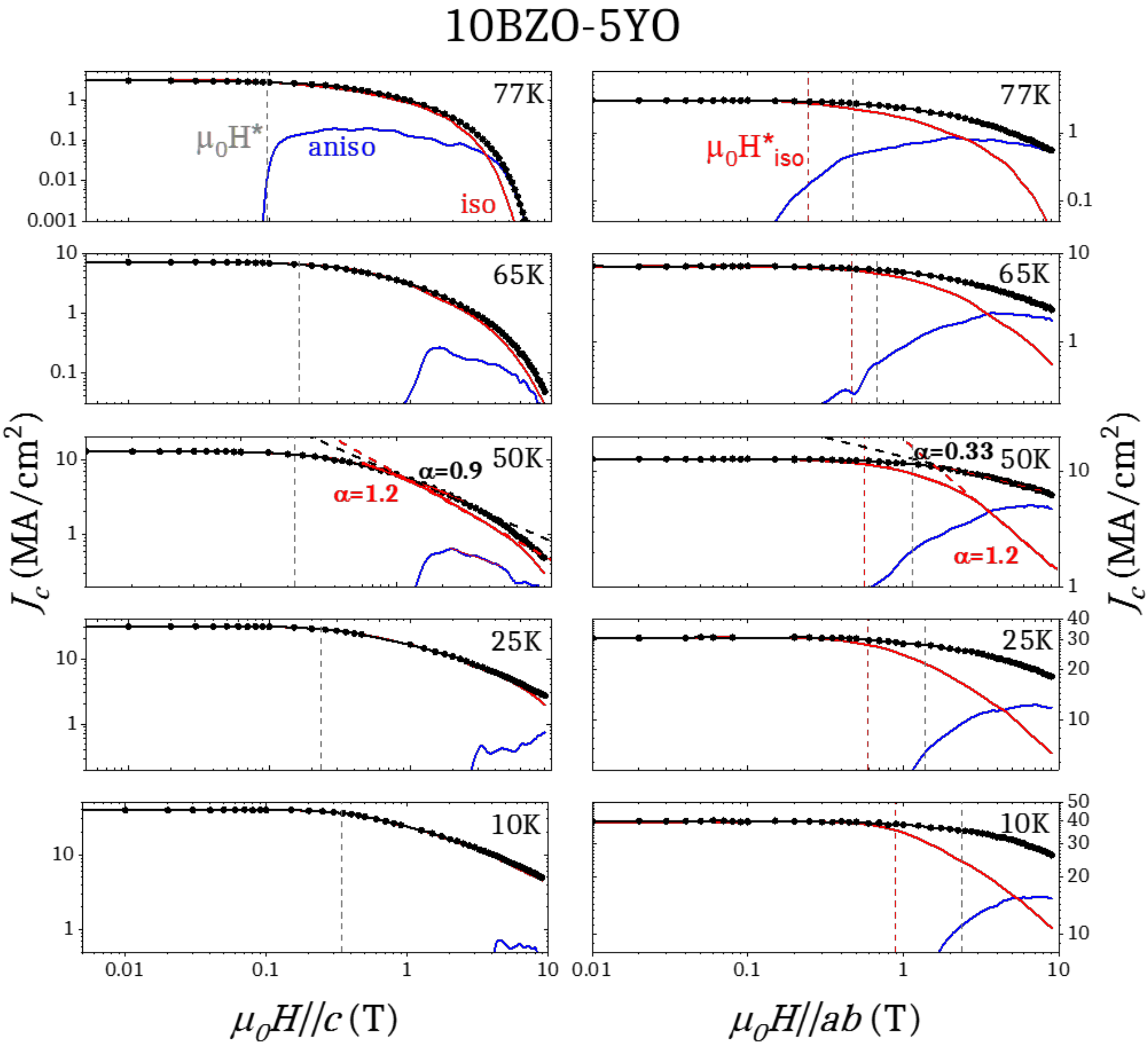

Figure 3.20: J_c(H) separation into J_c^{iso}(H) and J_c^{aniso}(H) for 10BZO-5YO at 77 K, 65 K, 50 K, 25 K and 5 K for H||c (left) and H||ab (right) orientations. Dashed vertical lines indicate μ_0H* and $\mu_0 H^*_{\mathrm{iso}}$ magnetic fields. Dashed inclined lines are examples of linear fittings to the power-law equation $J_c(H) = A(\mu_0 H)^{-\alpha}$.

Finally, in the case of the mixed 10BZO-5YO nanocomposite shown in figure 3.20, the isotropic-anisotropic disentanglement leads again to the vanishing of the twin boundary contribution for H||c and the appearance of anisotropic defects for H||ab that are effective in the single vortex pinning regime also at high temperatures.

This sample is especially dominated by the isotropic contribution for H||c except near the irreversibility line at high fields and temperatures. For H||ab, the competition between isotropic and anisotropic contributions of the same magnitude is again reproduced at high magnetic fields.

Another feature of 10BZO-5YO is that α^{iso} is particularly large. It reaches values in the range of $\sim 1-1.2$ for H||c and $\sim 0.7-1.2$ for H||ab, whereas α reaches $\sim 0.6-0.8$ and $\sim 0.3-0.6$ respectively. The remarkably strong difference between α^{iso} for 10BZO-5YO and 8BYTO nanocomposites despite the similar final α for H||ab indicates a different arrangement of the planar defects parallel to ab, leading to different isotropic and correlated pinning that can be effective at distinct regions of the H-T diagram.

Several works report decreased α values in nanocomposites down to 0.2 for H||c[110,112,114,117,147]. The induced defects in these cases are nanorods, irradiated columns and other correlated defects and it is very likely that the reduction of α is related to the raising of the anisotropic contribution of these defects. A few works report an increase of α in nanocomposites[37,113,116], attributed to the appearance of weak defects (and therefore, isotropic) or due to a loss of c-axis correlated disorder. In the films studied in this section, both the change in the isotropic contribution as the loss of c-axis correlated pinning contribute to the enlargement of the slope of the power law.

The particular extension of the single vortex pinning regime through anisotropic pinning centres for H||ab happens at all temperatures for nanocomposites but only at low temperatures for the pristine. This can be the reason to explain the high and low ratio $H^*_{\mathrm{nanocomposite}}/H^*_{\mathrm{pristine}}$ observed at high and low temperatures for H||ab in figure 3.12.

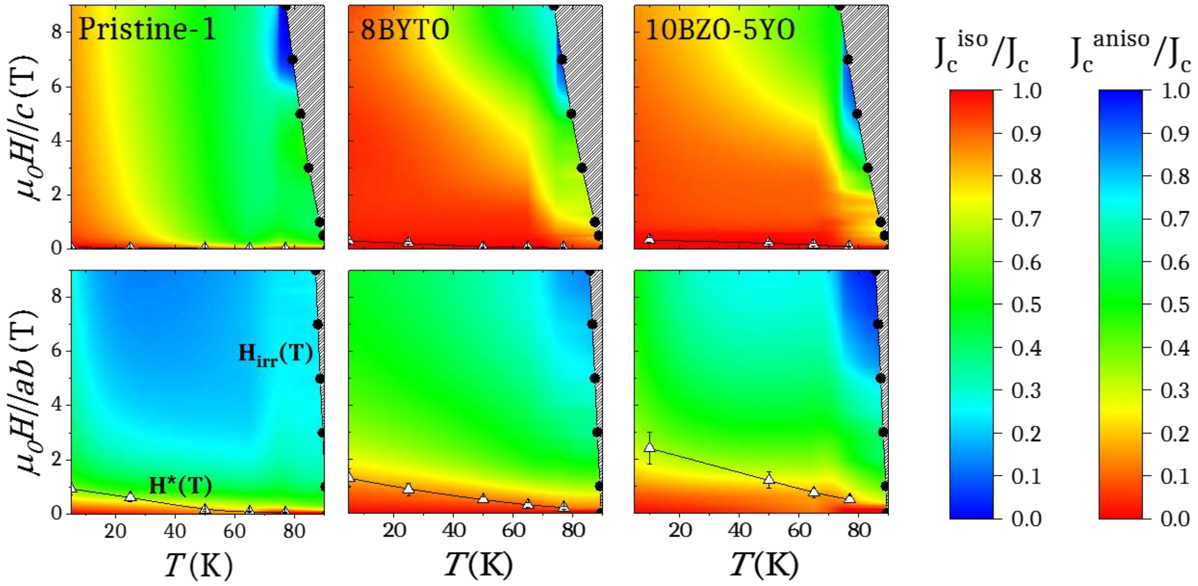

Figure 3.21: μ_0H-T color map of the ratios J_c^{iso}/J_c and J_c^{aniso}/J_c for Pristine, 8BYTO and 10BZO-5YO for H||c (above) and H||ab (below). Solid lines with circles and triangles correspond to $H_{\mathrm{irr}}(T)$ and $H^*(T)$ curves respectively.

After the isotropic-anisotropic separation of these three samples and applying the interpolation and fitting procedure explained in appendix A, it is possible to acquire the 3D surfaces for each of the pinning contributions normalized to the total J_c: the ratios J_c^{iso}/J_c and J_c^{aniso}/J_c. The calculation of this ratios leads to the inverted H-T color maps shown in figure 3.21 that identify by color the main regions of pinning dominance.

For nanocomposites, the dominance of isotropic pinning is enhanced in both, temperature and magnetic field, and the anisotropic pinning dominance is shrunk at high fields and temperatures for H||c. For H||ab, the dominance of isotropic pinning expands to larger magnetic fields of the order of 1 T, especially at low temperatures.

3.3.3 Relation of nanostrain and isotropic pinning

The ss-nanocomposites studied in this work, summarized as BZO-based and BYTO-based nanocomposites, have a nanostrain ε, γ_{eff} and isotropic pinning force ratio F_P^{iso}/F_P that are in agreement with the correlations deduced in previous works[75,126,149], plotted in figure 3.22. They all belong to a range of intermediate-high ε (0.15 – 0.3%), low γ_{eff} (1.5 – 3) and high F_P^{iso}/F_P (0.6 – 1).

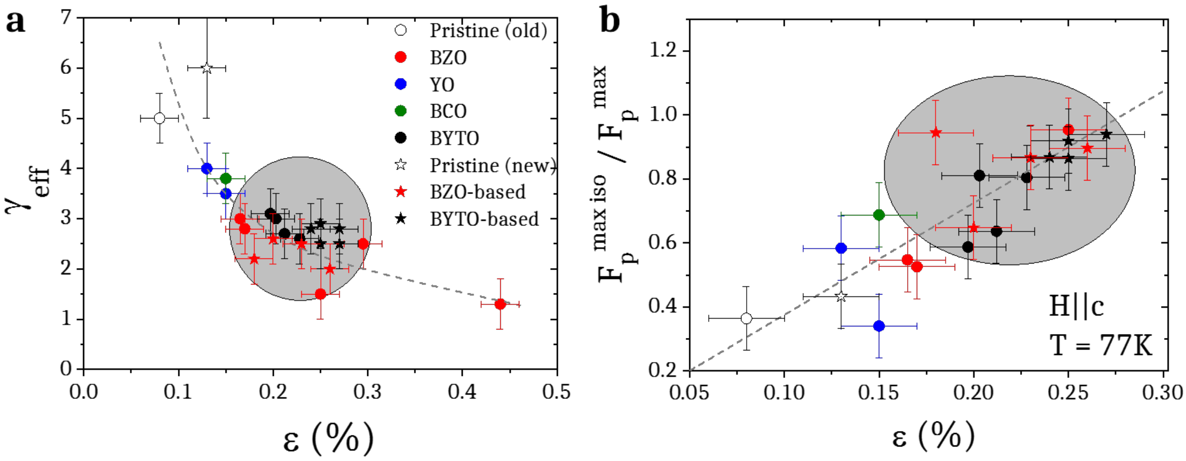

Figure 3.22: dependence of (a) γ_{eff} and (b) $F_P^{iso-max}/F_P^{max}$(77K,H||c) versus nanostrain ε for pristine and ss-nanocomposite films with different nanoparticle compositions and concentrations[75]. Samples particularly studied in this work are BZO-based and BYTO-based, whose graph region is marked in grey.

As it can be observed in figure 3.21, the $H^*(T)$ curve falls inside the H-T region that is mostly governed by isotropic pinning centres, especially for H||c. On the other hand, isotropic pinning correlates with nanostrained regions induced by the incorporation of nanoparticles. Hence, the increase of H^* should be related to the increase of ε in nanocomposites.

Figure 3.23 shows indeed the correlation between μ_0H^* and ε at 77 K, 50 K and 5 K for both H||c and H||ab orientations. A slight tendency between these two parameters is repeated at every temperature: μ_0H^* increases exponentially when ε is increased, confirmed by additional results in chapter 5. Therefore, a good strategy to enhance the single vortex pinning to higher magnetic fields could be focused on the achievement of even higher nanostrain in nanocomposites.

This tendency explains the importance of the induced nanostrain but also reveals that it can not be strictly distinguished as the unique cause of the enlargement of μ_0H*. Other kind of isotropic defects and also anisotropic defects, as already seen for H||ab in figures 3.18, 3.19 and 3.20 may slightly contribute to this enlargement.

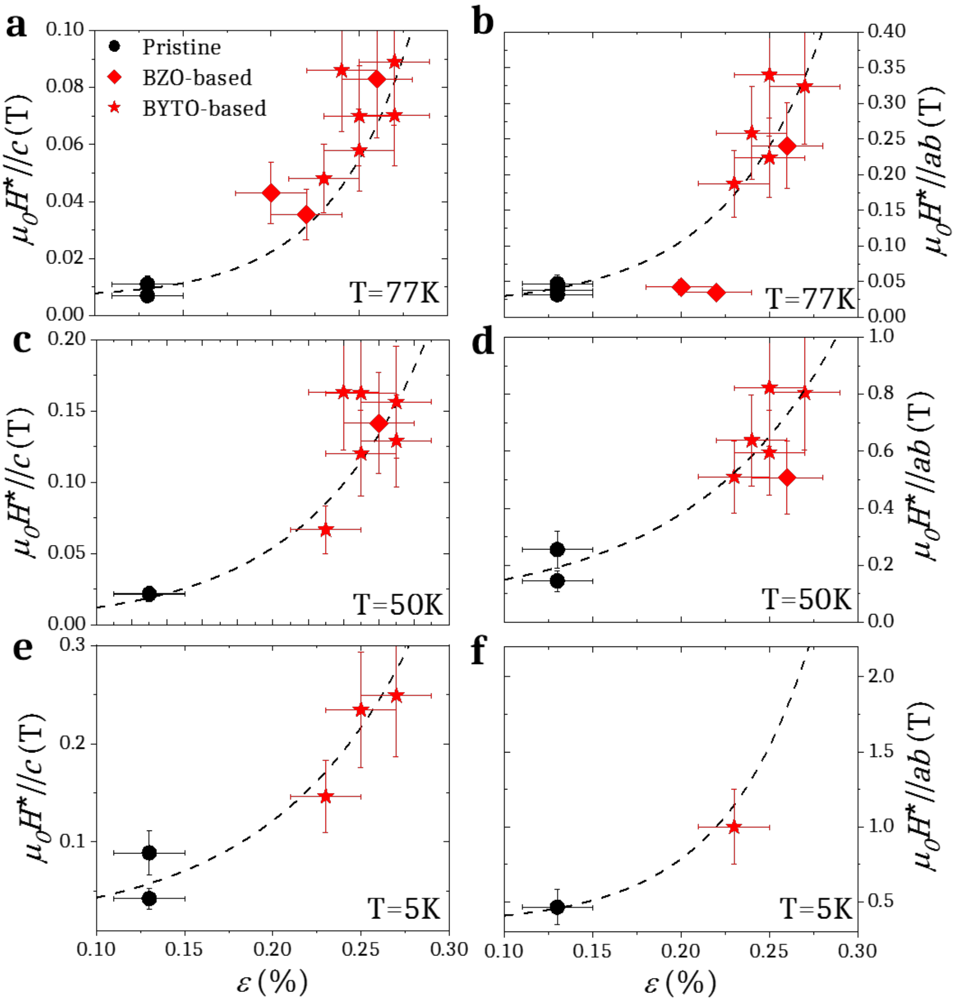

Figure 3.23: μ_0H* at (a-b) 77 K, (c-d) 50 K and (e-f) 5 K versus ε for pristine and ss-nanocomposites for H||c (left) and H||ab (right). Exponential dashed curves are guides to the eye, considering additional results from chapter 6.

3.4 Anisotropic pinning

3.4.1 Vortex trapping around the ab-orientation

As already commented in the discussion about figure 3.17, the width of the anisotropic $J_c(\theta)$ ab-peak is related to the interplay between the anisotropic pinning centres of intrinsic pinning and stacking fault pinning. In order to deepen the understanding of the widening of the ab-peak, the normalized anisotropic contribution $J_c^{aniso}/J_c^{aniso}(90°)$ is plotted versus (θ) around the H||ab orientation in figure 3.24 for a pristine film and mixed nanocomposites 6BYTO-5BZO and 10BZO-5YO at 50 K and several magnetic field intensities.

Nanocomposites clearly exhibit broader peaks, especially at low magnetic fields. The high $J_c^{aniso}(\theta)$ width values of the peak can be understood with the theoretical locking and staircase angular regimes for vortex orientations near the ab-plane orientation from figure 3.4. As long as vortices are still accommodated to the correlated defects, there will be an anisotropic pinning contribution and an associated $J_c^{aniso}(\theta)$ width. Therefore, it is reasonable to approximate the half of the FWHM of the $J_c^{aniso}(\theta)$ peak with the trapping angle θ_T that limits the staircase regime[75,131,166,167], indicated in figure 3.24 for the 10BZO-5YO sample at 9 T. The increase of θ_T in nanocomposites can be interpreted as an additional capability to accommodate vortices due to the presence of stacking faults and/or the bending of the CuO_2 planes.

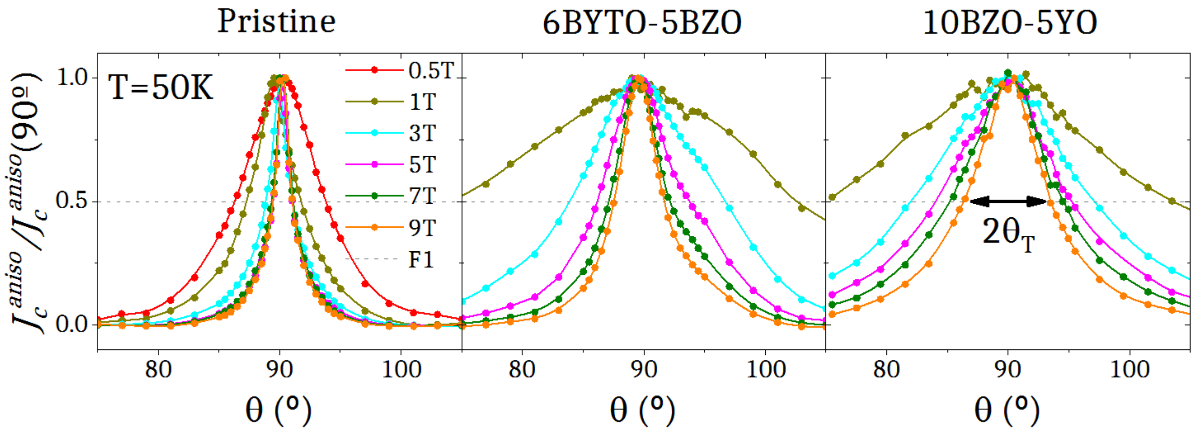

Figure 3.24: normalized anisotropic contribution $J_c^{aniso}/J_c^{aniso}(90°)$ as a function of the magnetic field orientation θ at 50 K for Pristine, 6BYTO-5BZO and 10BZO-5YO at 0.5 T, 1 T, 3 T, 5 T, 7 T and 9 T. The approximation of FWHM $\approx 2\theta_T$ is indicated for the 10BZO-5YO nanocomposite at 9 T.

Note that the width of peak, especially evident for the pristine sample, collapses at high magnetic fields. This means that θ_T decreases with increasing field at low fields and becomes almost field independent for high fields, indicative of a crossover from a low field regime characterized by a small H_Φ to a high field with very large H_Φ[131].

Considering the spacing between pinning centres analysed in STEM observations and applying equation 3.3 for calculating the matching field $\mu_0 H_\Phi$, stacking faults have associated matching fields of the order of unities or tenths of T whereas intrinsic pinning has thousands of T. The result is a crossover from extrinsic pinning domination at low fields leaded by stacking faults to intrinsic pinning domination at high fields.

The magnetic field dependence of θ_T is displayed for various samples in figure 3.25 at 77 K, 50 K, 25 K, and 5 K. The staircase angular limit θ_T decays with the magnetic field as $\theta_T \propto H^\eta$, where the obtained η ranges from 0.4 to 0.9, around the theoretical prediction of 0.75 for planar defects[7,131].

As evidenced by the angular plots, θ_T saturates at high magnetic fields to a minimum peak width θ_T^{sat} that cannot be further narrowed in the dominance of intrinsic pinning. For nanocomposites, the saturation of θ_T happens at slightly larger saturation magnetic fields $\mu_0 H^{sat}$ and the saturated trapping angle θ_T^{sat} is enhanced.

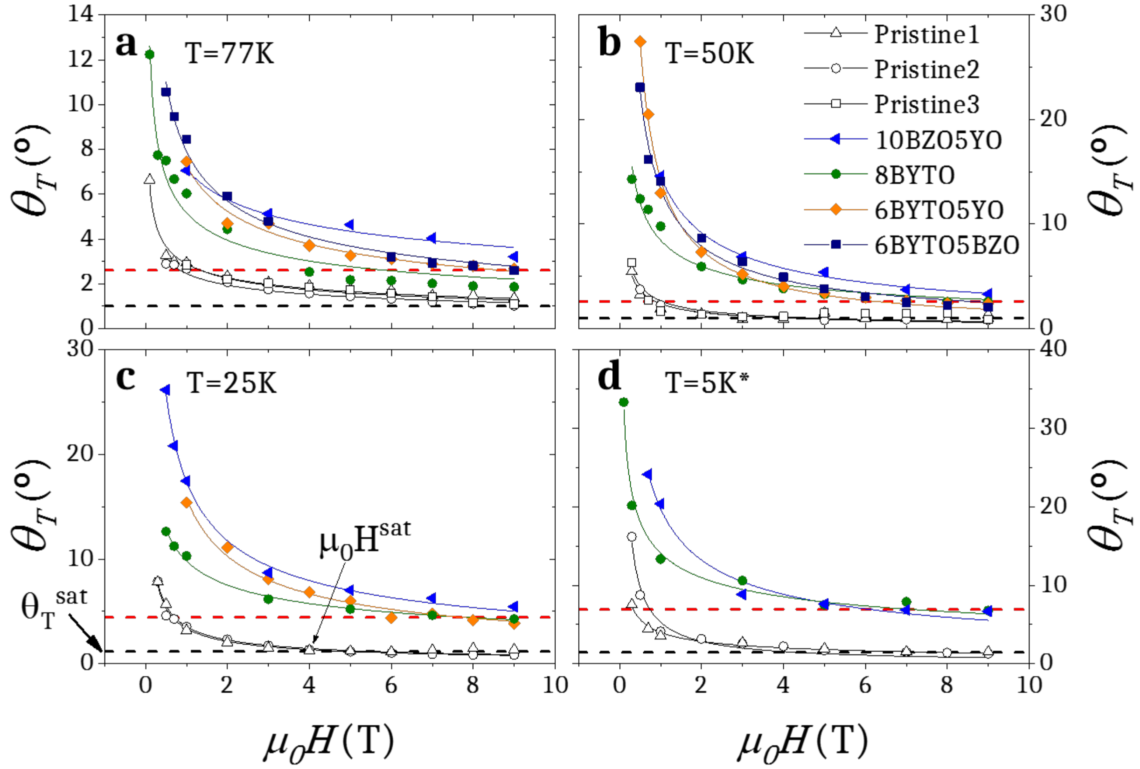

Figure 3.25: magnetic field dependence of θ_T at (a) 77K, (b) 50K, (c) 25K and (d) 5K for pristine and ss-nanocomposites. *:the results of 10BZO-5YO at 5K are actually measured at 10K.

The temperature dependences of the averaged θ_T^{sat} and $\mu_0 H^{sat}$ for pristine films and nanocomposite films from figure 3.25 are shown in figures 3.26(a-b). The difference between pristine and nanocomposites in θ_T^{sat} is accentuated at low temperatures, where nanocomposites reach θ_T^{sat} values of $\sim 7°$.

According to the crossover of different regimes characterized by disparate H_Φ, the $\mu_0 H^{sat}(T)$ line divides the H-T diagram in two regions of pinning dominance for H||ab: stacking fault pinning at low fields and high temperatures and intrinsic pinning at high fields and low temperatures, qualitatively in agreement with other works[131,168].

The high density of stacking faults in nanocomposites shift this crossover line to higher magnetic fields and lower temperatures. Especially for nanocomposites with a high density of stacking faults (the case of 10BZO-5YO, as will be shown in section 3.4.2), saturation is not completed up to 9 T.

Given the fact that the enhancement of nanostrain promoted by the stacking faults is responsible of the enlargement of H^* in all orientations, and that the effect of stacking faults can be evaluated by the widening of the trapping angle, figure 3.26(c-e) shows the plot of θ_T versus H^* at 77 K, 50 K and 5 K and 9 T for both H||c and H||ab. The linear trend between H^* and the ab-peak width corroborates the assumption that with the generation of stacking faults comes both the widening of vortex trapping and the increment of isotropic pinning centres.

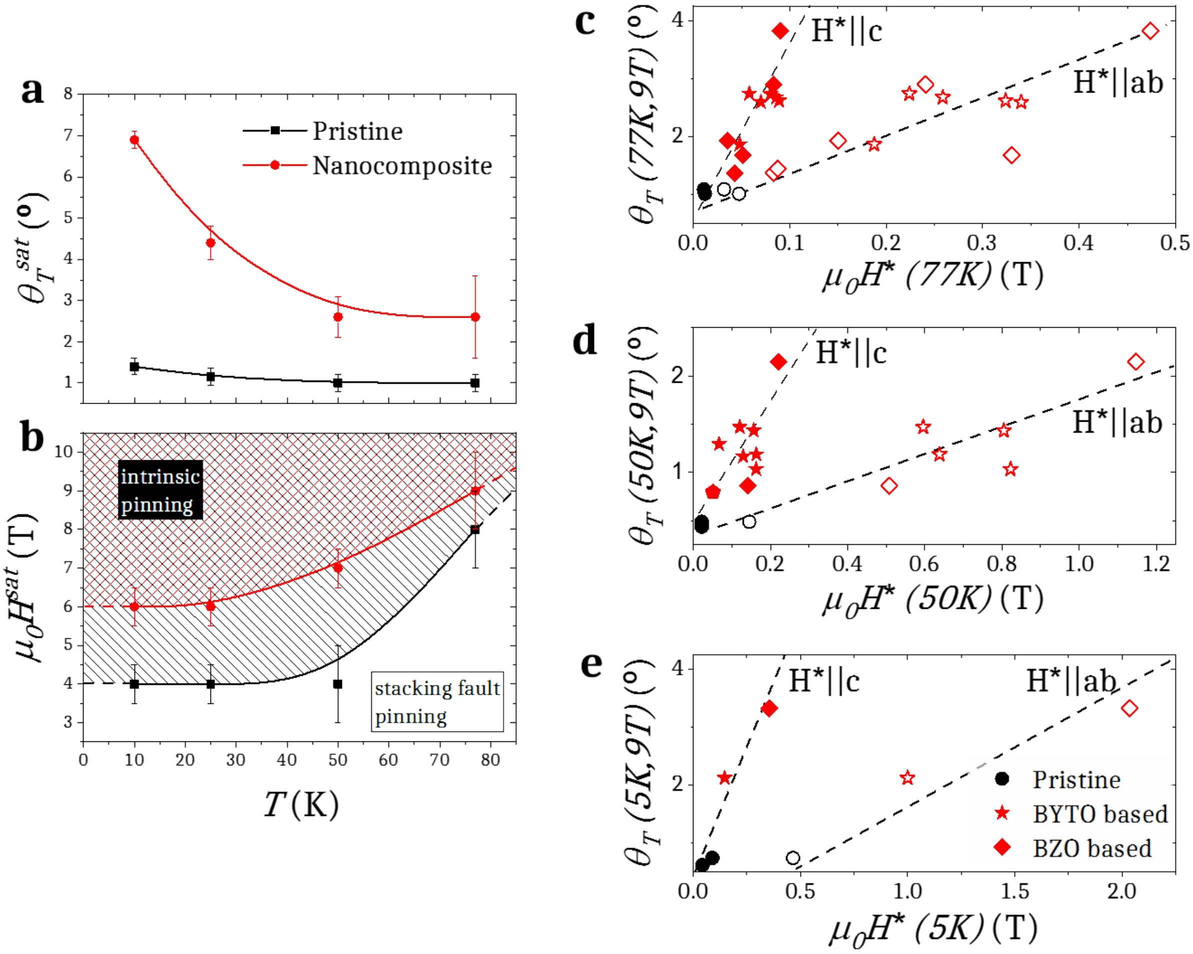

Figure 3.26: (left) averaged (a) θ_T^{sat} and (b) $\mu_0 H^{sat}$ as a function of temperature for pristine and ss-nanocomposites from figure 3.25. Plain regions below $\mu_0 H^{sat}$ indicate stacking fault pinning dominance whereas the striped regions above indicate regimes of intrinsic pinning dominance in the H-T diagram. (right) θ_T at 9 T as a funcion of $\mu_0 H^*$ for pristine and ss-nanocomposites at (c) 77 K, (d) 50 K and (e) 5 K. $\mu_0 H^*$ was calculated for H||c (closed symbols) and H||ab (open symbols).

3.4.2 Density of stacking faults and dislocations

The electric transport analysis of pinning centres has been correlated with the structural characterization performed by STEM in these same ss-nanocomposites (presented in more detail in another thesis[97]). This has allowed to identify and quantify the defect landscape present in these samples.

In figure 3.27, Z-contrast images for a pristine film and the 5BZO-5YO, 10BZO-5YO and 10BZO-5YOmod nanocomposites show the change in the microstructure with the inclusion of nanoparticles and the appearance of a different arrangement of stacking faults.

The density of stacking faults strongly increases in the 10BZO-5YO samples. However, there is no clear increase in the 5BZO-5YO, although the typology of stacking faults changes. The density and length of these Y124 intergrowths has been precisely evaluated

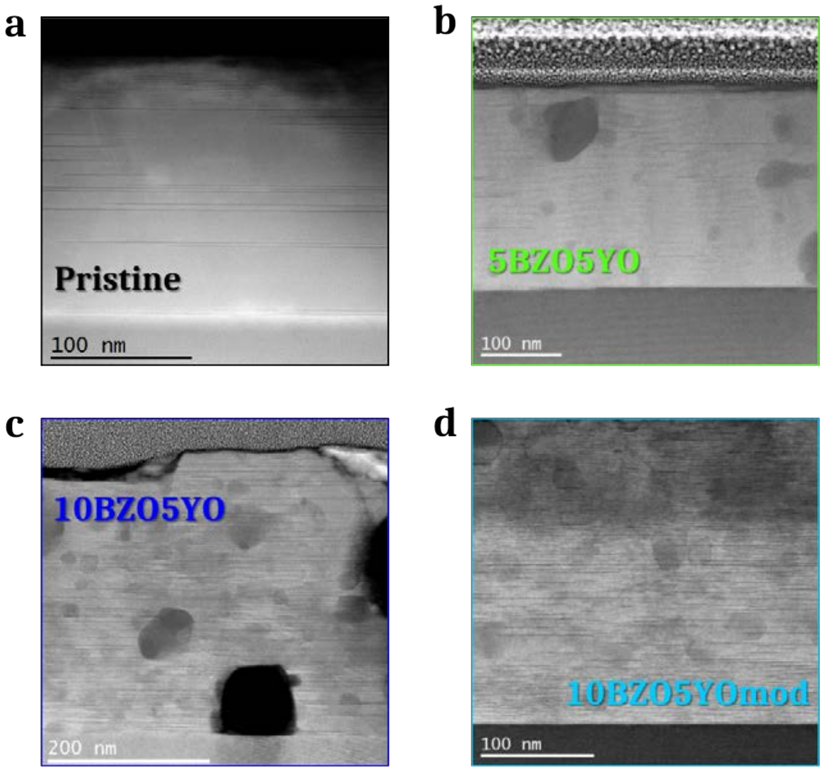

Figure 3.27: STEM Z-contrast images for (a) pristine and ss-nanocomposites (b) 5BZO-5YO, (c) 10BZO-5YO and (d) 10BZO-5YO mod, where stacking faults (black stripes) and nanoparticles are observed.

as explained in appendix B. The results of this analysis for the pristine and several ss-nanocomposites are displayed in the histogram fo figure 3.28, where the stacking fault density is plotted as a function of the stacking fault length d_{SF} (approximated diameter).

The concentration of short stacking faults ($d_{SF} < 50$nm) drastically increases in all nanocomposites compared to the pristine film that almost only possesses long stacking faults ($d_{SF} > 140$nm). Therefore the mean stacking fault length is shifted towards $30 - 50$ nm values in nanocomposites. 10BZO-5YO is the sample that exhibits largest density of stacking faults with most of the stacking fault lengths below 120 nm and at the same time the one that displays the highest μ_0H^*. However, there is no general correlation between the density of stacking faults and μ_0H^*. The length and distribution, that is different for each nanocomposite, may affect the generation of nanostrain, that is the defect that ultimately controls the shift of μ_0H^* as commented above.

For the direct quantification of nanostrain from STEM images, it is convenient to calculate the relative volume of nanostrained YBCO regions located at the edges of the stacking faults (see figures 3.29 (a-b)), in other words the relative volume of nanostrain in partial dislocations ρ_{dis}. It has been estimated in each sample with the combination of formulas B.10 and B.11 from appendix B by assuming that the strained regions in the bounding partial dislocations are cylindrical disk shaped.

The radius R_i of each disk corresponds to half of the observed length in Z-contrast images

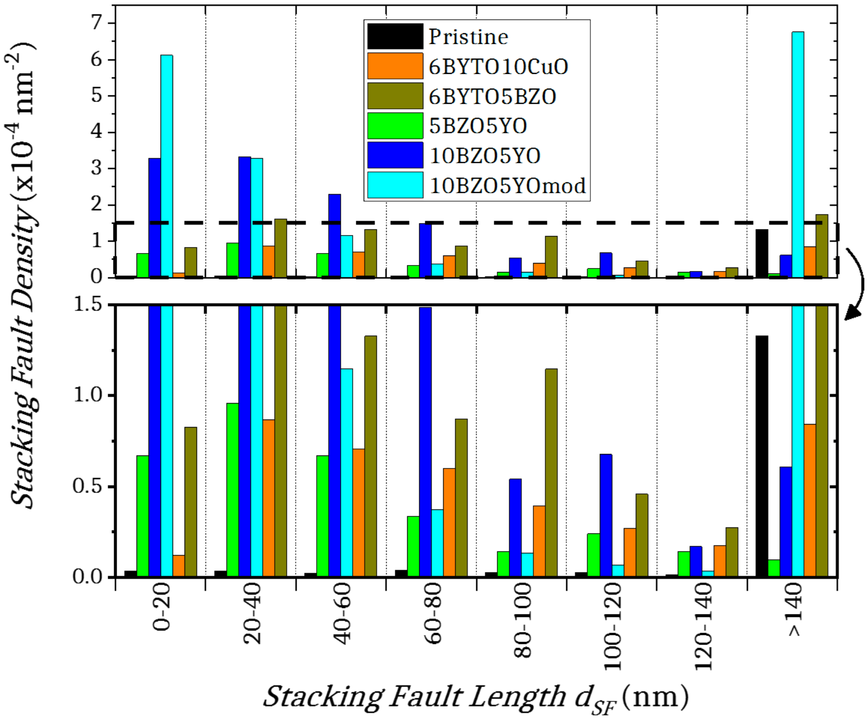

Figure 3.28: histogram of the stacking fault density corresponding to different stacking fault lengths for pristine and ss-nanocomposites analysed by STEM. The lower panel magnifies the histogram for low stacking fault densities.

as shown in figure 3.29 (a) and the thickness δ of the nanostrained disk both in in-plane and out-of-plane directions is approximately $\delta \sim 0.8$ nm, confirmed by GPA deformation analysis of the isolated stacking fault in figures 3.29 (c-d)[133].

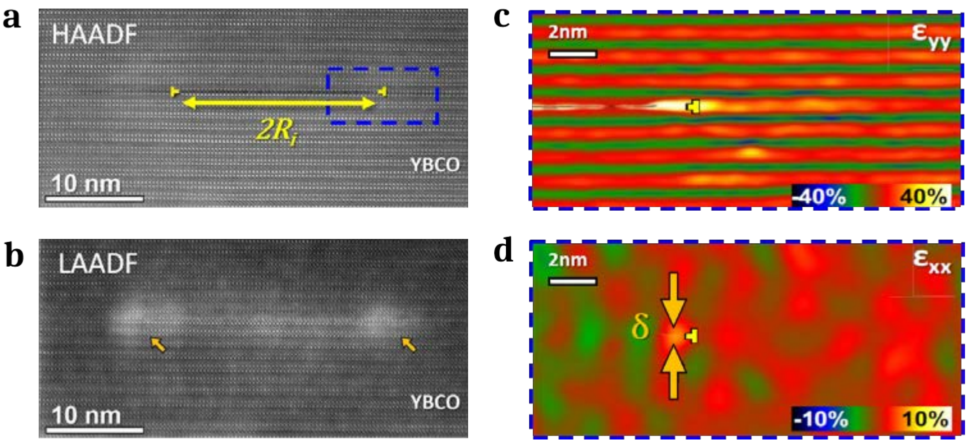

Figure 3.29: (a) HAADF and (b) LAADF STEM images of an isolated 25 nm long stacking fault. The yellow symbols in the images point to partial dislocations while the arrows to their surrounding strain fields. The right edge of the stacking fault is zoomed and analysed by GPA as shown by the (c) ε_{yy} and (d) ε_{xx} deformation maps along the [001] and [100] directions[133].

The circular shape of this defect is assumed according to the analysis of the Z-contrast planar view image in figure 3.30[75]. As explained in section 3.1.2, a stacking fault involves a shift of half unit cell along the b axis. In the magnified Fast Fourier filtered image of the planar view, Y124 intergrowths have been identified through the coinciding projection of Y123 and Y124 phases.

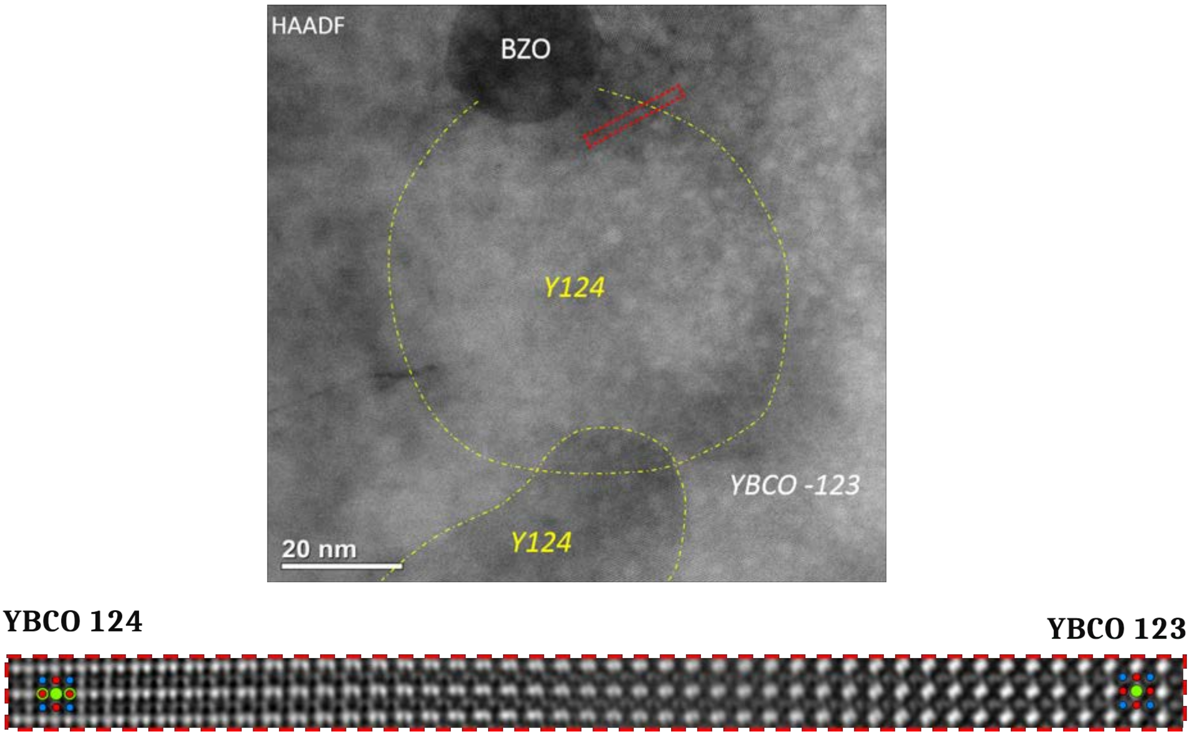

Figure 3.30: (above) STEM Z-contrast planar view obtained along the [001] axis of a BZO nanocomposite with a 13 % BZO content, where Y124 phases (stacking faults) are differentiated from Y123. (below) Fast Fourier filtered image of the magnified selected region above. The projection of the Y123 and Y124 phases is matched with the crystal lattice[75].

The observation of the in-plane round shape of stacking faults with diameters of 50-100 nm makes it possible to estimate the relative volume ρ_{dis} of the nanostrain associated to the partial dislocations. Figures 3.31(a-b) show a rough linear correlation between ρ_{dis} and μ_0H* for H||c at 77 K and 5 K, plotted for a pristine and different ss-nanocomposites. As commented before, $\mu_0\mathrm{H}^* \simeq \mu_0\mathrm{H}^*_{\mathrm{iso}}$ for H||c, and therefore it is envisaged that the pinning provided by the nanosized strain located at the partial dislocations is isotropic and responsible of the enlargement of the single vortex pinning regime, where the interaction between c-oriented vortices and the nanosized strain is illustrated in figure 3.31(c).

3.4.3 Loss of twin boundary coherence

A recurrent topic in this chapter has been the observation of a degradation of the effectiveness of twin boundary pinning in nanocomposites, as demonstrated by the rapid decay of J$_c$ at high fields and temperatures in figure 3.11(a), the decay of the irreversibility line for H||c displayed in figure 3.14(a) and the isotropic-anisotropic calculations of J$_c(\theta)$ in figure 3.17 and J$_c$(H) curves in section 3.3.2.

The origin of such degradation in the studied ss-nanocomposites can be better understood with the results of figure 3.32(a), that shows the relation between the irreversibility line temperature (at 9 T, for H||c) and the μ_0H* at 77 K for H||c. The nanostrained regions

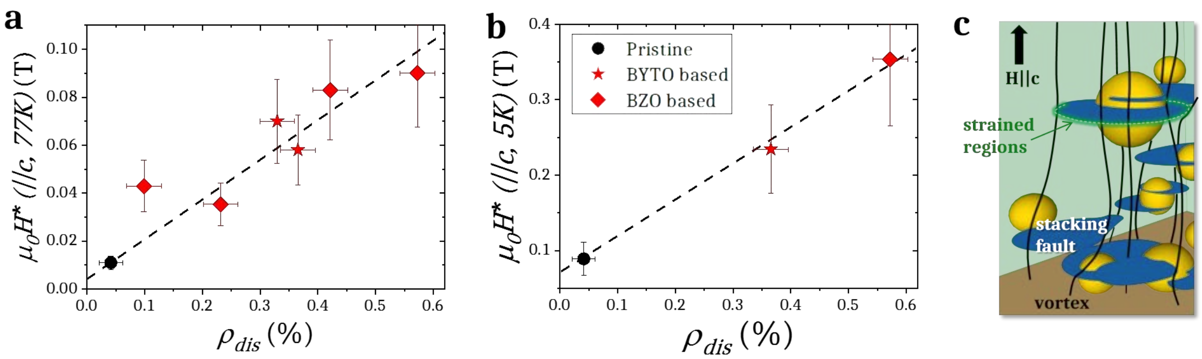

Figure 3.31: μ_0H^* for H||c (a) at 77 K and (b) 5 K plotted as a function of the partial dislocation relative volume ρ_{dis} for a pristine and various ss-nanocomposites. (b) Schematic view of c-oriented vortices pinned to the generated nanoscale strained regions.

both increase the isotropic pinning centres that are effective at H ∼ H* and reduce the effectiveness of the correlated pinning associated to twin boundaries that dominates at high fields and temperatures.

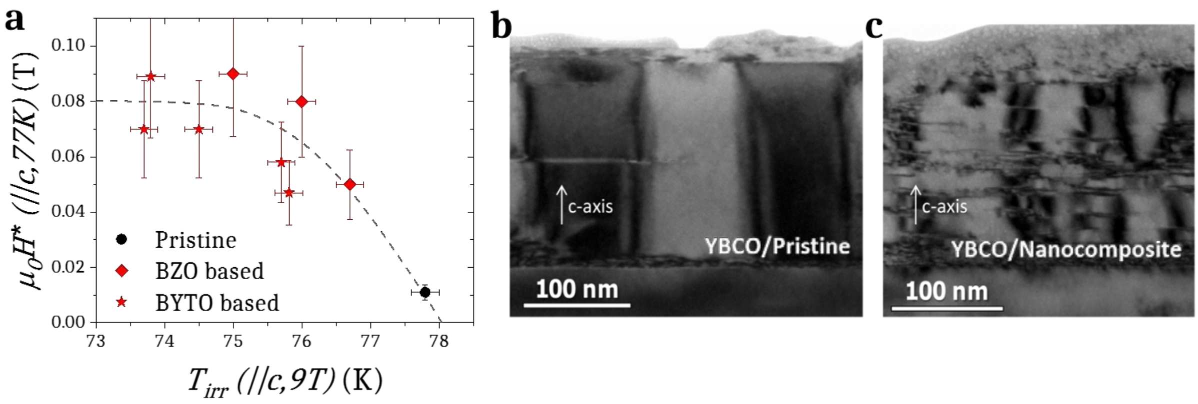

Figure 3.32: (a) μ_0H^* as a function of the irreversibility line point $\mathrm{T_{irr}(9T, H||c)}$. STEM ABF image with the $\tilde{g} = (2, 0, 0)$ diffraction vector of (b) a pristine sample and (c) a BYTO nanocomposite. Different contrasts correspond to different twin domains, separated by the twin boundaries.

As observed by comparison of figures 3.32(b-c), the coherence of twin boundaries along the c-axis in the nanocomposite is broken by the emergence of ab-planar stacking faults[130,139], also observed in detail in figure 3.7.

It is important to remark that although twin boundary planes with no vertical coherence are not very effective pinning centres at high temperatures (close to the irreversibility line), they preclude vortex channelling at low temperatures, thus avoiding the J_c minima observed in current/field configurations where channelling effects may induce fast vortex motion[129,130].

Although the coherence is clearly broken, the embedded secondary phases act as extra nucleation centers for the formation of twin boundaries, resulting in films with higher density of segmented twin boundaries and shorter twin spacing[139], as it can be observed in figures 3.32(b-c).

3.5 Conclusions

The immediate remarkable property of CSD ss-nanocomposites is the enlargement of the single vortex pinning regime to higher crossover magnetic fields H* for both H||c and H||ab, providing larger J_c values at intermediate magnetic fields (~ 1 T) for high temperatures and up to 9 T for low temperatures.

It has been demonstrated that the single vortex pinning regime is mainly dominated by isotropic pinning and therefore its enlargement is related to a higher density of isotropic pinning centres, although anisotropic pinning centres also play an important role for H||ab.

Due to the relation of the increase of nanostrain ε measured by XRD and the enlargement of H*, the isotropic pinning centres dominating the single vortex pinning regime are envisaged to be nanostrained regions, which are believed to be induced by the generation of a high density of stacking faults, as confirmed by STEM observations and by the linear relation between the ab-peak trapping angle θ_T and H* for H||c.

In particular, the statistical analysis of stacking faults observed in the STEM images of the studied ss-nanocomposites has allowed us to quantify the relative volume of the nanostrained regions $H^*(\rho_{dis})$ located at the surrounding partial dislocations and to identify them as the main responsible defects of the single vortex pinning regime enlargement.

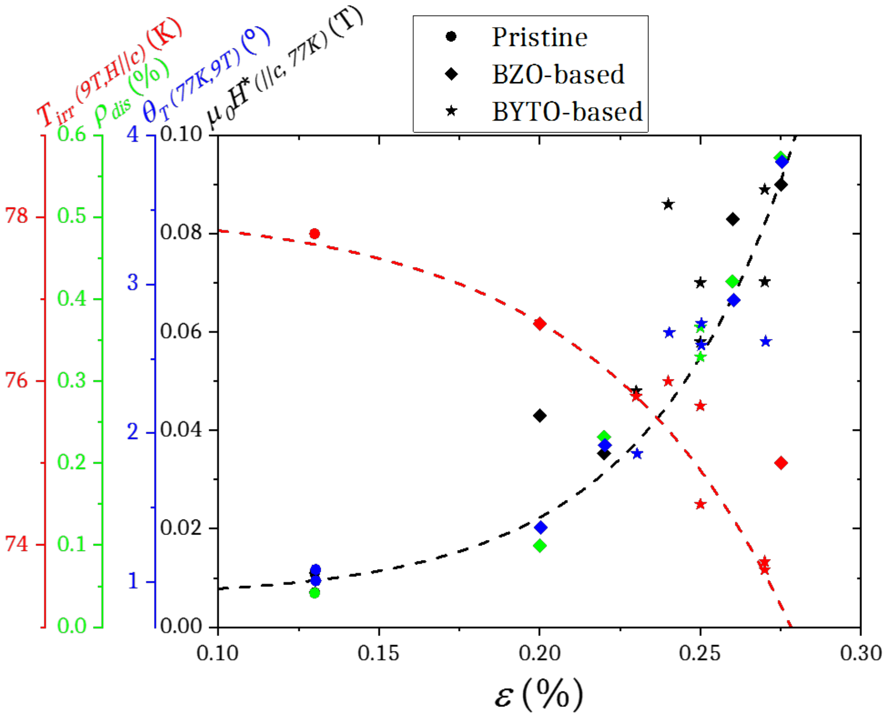

Figure 3.33: $T_{irr}(9T, H||c)$, ρ_{dis}, $\theta_T(77K, 9T)$ and $\mu_0 H^*(77K, H||c)$ as a function of ε for pristine and ss-nanocomposites.

Furthermore, the generation of a high density of stacking faults has shown to affect as well the anisotropic pinning performance for both H||ab and H||c.

For H||ab, the crossover line that separates the region where intrinsic pinnig dominates over stacking fault pinning, and vice versa, characterized by different matching fields, is shifted to larger magnetic fields and lower temperatures in stacking-fault-rich nanocomposites.

For H||c, the dominant anisotropic pinning centres for ss-nanocomposites are the twin boundaries. However, a decrease of twin boundary pinning has been identified at large magnetic fields and temperatures causing a decrease of the irreversibility line T_{irr} and an increase of the α value.

To summarize, the different relations $H^*(\varepsilon)$, $H^*(\theta_T)$, $H^*(\rho_{dis})$ and $H^*(T_{irr})$ are merged together in figure 3.33, where H^*, θ_T, ρ_{dis} and T_{irr} are plotted versus nanostrain with adjusted y-scales. This plot illustrates how an specific ε is simultaneously associated to changes that affect the isotropic and the anisotropic pinning performance for both H||c and H||ab.

CHAPTER 4

STRENGTH OF PINNING CENTRES IN CSD NANOCOMPOSITES

From the combination of magnetic field orientation and temperature dependences of J_c, it is possible to determine the densities and thermal pinning energies of isotropic-weak, isotropic-strong and anisotropic-strong pinning contributions associated to the diverse pinning centres present in YBCO films.

In this chapter, the separation of pinning contributions has been studied in CSD ss-nanocomposites, with the idea to elucidate the most adequate pinning landscape for high critical current performances of coated conductors at specific operating conditions[40].

4.1 Strong and weak pinning

The critical current density decays with increasing temperature. At higher temperatures, the radius of vortices ξ broadens (see equation 1.7), their elasticity increases and thermal activation is in general more notable, favouring altogether vortex depinning.

Figure 4.1 shows J_c(T) curves for diverse pristine and ss-nanocomposites from table 3.1, for both H||c and H||ab at 1 T and 9 T.

In general, nanocomposites exhibit higher J_c values than pristine films at these magnetic fields almost along the entire temperature range, especially for H||c. It is remarkable the performance of 10BZO-5YO nanocomposite, showing the largest critical current densities for both orientations, which are outstanding at very low temperatures at 1 T, reaching 29 and 43 MA/cm^2 for H||c and H||ab respectively.

As explained in section 3.1.1.1, the J_c(T) dependence is described theoretically by weak (as oxygen or copper vacancies) and strong (as stacking faults, twin boundaries or nanostrain) vortex pinning models[7,44,98].

In the films studied in this work, both types of defects coexist. In a first approximation, without considering interaction between them, J_c(T) can be described as the direct sum of J_c^{wk}(T) and J_c^{str}(T) from equations 3.1 and 3.2:

$$J_c(T) = J_c^{wk}(T) + J_c^{str}(T) \tag{4.1}$$

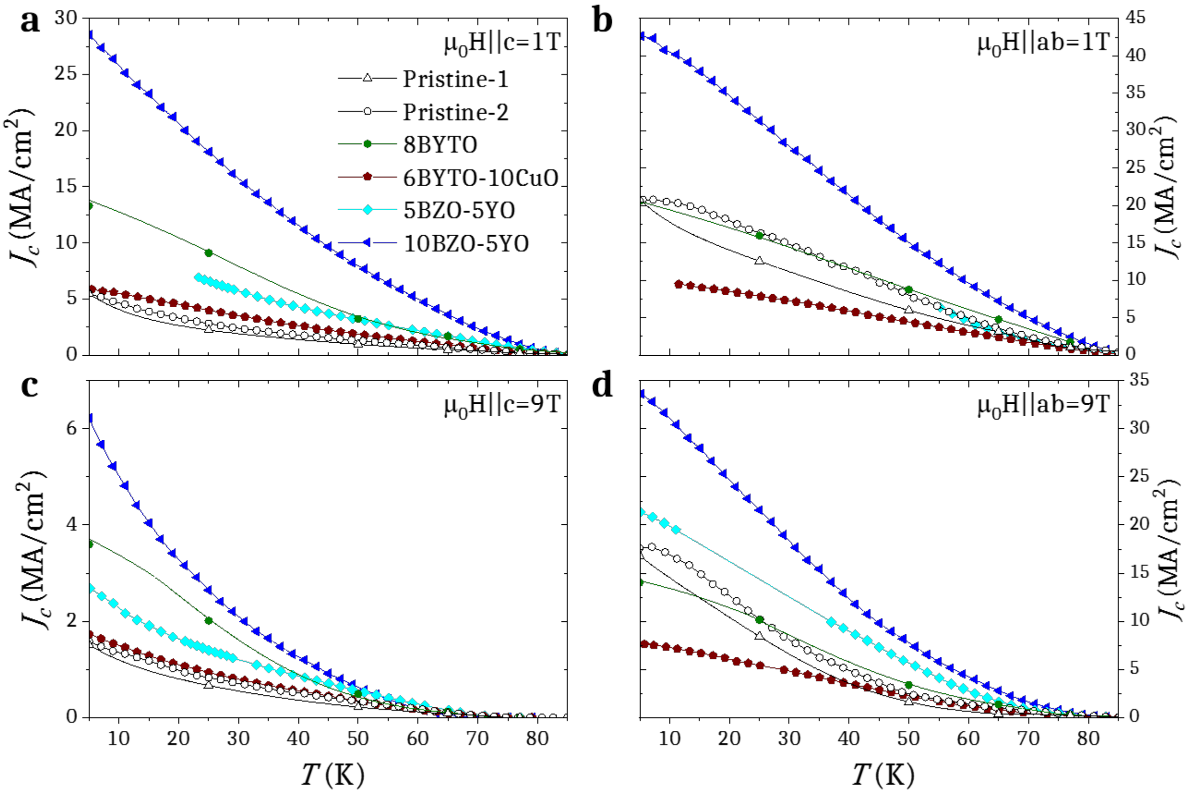

Figure 4.1: J_c as a function of temperature for pristine and ss-nanocomposites at (above) 1 T and (below) 9 T for (left) H||c and (right) H||ab.

From in-field angular measurements and the Blatter scaling approach[7], J_c can be also disentangled into J_c^{iso} and J_c^{aniso} regarding the anisotropy of the defects. Isotropic pinning centres can be either point or nanosized defects, promoting weak and strong pinning respectively. However, anisotropic defects are always considered to act as strong pinning centres. Therefore, $J_c(T)$ can be also described by the sum of three contributions:

$$J_c(T) = J_c^{iso-wk}(T) + J_c^{iso-str}(T) + J_c^{aniso-str}(T) \tag{4.2}$$

Where J_c^{iso} is the sum of the isotropic-weak (i-w) contribution J_c^{iso-wk} and the isotropic-strong (i-s) contribution $J_c^{iso-str}$, whereas the anisotropic-strong (a-s) contribution $J_c^{aniso-str}$ corresponds directly to J_c^{aniso}.

The fit of the sum of these three contributions is plotted in figure 4.2 for the 10BZO-5YO nanocomposite at 9 T for H||c. It is observed that isotropic strong defects dominate at a large temperature range and that the data is nicely fitted in the entire temperature range for this nanocomposite. However, the fitting models are strictly valid up to 60-70 K, as can be observed by deviations from $J_c(T)$ data when J_c is plotted in a logarithmic scale, as shown in appendix A in figure A.3(a).

In the films studied in this work, i-w is generally associated to vacancies, i-s to the nanostrained regions and a-s to twin boundaries for H||c and to stacking faults and intrinsic pinning for H||ab.

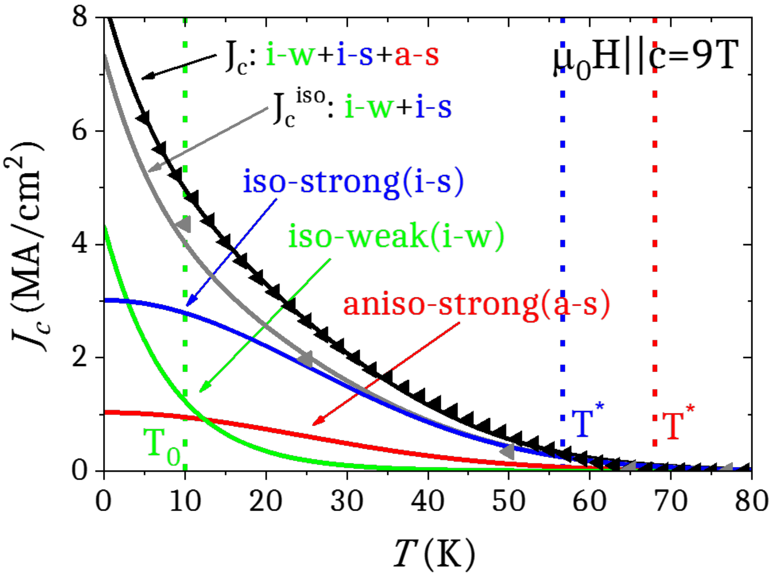

Figure 4.2: experimental data of $J_c(T)$ for 10BZO-5YO nanocomposite at 9 T for H||c. $J_c^{iso}(T)$ points are scattered at 10, 25, 50, 65 and 70 K, deduced from $J_c(\theta)$ curves. Solid lines correspond to the fit of the data to the equation 4.2, where contributions are also indicated. Dashed lines show the thermal pinning energies T_0, $T^*_{iso-str}$ and $T^*_{aniso-str}$.

The separation of J_c^{iso-wk}, $J_c^{iso-str}$ and $J_c^{aniso-str}$ in films with different defect landscape allows to evaluate, separate and quantify the densities and energies associated to the different kinds of natural and artificial pinning centres[35,40,98,115]. Therefore, it is possible to analyse their role in the final pinning behaviour at different temperatures and magnetic fields, providing a unique tool to design the best vortex pinning landscape under different operating conditions.

4.2 Temperature dependence of pinning contributions

The temperature dependence of the pinning contributions for 10BZO-5YO, the nanocomposite with larger relative volume of partial dislocations, has been compared with Pristine-2 in order to evaluate and quantify the dominant pinning centres active at different regions of the H-T phase diagram.

Figure 4.3(a) plots $\log(J_c)$ versus T^2 for both samples at 1 T for H||c, where the curve is linearly fitted to the characteristic curve of strong pinning (equation 3.2). Deviation from the linear fits is observed at low temperatures, where i-w contribution plays an important role, and at high temperatures when approaching the irreversibility line.

The weights of the different pinning contributions are plotted in figure 4.3(b) for the nanocomposite and in 4.3(c) for the pristine film. All contributions play an important role in the case of the pristine sample. At low temperatures (5 K), i-w and i-s contributions are similar, whereas a-s contribution, associated to the correlated twin boundaries, starts to be relevant at high temperatures (60-90 K) in comparison with the other contributions.

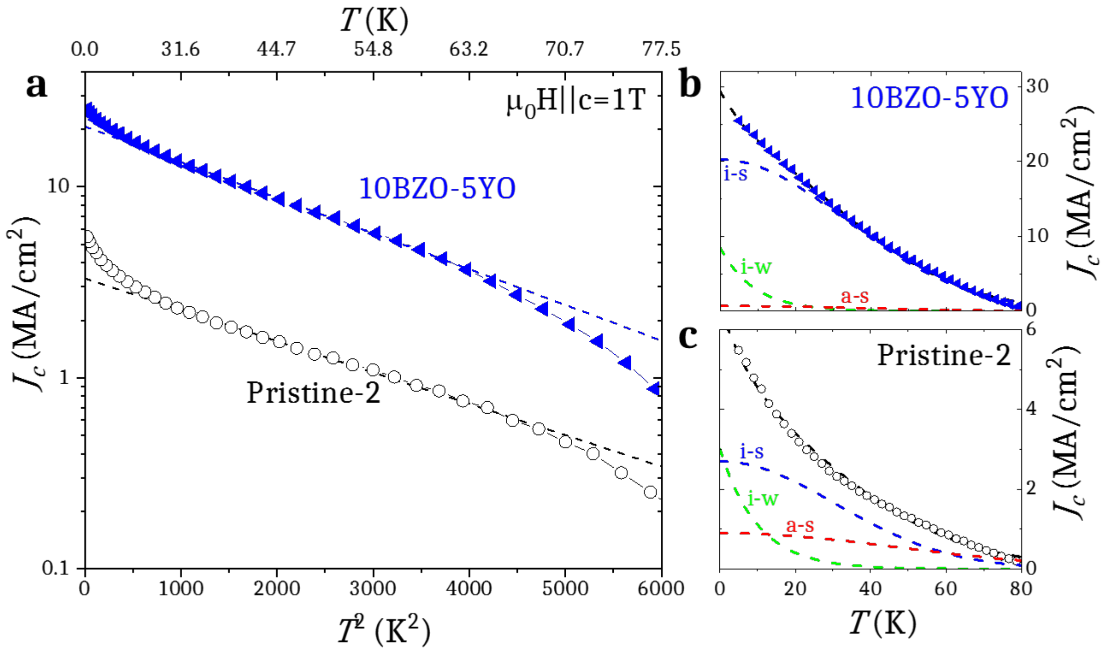

Figure 4.3: (a) Log(J_c) versus T^2 for 10BZO-5YO ss-nanocomposite and Pristine-2 at 1 T for H||c. The linear fits corresponding to a strong pinning behaviour is shown with dashed lines. (b-c) Temperature dependence of J_c and i-s, i-w and a-s contributions obtained by fitting equation 4.2 for (b) 10BZO-5YO and (c) Pristine-2.

For the nanocomposite instead, the i-s contribution, associated with the nanostrain, is strongly enhanced in the whole temperature range and utterly dominates the pinning performance at these conditions. Although it is not dominant, the i-w contribution is also notably larger in the nanocomposite, indicating an increase of the density of weak defects. On the other hand, the contribution of twin boundaries, associated to a-s pinning, is practically negligible compared to the other contributions.

Next, the same study is performed for H||ab, shown in figure 4.4. Both samples exhibit a nice strong pinning fit from low temperatures until approaching T_{irr}, which is similar for both samples at this orientation, as shown in figure 3.14(c).

The strong domination comes from i-s for the nanocomposite (see figure 4.4(b)) and from the competition between i-s and a-s in the case of the pristine film (see figure 4.4(c)). The enhancement of i-s and i-w observed for H||c is similarly reproduced for H||ab.

The same analysis is implemented at 9 T, shown in figure 4.5 for H||c and figure 4.6 for H||ab. The significant deviation in figure 4.5(a) from the strong pinning fit at very low temperatures reveals the importance of weak pinning at high fields for H||c. Indeed, the evaluation of contributions shown in figures 4.5(b-c) displays i-w domination at very low temperatures.

At higher temperatures for H||c, i-s dominates for the nanocomposite, whereas a-s and i-s similarly contribute to the final J_c for the pristine sample. On the other side, a-s for H||ab, associated to intrinsic pinning and stacking fault pinning, is dominant for both samples, shown in figure 4.6(b-c). Anisotropic defects determine the pinning performance

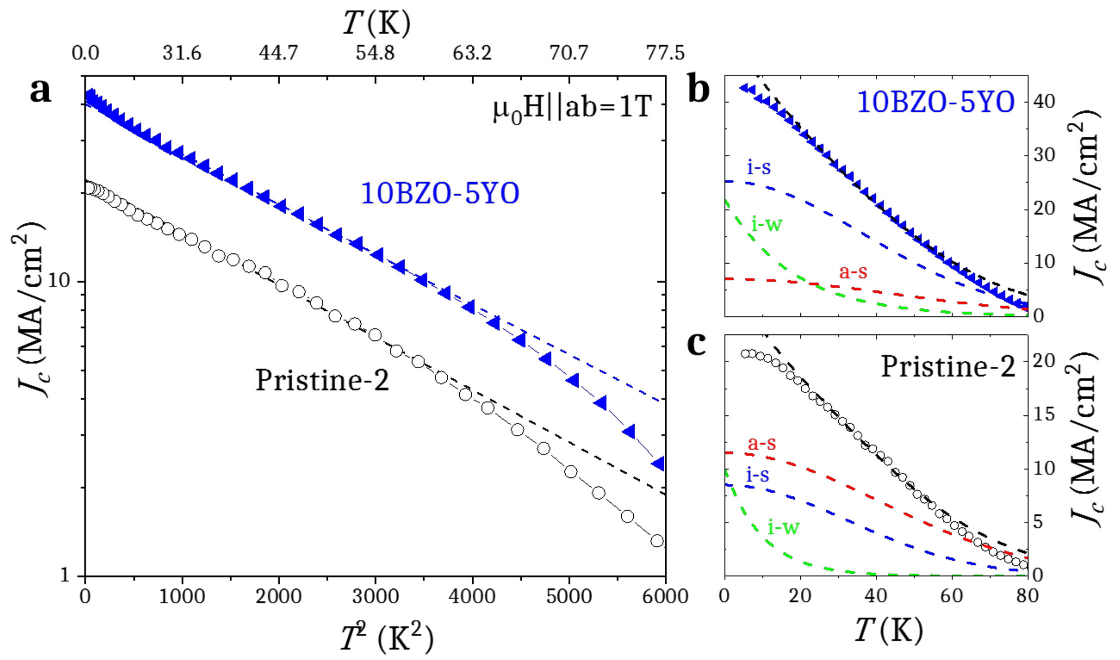

Figure 4.4: (a) log(J_c) versus T^2 for 10BZO-5YO ss-nanocomposite and Pristine-2 at 1 T for H||ab. The linear fits corresponding to a strong pinning behaviour is shown with dashed lines. (b-c) Temperature dependence of J_c and i-s, i-w and a-s contributions obtained by fitting equation 4.2 for (b) 10BZO-5YO and (c) Pristine-2.

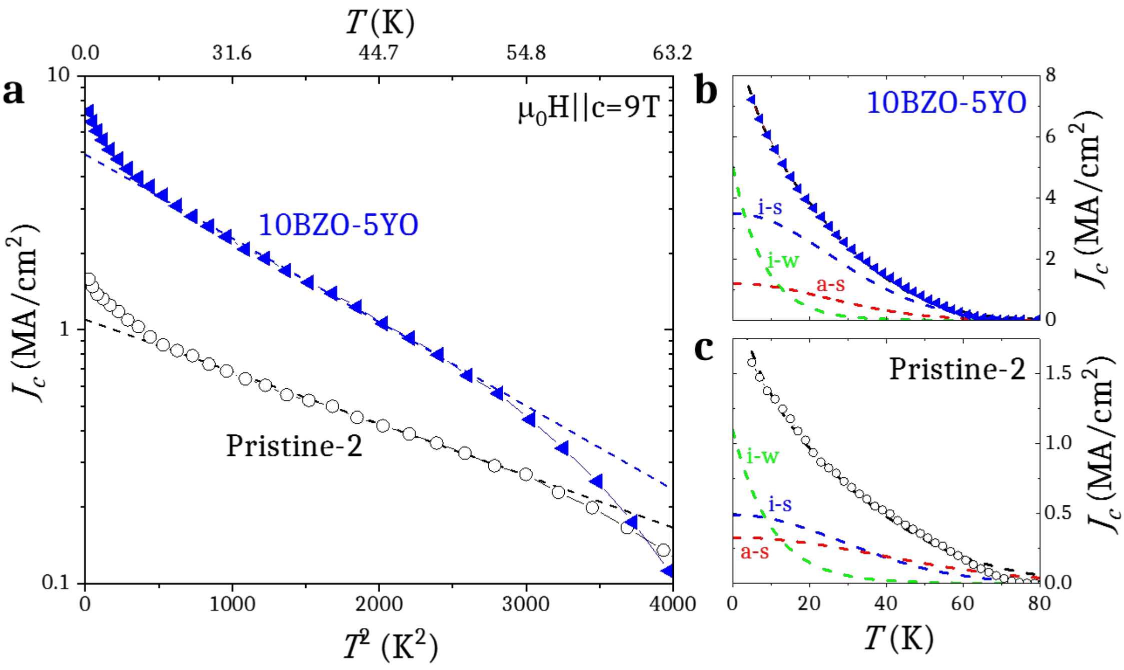

Figure 4.5: (a) log(J_c) versus T^2 for 10BZO-5YO ss-nanocomposite and Pristine-2 at 9 T for H||c. The linear fits corresponding to a strong pinning behaviour is shown with dashed lines. (b-c) Temperature dependence of J_c and i-s, i-w and a-s contributions obtained by fitting equation 4.2 for (b) 10BZO-5YO and (c) Pristine-2.

in the pristine film and compete in the nanocomposite with the nanostrain associated to the i-s contribution, that also plays an important role.

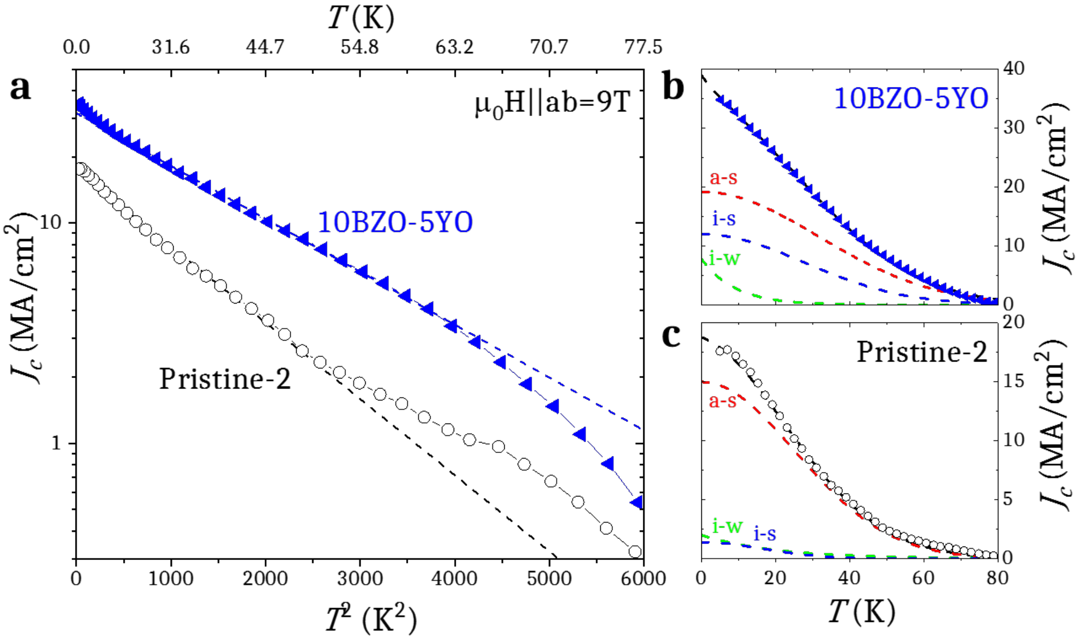

Figure 4.6: (a) log(J_c) versus T^2 for 10BZO-5YO ss-nanocomposite and Pristine-2 at 9 T for H||ab. The linear fits corresponding to a strong pinning behaviour is shown with dashed lines. (b-c) Temperature dependence of J_c and i-s, i-w and a-s contributions obtained by fitting equation 4.2 for (b) 10BZO-5YO and (c) Pristine-2.

Therefore, the strong pinning nicely fits down to very low temperatures for both films. However, for the pristine sample, that is fully dominated by a-s, J_c values go above the fit at high temperatures, which may be related to the interplay between different anisotropic defects parallel to the ab-planes with distinctive characteristic temperatures T*: intrinsic pinning and planar Y124 intergrowths.

The full analysis of these three contributions at different magnetic fields allows to illustrate the magnetic-field–temperature evolution of the pinning provided by different pinning centres in the H-T diagram, finally developed in section 4.5.

4.3 Magnetic field dependence of pinning contributions

The J_c(T) behaviour and therefore the pinning contributions originated by weak-strong fits have been evaluated for different magnetic fields from J_c(H) obtained at different temperatures (from section 3.3.2). For example, J_c(T), J_c^{iso}(T) and J_c^{aniso}(T) curves are plotted for the 8BYTO nanocomposite at different magnetic fields in figure 4.7, with the respective fits: $J_c = J_c^{wk}(T) + J_c^{str}(T)$, $J_c^{iso} = J_c^{iso-wk}(T) + J_c^{iso-str}(T)$ and $J_c^{aniso} = J_c^{aniso-str}(T)$.

The fits of J_c^{iso}(T) and J_c^{aniso}(T) are performed simultaneously so that J_c^{iso-wk}(T) +

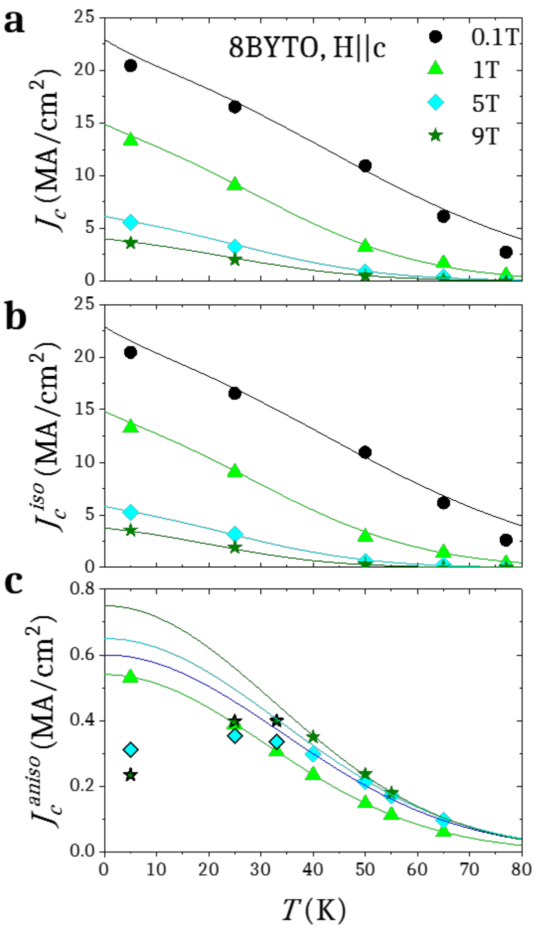

Figure 4.7: temperature dependence of (a) $\mathrm{J_c}$, (b) $\mathrm{J_c^{iso}}$ and (c) $\mathrm{J_c^{aniso}}$ for the 8BYTO ss-nanocomposite at 0.1, 1, 5 and 9 T for H||c. Solid lines correspond to (a) $\mathrm{J_c^{wk}(T) + J_c^{str}(T)}$, (b) $\mathrm{J_c^{iso-wk}(T) + J_c^{iso-str}(T)}$ and (c) $\mathrm{J_c^{aniso-str}(T)}$ fits. Symbols with black edge have not been considered for the fits.

$\mathrm{J_c^{iso-str}(T)} + \mathrm{J_c^{aniso-str}(T)}$ also fits well the total $\mathrm{J_c}$, as in figure 4.2.

As it is seen in figure 4.7(c), $\mathrm{J_c^{aniso}(T)}$ cannot be completely fitted down to 0 K at high fields as 5 T or 9 T for H||c, where $\mathrm{J_c^{aniso}}$ falls below the fit of $\mathrm{J_c^{aniso-str}}$. This issue can be attributed to the vortex channelling along the twin boundaries[129,130], which would give a negative $\mathrm{J_c^{aniso}}$ contribution in this model.

In this analysis, we have fitted $\mathrm{J_c^{aniso}(T)}$ omitting the points with a channelling negative contribution for simplicity. This means that anisotropic contributions obtained at low temperatures and high magnetic fields are larger than in reality, especially for the pristine sample, where the channelling effect of twin boundaries is stronger.

The $\mathrm{J_c^{aniso}}$ contribution at low magnetic fields (below 0.5 T) is very small in comparison to $\mathrm{J_c^{iso}}$ and its temperature dependence cannot be well described.

The same analysis from figure 4.7 has been performed in 8BYTO, 10BZO-5YO and Pristine-1 (the three samples studied in section 3.3.2) for both H||c and H||ab. The magnetic field dependences of different $\mathrm{J_c(0K)}$, associated to the density of each type of defect (i-w, i-s and a-s), are plotted in figures 4.8(a-c).

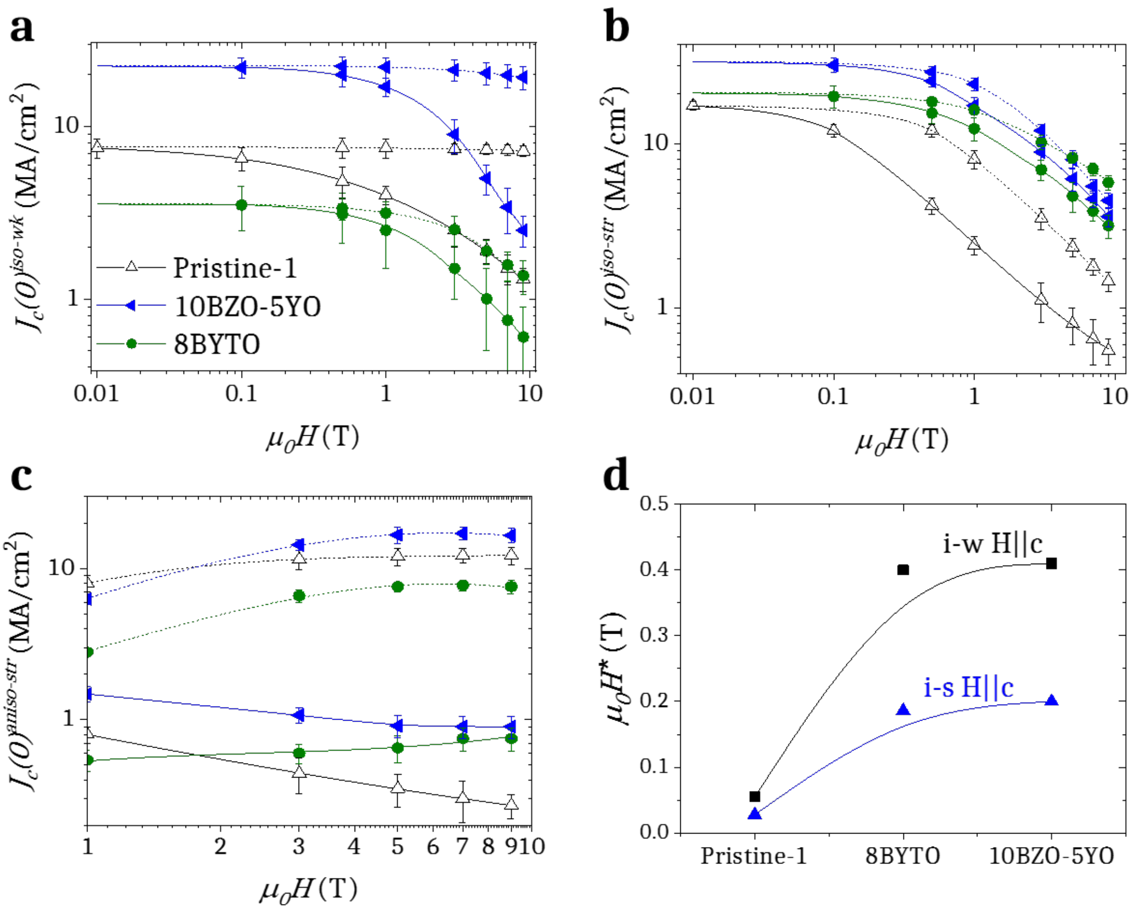

Figure 4.8: magnetic field dependence of the pinning contributions at 0 K for Pristine, 10BZO-5YO and 8BYTO films. (a) $J_c(0)^{iso-wk}(H)$, (b) $J_c(0)^{iso-str}(H)$ and (c) $J_c(0)^{aniso-str}(H)$ are plotted for (solid lines) H||c and (dashed lines) H||ab. (d) H* values of i-s and i-w for H||c.

$J_c(0)^{iso-weak}$ and $J_c(0)^{iso-strong}$ decay with magnetic field (figure 4.8(a-b)) in a very similar way than the total J_c, whose magnetic field dependence is explained in section 3.1.1.2. First, there is a plateau characteristic of single vortex pinning. Then, at a given magnetic field H^*, $J_c(0)$ decays following a power law $J_c \propto H^{-\alpha}$.

However, the magnetic field dependence of $J_c(0)^{aniso-str}$ (figure 4.8(c)) is not this much familiar. For H||c, a decay power law is perceived for the pristine $J_c(0)^{aniso-str}(H)$ but an unexpected increase is observed for nanocomposites, especially for 8BYTO. This can be clearly observed for H||ab in all samples, where $J_c(0)^{aniso-str}(H)$ rises up to a plateau at high magnetic fields.

A possible interpretation of such $J_c(0)^{aniso-str}(H)$ increasing behaviour is that anisotropic pinning centres, despite the high density and their effective pinning wells, are undermined by the domination of strong isotropic pinning centres at low magnetic fields, where vortices are pinned more easily by the isotropic defects that are randomly and homogeneously distributed. In contrast, only few vortices are pinned by few anisotropic defects, that are less favourable given the need of long correlation of the defect length with the vortex orientation.

At higher magnetic fields, when i-s and i-w contributions start to decay, the amount of vortices that are pinned by anisotropic defects rises, including localized strong correlated defects, implying an increase of $J_c(0)^{aniso-str}$. Once the single vortex pinning regime has been completed for all contributions, $J_c(0)^{aniso-str}$ decreases due to vortex-vortex interactions, as observed above 1 T for H||c in the case of the pristine sample in figure 4.8(c).

The larger $J_c(0)^{aniso-str}$ values obtained for nanocomposites can be very likely related to the reduction of the twin domain spacing and therefore and enhanced density of twin boundaries with a short vertical coherence observed in nanocomposite films[139].

The contribution associated to i-s defects is higher for both nanocomposites than for the pristine film (figure 4.8(b)). As discussed previously, the nanostrained regions given by the presence of a large density of partial dislocations surrounding the stacking faults act as very effective i-s pinning centres. This contribution is principally enhanced at low and intermediate fields, but also remains higher at high fields in comparison with the pristine sample.

Moreover, the 10BZO-5YO nanocomposite, whose defect landscape is characterized by a large density of short stacking faults (analysed in section 3.4.2), exhibits an important increase of the contribution associated to i-w defects (see figure 4.8(a)), which is in general ascribed to point defects as oxygen vacancies or atomic defects.

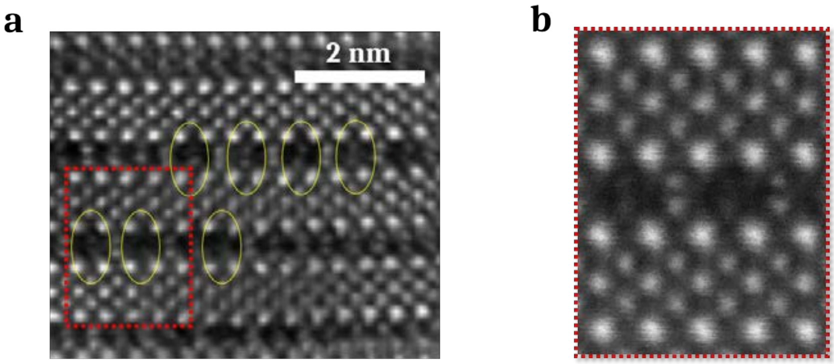

Figure 4.9: (a) high resolution Z-contrast TEM cross section image of a 10% BZO ss-nanocomposite with a large density of stacking faults. Some O-decorated Cu vacancies are indicated by yellow circles. (b) Magnification of the selected region in (a).

In the case of YBCO films with a large concentration of stacking faults, a huge density of complex point-like defects made up of clusters including two Cu vacancies decorated by three O vacancies (O-decorated Cu vacancies) were detected, embedded in the Y124 intergrowths[133,135]. Figure 4.9 shows a high-resolution STEM image of highly strained films with a large amount of stacking faults. Note that the double Cu-O chain exhibits an irregular contrast that corresponds to the Cu-O cluster vacancies.

O-decorated Cu vacancies are present in all YBCO films containing stacking faults. The presence of these defects has been explained in a recent publication[135]: since the precursor solutions used for the growth of the films had a stoichiometry of Y123, the extra amount of Cu needed for the formation of Y124 intergrowths would lead to a local Cu off-stoichiometry, a situation that worsens in the case of Y123 nanocomposites where the number of Y124 intergrowths multiplies. However, this detrimental effect is not observed, since the system balances any Cu deficiency by forming this complex point defect within the double chain.

The density of these clusters is unknown and a way to quantify their density should be envisaged to go deepen in this analysis.

These point defects may act as very effective i-w pinning sites since the enhancement of $J_c(0)^{iso-wk}$ is particularly observed in films with a very high density of stacking faults. However, not all the stacking fault scenarios produce an increase of the density of this kind of point defect compared with a pristine YBCO sample. The 8BYTO nanocomposite exhibits even lower $J_c(0)^{iso-wk}$ values.

The results indicate that the best pinning landscape to enhance at the same time i-s and i-w pinning centres is that with a large density of short stacking faults. What is common in nanocomposites with different typology of stacking faults is the enlargement of the single vortex pinning regime for both i-s and i-w contributions for H||c, with $\mu_0 H^*$ of 0.2 T and 0.4 T respectively, much larger than that one observed for the pristine sample, shown in figure 4.8(d).

The particular landscape observed in the 10BZO-5YO nanocomposite is the one providing not only largest isotropic contributions, but also the largest a-s contributions (see figure 4.8(c)), associated to a large amount of segmented twin boundaries for H||c and of short stacking faults for H||ab, as shown in figure 3.27(c).

4.4 Vortex pinning thermal energies

The characteristic pinning temperatures T^* and T_0, for strong and weak pinning centres respectively, account for their pinning potential energy in relation with $k_B T$. Figure 4.10 shows $T^*_{iso-str}(H)$, $T^*_{aniso-str}(H)$ and $T_0(H)$ dependences for the three samples analysed in the previous section for H||c.

Coloured bands show the dispersion range of the different characteristic temperatures obtained for these samples: 70-130 K for $T^*_{aniso-str}$, 50-90 K for $T^*_{iso-str}$ and 5-20 K for T_0.

Note that the obtained temperature values for each contribution are very similar regardless the sample, with a general trend of decreasing the pinning energy when increasing the magnetic field. This can be understood because these samples have the same kind of defects, which present a typical reduction of vortex pinning due to thermal activation, although the amount of each defect is particular for each sample, as observed in the previous section. However, the size of the defects can noticeably change and therefore there are still remarkable differences from sample to sample.

The larger dispersion in the energy values is obtained for the anisotropic-strong pinning contribution. In this case, lower T^* values are obtained for the 10BZO-5YO nanocomposite ($T^* \sim 60 - 70$ K) in accordance with a lower irreversibility line H_{irr} (see figure 3.14(a)) associated to the presence of segmented twin boundaries due to a large density of stacking faults. In contrast, the pristine sample shows the highest T^* values and highest H_{irr}.

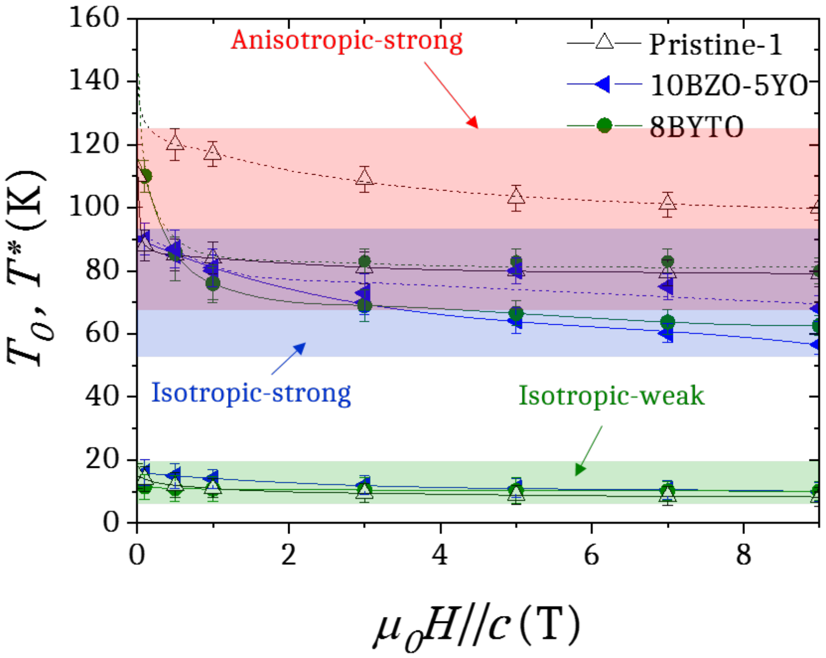

Figure 4.10: magnetic field dependence of T_0 (solid lines, green region), $T^*_{iso-str}$ (solid lines, blue region) and $T^*_{aniso-str}$ (dashed lines, red region) for Pristine, 10BZO-5YO and 8BYTO samples for H||c.

The same dependences are plotted in figure 4.11 for H||ab. The dependences are very similar, only that characteristic temperatures are slightly larger, in accordance with the existence of different anisotropic defects at this orientation.

Temperature dispersion ranges span 5-20 K for T_0, 60-110 K for $T^*_{iso-str}$ and 70-160 K for $T^*_{aniso-str}$. $T^*_{aniso-str}$ is larger for nanocomposites, in agreement with a deeper pinning potential well provided by stacking faults in comparison to intrinsic pinning, more dominant in the pristine sample. $T^*_{aniso-str}$ is especially larger for 8BYTO nanocomposite. That can be understood by a stronger longitudinal coherence when stacking faults are longer (usually BYTO-based nanocomposites own long stacking faults[76], see also figure 3.28), similar to the reasoning used for twin boundaries for H||c.

In what regards the values of the characteristic isotropic-weak pinning temperature T_0, there is a small increase for nanocomposites for both H||c and H||ab, suggesting a modification of the point-like defect landscape probably provided by the appearance of the new O-decorated Cu vacancies.

The magnetic field dependence of characteristic temperatures flatten at high magnetic fields. Figure 4.12 shows the temperature dependence of each normalized pinning contribution considering their averaged characteristic pinning energies at 9 T, where the width of each contribution corresponds to the dispersion obtained by the analysis of the three different samples.

Due to the fast temperature decay of i-w pinning, this contribution is only relevant

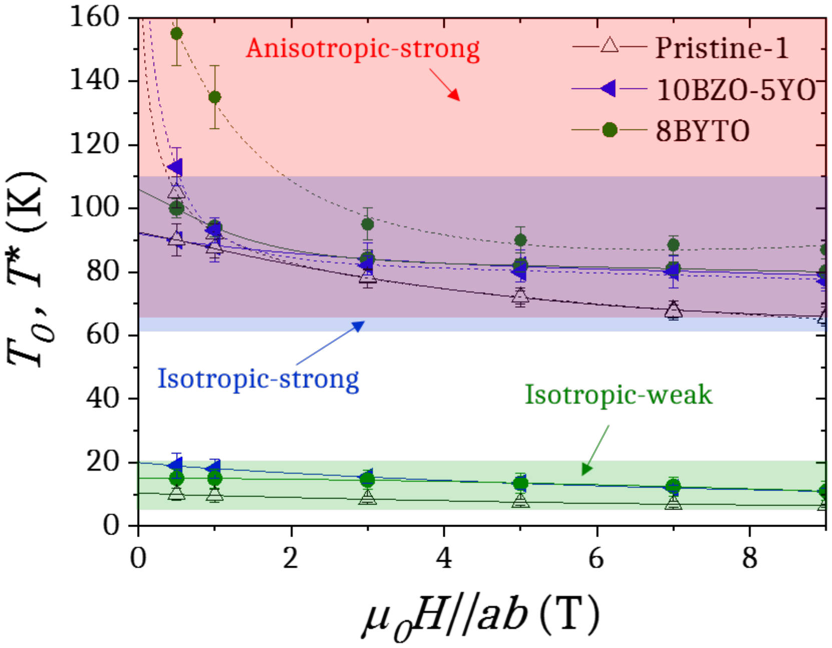

Figure 4.11: magnetic field dependence of T_0 (solid lines, green region), $T^*_{\mathrm{iso-str}}$ (solid lines, blue region) and $T^*_{\mathrm{aniso-str}}$ (dashed lines, red region) for Pristine, 10BZO-5YO and 8BYTO samples for H||ab.

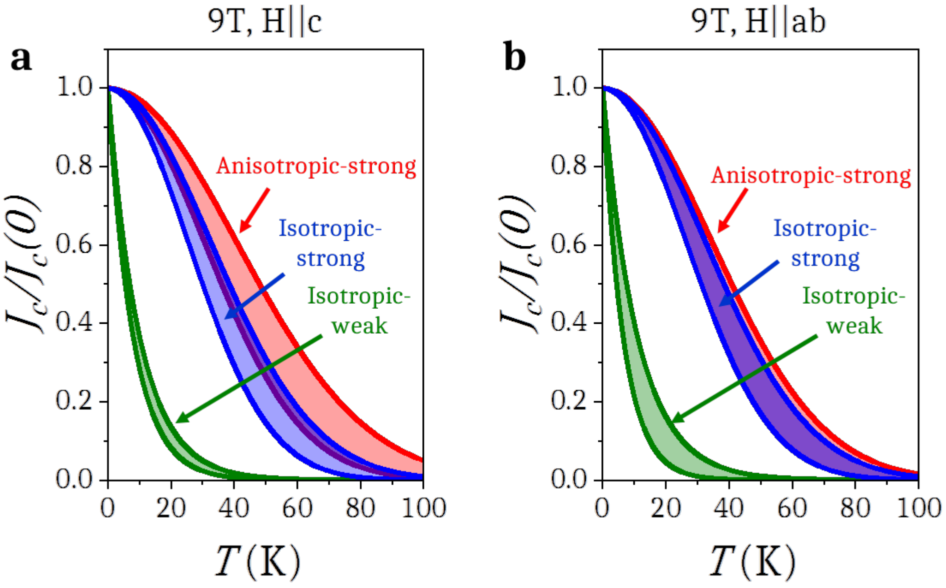

Figure 4.12: temperature dependence of normalized pinning centre contributions considering their characteristic vortex pinning energies for (a) H||c and (b) H||ab at 9T.

at low temperatures (< 40 K). I-s pinning, with an intermediate $J_c(T)$ is relevant at intermediate-high temperatures. The large values of T^* obtained for the a-s pinning contribution make it active up to very high temperatures, being the one with the largest irreversibility field for H||c and competing with similar values to i-s pinning for H||ab.

It is important to remark though, that besides the thermal energy associated to each contribution, what does differ from sample to sample is the density of defects and therefore the value of $J_c(0)$, analysed in the previous section.

4.5 H-T diagrams of pinning contributions

The analysis of both temperature and magnetic field dependences can be merged by the three dimensional plot $J_c(T, H)$ of pinning contributions in the magnetic phase diagram, limited by the irreversibility line $H_{irr}(T)$, following the procedure explained in appendix A. In doing so, it is possible to have a full picture of the dominant pinning contributions evaluated in the previous sections at different conditions of the phase diagram, and associate changes in the diagram to particular defect landscapes characteristic of each type of nanocomposite.

In this section, Pristine-1, 8BYTO and 10BZO-5YO samples are analysed for both H||c and H||ab. The J_c contributions from the three samples are also compared at particular conditions of the phase diagram, plotted versus each partial dislocation relative volume ρ_{dis} (defined in chapter 3).

4.5.1 Diagrams for H parallel to the c-axis

The ratios of the three pinning contributions J_c^{iso-wk}/J_c, $J_c^{iso-str}/J_c$, $J_c^{aniso-str}/J_c$ are plotted for H||c in the diagrams of figure 4.13, showing colour H-T maps of pinning domination similar to other ones that have been previously reported[35,123,167] for comparable pristine and BZO/BYTO-nanocomposites.

The main feature of nanocomposites is a huge increase of the region dominated by i-s pinning. While in the pristine, i-s pinning only dominates at very low magnetic fields, for nanocomposites it is extended up to 5-10 T. This extension is linked to a shrinkage of the a-s contribution, that dominates a very small region at high magnetic fields and temperatures close to the irreversibility line.

At low temperatures, i-w is the most relevant contribution for the pristine film. In the case of nanocomposites two different cases are obtained: 8BYTO, the nanocomposite with large stacking faults, is fully dominated by i-s, whereas 10BZO-5YO, with shorter stacking faults and a larger density of partial dislocations, shows an important contribution of weak pinning as well.

Figure 4.14 presents an analysis of the J_c values of each contribution for the three samples for H||c, plotted versus ρ_{dis} at 1 T and 9 T at the temperatures of 0 K, 50 K and 70 K. Note that ρ_{dis} for 8BYTO nanocomposite is not a direct measure from STEM images but a deduction from the correlations developed in chapter 3.

As discussed throughout the whole analysis, the contribution of i-w defects is very relevant at low temperatures. It is especially important for a large density of dislocations, in agreement with a possible larger quantity of Cu-O vacancies. At these temperatures, a-s contributions are rather low for all ρ_{dis}, and i-w directly competes with the i-s (both with increasing $J_c(\rho_{dis})$ dependence) with similar weights, except at intermediate ρ_{dis}, where i-s is much larger than i-w.

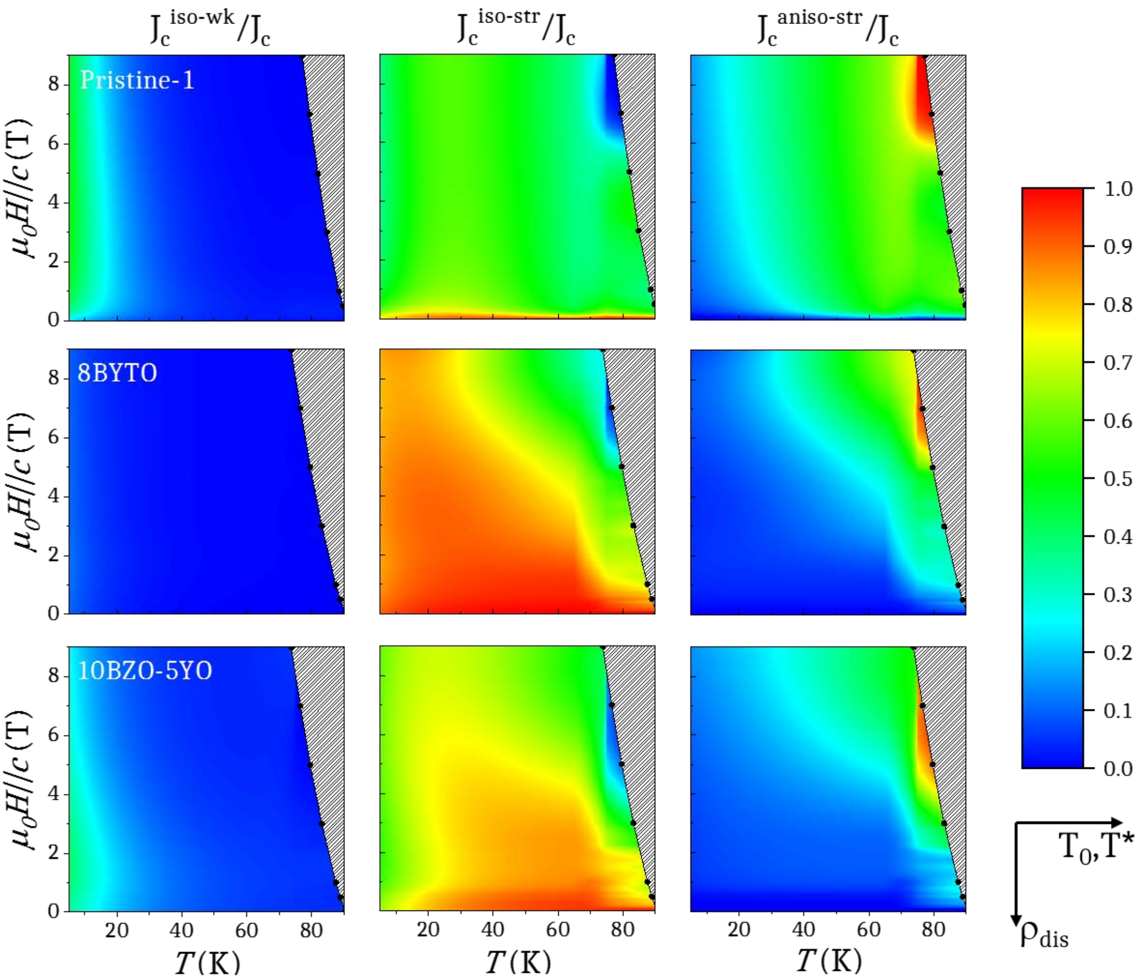

Figure 4.13: H-T color map of the ratios J_c^{iso-wk}/J_c, $J_c^{iso-str}/J_c$ and $J_c^{aniso-str}/J_c$ (to the right, increasing T_0/T^*) for Pristine-1, 8BYTO and 10BZO-5YO (downwards, increasing ρ_{dis}) for H||c. The line with circles corresponds to $H_{irr}(T)$.

At intermediate temperatures , the i-w contribution practically vanishes. At low fields, the critical current density is mainly determined only by the i-s contribution, that increases continuously with ρ_{dis}. At high fields, the i-s contribution competes with the a-s one. At intermediate ρ_{dis}, the sum of contributions is the largest, where the i-s associated to the nanoscale strained regions flattens with ρ_{dis} and the a-s contribution associated to the twin boundaries starts to decay with ρ_{dis}.

Lastly at high temperatures, the dominant contribution at low fields is i-s, that increases with ρ_{dis}, and the dominant contribution at high fields is the a-s, that decreases with ρ_{dis}. For low fields and low ρ_{dis} and large fields and large ρ_{dis}, the contributions of i-s and a-s are comparable.

The pristine sample with lowest ρ_{dis} shows the best performance at large temperatures and large fields, thanks to the large a-s contribution associated to large characteristic pinning temperature T^* of long coherent twin boundaries. In contrast, the 10BZO-5YO nanocomposite with largest ρ_{dis}, shows lower a-s contributions although it exhibits the largest $J_c(0)^{aniso-str}$ in figure 4.8, given the low T^* associated to the segmented twin

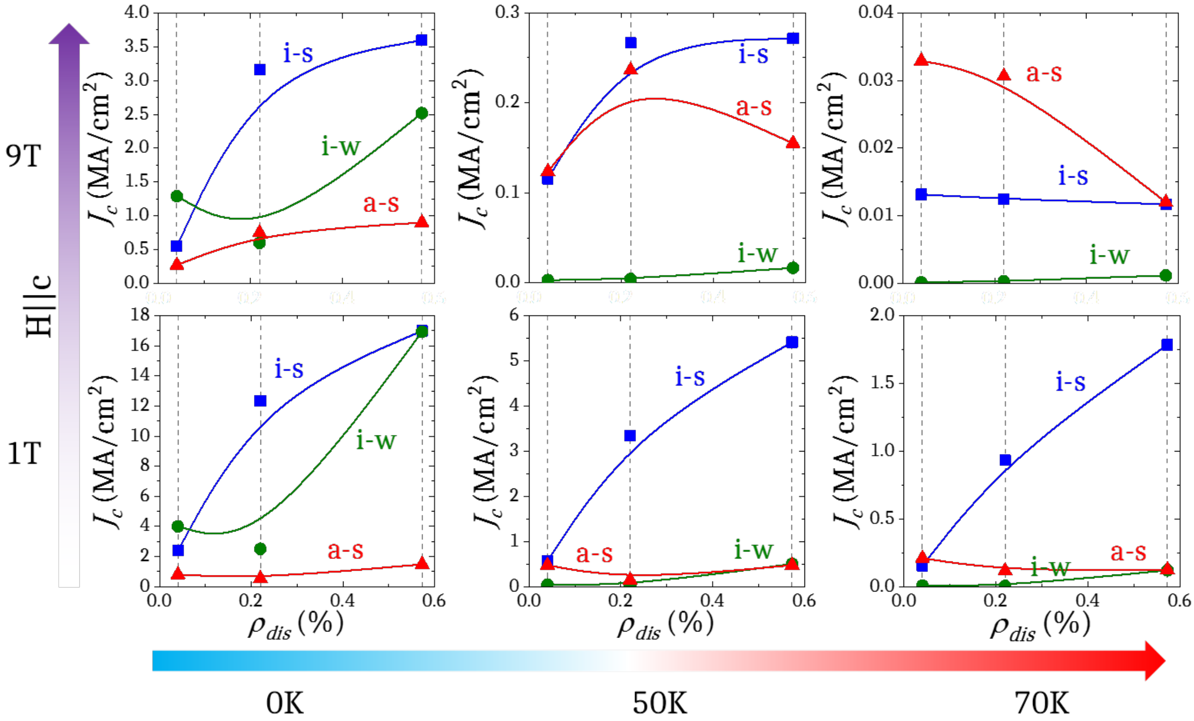

Figure 4.14: evolution of different pinning contributions to J_c as a function of ρ_{dis} for Pristine-1 and 8BYTO and 10BZO-5YO ss-nanocomposites (increasing ρ_{dis}) in the H-T phase diagram for H||c.

boundaries.

4.5.2 Diagrams for H parallel to the ab-planes

The same analysis is extended to H||ab, where H-T diagrams have not been reported yet. The ratios for the pristine and the two nanocomposites are plotted in the diagrams of figure 4.15.

Like for H||c, the i-w pinning contribution is relevant both for the pristine and the BZO-YO nanocomposite at low temperatures, whereas it remains inappreciable for the BYTO nanocomposite.

Besides, the competition between i-s and a-s pinning contributions takes control of the pinning performance at higher temperatures. I-s pinning domination is clear at very low magnetic fields, which is extended up to 0.5 T for the pristine and up to 1-2 T for nanocomposites, attributed to the increase of nanostrain.

On the other hand, a-s pinning (associated to intrinsic pinning and stacking fault pinning) clearly dominates at high magnetic fields and temperatures. The pristine sample, characterized by intrinsic pinning domination (see figure 3.26(b)), shows a very wide region of a-s pinning domination. In contrast, nanocomposites, characterized by a different interplay between stacking fault pinning and intrinsic pinning, show a reduced region of a-s pinning domination located close to the $H_{irr}(T)$ with very large $J_c^{aniso-str}/J_c$ ratios, especially for the BZO-YO nanocomposite with a huge density of short stacking faults.

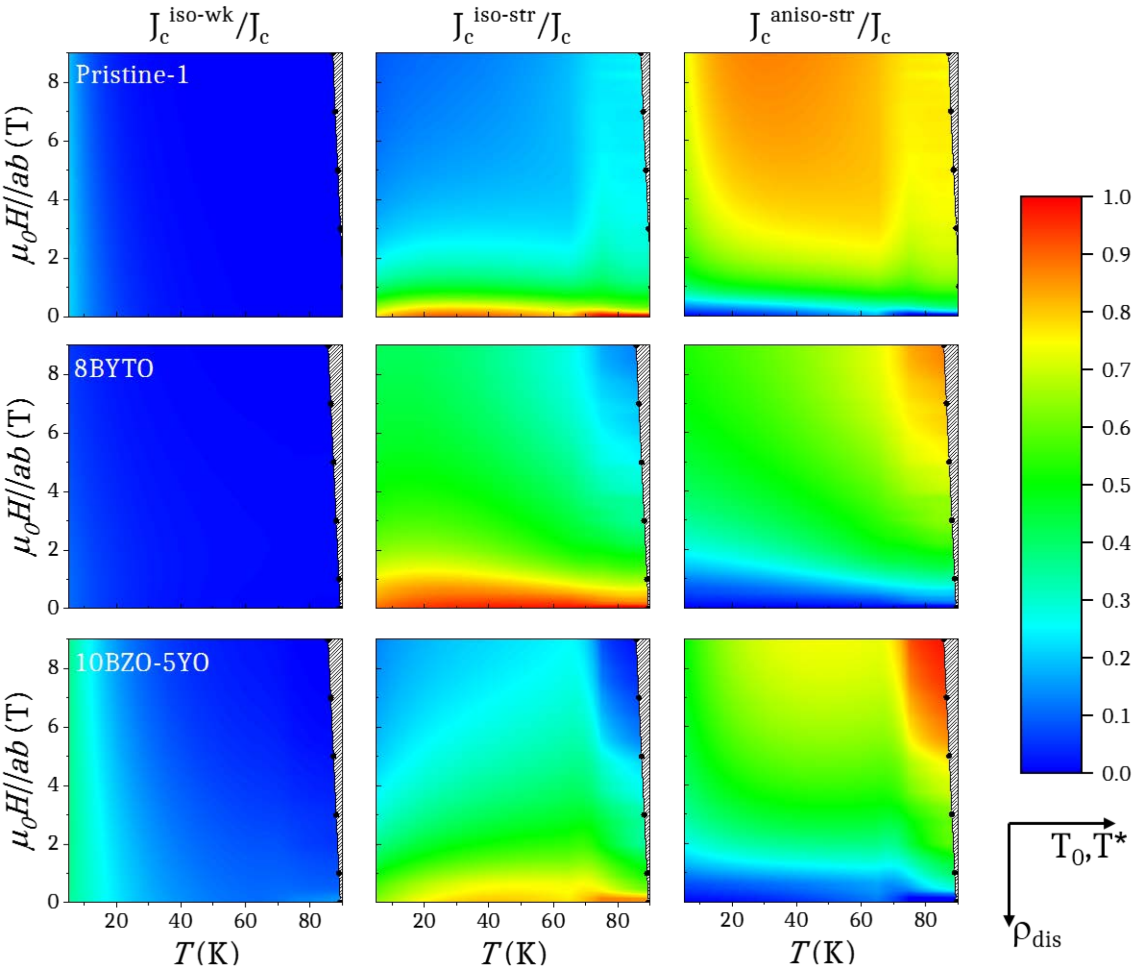

Figure 4.15: H-T color map of the ratios J_c^{iso-wk}/J_c, $J_c^{iso-str}/J_c$ and $J_c^{aniso-str}/J_c$ (to the right, increasing T_0/T^*) for Pristine-1, 8BYTO and 10BZO-5YO (downwards, increasing ρ_{dis}) for H||ab. The line with circles corresponds to $H_{irr}(T)$.

The results of the J_c values of each contribution at different conditions of the H-T diagram for H||ab shown in figure 4.16 reveal again the importance of i-w pinning at low temperatures, that is particularly strong for large ρ_{dis}. At low fields, i-w competes with the i-s that continuously increases with ρ_{dis} and at high field it competes with a-s, associated in this orientation to intrinsic pinning and stacking faults, that is also particularly strong for large ρ_{dis}. Both i-w and a-s contributions present a minima at intermediate ρ_{dis}, but further samples should be analysed at the region of intermediate ρ_{dis} to conclude about this.

At higher temperatures (50 K and 70 K), the i-w pinning diminishes due to the low T_0 and the pinning performance is dominated by i-s pinning at low fields in nanocomposites, since it increases with ρ_{dis}. For low fields, the a-s is very important and independent of the increase of ρ_{dis}, becoming less important for samples with larger ρ_{dis} due to the increase of i-s. In contrast, at high fields, the a-s contribution increases with ρ_{dis} (in agreement with additional pinning provided by stacking faults) and is moreover the dominant one for any density of dislocations.

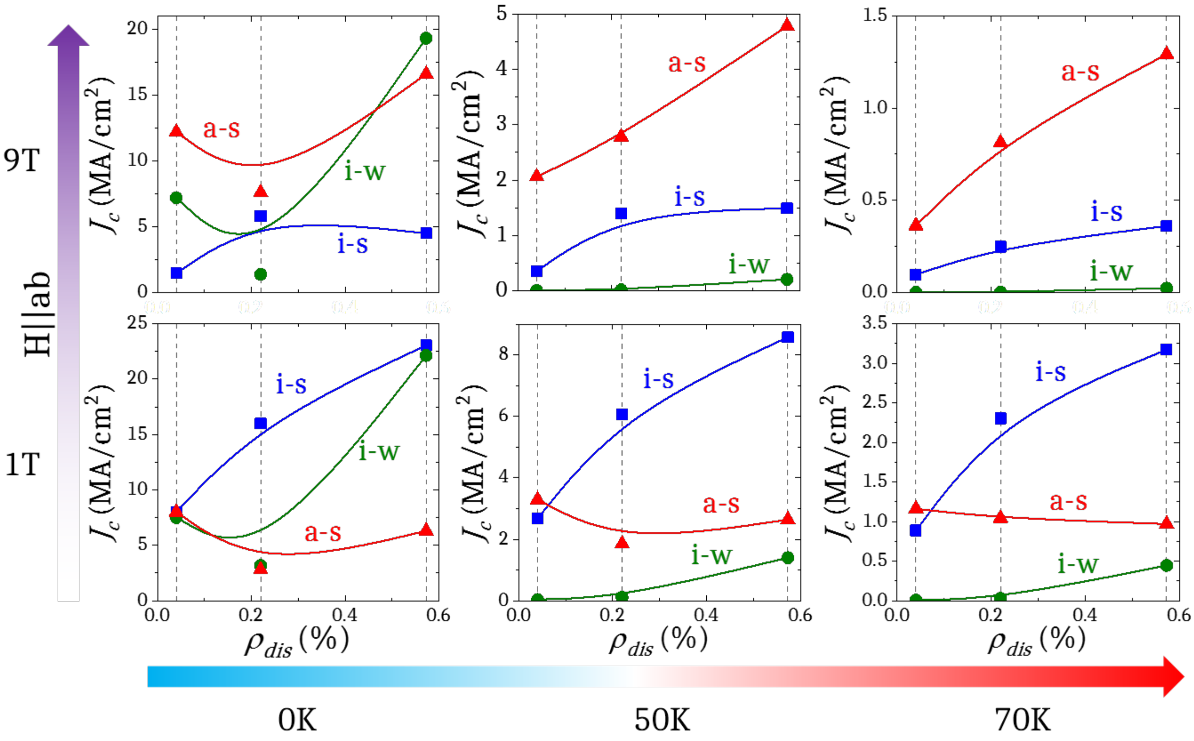

Figure 4.16: evolution of different pinning contributions to J_c as a function of ρ_{dis} for Pristine-1 and 8BYTO and 10BZO-5YO ss-nanocomposites (increasing ρ_{dis}) in the H-T phase diagram for H||ab.

4.6 Pinning contributions of I_c at high magnetic fields

As an example of the insights that one can get from the analysis of the different pinning contributions, the temperature dependence of the absolute critical current I_c is analysed, where I_c is the total current that flows through a superconducting film with critical current density J_c and thickness t: $I_c(H, \theta, T) = J_c(H, \theta, T) \cdot t$.

The $I_c(T)$ dependence for different samples is compared at 9 T for H||c in figure 4.17(a), where 120 nm and 700 nm thick pn-nanocomposites (studied in chapter 6) have been incorporated for completeness.

One can see from the graph that the $I_c(T)$ performance strongly changes from sample to sample with very different values of $I_c(9T, 5K)$. According to the analysis performed in the previous section for H||c, the main contributions at this particular field and temperature are in general i-w and i-s pinning. $I_c(T)$ curves shown in figure 4.17(a) are fitted with: $I_c(T) = I_c(0)^{wk} + I_c(0)^{str}$. The $I_c(0)^{wk}$ and $I_c(0)^{str}$ parameters resulting from the fits for each sample are plotted in figure 4.17(b) as a function of ρ_{dis}. Note that ρ_{dis} values for 8BYTO, PN 13ZO and PN 20BZO have been deduced from the correlations developed in chapter 3.

It is observed that in general both weak and strong contributions of the absolute critical current enhance with increasing ρ_{dis}. Both 8BYTO and PN 20BZO nanocomposites,

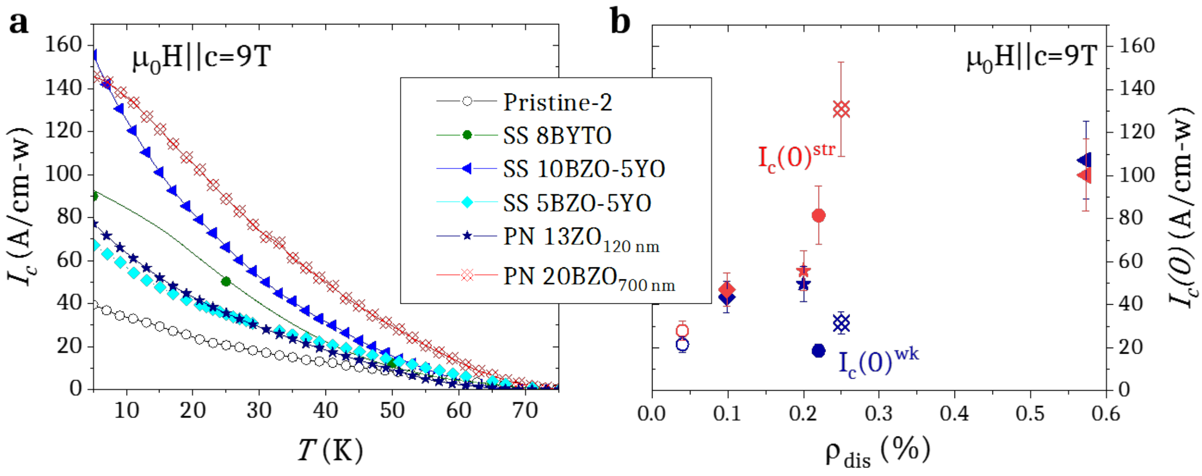

Figure 4.17: (a) $I_c(T)$ dependence obtained at 9 T for H||c for different pristine, ss-nanocomposites and a thick pn-nanocomposite. (b) Weak (red) and strong (blue) contributions to $I_c(0)$ for the samples shown in (a) as a function of ρ_{dis}.

with intermediate ρ_{dis}, show an increase of the strong but not on the weak contributions, suggesting that further tuning should be done in order to increase the weak pinning contribution and therefore enhance I_c to even larger values at these conditions.

To summarize, the increase of the density of dislocations ρ_{dis} assures an enhancement of the isotropic contributions, which can be accompanied with an enhancement of the weak contribution whose origin is still not fully determined.

4.7 Conclusions

The analysis reported in this chapter provides additional understanding to sort out and quantify the pinning strength and energies associated with different pinning centres (isotropic-strong, isotropic-weak and anisotropic-strong) in TFA-CSD nanocomposites.

It also allows to follow the evolution of the different pinning contributions as a function of temperature, magnetic field intensity and orientation, providing a good tool for designing the desired pinning landscape under different operating conditions.

The correlation between pinning contributions and the defect landscape in CSD nanocomposites has been established. In particular, nanocomposites show the best pinning performance. By artificially introducing a unique defect in the YBCO matrix, stacking faults, the nanostructure is strongly modified and causes diverse changes in the pinning contributions scenario:

- A large increase of the isotropic-strong contribution for all orientations associated with nanostrained regions around the stacking faults, especially effective at low and intermediate fields and intermediate temperatures.
- An enhancement of the isotropic-weak contribution when stacking faults are short, effective at low temperatures (< 20 K) at any field, possibly related to Cu-O cluster vacancies hosted by Y124 intergrowths.

- A reduction of anisotropic-strong pinning at large magnetic fields and high temperatures for H||c, related to the twin boundary coherence loss, evidenced by a decrease of $T^*_{\mathrm{aniso-str}}$. At low temperatures instead, nanocomposite exhibit large anisotropic-strong pinning due to the large density of segmented twin boundaries.
- An enhancement of anisotropic-strong pinning at high magnetic fields and temperatures for H||ab, related to the additional pinning provided by the ab-planar stacking faults with larger characteristic temperature $T^*_{\mathrm{aniso-str}}$.

The intensity of each contribution is different for each defect landscape. The increase of isotropic-strong contribution is common in all nanocomposites. However, the increase of other contributions are not so evident for any nanocomposite, being more susceptible to the specific changes in the nanostructure caused by different types of stacking fault arrangements. In particular, the isotropic-weak contribution is enhanced except in some nanocomposites with intermediate ρ_{dis}. Large anisotropic-strong contributions can be also obtained in nanocomposites with short stacking faults, although the $T^*_{\mathrm{aniso-str}}$ is substantially reduced for H||c.

This analysis suggests that an ideal landscape with high performance at any region of the H-T diagram would be that one with a high density of short stacking faults, promoting the formation of large densities of partial dislocations, Cu-O vacancy clusters and c-oriented twin boundaries, if possible concomitant with a preserved long coherence of these last mentioned planar defects. In this way, large critical current densities would be obtained at any orientation by the combination of isotropic and anisotropic defects that would be effective up to high temperatures with large thermal pinning energies.

CHAPTER 5

VORTEX CREEP IN CSD NANOCOMPOSITES

Magnetic flux creep in HTS is an important issue since it sets relevant limits on the possible applications of these materials that need to be addressed.

In this chapter, a thorough analysis from transport measurements on flux creep rate dependences with temperature, magnetic field intensity and magnetic field orientation are performed in CSD ss-nanocomposites. This has enabled us to acquire fundamental knowledge of the relation between microstructure and the vortex dynamics that affects the final electrical performance of coated conductors.

5.1 Magnetic flux creep relaxation

Magnetic relaxation determines the temperature and time dependence of J_c, controls the shape of electric-field–current-density curves and dictates limits to the stability of high-temperature superconductor devices[48].

Flux creep rates have been usually determined by the time decay of magnetization through inductive methods. However, flux creep manifests in many other ways. Among them, electrical transport measurements can be used to deduce the creep rate from the power law electric-field–current-density dependence.

5.1.1 Inductive magnetic flux creep

An important manifestation of magnetic flux creep is the decay of both the current density and magnetization M with time. Coming back to the equation 1.16, and considering the two potentials from equations 1.17 and 1.19, the hopping rate in the flux creep regime is expressed respectively by R_{lin} and R_{log} (where lin and log refer to the consideration of a linear and a logarithmic net potential pinning barrier dependence with the current density):

$$R_{lin} = R_0 e^{-U_P/k_B T} e^{U_P J/k_B T J_0} \tag{5.1}$$

$$R_{log} = R_0 e^{-U_P/k_BT} \frac{J}{J_0}^{U_P/k_BT} \tag{5.2}$$

R/R_0 can be replaced by t_0/t, where t is time and t_0 the effective hopping attempt time associated to the attempt frequency R_0. Then, the current density can be expressed as a function of time J(t), respectively by J_{lin} and J_{log}:

$$J_{lin}(t) = J_0 \left[1 - \frac{k_BT}{U_P} \ln\left(\frac{t}{t_0}\right)\right] \tag{5.3}$$

$$J_{log}(t) = J_0 \exp\left[1 - \frac{k_BT}{U_P} \ln\left(\frac{t}{t_0}\right)\right] \tag{5.4}$$

Note that both expressions of J decay with time. The term in brackets is usually called the flux creep reduction factor. Figure 5.1(a) shows J_c versus time from an inductive magnetic relaxation measurement of a pristine CSD YBCO film under a magnetic field of 1 T. J_c, calculated by applying equation 1.12, decays logarithmically with time, as shown in figure 5.1(b).

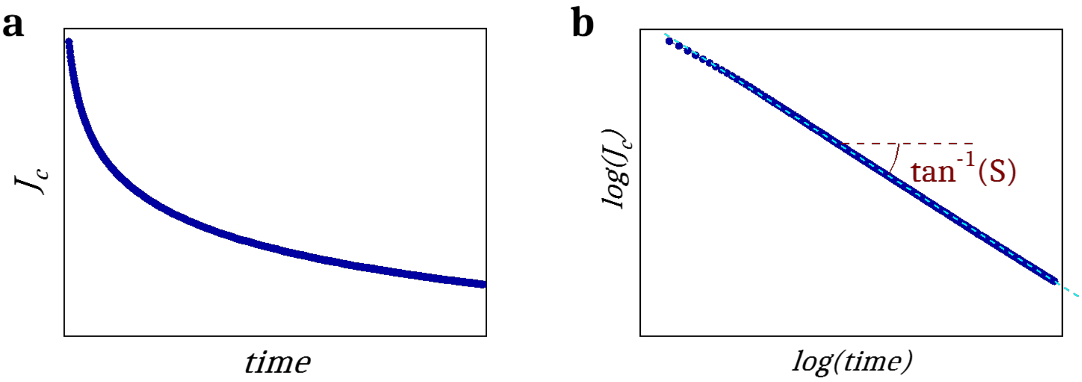

Figure 5.1: (a) linear and (b) logarithmic scale plots of J_c as a function of time for a pristine YBCO film at T=20 K and $\mu_0H||c = 0.1T$.

The normalized flux relaxation rate or normalized creep rate S is defined as the logarithmic derivative of magnetization versus time[48].

$$S \equiv -\frac{1}{M}\frac{\mathrm{d}\,[M]}{\mathrm{d}\,[\ln t]} = -\frac{\mathrm{d}\,[\ln M]}{\mathrm{d}\,[\ln t]} = -\frac{\mathrm{d}\,[\ln J]}{\mathrm{d}\,[\ln t]} \tag{5.5}$$

The J(t) relations derived from a linear and a logarithmic potential barrier U(J) lead to a flux creep rate S (S_{lin} and S_{log} respectively) that depends on temperature and the pinning barrier as:

$$S_{lin} = \frac{k_BT}{U_P - k_BTln\frac{t}{t_0}} \tag{5.6}$$

$$S_{log} = \frac{k_B T}{U_P} \tag{5.7}$$

In the typical case of $U_P >> k_B T \ln(t/t_0)$, S_{lin} matches the expression for S_{log}. On the other hand, the collective flux creep theory[7,169] assumes weak random pinning and treats the flux-line system as an elastic medium, leading to a current-time dependence with the expression $J_{col}(t)$:

$$J_{col} = J_0 \left[1 + \frac{\mu k_B T}{U_P} \ln\left(\frac{t}{t_0}\right) \right]^{-1/\mu} \tag{5.8}$$

Where the exponent μ is an interpolation factor that is different for each vortex state represented in figure 1.13, and hence it may depend on magnetic field and temperature. This current-time relation leads to a flux creep rate for collective creep S_{col}:

$$S_{col} = \frac{k_B T}{U_P + \mu k_B T \ln(t/t_0)} \tag{5.9}$$

The monotonic increase of S with respect to the temperature derived from equations 5.6 and 5.7 is not fully in agreement with experimental results, especially in HTS where S shows a different temperature dependence in four temperature regimes[48] (see figure 5.2).

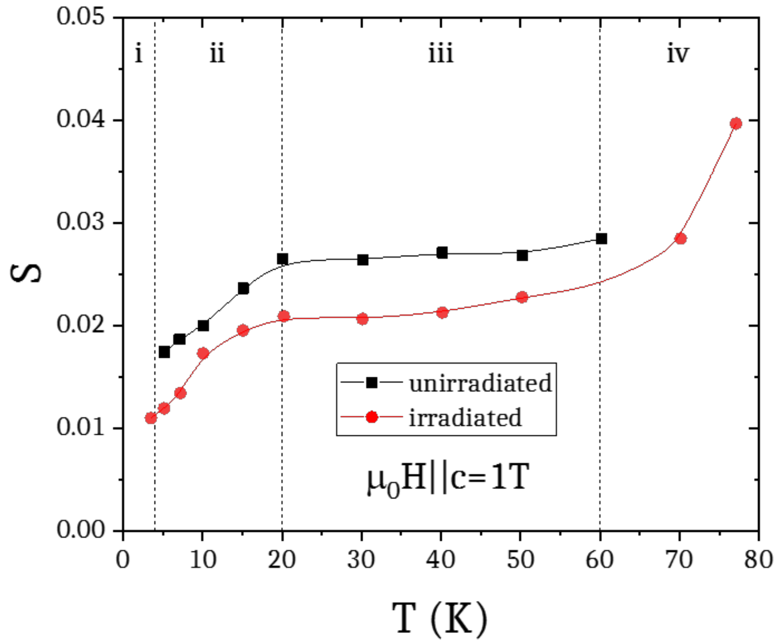

Figure 5.2: temperature dependence of the normalized relaxation rate S for unirradiated and irradiated YBCO crystals in an applied magnetic field of 1 T for H||c. Adapted from[48,170].

At very low temperatures, below 5 K, the magnetic relaxation is finite, attributed to quantum tunnelling of vortices (region i). In the range of 5-20 K, S increases roughly linear with temperature and is well adjusted to the Anderson-Kim model (region ii). At intermediate temperatures (from ~ $0.2T_c$ until ~ $0.8T_c$), S reaches in some films a plateau with a constant value in the range of 0.02-0.04 for fields of the order of 1 T (region iii). In other films, a broad S(T) peak can be observed at this region. At very high temperatures, the creep rate S increases abruptly to very large rates. This last region (region iv) is the plastic creep region whereas the previous ranges belong to the elastic creep region.

Equation 5.9 predicts that the normalized relaxation rate decreases with time in some regions and also predicts the experimentally found S(T) plateau at high temperatures: when $\mu \mathrm{k_B T} \ln(\mathrm{t/t_0}) >> \mathrm{U_P}$, then $\mathrm{S_{col}} \approx 1/\mu \ln(\mathrm{t/t_0})$. Therefore, results can be better adjusted to this theoretical model.

5.1.2 Electrical transport flux creep

As explained in section 1.6.2, the flux creep rate is responsible of the rounded shape of the E-J characteristics. In particular, it is demonstrated that the E-J relation can be fairly described by a power law $\mathrm{E} \propto \mathrm{J^n}$ in the flux creep regime. The comparison of equations 1.21 and 5.7 suggest an inverse correlation between n and S.

Sun et al[171] measured the exponent n deduced from both magnetic and transport measurements. The two kind of measurements showed a consistent trend and nearly overlapped n(T), confirming a phenomenological correlation between magnetic relaxation and the shape of electrical transport J-E characteristics, even if magnetic relaxation over hundred seconds corresponds to a dissipation level orders of magnitude below that of faster transport measurements.

An E-J power law relation $\mathrm{E} \propto \mathrm{J^n}$ with n >> 1 can be combined with the Maxwell equations and the critical state model. Under these assumptions, equations lead to a time dependence of the current density[171,172]:

$$\ln J(t) = \ln J_0 - \frac{1}{n-1} \ln\left(\frac{t}{\tau_0} + 1\right) \tag{5.10}$$

Where τ_0 is a time constant related to $\mathrm{J_0}$, n and the dimensions of the film. In the long time limit ($\mathrm{t} >> \tau_0$), the result for S using definition 5.5 is:

$$S = \frac{1}{n-1} \tag{5.11}$$

Hence, in this approximation, S is nearly inversely proportional to n. Therefore, from this relation, it is possible to measure magnetic flux creep values directly from the slope of the logarithmic current-dissipation dependence. Electrical transport measurements have the benefits of less time consumption and capacity to broaden the study of creep to other field orientations, unreachable by inductive magnetic methods.

Figure 5.3(a) shows the E-J curves in logarithmic scale obtained from electrical transport measurements for a pristine sample. Linear fits are performed using different electric field ranges, where the slope corresponds to the exponent n of the power law, in order to find the range with less standard error of S and also evaluate the variation of S regarding

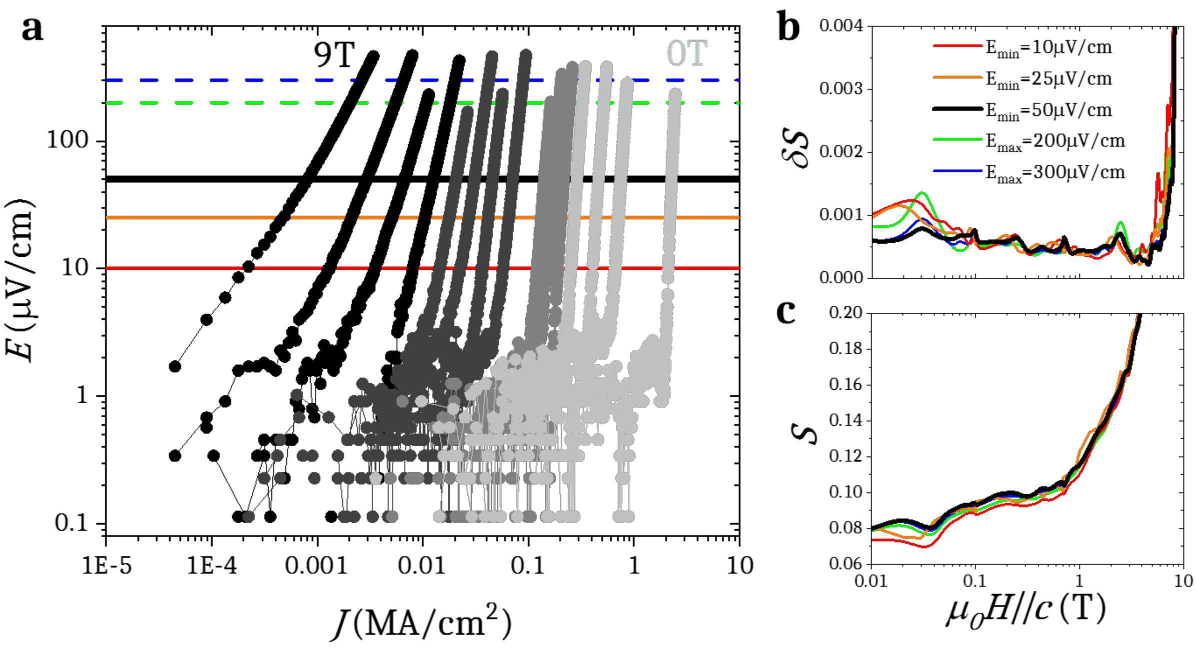

Figure 5.3: linear fit of logarithmic E-J characteristics. (a) E-J characteristics for Pristine-2 sample at 77 K and applied magnetic fields of 0, 0.1, 0.2, 0.4, 0.6, 0.8, 1, 2, 3, 4, 5, 6, 7, 8, and 9 T for H||c. Solid lines represent the E_{min} and dashed lines the maximum electrical field E_{max} used for the different fitting ranges. On the right, magnetic field dependence at 77 K of (b) the standard error from the fit δS and (c) the flux creep rate S obtained by applying the different fitting ranges.

the choice of the electric field fitting range. Solid lines represent minimum electric fields E_{min} for fitting ranges that begin at E_{min} and end at the highest point of each curve. The dashed lines represent maximum electrical fields E_{max} for fitting ranges that begin at $E_{min} = 50\mu V/cm$ and end at E_{max}.

The standard error of the slope δN is propagated to the standard error of the creep rate δS, following the equation:

$$\delta S = \frac{1}{(n-1)^2}\delta n \tag{5.12}$$

A minimum electric field $E_{min} = 50\mu V/cm$ provides the fitting range with less standard error (see figure 5.3(b)). Therefore, it is the one used in this thesis. In any case, the maximum discrepancy for S values obtained using the different fitting ranges reaches $\sim 10\%$ at low fields (see figure 5.3(c)).

In order to confirm the validity of S from electrical transport measurements for describing the magnetic flux creep, a comparison is shown in figure 5.4 of the obtained results by using electrical transport and inductive magnetic (dc SQUID magnetometry) measurements for analogous samples.

Similar orders of magnitude and features are observed in the results achieved by using both methods. S increases with T, except during the plateau or S(T) peak at intermediate

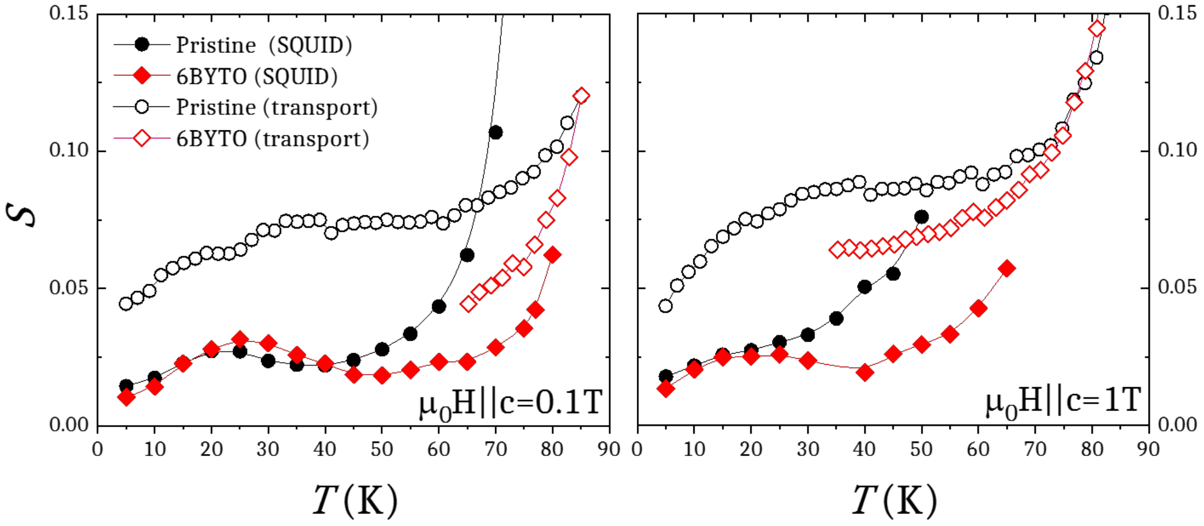

Figure 5.4: temperature dependence of S from electric transport (open) and dc SQUID magnetometry (closed). Curves were measured for two similar pristine samples (circles) and BYTO nanocomposites (diamonds) at 0.1 and 1 T for H||c.

temperatures. However, creep rates from electrical transport measurements slightly differ from rates calculated with inductive ones. At low temperatures, S values from electrical transport are slightly larger. In contrast, at high temperatures in the region of the plastic creep regime, the S parameter abruptly increases sooner for the inductive magnetic measurements. Such discrepancy can be related to distinctive vortex dynamics involved in each kind of experiment where the time scales ($\sim$ 1 hour for SQUID measurements and $\sim$ 1 second for transport) and the electric field windows ($10^{-3} - 10^{-7} \mu$V/cm for SQUID measurements and $1 - 100\mu$V/cm for transport measurements[87,173]) are different.

Furthermore, it is different to apply a constant field with a corresponding induced current that relaxes with time (in the inductive measurement) than applying an increasing current as a driving force (in the transport measurement). Therefore, results in both methods, although showing similar trends, should not be exchanged. In the rest of this work, the presented results of S are achieved by electric transport measurements, except when referred as "S_{ind}", which stands for inductive magnetic flux creep rate.

5.1.3 Vortex thermal excitations in correlated defects

When pinning is dominated by the presence of a high density of correlated pinning centres as columnar tracks, twin boundaries or intrinsic pinning, the vortex phase can be understood as a Bose glass, in which vortices are localized on the anisotropic pins and the liberation of a segment from the vortex line takes place via thermal activation. The size of such liberation is determined by balancing the cost in the elastic and pinning energy of the flux line against the energy gain from the Lorentz-like force, giving rise to different vortex depinning scenarios regarding the applied current density[7,36,44,174,175], depicted in figure 5.5(a).

At high current densities, relaxation takes place via nucleation and expansion of half-

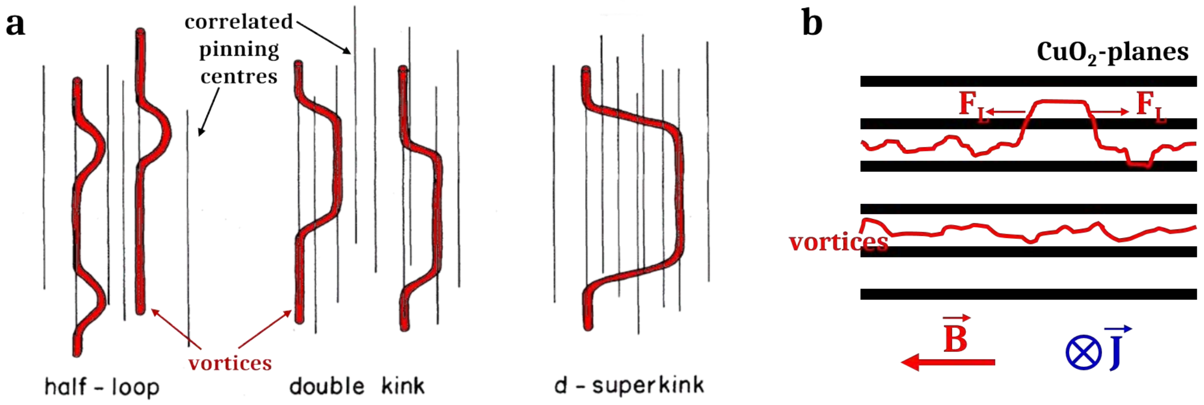

Figure 5.5: (a) schematic representations of a half-loop, a double kink and a double super-kink in a system with correlated pinning centres (adapted from Blatter et al[7]) and (b) a double kink in a layered cuprate endowed with intrinsic pinning.

loops, where the displacement of the depinned vortex segment is smaller than the pinning centres spacing. As current decreases, the size of the critical nucleus grows and reaches the nearest pinning centre, allowing the vortex to hop to a distant unoccupied defect with nearly the same energy, known as double kink excitation. For intermediate current densities, double kinks are the typical excitations. Ideally, there is no energetic barrier for the expansion of a double kink. Only the orientation splay and the energy dispersion of the pinning wells precludes the expansion of double kinks[144,148,174–176]. Finally, at low current densities, it is convenient for the vortex to form a double superkink, whose excitation size is larger than the pinning sites spacing, entering into the so-called variable range hopping regime.

Whereas half-loops and double superkinks involve regimes with glassy behaviour, the spread of double kinks involves a non-glassy behaviour: once a double kink is created there is no energy barrier preventing the entire vortex from moving to the next columnar defect and S can be arbitrarily large[36,130,174]. A peak observed at intermediate temperatures in the S(T) dependence for H||c is usually attributed to expansion of double kink excitations due to correlated c-axis columnar defects and/or planar twin boundaries[36,37,39,130,174,177–179]. The effect of double kink, and therefore the S(T) peak, is observed as long as H is smaller than the matching field H_Φ[148,174,178] associated to the correlated defects.

For H parallel to the ab-planes, thermal excitations have been identified in layered superconductors by several electrical transport measurements[131,159,180,181] in the staircase and locking regimes (depicted in figure 3.4). An inverse correlation between $J_c(\theta)$ and $N(\theta)$ is observed at temperatures below 80 K for YBCO, attributed to double kink excitations rising from the periodic correlated intrinsic pinning, as sketched in figure 5.5(b). This effect is observed up to the highest measured magnetic fields due to a huge estimated $\mu_0 H_\Phi$ for intrinsic pinning (~ 1000 T). The anti-correlation of J_c versus n has been also observed for H parallel to the c-axis below matching fields associated to nanocolumns[148].

5.2 Correlation between J_c and S

In a direct approximation, J_c is the current density required to tilt the barrier pinning potential J_c and hence $J_c \propto U_P$. On the other side, S is inversely or nearly inversely proportional to U_P (see equations 5.6 and 5.7). An inverse correlation between J_c and S is therefore expected.

Figure 5.6 shows S as a function of J_c for multiple samples studied in this thesis, at different conditions of temperature and magnetic fields. The statistical analysis reveals an inverse continuous correlation where S decays with increasing J_c.

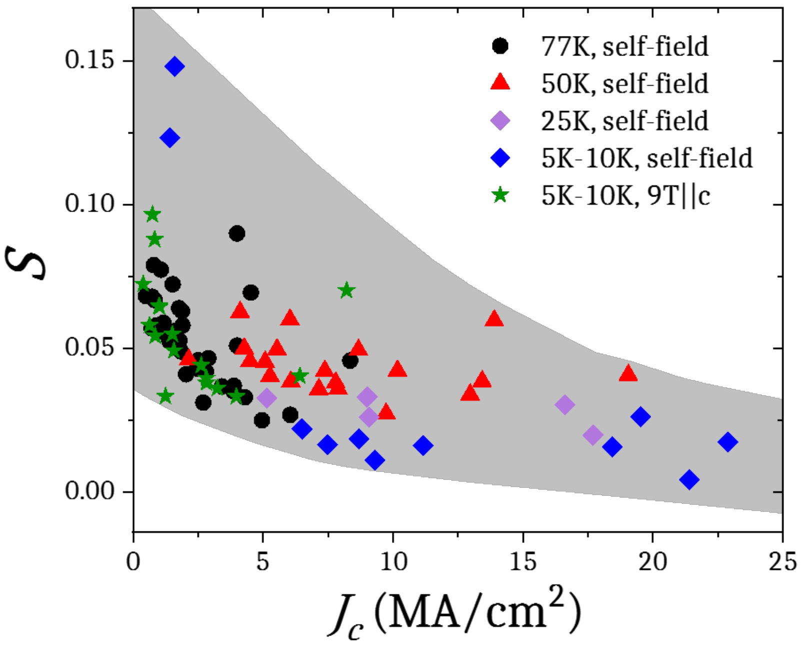

Figure 5.6: S versus J_c at different conditions of temperature and magnetic fields for multiple samples.

The magnetic field dependence of both magnitudes is depicted in figure 5.7 for H||c and H||ab at low and high temperatures for Pristine-2 and 8BYTO nanocomposite. At 77 K, the nanocomposite shows as expected enhanced J_c and reduced S at low and intermediate fields in comparison with the pristine sample.

As discussed in chapter 3, there is a crossing of J_c(H) curves for H||c at 77 K that occurs at high magnetic fields, related to a reduction of H_{irr} in nanocomposites explained by the loss of twin boundaries coherence. This crossing is shifted to lower magnetic fields in the case of the creep rate curves. Whereas the intersection of J_c at 77 K occurs at 6 T for H||c or at $\sim$ 30T after extrapolation for H||ab, the intersection of S occurs at an earlier stage, precisely at 2 T for H||c and 5 T for H||ab. At 10 K, the intersection is shifted to higher magnetic fields, enlarging the region where the nanocomposite provides simultaneously higher flux pinning and lower flux creep.

In conclusion, J_c and S are somehow inversely correlated, although their evolution does not completely coincide along temperature and magnetic field, sensing different notions

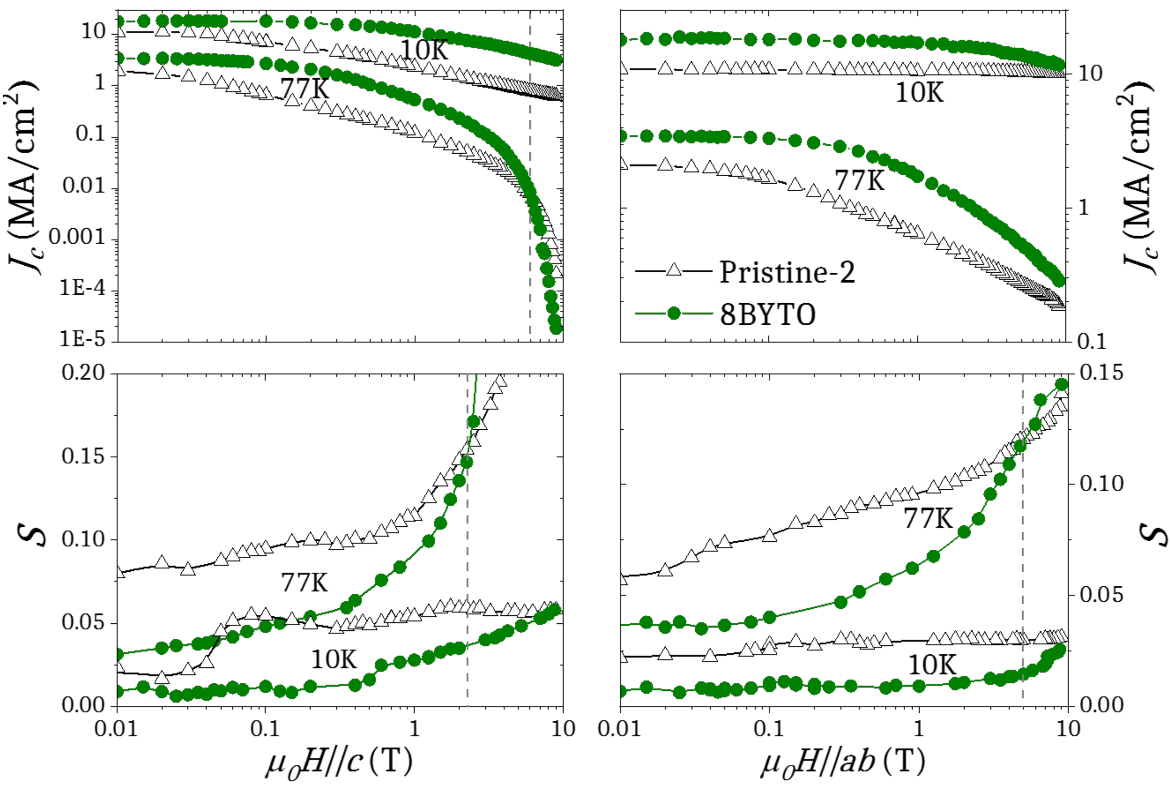

Figure 5.7: magnetic field dependence of (above) J_c and (below) S for H||c and H||ab at 77 K and 10 K for Pristine-2 (open) and 8BYTO nanocomposite (closed). Dashed lines indicate the field where 77 K curves intersect.

of the pinning potential wells. For example, thermal excitations strongly affect the value of S but not that one of J_c, unless it is measured in a long time scale.

5.3 Temperature dependence of vortex creep

As explained in section 5.1.1, the temperature dependence of S is divided in different regions. In this section, the temperature dependence of S is studied for both H||c and H||ab for pristine and nanocomposites in order to elucidate the role that the microstructure plays in relation with creep, paying special attention to the hypothetical observation of the effect of double kink thermal excitations, indicative of recurrent correlated strong pinning.

5.3.1 Vortex Creep for H parallel to the c-axis

In order to investigate the way to reduce vortex creep to its recently reported universal lower limit[182], several studies in nanostructured HTS have been concentrated in the last years on the interplay between defects and vortex dynamics by the use of magnetic relaxation inductive methods when the magnetic field is applied parallel to the c-axis.

Along this broad scope of studies, S(T) peaks have been observed attributed to vortex sliding along nanoparticle surfaces[183] and mostly to the expansion of double kinks between adjacent correlated defects: irradiated columnar defects[102,174,177,178,184], self assembled columnar defects[36,179,185] and/or twin boundaries[37,39,186,187]. S(T) peaks were observed at 20-35 K under magnetic fields below the matching field B_Φ of each particular defect, usually ranging from 0.5 T to 5 T.

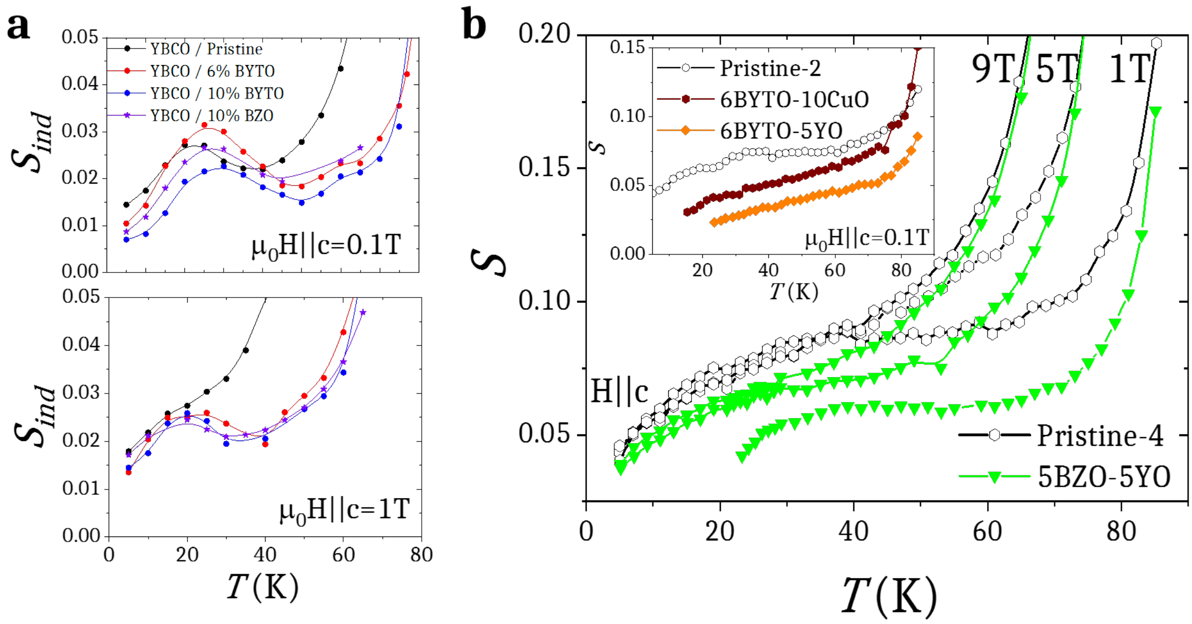

Figure 5.8: temperature dependence of flux creep S for H||c. (a) Magnetic inductive creep rate S_{ind} as a function of temperature for a pristine and BYTO and BZO nanocomposites at 0.1 T (above) and 1 T (below). (b) Temperature dependence of electrical transport flux creep S at 1, 5 and 9 T for Pristine-4 and 5BZO-5YO nanocomposite. Inset shows S(T) for Pristine-2, 6BYTO-10CuO and 6BYTO-5YO at 0.1T.

Figure 5.8(a) shows particular results obtained by magnetic inductive measurements for CSD YBCO pristine and BYTO and BZO ss-nanocomposites in previous works[123,187]. At 0.1 T, a S_{ind}(T) peak, associated to the formation of double kinks, is observed for all samples. In contrast, at 1 T, the peak is observed only for nanocomposites, ascribed to the reminiscence of short-length twin boundary correlation, which is in agreement with a larger B_Φ ascribed to a larger density of twin boundaries.

Although nanocomposites present poorly-coherent segmented twin boundaries along the c-axis, they can be long enough to allow the formation of double kinks where just short lengths of the vortex are necessary[36]. Nevertheless, it is important to note that the maximum value ot this peak $S_{max} \sim 0.025 - 0.03$ is much smaller than the reported for YBCO crystals and films with strong columnar defects[102,174,177,178,184], where values of $S_{max} \sim 0.08 - 0.1$ are achieved at 0.5-1 T.

In the case of the S(T) dependence obtained from electrical transport measurements shown in figure 5.8(b), nanocomposites show reduced creep in comparison to pristine samples, especially at low fields and low temperatures. The sample 5BZO-5YO remains low in creep in comparison to the pristine sample up to 9T and up to high temperatures when entering the plastic creep region.

The peak for H||c associated to twin boundaries cannot be recognized, including measurements at 0.1 T in the inset. Only the 5BZO-5YO nanocomposite S(T) dependence somewhat resembles a tiny double kink peak at 1 T and 40 K. The temperature dependence of this sample has not been measured at lower fields.

5.3.2 Vortex Creep for H parallel to the ab-planes

When vortices lie parallel to the ab-planes, they are on one side strongly pinned due to strong correlated intrinsic pinning and stacking fault pinning. However, on the other side, the periodic and correlated pinning centres ascribed to intrinsic pinning, with matching fields as high as $\mu_0 H_\Phi \sim 1000T$, facilitates easy thermal activated vortex motion through the proliferation of double kink excitations.

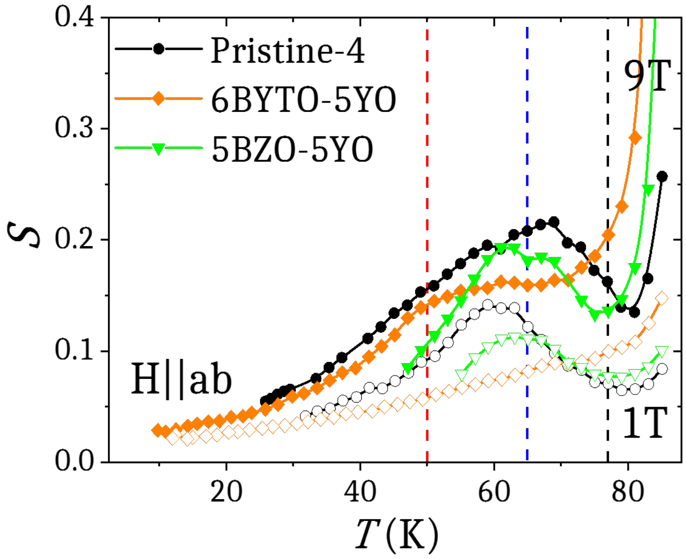

Figure 5.9: temperature dependence of flux creep S for H||ab at 1 T (open symbols) and 9 T (closed symbols) for Pristine-4, 6BYTO-5YO and 5BZO-5YO nanocomposites. Dashed lines correspond to the temperatures where S(θ) is analysed in figure 5.11 for 5BZO-5YO.

There are to our knowledge no reports yet on temperature dependent creep rates for H||ab before this work, which has been recently published[188]. Figure 5.9 shows S(T) at 1 T and 9 T for a pristine sample and two nanocomposites, 5BZO-5YO and 6BYTO-5YO, with increasing densities of stacking faults (further explained in the following section).

Comparably to what happens for H||c and for the magnetic field dependence S(H), magnetic relaxation creep rates are smaller for nanocomposites except at high temperatures when approaching the irreversibility line in the plastic creep regime.

Besides the monotonic increase of S with temperature, a prominent S(T) peak arises at the temperature region that comprises 50 K to 80 K, especially notable for the pristine and 5BZO-5YO nanocomposite, the two samples with less concentration of stacking faults and therefore more dominated by intrinsic pinning.

For the stacking-fault–rich 6BYTO-5YO nanocomposite, the peak vanishes at low magnetic fields, confirming that the presence of artificially induced stacking faults modifies the structure of the CuO$_2$ planes and its effect on thermal activation, precluding the formation of double kinks and thus obtaining lower creep rates for a large range of temperatures.

Motivated by the analysis of the nature of this S(T) peak, figure 5.10 displays the angular dependence around $\theta = 90°$ of J$_c$ and n in the case of the Pristine-4 sample. In figure 5.10(a), at 77 K and 1 T (out of the S(T) peak, as observed in figure 5.9), J$_c$(θ) and n(θ) are proportionally correlated. In contrast, in figure 5.10(b), at 65K and 9 T (inside of the S(T) peak), J$_c$(θ) and n(θ) exhibit inverse correlation, already reported in several works for layered superconductors[131,159,180,181] where the n(θ)-dip is ascribed to a loss in the pinning energy due to the expansion of double kinks mediated by intrinsic pinning.

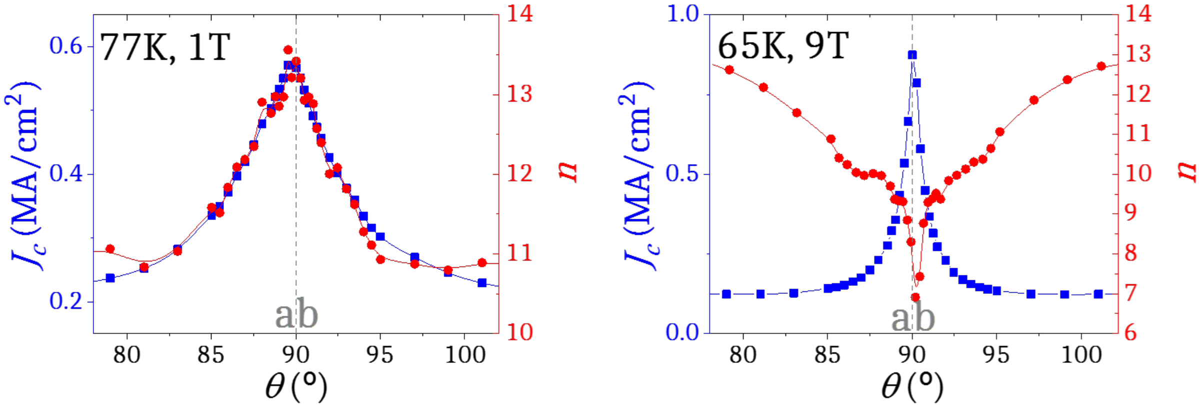

Figure 5.10: J$_c$(θ) (squares) and N(θ) (circles) for Pristine-4 sample at (a) 77 K, 1 T and (b) 50 K, 9 T.

The inverse correlation between n and S obtained in equation 5.11 implies that an n(θ)-peak and an n(θ)-dip correspond to an S(θ)-dip and an S(θ)-peak respectively. The S(θ) dependence around H||ab is plotted in figure 5.11 for the 5BZO-5YO sample at 9 T at the three temperatures indicated in figure 5.9.

At 77 K, one finds as expected for a direct J$_c$-n correlation a minimum in the S(θ) curve at $\theta = 90°$. With decreasing temperature, the sample reaches the temperature T* where the vortex core diameter 2ξ_c drops below the periodic separation of CuO$_2$ planes. Applying equation 1.7 and taking into account the crystallographic structure of the YBCO triple perovskite, T* follows the equation:

$$2\frac{\xi_0}{\sqrt{1-T^\star/T_c}} = \frac{2}{3}d \tag{5.13}$$

Where d is the c-axis lattice parameter, corresponding to a length of 1.17 nm[30]. In the samples studied here T* ∼ 60K. Thus, close to T* at 65 K, vortices start to be strongly localized in the intrinsic single pinning wells so that double kink excitations take place from one pinning centre to the other. Therefore, the S(θ) curve exhibits a peak at this temperature, which spans an orientation width of 5° and widens as temperature decreases.

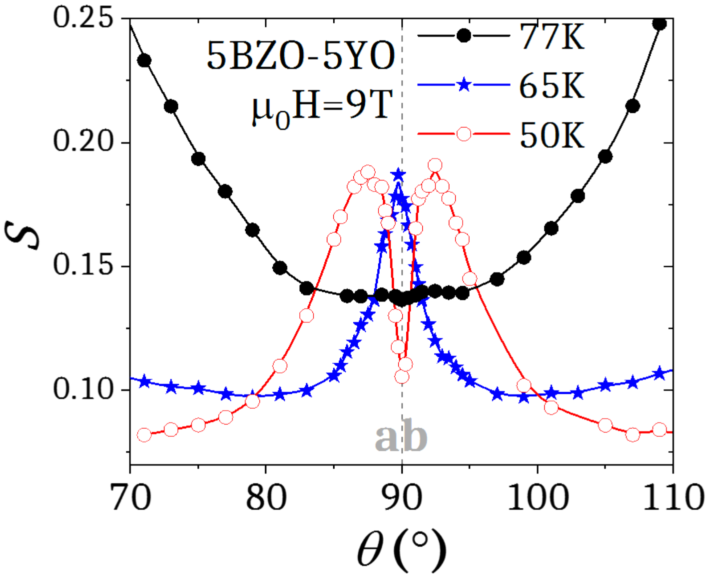

Figure 5.11: angular dependence of flux creep S around H||ab for the 5BZO-5YO nanocomposite at 77, 65 and 50 K at 9 T.

However, at lower temperatures (50 K in this case), a narrow S(θ)-dip arises at the centre of the S(θ)-peak, indicative of a lock-in transition[7], also reported in other electrical transport studies[159,181]. This latter effect shows that at low temperatures the thermal energy k_BT is not large enough to cause movement of vortices through double kink formation when they lie almost parallel to the CuO_2 planes. On the contrary, vortices get locked between the planes.

The S(θ)-peak observed at 65 K and its evolution with increasing and decreasing temperature manifests that the S(T)-peak arising for H||ab is ascribed to the expansion of double kinks, occurring at a very narrow region of magnetic field orientations.

5.4 Pinning regimes for H parallel to ab from creep evaluation: intrinsic pinning and stacking fault pinning

As discussed above, temperature and magnetic field are key conditions for the observation of the S(θ)-peak around H||ab. However, the appearance of this peak does not occur at the same conditions for films with different microstructures, which means that the interplay between the CuO_2 planes (origin of intrinsic pinning) and the generated planar stacking faults is critical for the observation of these thermal excitations.

For example, figure 5.12 shows the S(θ) dependence around $\theta = 90°$ obtained at the same conditions for two samples with very different microstructures. At 50 K and 9 T, Pristine-4 (characterized by a very regular YBCO structure barely faulted) exhibits an S(θ)-peak, whereas 8BYTO nanocomposite (characterized by a large density of stacking faults and a distorted YBCO matrix) exhibits an S(θ)-dip. Thus, different samples can display divergent S(θ) behaviours when measured at the same conditions.

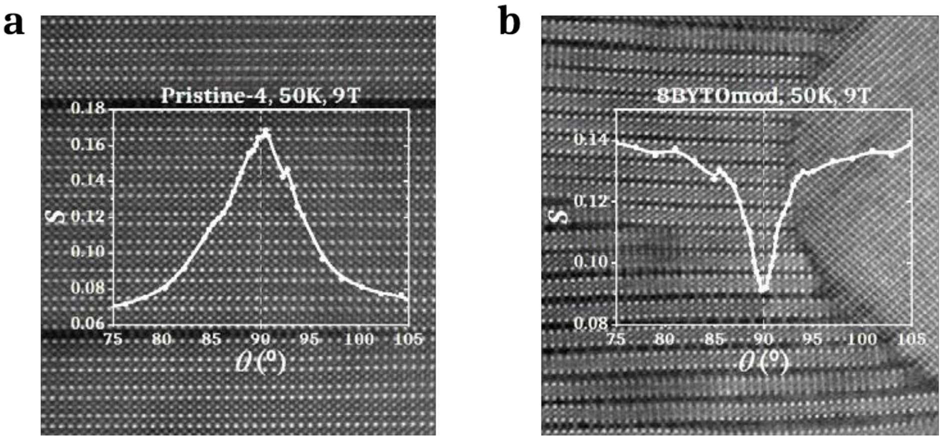

Figure 5.12: S(θ) at 50 K and 9 T for (a) Pristine-4 and (b) 8BYTOmod nanocomposite. The high resolution STEM images in the background correspond to the expected microstructures, observed for similar samples.

By analizing S(θ) dependences at particular conditions of temperature and magnetic field it is possible to determine a lower crossover line $\mu_0 H_{cr1}(T)$ in the H-T diagram, separating creep regions for a variety of pristine samples (see figure 5.13(a)).

For a given temperature, $\mu_0 H_{cr1}(T)$ is the magnetic field that separates the observation of the S(θ)-dip (at lower fields), defined by a negative average slope $^{dS}/_{d\theta}$ between $\theta = 70°$ and $\theta = 90°$, from the observation of the S(θ) peak (at higher fields), defined by a positive average slope $^{dS}/_{d\theta}$ between $\theta = 70°$ and $\theta = 90°$.

At high temperatures and low magnetic fields, the S(θ)-dip is observed. In the other limit, at low temperatures and high magnetic fields, the S(θ)-peak is found. The transition from the S(θ)-dip to the S(θ)-peak is in general not abrupt, defining a region in-between where the peak is not completely formed below the upper crossover line $\mu_0 H_{cr2}(T)$ (see insets of figure 5.13(a)).

For a given temperature, $\mu_0 H_{cr2}(T)$ is the magnetic field that separates the observation of the not completely formed S(θ)-peak (at lower fields), characterized by some regions with a negative average slope $^{dS}/_{d\theta}$ between $\theta = 70°$ and $\theta = 90°$, from the observation of the completely formed S(θ) peak (at higher fields), defined by a full-range positive average slope $^{dS}/_{d\theta}$ between $\theta = 70°$ and $\theta = 90°$.

As commented before, the presence of the S(θ)-peak is related to the thermal excitations aided by the recurrent distribution of the intrinsic pinning wells, as sketched in figure 5.14(a). Thereby, the region above the crossover line $\mu_0 H_{cr1}(T)$ is dominated by intrinsic pinning, whereas the region below is dominated by pinning caused by defects that destabilize the periodicity of intrinsic pinning thus avoiding double kinks formation. In these films, stacking fault pinning consisting of Y124 intergrowths is the main responsible source of such disruption.

In figure 5.13(b), $\mu_0 H_{cr1}(T)$ crossover lines are depicted for numerous nanocomposite films. The crossover happens to be shifted to larger magnetic fields and lower tempera-

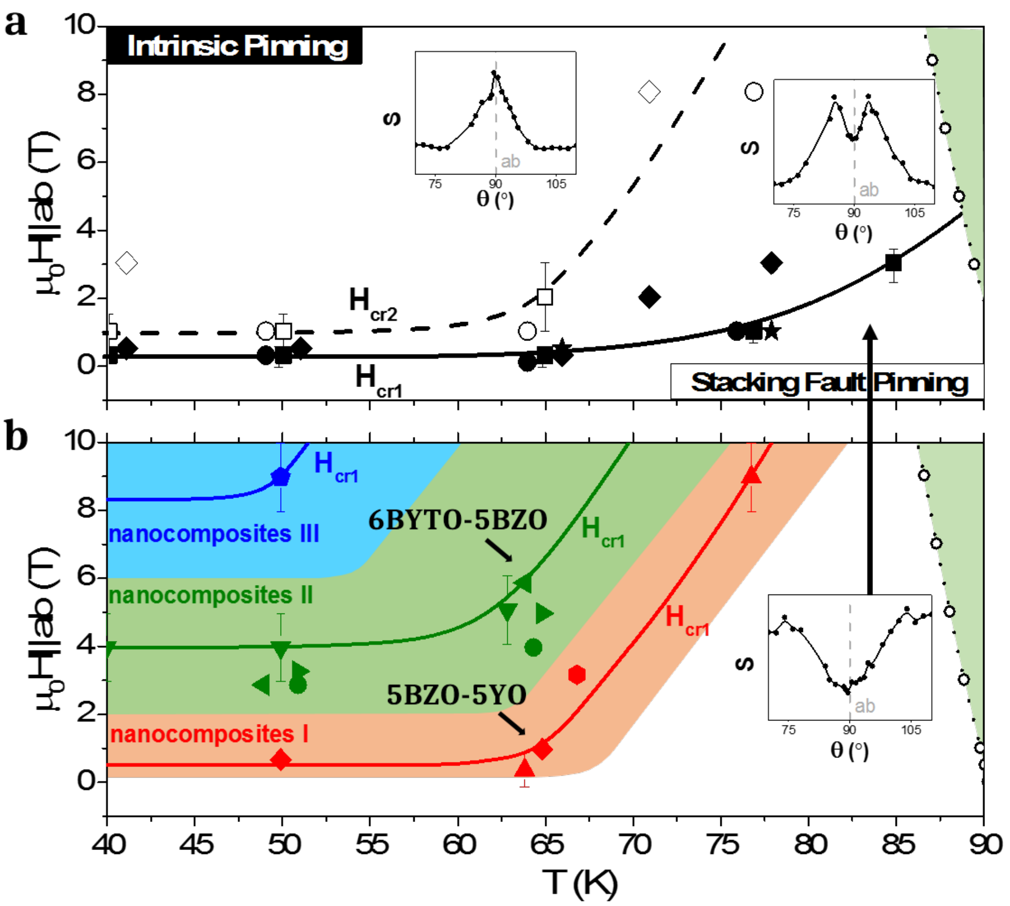

Figure 5.13: H-T phase diagram for H||ab. Closed symbols (experimental results) and solid lines (guides to the eye) represent the lower crossover line $\mu_0H_{cr1}(T)$ for (a) pristine and (b) nanocomposite films. The open symbols (experimental results) and dashed line (guide to the eye) represent the upper crossover line $\mu_0H_{cr2}(T)$. The insets show the S(θ) dependence for a pristine sample in the regions of the diagram separated by the crossover lines in figure (a). The dotted lines with circles refer to the experimental $H_{irr}(T)$ for representative (a) pristine and (b) nanocomposite samples. Crossover points are plotted for a large variety of samples (each type of symbol corresponds to one sample). Error bars are only indicated for representative samples. Three typologies of nanocomposites are identified regarding the region of $\mu_0H_{cr1}(T)$. The arrows in (b) point out two samples graphed in figure 5.17.

tures for nanocomposites in comparison to pristine films. This shift is consequently given by the changes in the microstructure. In fact, a structure dominated by the nanoparticles-emerging staking faults strongly modifies the periodic scenario of the CuO_2 planes responsible for intrinsic pinning by means of distortion of the planes and generation of a stronger pinning region that hinders double kink proliferation, as sketched in figure 5.14(b).

The general trend that is observed by studying a large variety of nanocomposites is that stacking fault pinning dominates in a wider range the diagram whenever nanoparticles are introduced, leading to small distortions in several films (nanocomposites I), to larger distortions for the majority of the studied films (nanocomposites II), and to very large distortions that dominate the whole studied diagram in some particular cases (nanocomposites III), identified in figure 5.13(b) with different colours. The separation of stacking

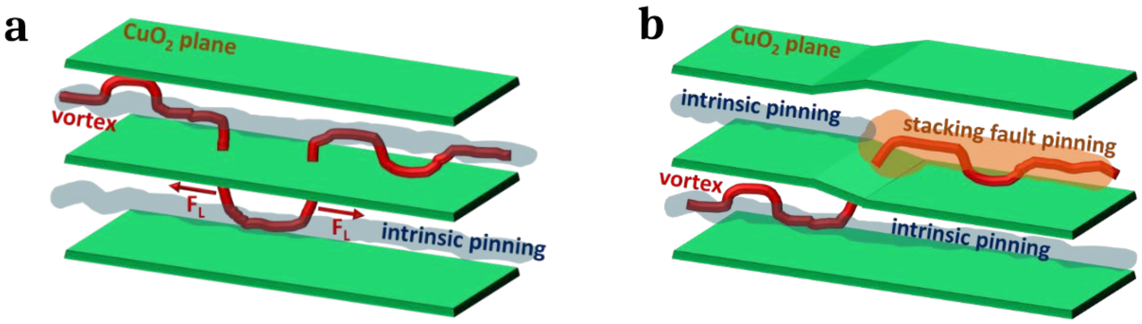

Figure 5.14: representation of (a) the formation of a double kink given by periodical intrinsic pinning and (b) the formation of a kink in the modified CuO_2 planes scenario caused by the emergence of a stacking fault. F_L is the Lorentz-like force driven by the interaction between the flux line and the applied current.

fault pinning and intrinsic pinning regimes delimited by $\mu_0H_{cr1}(T)$ is very similar to the one obtained with the $\mu_0H^{sat}(T)$ crossover line in figure 3.26(b) by analysing the trapping angle.

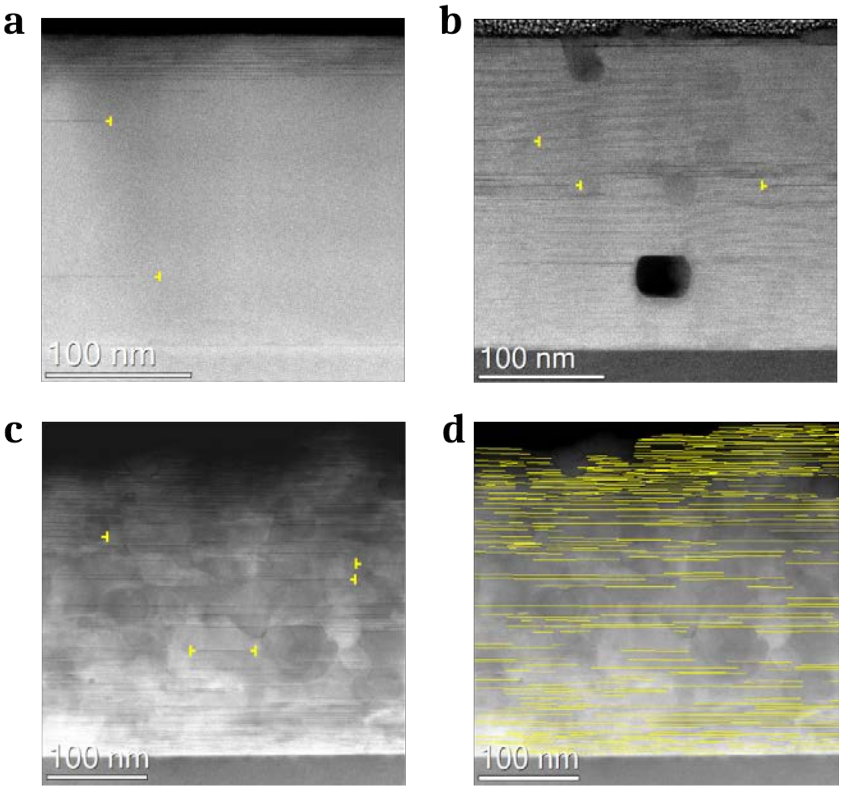

Figure 5.15: STEM characterization of films with different stacking fault densities. Z-contrast low magnification images for (a) a pristine film, (b) 5BZO-5YO nanocomposite (group I) and (c) 6BYTO-5BZO nanocomposite (group II), where Y124-intergrowths can be recognized by black stripes. The identification of stacking faults for 6BYTO-5BZO is marked in yellow stripes in image (d).

The STEM images shown in figure 5.15(a-c) illustrate the change in stacking fault concentrations, where the densities have been calculated by dividing the number of identified stacking faults (as shown in figure 5.15(d)) by the total YBCO area. The pristine sample, 5BZO-5YO and 6BYTO-5BZO nanocomposites (from groups I and II, whose $\mu_0\mathrm{H}_{\mathrm{cr1}}(65\mathrm{K})$ are pointed out with arrows in figure 5.13), present stacking fault densities of $3.2 \cdot 10^{-4}$ nm^{-2}, $6.4 \cdot 10^{-4}$ nm^{-2} and $2.2 \cdot 10^{-3}$ nm^{-2} respectively. 10BZO-5YO (nanocomposite III) presents a density of $2.8 \cdot 10^{-3}$ nm^{-2}, calculated from figure 3.27(c).

Thus, a correlation between the crossover field $\mu_0\mathrm{H}_{\mathrm{cr1}}(\mathrm{T})$ and the stacking fault density can be established, in agreement with the enhancement of the region dominated by stacking fault pinning when the density is larger.

5.5 Isotropic collapse of creep

Similarly to the methodologies presented for $\mathrm{J_c}$ in some works[98,155], the Blatter scaling approach[120] can be applied for S as well, strongly widening the possibilities used until now for the evaluation of flux creep mechanisms, especially in YBCO films and nanocomposites where different pinning centres coexist with distinct contributions that may be separated by angular dependent results.

Figures 5.16(a-d) show the isotropic collapse of several $\mathrm{S}(\theta)$ curves at 65 K when plotted as a function of the effective magnetic field $\mathrm{H_{eff}} = \mathrm{H}(\cos^2\theta + \gamma_{\mathrm{eff}}^{-2}\sin^2\theta)^{1/2}$ for a pristine and several nanocomposite samples from each group (I, II and III) with an effective anisotropy γ_{eff} of 6 for the pristine and 2-2.5 for nanocomposites. This low γ_{eff} is equal to the values obtained from $\mathrm{J_c}$ and $\mathrm{H_{irr}}$ measurements, which has been demonstrated to be caused by the nanoscale strained regions generated at the surroundings of the Y124-intergrowths, as discussed in chapter 3.

Correlated pinning may affect vortex dynamics along a wide range of magnetic field orientations[189]. Thermal excitations of different nature can provoke large and broad changes in S, causing the inability to collapse the isotropic contribution at wide regions in the H-T diagram, as for instance in figure 5.16(a) above 3 T, where the anisotropic contributions around H||c strongly affect the creep rates for the pristine sample. At some temperatures, it is not collapsable at all.

Nanocomposites mostly inhibit the anisotropic contributions around H||c due to the coherence breaking of twin boundaries and preclude the formation of double kink thermal excitations, hence facilitating the collapse of the isotropic contribution of flux creep $\mathrm{S^{iso}}$, which is in general clearly observable as in figures 5.16(b-d).

For 5BZO-5YO nanocomposite (from nanocomposites I), thermal excitations are very obvious for H||ab, suggesting a very well preserved ordered planar structure that favours the proliferation of double kinks in spite of the emerging stacking faults. On the other hand, the effect of twin boundaries for H||c almost vanishes, where only a small decrease of S is observed.

For 6BYTO-5BZO and 10BZO-5YO (from nanocomposites II and III, respectively), the collapse of $\mathrm{S^{iso}}(\mathrm{H_{eff}})$ is very similar. Curves are almost fully isotropic. In the case of 10BZO-5YO, S decreases with respect to $\mathrm{S^{iso}}$ for H||ab, which means that creep is not

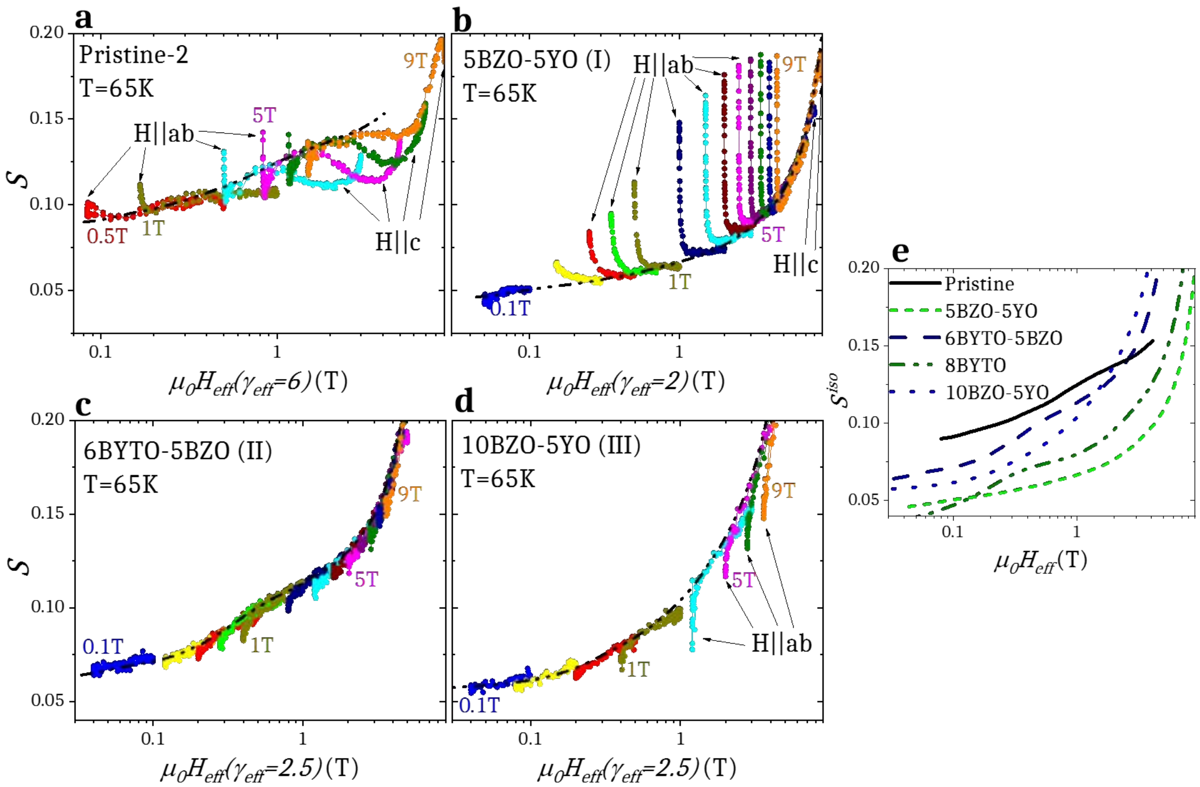

Figure 5.16: S(θ) as a function of μ_0H$_{\text{eff}}$ with corresponding γ_{eff} for (a) Pristine-2 and (b) 5BZO-5YO, (c) 6BYTO-5BZO and (d) 10BZO-5YO nanocomposites (from groups I, II and III respectively) at 65 K. The dashed line is the identification of the collapsed S$^{\text{iso}}$(H$_{\text{eff}}$) line. Deviations from the collapsed values are identified for orientations close to H||ab and H||c. (e) Comparison of S$^{\text{iso}}$(H$_{\text{eff}}$) for pristine and nanocomposites.

only avoided annulling the propagation of double kinks but it is also reduced with an anisotropic pinning contribution.

In figure 5.16(e), the S$^{\text{iso}}$(H$_{\text{eff}}$) curves for pristine and nanocomposite samples are compared. S$^{\text{iso}}$ is smaller in nanocomposites up to a certain magnetic field, in the range of 2-9 T at 65 K. The large increase of S$^{\text{iso}}$ related to the entering in the plastic creep region appears at different magnetic fields for each particular nanocomposite.

The angular dependence of S and S$^{\text{iso}}$ is plotted in figure 5.17 for nanocomposites 6BYTO-5BZO and 5BZO-5YO, whose μ_0H$_{\text{cr1}}$(65 K) are pointed out with arrows in figure 5.13 and whose microstructure is observed in the STEM images in figure 5.15(b-c). S(θ) and S$^{\text{iso}}$(θ) are plotted at 2 and 3 T respectively, which means that 6BYTO-5BZO is in the stacking fault pinning dominated region whereas 5BZO-5YO is in the intrinsic pinning dominated region.

The 5BZO-5YO sample, which is in the H-T region of intrinsic pinning domination, exhibits a large S(θ)-peak for H||ab, ascribed to double kinks jumping across the regular intrinsic pinning centres, that corresponds to the anisotropic flux creep contribution S$^{\text{aniso}}$. In contrast, the 6BYTO-5BZO nanocomposite, which is in the H-T region of stacking fault pinning domination, shows a decrease of S given by the S$^{\text{aniso}}$ contribution that indicates the effect of correlated pinning centres hampering vortex flux motion.

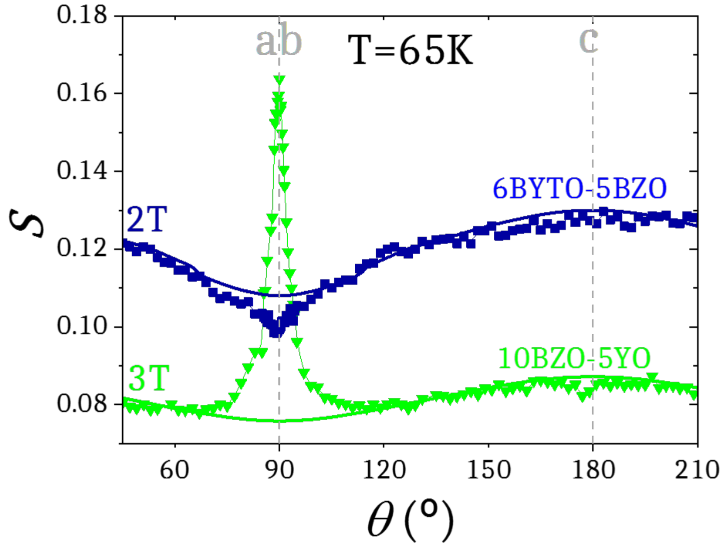

Figure 5.17: angular dependence of S and S^{iso}. Curves were measured at 65 K at 2 and 3 T for 6BYTO-5BZO (nanocomposites II) and 5BZO-5YO (nanocomposites I) respectively. Solid lines represent the isotropic contribution $S^{iso}(\theta)$, obtained from the scaling $S^{iso}(H_{eff}(\theta))$ in figures 5.16(b-c).

For H||c, neither an increase nor a decrease is observed in both nanocomposites, suggesting that the lack of coherence of twin boundaries due to the presence of stacking faults impedes flux jumping across these correlated defects and do not additionally hamper flux relaxation neither.

In order to further analyse the different contributions to the relaxation mechanisms, figure 5.18 shows S and S^{iso} versus magnetic field at 77 K and 65 K for the pristine and nanocomposite samples from figure 5.7, where 8BYTO is a nanocomposite from the group II.

For H||c, S^{iso} exceeds the absolute S continuously, especially for the pristine film, indicative of a decrease of relaxation induced by correlated defects acting as pinning centres and preventing flux relaxation, in agreement with the observation of pinning carried out by twin boundaries in this type of films[130].

For H||ab, a similar situation is observed for the nanocomposite, where stacking fault dominates, thus preventing flux relaxation. However, the pristine undergoes an important change from 77 K to 65 K. Double kink excitations start being formed at the lower temperature (approaching $T^{\star}$) when the vortex core fits the intrinsic pinning spacing, boosting thermal flux activation and therefore showing an increase of flux creep.

The intersection of the S curves for both H||c and H||ab, which is detrimental for the use of nanocomposites at high magnetic fields, shifts to higher fields when temperature decreases. Moreover, the capability of the nanocomposite of preserving a decrease of S coming from S^{aniso} results in S values that are far below the ones that we obtain in the pristine sample at the temperature of 65 K.

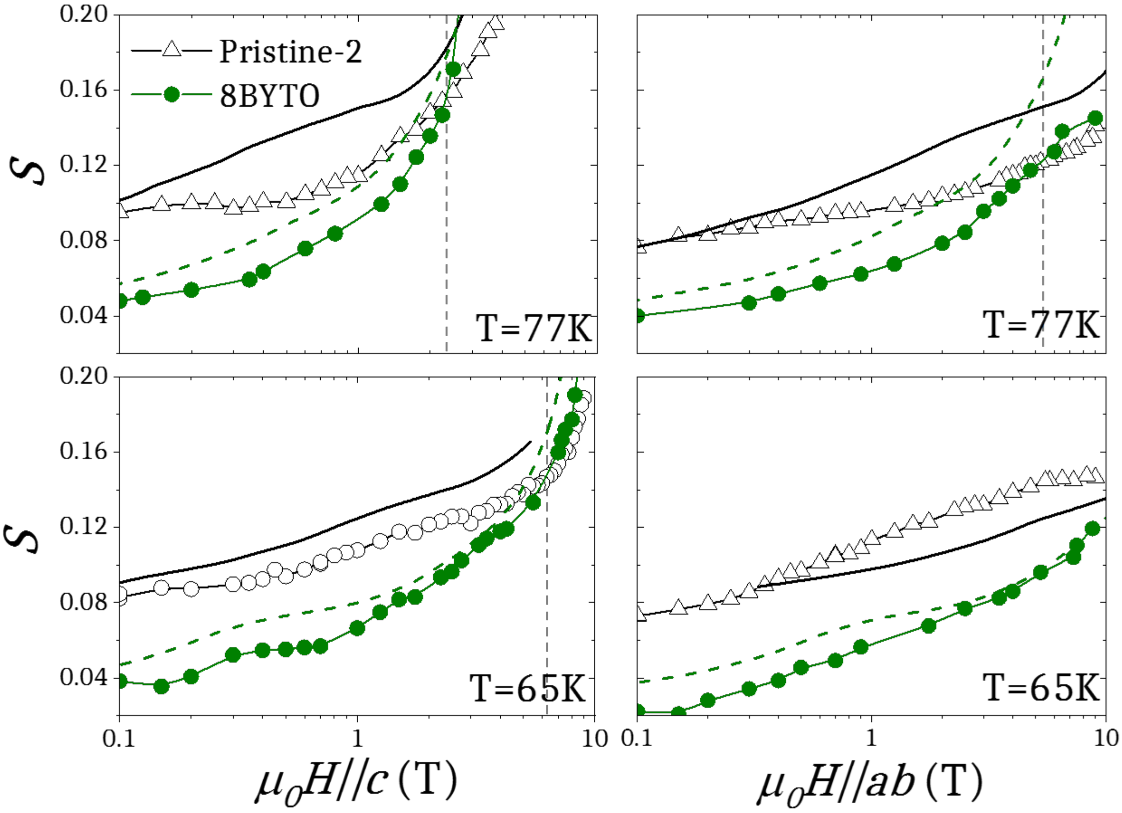

Figure 5.18: magnetic field dependence of S (experimental points) and S^{iso} (simple lines) for H||c and H||ab for Pristine-2 (open symbols, solid lines) and 8BYTO (closed symbols, dashed lines) samples at 77 K and 65 K. Straight dashed lines show the magnetic field where S curves intersect.

5.6 Conclusions

The first important conclusion from this chapter is that the magnetic relaxation creep rate S can be obtained from electrical transport measurements. The experimental results are not accurately comparable to the values obtained from inductive methods and results should not be exchanged although similar trends are observed. As a matter of fact, the vortex dynamics involved in each kind of method is different due to the use of different time scales and electric field windows. However, results from transport measurements qualitatively reproduce the same features reported by other methods and present slightly larger creep values, in accordance to the use of a larger electric field criterion.

In comparison to inductive methods, S from electrical transport measurements can be measured more rapidly an can be easily expanded to the full angular range of the magnetic field orientation. In this way, the evolution of $S(T, H, \theta)$ has been studied in this work by comparing pristine and ss-nanocomposites films with different stacking faults scenarios.

The effect of double kink excitations has been identified by the observation of an $S(\theta)$-peak around H||ab and a concomitant S(T)-peak in the temperature dependence. The introduction of stacking faults and deformation of the CuO_2 planes impede the propagation of such thermal excitations, which would imply a strong increase of the creep rate.

The identification of double kinks in the H-T diagram allows to separate the dominance of intrinsic or stacking fault pinning according to the favouring and hindering tendency of each kind of pinning centre to form these excitations.

Such separation of intrinsic pinning and stacking fault pinning regimes has leaded to the recognition of three groups of nanocomposites with different stacking fault densities (low, intermediate and high) that provoked respectively weak, moderate and strong distortions of the planar microstructure originally dominated by intrinsic pinning in pristine films. The proliferation of double kinks has been precluded in the entire studied H-T diagram for those nanocomposites with largest density of stacking faults.

The application of the isotropic Blatter scaling approach to the angular analysis of the creep rate S has given as a result a new methodology to evaluate the anisotropy of vortex creep, allowing to separate S^{iso} and S^{aniso} contributions, similarly to the methodology already developed for J_c.

This methodology has enabled to evaluate the evolution of $S^{iso}(H)$ for each group of nanocomposites and has allowed to identify the extra anisotropic contributions $S^{aniso}(H)$ manifested by increments of creep provoked by correlated vortex thermal activation or decrements of creep caused by strong correlated vortex pinning. In general, nanocomposites reduce S and S^{iso} except at high temperatures and high magnetic fields.

CHAPTER 6

VORTEX PINNING CHALLENGES OF CSD NANOCOMPOSITES

In previous chapters, the main electrical properties of ss-nanocomposites have been analysed in relation with the microstructural information gathered by STEM and x-ray diffraction, in order to investigate the vortex pinning and vortex creep influence on the superconducting performance given by particular defect landscapes.

In this chapter, the vortex pinning analysis is extended to CSD YBCO nanocomposite films grown by a novel challenging approach: pn-nanocomposites, distinguished by the incorporation of preformed nanoparticles in the precursor solution.

Besides, the influence of the heating process has been also investigated for these particular nanocomposites. Apart from the conventional heating process, some pn-nanocomposites have been grown with a flash heating ramp that avoids coarsening of the nanoparticles.

Moreover, some pristine and pn-nanocomposites have been deposited through spin-coating multideposition or inkjet printing single-deposition, acquiring films up to ~ 1 μm thick.

Finally, the critical current properties of the different kind of films (pristine, ss-nanocomposites and pn-nanocomposites; thin and thick; from conventional or from flash heating processes) have been analysed for first time at very high magnetic fields up to 35 T, exploring the underlying vortex physics governing the electrical performance at the high magnetic field region aimed by magnet and power applications.

6.1 Thin and thick nanocomposites from preformed nanoparticles

As learned from the analysis in chapters 3, 4 and 5, the singular microstructure or defect landscape is crucial for the final electrical performance of the nanocomposite film.

However, the complex growth mechanisms involved in ss-nanocomposites, including kinetic and thermodynamic effects, complicate the quest of a method to precisely control the microstructure. In particular, the size and morphology of the embedded nanoparticles, as well as the secondary induced defects, are difficult to control, in detriment of accurate pinning engineering and satisfactory reproducibility.

For this reason, it is interesting to explore new growth methods where the microstructure control path can be designed. The use of colloidal solutions with preformed nanoparticles has appeared as an appealing alternative method where the key advantage is the tight control of the desired composition, size and concentration of the nanoparticles.

This is needed to optimize the balance between the superconducting current percolation and vortex pinning efficiency. However, the progress on this approach was still at an early stage before the beginning of this thesis[78,190,191].

Thanks to an interdisciplinary investigation within the framework of the Eurotapes project[56], nanocomposites with preformed nanoparticles of CeO_2, ZrO_2, HfO_2, $BaZrO_3$ and $BaHfO_3$, sometimes referred in this thesis as CeO, ZO, HO, BZO and BHO respectively, have been successfully grown, whose primary results have been currently published[66,78,79].

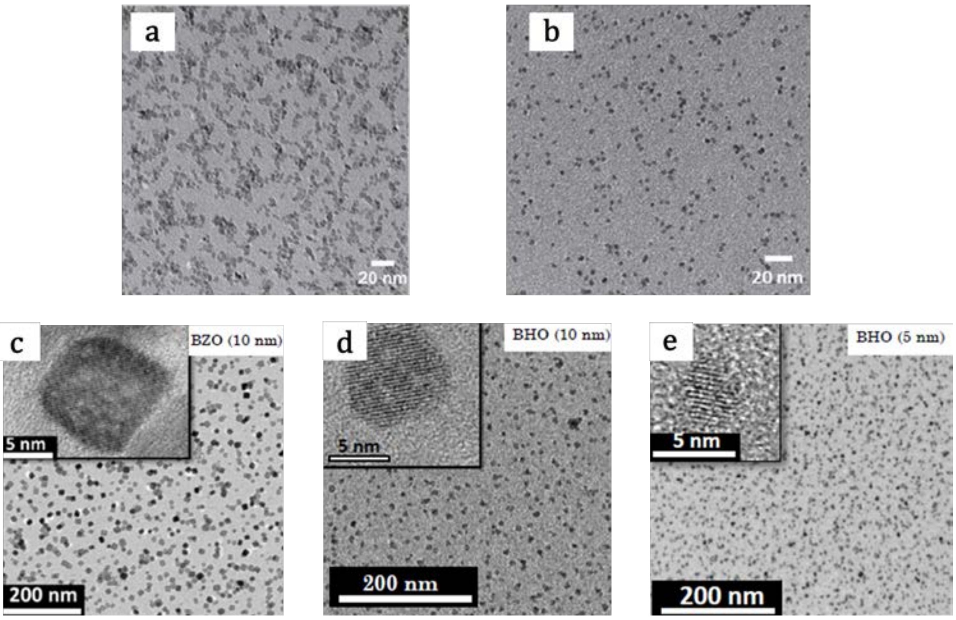

Figure 6.1: TEM images of the (a) ZrO_2 ($\sim 7-15$ nm), (b) CeO_2 ($\sim 2-3$ nm), (c) $BaZrO_3$ (~ 10 nm), (d) $BaHfO_3$ (~ 10 nm) and (e) $BaHfO_3$ (~ 5 nm) nanoparticles in colloidal solutions. Insets in (c-e) are high resolution TEM images of the corresponding individual nanoparticles.

The morphology and size of synthesized preformed nanoparticles in the colloidal solution can be observed in figure 6.1, that shows TEM images of nanoparticles from different compositions used for the growth of pn-nanocomposites whose electrical performance will be discussed in this chapter.

Figures 6.1(a-b) show ZrO_2 and CeO_2 spherical nanoparticles synthesized via microwave activation by a solvothermal synthesis process. ZrO_2 nanoparticles are monoclinic and have diameters of $\sim 7-15$ nm, whereas CeO_2 nanoparticles are cubic with diameters of $\sim 2-3$ nm[78].

Figures 6.1(c-e) show $BaZrO_3$ (square-like) and $BaHfO_3$ (spherical) nanoparticles synthesized via thermal activation by a solvothermal synthesis process achieving sizes of $\sim$ 5 nm or $\sim$ 10 nm[74], both with cubic perovskite crystal structure.

ZrO_2, CeO_2, HfO_2, $BaHfO_3$ and $BaZrO_3$ nanoparticles have been used for the successful growth of thin $\sim$ 150 nm pn-nanocomposite films deposited by single layer spin-coating. In addition, the $BaZrO_3$ nanoparticle composition has been used for the growth of thick ($\sim$ 1 μm) nanocomposite films by single layer inkjet-printing.

The crystal structure of nanoparticles was deduced from XRD measurements and the statistical average of the nanoparticle size in the colloidal solution was further confirmed by XRD and dynamic light scattering observations[78,79,192].

6.1.1 Microstructural phenomena and nanoparticle distribution

Depending on the nanoparticle composition, size and distribution, different phenomena occur during the growth process, yielding to diverse microstructural scenarios that have set important difficulties and challenges for the improvement of the use of colloidal solutions. This effects can be visualized either by XRD or STEM analysis: inhomogeneous distribution of the preformed nanoparticles, chemical reactivity of the nanoparticles with the YBCO precursors, coarsening of the nanoparticles during the high temperature annealing steps or aggregation of nanoparticles.

In the case of nanocomposites grown from CeO_2 nanoparticles, the presence of $BaCeO_3$ has been identified instead of CeO_2 by XRD $\theta - 2\theta$ scans[78] and by STEM images as in figure 6.2, confirming the reactivity between the BaF_2 precursor and CeO_2 during the growth process, already reported for CeO_2 cap layers[193].

CeO_2 nanocomposite films are highly epitaxial. However, when initial nanoparticles are small ($\sim 2 - 3$ nm), $BaCeO_3$ nanoparticles preserve the original size but get segregated at the YBCO film surface (see figure 6.2(a)). On the contrary, when the initial nanoparticles are bigger ($\sim$ 6 nm), they coarsen so that final $BaCeO_3$ nanoparticles are around 10-30 nm in size and remain trapped in the YBCO matrix (see figure 6.2(b)). Such different behaviours are well contrasted by the pushing/trapping phenomena described for solid-liquid interfaces[194,195], where the interaction of particles at the interface is influenced by various parameters such as the size of the particle, that is either pushed or trapped for small and big sizes respectively.

In the case of nanocomposites grown from ZrO_2 nanoparticles, a similar chemical reactivity has been detected[78,79], leading to modified secondary phases consisting of $BaZrO_3$ nanoparticles. In the nanocomposite shown in figure 6.3(a), the nanoparticle size has increased from initial 7 nm ZrO_2 nanoparticles up to final 12-25 nm $BaZrO_3$ nanoparticles. Metal oxides such as ZrO_2, HfO_2 or CeO_2 have a large tendency to react with Ba, giving rise to the perovskite structure $BaMO_3$ (M=Zr, Ce, Hf)[193,196–198]. Consequently, cation stoichiometry becomes slightly uncompensated and $Y_2Cu_2O_5$ and Y_2O_3 nanoparticles can be formed. In order to avoid this effect, Ba has been compensated with an extra amount in the initial solution.

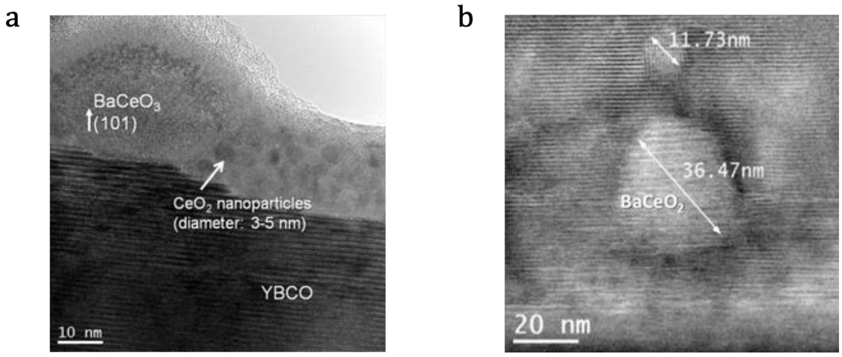

Figure 6.2: TEM images of nanocomposites grown with (a) 2 nm and (b) 6 nm initial CeO_2 nanoparticles. In (a), $BaCeO_3$ formation and CeO_2 pushed nanoparticles are detected in the surface of the film. In (b), trapped $BaCeO_3$ nanoparticles with random orientation are indicated.

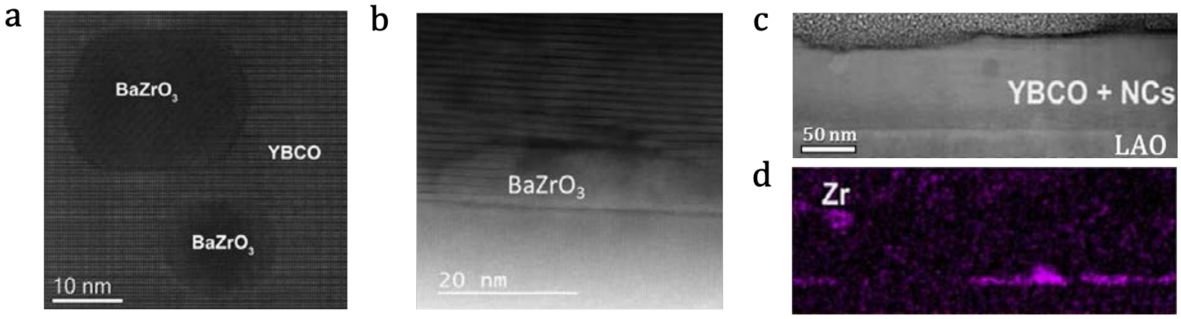

Figure 6.3: STEM Z-contrast images of (a) a 10 % ZrO_2 nanocomposite with coarsened $BaZrO_3$ nanoparticles and (b) a 16 % ZrO_2 nanocomposite with $BaZrO_3$ nanoparticles nucleating at the substrate interface. (c) Zr EDX map a 15 % ZrO_2 nanocomposite obtained after the pyrolysis treatment containing a pristine YBCO seed layer. (d) Z-contrast image (above) and Zr EDX map (below) after crystallization of a 10 % ZrO_2 nanocomposite containing a pristine YBCO seed layer.

Another problematic phenomenon that occurs when growing ZrO_2 pn-nanocomposites is the accumulation of nanoparticles that nucleate epitaxially at the LAO substrate interface[78,79] (see figures 6.3(b-d)), also observed in ss-nanocomposites[75]. High nanoparticle loadings led in many occasions to the nucleation of nanoparticles at the interface perturbing the texture quality of the films, since YBCO needs to nucleate on some $BaZrO_3$ at the substrate interface, favouring other crystallographic orientations different to c-axis.

However, the introduction of a pyrolysed YBCO ultrathin film as a seed layer allows to promote the homoepitaxial growth of the nanocomposite film and preserve a high quality film texture even when the percentage of plane YBCO interface is reduced at high concentration of preformed nanoparticles[66,78,79,199].

In order to obtain high quality pn-nanocomposites, it has been mandatory to find a way to avoid chemical reactivity and nanoparticle agglomeration, which do not allow to keep a tight control on the final stoichiometry and nanostructure of the film. For this reason, it has been a very important achievement the successful preparation, for first time, of stable and small non-reactive $BaZrO_3$ and $BaHfO_3$ preformed perovskite nanoparticles[66,199].

These nanoparticles already led to extraordinary results synthesized as spontaneous segregated nanoparticles in ss-nanocomposites[126,200,201]. For the growth of $BaZrO_3$ and $BaHfO_3$ nanocomposite layers, the pyrolysed YBCO ultrathin film seed layer with a minimum thickness of 25 nm has been used to ensure a good epitaxy, necessary to ensure c-axis YBCO oriented growth for nanoparticle loads larger than 12 %M[199].

Figure 6.4 shows J_c^{sf} (SQUID) at 5 K and 77 K as a function of the nanoparticle concentration for $BaZrO_3$ ss-nanocomposite and pn-nanocomposite films (of $\sim$ 10 nm nanoparticles). It is observed that the colloidal solution approach allows to preserve desirable superconducting performances at larger nanoparticle concentrations. 20% $BaZrO_3$ has been identified as the maximum concentration of nanoparticles which keeps a large percolating critical current density, then J_c^{sf} starts to decrease in agreement with observed out-of-plane texture degradation[74]. This result can be very likely shifted to larger molar concentrations if smaller particles were used.

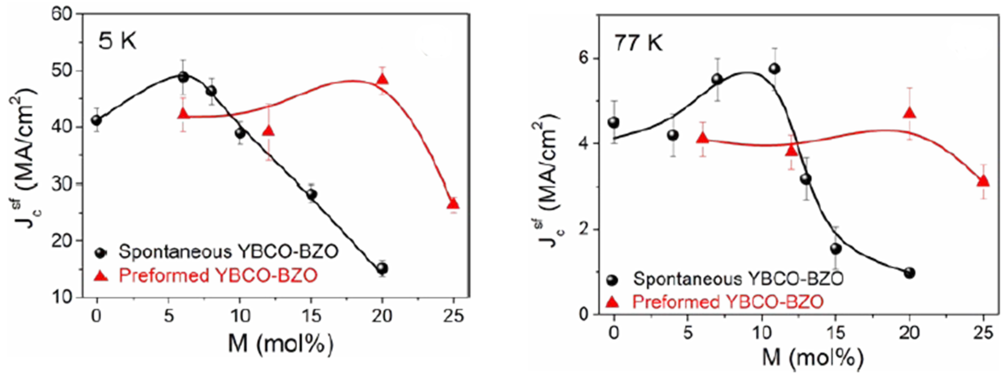

Figure 6.4: J_c^{sf} (SQUID) as a function of the molar concentration for BZO ss-nanocomposite and pn-nanocomposite films at (a) 5 K and (b) 77 K.

Different composition and nanoparticle sizes have been used for the growth of preformed 20% $BaZrO_3$ and 20% $BaHfO_3$ nanocomposites on top of 50 nm seed layers, shown in Z-contrast images in figures 6.5(a-c). In all cases, the seed layer contains a high density of long stacking faults and nanoparticles are homogeneously distributed throughout the nanocomposite layer. Stacking faults are mainly located near the surface of the film for the 20% $BaZrO_3$ nanocomposite. In contrast, a large concentration of stacking faults is located throughout the full thickness in the case of 20% $BaHfO_3$ nanocomposites, being slightly shorter for the smaller nanoparticles.

The nanoparticles observed in figures 6.5(d-e) display an square-like shape for BZO nanoparticles and an spherical shape for BHO nanoparticles, confirming that the initial shape observed in the colloidal solution (see figures 6.1(c,e)) is preserved and the nanoparticle size is subjected to a limited increase from 10 nm to 20 nm. In the case of 5 nm BHO nanoparticles, there is also a minimal coarsening driving to a final mean size of 10 nm (see figure 6.5(f)).

It has been shown from SQUID inductive measurements, that smaller nanoparticles lead to larger μ_0H^* values and therefore are beneficial for the increase of the pinning efficiency at applied magnetic fields[74,199].

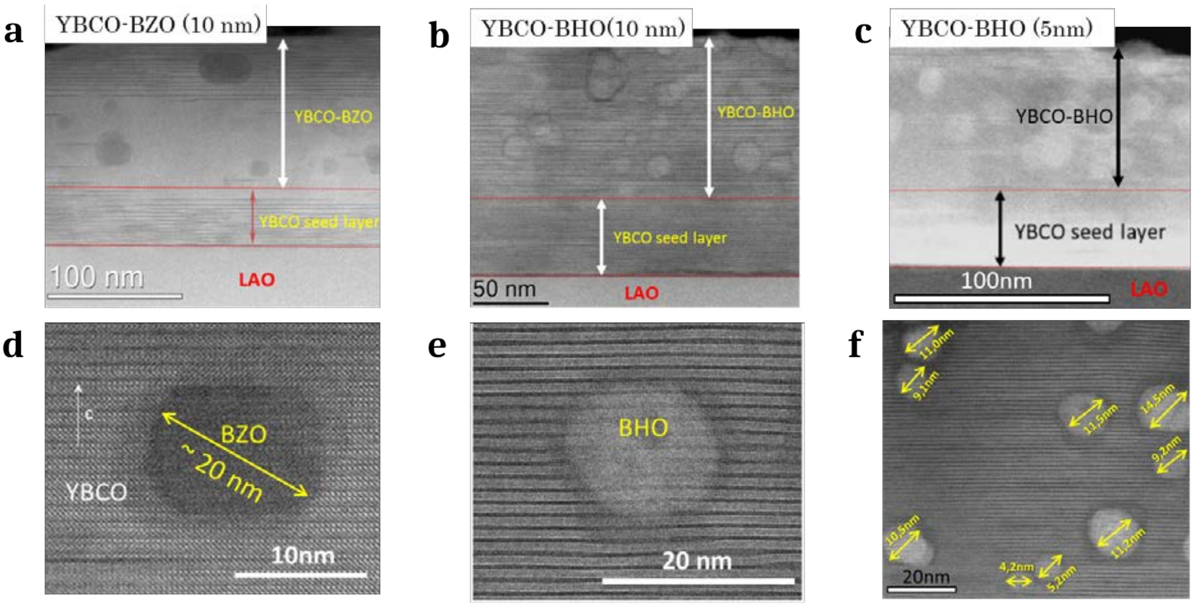

Figure 6.5: STEM Z-contrast images of pn-nanocomposites grown from (a,d) 20 % $BaZrO_3$ (10 nm), (b,e) 20 % $BaHfO_3$ (10 nm) and (c,f) 20 % $BaHfO_3$ (5 nm) preformed nanoparticles on top of 50 nm YBCO seed layers.

In order to additionally tune the Y124 intergrowths scenario, complementary investigation has been accomplished in BHO pn-nanocomposites that have been grown with the flash heating process described in section 2.1.4. The flash heating thermal process increases the nucleation rate, which leads to a higher amount of stacking faults in comparison with conventional thermal process, presumably generated in the contact between grains to relieve energy[132].

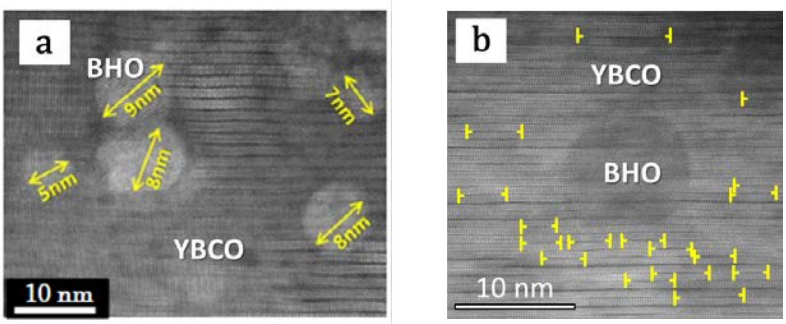

Figure 6.6: high resolution STEM Z-contrast images of a nanocomposite with 20 % $BaHfO_3$ (5 nm) grown under the flash heating process showing (a) several nanoparticles where the size is indicated and (b) an isolated nanoparticle surrounded by short stacking faults (indicated by yellow arrows).

Figure 6.6 shows Z-contrast images of a 20 % $BaHfO_3$ pn-nanocomposite films grown under the flash heating process. Figure 6.6(a) reveals that the nanoparticle diameter after the YBCO growth ($\sim$ 7 nm) almost coincides with the diameter of the initial 20 % $BaHfO_3$ nanoparticles in the colloidal solution ($\sim$ 5 nm, see figure 6.1(e)). This result indicates that the coarsening effect of nanoparticles has been minimized by the application of the flash heating process.

The relative volume of spherical nanoparticles in the nanocomposite film ρ_{NP} is equal to the volume density of nanoparticles $\mathrm{n_R}$ with an average radius R multiplied by the volume of the nanoparticle:

$$\rho_{NP} = n_R \frac{4}{3} \pi R^3 \tag{6.1}$$

For the same molar concentration and thickness, the partial volume of nanoparticles is the same. In this case, the density of nanoparticles is 3 times larger for nanoparticles with an average diameter of 7 nm than for the others with 10 nm ($\mathrm{n}_{3.5} = \frac{5^3}{3.5^2}\mathrm{n}_5 \approx 3\mathrm{n}_5$).

Furthermore, it is observed in figure 6.6(b) that the stacking faults surrounding the nanoparticles show a much shorter length in comparison with the previously commented pn-nanocomposites grown under a conventional thermal process illustrated in figure 6.5. As discussed in chapter 3, the amount of nanostrain generated at the partial dislocations surrounding the stacking faults can be calculated by means of the relative volume of partial dislocations ρ_{dis}, which given the case of identical number of stacking faults, it is larger in the case that stacking faults are shorter (see appendix B). Therefore, the flash heating process in nanocomposites offers several advantages: faster processing, preserves small nanoparticle size and generates larger relative volume of partial dislocations.

6.1.2 Magnetic field dependence of $\mathrm{J_c}$ for nanocomposite thin films from preformed nanoparticles

Several pn-nanocomposites described in the previous section have been electrically characterized with magnetic field dependent transport measurements in order to evaluate their pinning performance, whose nanostrain and main electrical transport properties are shown in table 6.1.

The pn-nanocomposites here presented show high current performance, with values of $\mathrm{J_c^{sf,77K}}$ ranging $\sim 1-5$ MA/cm^2, which are similar to the results obtained for ss-nanocomposites. $\mathrm{T_c}$ values are in the range of $\sim 88.5 - 92$ K, which means that optimal doping is obtained, although some specific nanocomposites show slight $\mathrm{T_c}$ decrease and many of them a broad $\Delta\mathrm{T_c}$, which can be related to the microstructural phenomena described in the previous section. In particular, the nanocomposite 8CeO that presented nanoparticle accumulation at the film surface (see figure 6.2(a)) shows the broadest $\Delta\mathrm{T_c}$.

Figure 6.7 shows the magnetic field dependence for H||c of $\mathrm{J_c}$ and $\mathrm{J_c/J_c^{sf}}$ for these samples at 77 K. In figure 6.7(a), similarly to ss-nanocomposites, pn-nanocomposites except 8CeO surpass the critical current densities of the pristine film at low and intermediate magnetic fields, up to a crossing characterised by the fast decay of $\mathrm{J_c}$ when approaching $\mathrm{H_{irr}}$.

13ZO shows the best dependence with applied magnetic field at 77 K, as observed in figure 6.7(b). The largest $\mu_0\mathrm{H}^* \sim 70$ mT is identified for 13ZO and 20BHO-FH, whereas 8CeO barely enlarges 1 mT with respect to the pristine one ($\mu_0\mathrm{H}^* \sim 15$ mT), presenting the same strong decay at high fields as other nanocomposites.

NAME	COMPOSITION	T_c (K)	ΔT_c (K)	$J_c^{sf,77K}$ (MA/cm^2)	ε (%)
8CeO	$YBa_2Cu_3O_{7-\delta}$+ 8%M CeO_2 (∼2 nm)	90.9	9.3	2.0	0.18
13ZO	$YBa_2Cu_3O_{7-\delta}$+ 13%M ZrO_2 (∼10 nm)	91.8	5.1	1.2	0.26
16ZO	$YBa_2Cu_3O_{7-\delta}$+ 16%M ZrO_3 (∼10 nm)	90.7	2.3	4.6	0.23
12BZO	$YBa_2Cu_3O_{7-\delta}$+ 12%M $BaZrO_3$ (∼10 nm)	91.9	7.8	2.1	0.21
12BHO	$YBa_2Cu_3O_{7-\delta}$+ 12%M $BaHfO_3$ (∼10 nm)	90.9	3.6	4.0	0.20
20BHO-FH*	$YBa_2Cu_3O_{7-\delta}$+ 20%M $BaHfO_3$ (∼5 nm)	88.6	5.7	3.0	0.24

Table 6.1: pn-nanocomposites. Main electrical properties and nanostrain for pn-nanocomposite thin films. The name of pn-nanocomposites is preceded by PN when needed for comparison. In composition, the molar concentration and the nanoparticle size in the initial colloidal solution is indicated. *: FH stands for flash heating.

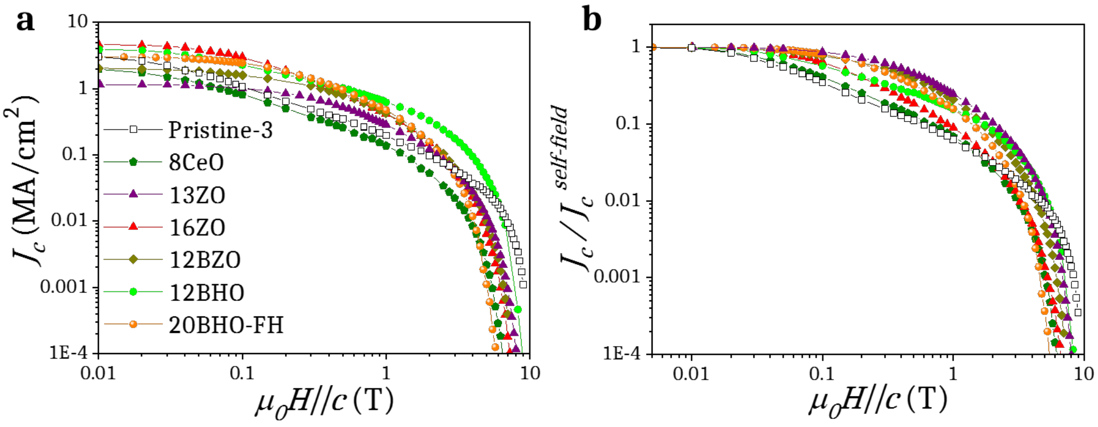

Figure 6.7: magnetic field dependence of (a) J_c and (b) normalized J_c/J_c^{sf} for pristine and pn-nanocomposite thin films at 77 K for H||c.

$\mu_0 H^*$ is analysed as a function of temperature for several pn-nanocomposites in figure 6.8. For H||c, 13ZO and 20BHO-FH exhibit the largest $\mu_0 H^*$. For H||ab, 13ZO shows again the largest $\mu_0 H^*$ whereas 20BHO-FH was not measured for this orientation.

The increase of $\mu_0 H^*$ has been attributed in chapter 3 mainly to the isotropic contribution coming from a higher density of partial dislocations explained by the presence of large amount of short stacking faults. This interpretation is in agreement with the microstructure observed in these pn-nanocomposites.

In the case of 13ZO, the formation of BZO nanoparticles after reaction, has generated in many cases the formation of highly strained BZO/YBCO interfaces and short stacking faults[79]. In the case of 20BHO-FH, a large quantity of short stacking faults emerge

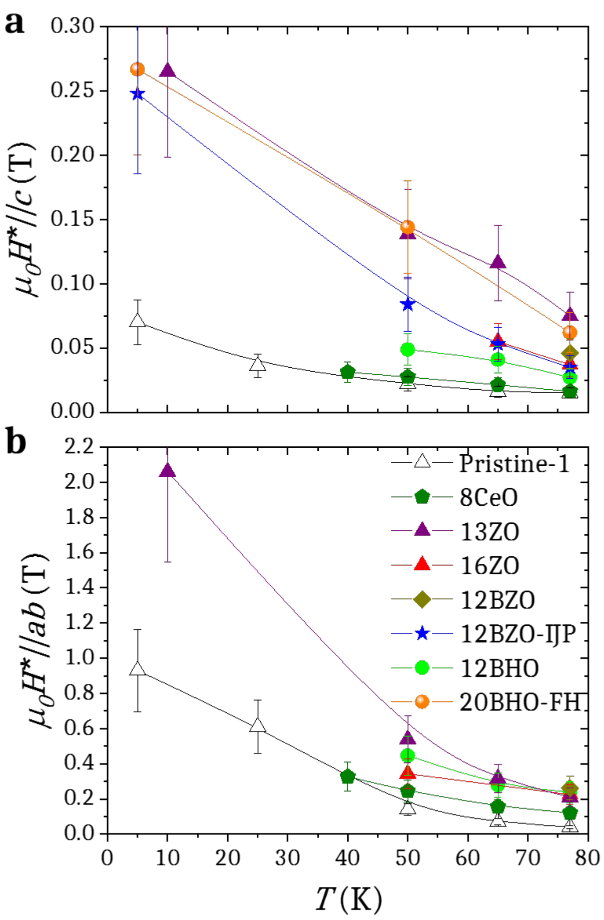

Figure 6.8: temperature dependence of μ_0H* for (a) H||c and (b) H||ab for pristine and pn-nanocomposites.

at the surroundings of the small nanoparticles, as observed in figure 6.6(b)[199]. The second approach permits to obtain a better control of the stacking fault formation and larger superconducting cross section for the current flow thanks to the small radius of nanoparticles.

In contrast, BHO and BZO pn-nanocomposites grown with a conventional thermal process enhance μ_0H* up to intermediate values in comparison with the discussed samples. The microstructures observed in figure 6.5 exhibit a large quantity of stacking faults, but the majority of them are very long, so that the generation of partial dislocations is not adequately promoted.

Isothermal J$_c$(H||c) curves are shown in figure 6.9(a) for a pristine film, the most outstanding ss-nanocomposite (the mixed 10BZO-5YO) and two BHO pn-nanocomposites (grown with conventional and flash heating thermal processes) at 77 K, 50 K and 5 K. Pn-nanocomposites exhibit very similar critical current densities to the ones from the mixed ss-nanocomposite and surpass those ones from the pristine sample up to 9 T below 50 K. The J$_c$(H, T, θ) 3D surface of the pn-nanocomposite 20BHO-FH has been calculated from the temperature fit of the J$_c$(H) curves in figure 6.9(a) following the procedure developed in appendix A. The result is shown in figure 6.9(b), which resembles very well the shape of the ss-nanocomposite surface in figure 3.13(e).

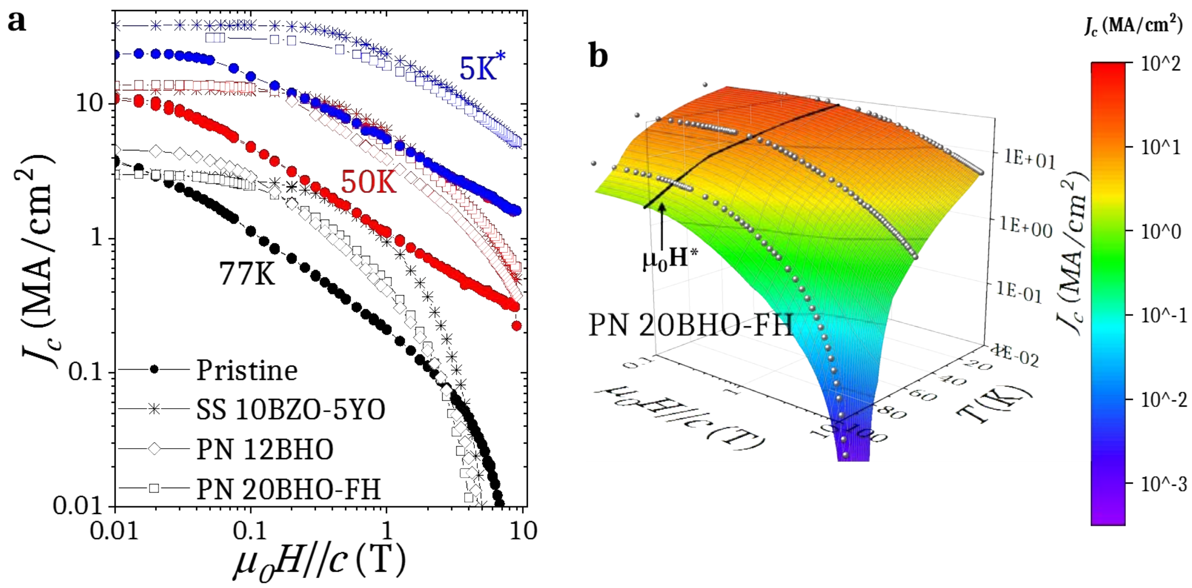

Figure 6.9: (a) magnetic field dependence of J_c for H||c at temperatures of 77, 50, and 5 K (*:10 K for SS 10BZO-5YO) for Pristine-1, SS 10BZO-5YO, PN 12BHO and PN 20BHO FH. (b) 3D $J_c(H, T)$ surface for PN 20BHO FH for H||c.

Also the angular dependence and the isotropic collapse for pn-nanocomposites is very similar to ss-nanocomposites. For example, $J_c(\theta)$ at 77 K is plotted in figure 6.10 for PN 12BHO.

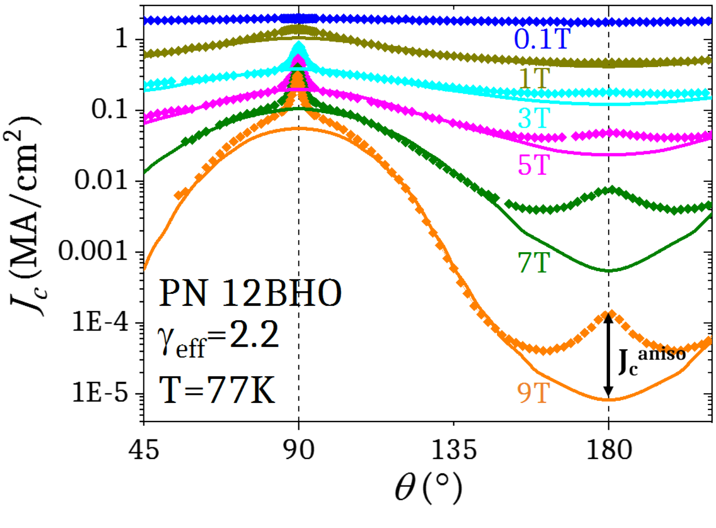

Figure 6.10: $J_c(\theta)$ dependence at 77 K for PN 12BHO at 0.1-9 T. Solid lines correspond to the isotropic contribution $J_c^{iso}(\theta)$ with $\gamma_{eff} = 2.2$. Double-headed arrow indicates the $J_c^{aniso}(9T, H||c, 77K)$ contribution.

There is a widening of the ab-peak and a lowering of the c-peak in comparison with the pristine in figure 3.17(a), related to the commented changes in stacking faults and twin boundaries, although less noticeable than for the ss-nanocomposite in figure 3.17(b). In particular, the alteration in the twin boundary coherence is small for PN 12BHO for H||c, with $J_c^{aniso}(9T, H||c, 77K) = 1.2 \cdot 10^{-4}$ MA/cm^2, larger than for the ss-nanocomposite ($1.0 \cdot 10^{-5}$ MA/cm^2) and closer to the value of the pristine sample

($4.5 \cdot 10^{-4}$ MA/cm^2).

The γ_{eff} range, measured for the different pn-nanocomposite films, spans from 2.2 to 3.2, the same γ_{eff} region obtained for ss-nanocomposites in figure 3.22(a).

6.1.3 Thick films from multilayered spin-coating and inkjet printing

Multideposited spin-coating and inkjet printing are two methods that have been investigated with the aim to explore the possibilities to carry high currents in CSD films by increasing the film thickness ($I_c = J_c \cdot t$). Inkjet printing has the special interest that the process is scalable and can be technically incorporated in manufacturing plants.

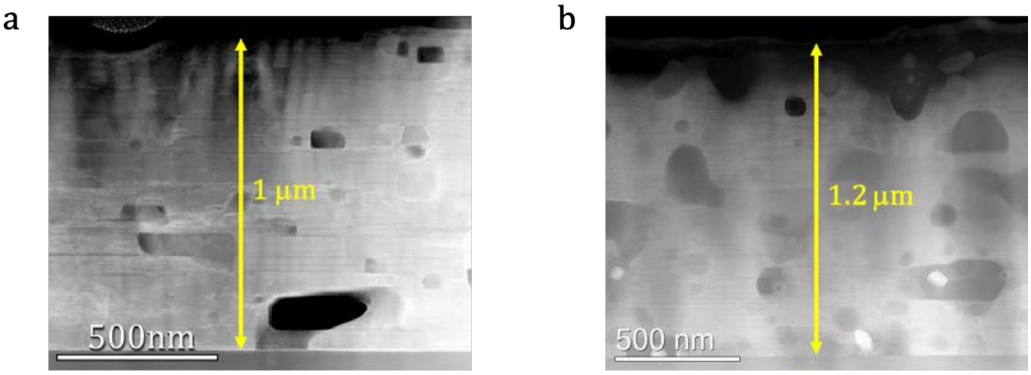

Figure 6.11: Z-contrast STEM images of (a) a 1 μm multilayered spin-coated and (b) a 1.2 μm inkjet printed pristine thick films.

Pristine thick films were successfully grown with both approaches up to a thickness of ~ 1.2 μm maintaining a good epitaxy from the substrate to the surface. Z-contrast images are shown in figure 6.11 displaying a good texture quality, even though secondary phases and pores are still present in the films for both cases.

The electrical superconducting properties T_c and $J_c^{sf,77K}$ measured for several pristine samples of different thickness from the group at ICMAB are plotted in figure 6.12 as a function of the film thickness t for single layer spin-coating, multilayered spin-coating and single layer inkjet printing deposited samples.

Whereas T_c shows a constant value beyond 150 nm, $J_c^{sf,77K}$ decays with increasing thickness after 100 nm. This decay is not ascribed to any thickness dependent universal law[100], but may be attributed to detrimental microstructural defects as precipitates and pores observed in the STEM images in figure 6.11. Recent results in advanced multilayered YBCO films grown on top of $Ce_{0.9}Zr_{0.1}O_2$ buffered yttria-stabilized zirconia substrates show inductive J_c results that would shift the dependence line to larger J_c^{sf} values (~ 4 MA/cm^2) for a large thickness of ~ 1 μm[72], suggesting an improved quality of the microstructure.

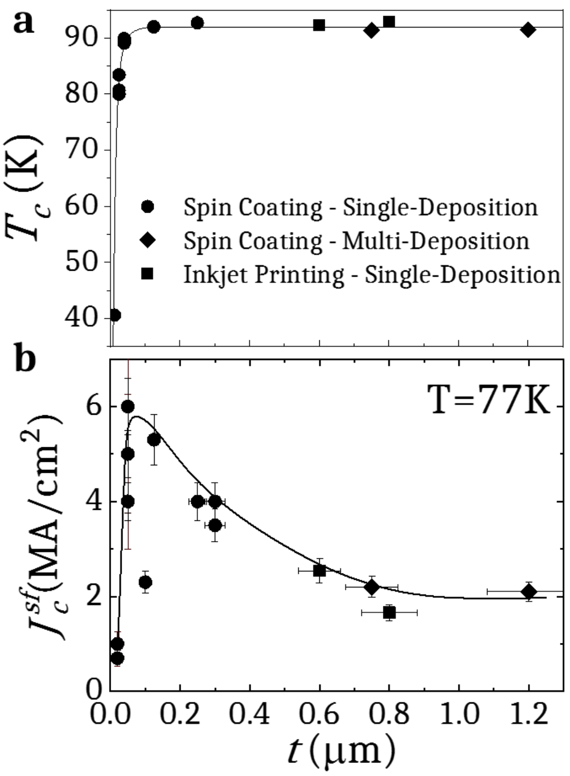

Figure 6.12: (a) T_c and (b) $J_c^{sf,77K}$ as a function of thickness for multiple samples measured historically at ICMAB's group. Solid lines are guides to the eye.

6.1.3.1 Inkjet printed nanocomposite films from preformed nanoparticles

Both processes presented here to obtain thicker YBCO films (multideposited spin-coating and inkjet printing) are essentially valid to prepare CSD nanocomposite films in order to enhance the critical current performance at high magnetic fields. Here, results on 12% and 20% BZO pn-nanocomposite inkjet printing thick films are presented. The microstructure of both nanoparticle concentrations can be observed in the STEM LAADF and HAADF images in figure 6.13.

Nanoparticles are randomly oriented and homogeneously distributed in both films, causing a rich stacking fault landscape that exhibits abundant highly strained regions, identified with whitish colour in the LAADF images (figures 6.13(a,c)). Nanoparticle sizes fall in the range of 10-20 nm (see figures 6.13(b,d)), indicating minimal coarsening with respect to initial nanoparticles, as equally observed in thin BZO pn-nanocomposite films in figures 6.5(a-b).

Although some nanoparticles start to agglomerate in the case of the 20% BZO pn-nanocomposite, seen in the image below in figure 6.13(d), this nanocomposite still shows better properties than 12% BZO indicating that these agglomerations are not drastic and that the density of effective pinning defects is larger.

The electrical transport superconducting properties of the main thick film samples studied in this thesis (pristine and pn-nanocomposites) are summarized in table 6.2. It is worth mentioning the outstanding T_c and ΔT_c values. The 12BZO-IJP and Pristine-MD-2

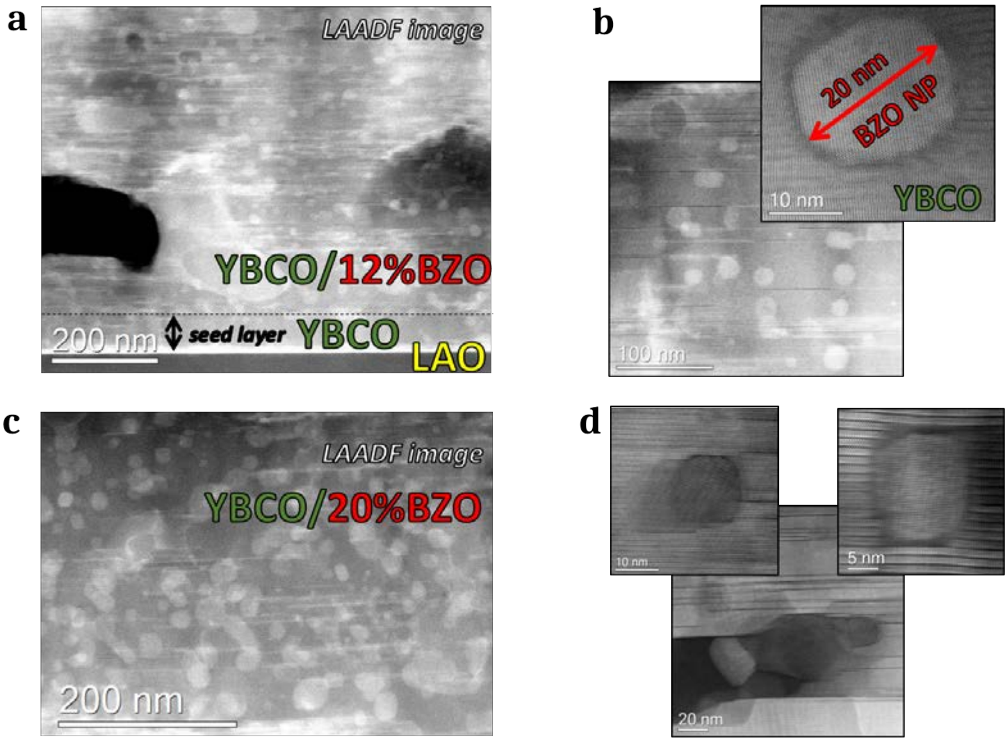

Figure 6.13: STEM images of BZO pn-nanocomposite thick films deposited by inkjet printing. (a) LAADF and (b) LAADF/HAADF images of the 12%BZO 850 nm thick nanocomposite. (c) LAADF and (d) HAADF images of the 20%BZO 700 nm thick nanocomposite.

samples exhibit respectively the largest T_c and narrowest ΔT_c from the samples measured in this thesis.

NAME	COMPOSITION	t (nm)	T_c (K)	ΔT_c (K)	$J_c^{sf,77K}$ (MA/cm^2)	ε (%)
Pristine-MD-1*	$YBa_2Cu_3O_{7-\delta}$	750	92.6	2.5	2.0	-
Pristine-MD-2*	$YBa_2Cu_3O_{7-\delta}$	1200	91.6	0.4	2.1	-
Pristine-IJP$^+$	$YBa_2Cu_3O_{7-\delta}$	600	91.4	2.4	~2	-
12BZO-IJP$^+$	$YBa_2Cu_3O_{7-\delta}$+ 12%$BaZrO_3$	850	92.9	2.0	2.7	0.21
20BZO-IJP$^+$	$YBa_2Cu_3O_{7-\delta}$+ 20%$BaZrO_3$	700	92.5	2.7	3.4	0.26

Table 6.2: thick Films. Main electrical properties and nanostrain for pristine and pn-nanocomposite thick films. *: MD stands for multideposition. $^+$: IJP stands for inkjet printing.

$J_c^{sf,77K}$ is larger for thick pn-nanocomposites than for pristine thick films. Despite the minimal coarsening and the slight agglomeration of nanoparticles, the critical current densities obtained in these thick nanocomposites are excellent. The magnetic field dependent J_c at 77 K for H||c is plotted in figure 6.14 in comparison with pristine thin and thick films.

As observed in figure 6.14(a), in contrast to the pristine inkjet printed thick film, BZO pn-nanocomposites surpass the J_c values for the pristine thin film along the entire studied magnetic field range (0.01-9 T).

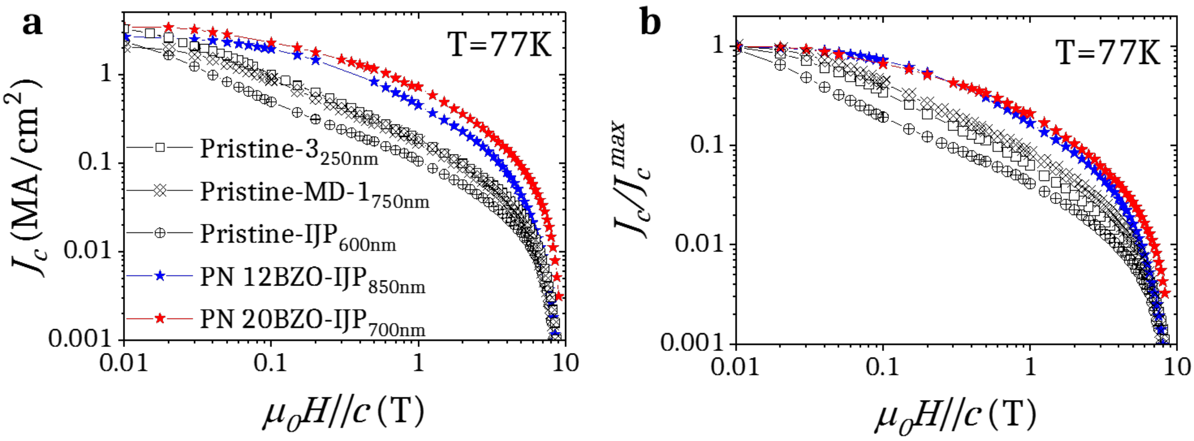

Figure 6.14: magnetic field dependence of (a) J_c and (b) normalized J_c/J_c^{sf} for a pristine thin and thick films and pn-nanocomposite thick films at 77K for H||c.

Interestingly, these nanocomposites offer at 77 K as good performance as pristine films in the vicinity of the irreversibility line at high fields both in absolute J_c and normalized J_c/J_c^{sf}, observed in figure 6.14(b). In particular, 20BZO-IJP outstands by displaying the largest J_c values at 9 T and 77 K for the CSD YBCO nanocomposites analysed until now, meaning that the loss of the twin boundary coherence is avoided and/or compensated by an alternative source of pinning.

In order to deepen the understanding of this issue, $H_{irr}(T/T_c)$ is plotted in figure 6.15(a) for the BZO thick pn-nanocomposites in comparison with thin and thick pristine films and a thin pn-nanocomposite with largest $H_{irr}(T)$ in each case. BZO thick pn-nanocomposites show clearly larger irreversibility lines than thin pn-nanocomposites, even slightly larger than the pristine thin film in the case of 20BZO-IJP.

The angular dependence of J_c is plotted for 20BZO-IJP in figure 6.15(b), where typical stacking-fault-related widened ab-peaks are observed. The c-peak is however very prominent, and the quantification of $J_c^{aniso}(9T, H||c, 77K)$ yields $2.4 \cdot 10^{-3}$MA/cm^2, larger than the one for the pristine thin film of figure 3.17. Furthermore, the isotropic contribution $J_c^{iso}(9T, H||c, 77K)$ is of the order of 10^{-4}MA/cm^2, much larger than the ones observed for nanocomposite thin films in figures 3.17 and 6.10 ($10^{-7} - 10^{-6}$MA/cm^2). Altogether contribute to the gain of a final $J_c(9T, H||c, 77K) = 2.8 \cdot 10^{-3}$ MA/cm^2.

As it has been discussed in chapter 4, the anisotropic-strong contribution at 0 K for H||c (ascribed to the density of twin boundaries) is larger in nanocomposites than in pristine samples, but on the other side the pinning is less effective at high temperatures due to the coherence loss that provokes a decrease of $T^*_{aniso-str}$.

As a matter of fact, the recovery of the H_{irr} can be given by a larger increase of the density of twin boundaries or by the recovery of a long coherence length of these defects. Section 6.2.2 takes up this discussion when studying the temperature dependence of one

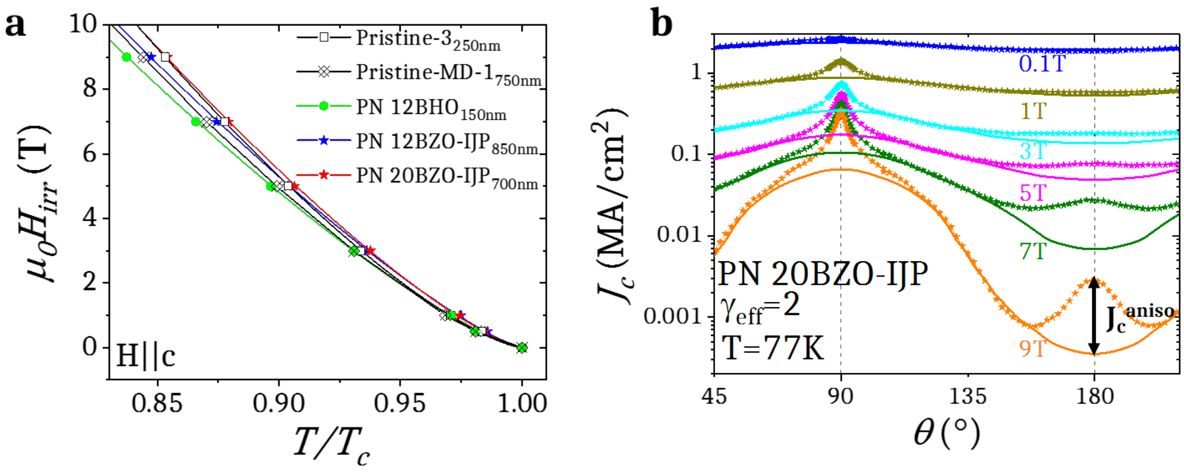

Figure 6.15: (a) reduced temperature dependence of the irreversibility line $H_{irr}(T/T_c)$ for Pristine-3 and 12BHO, 12BZO-IJP and 20BZO-IJP pn-nanocomposites for H||c. (b) $J_c(\theta)$ dependence at 77 K for 20BZO-IJP at 0.1-9 T. Solid lines correspond to the isotropic contribution $J_c^{iso}(\theta)$ with $\gamma_{eff} = 2$. Double-headed arrow indicates the $J_c^{aniso}(9T, H||c, 77K)$ contribution.

of these thick pn-nanocomposites at very high magnetic fields. In any case, it means that there is still room for H_{irr} enhancement by the increase of thickness and the modification of the arrangement of twin boundaries.

6.1.3.2 Boost of the absolute critical current I_c

The total critical current capable to flow through the superconducting film of thickness t defined as $I_c = J_c \cdot t$ is one of the most relevant parameters for the evaluation of the performance of a coated conductor, usually measured as A/cm − width, the amperes that can flow in a 1 cm wide conductor[53,56,72].

In order to summarize the electrical performance of BZO thick pn-nanocomposites, their magnetic field dependence of I_c for H||c at 77 K and 5 K is plotted in figure 6.16(a) in comparison with other pristine films with different thickness and deposition techniques.

This plot highlights the benefit of combining large thickness and incorporation of preformed nanoparticles. Thick pn-nanocomposites show the largest I_c values above 0.1 T and up to 9 T at 77 K. At 5 K, 20BZO-IJP shows the highest performance, capable to transport 1650 A/cm-width at self-field and 200 A/cm-width at 9 T, demonstrating the feasibility of using CSD nanocomposite films for high current applications, close to the best performances achieved so far in vacuum-deposited films with similar thickness[202–205].

I_c is plotted versus thickness for the same samples at the particular conditions of [77K,0.01T], [77K,1T] and [5K,9T] in figure 6.16(b). At high temperatures and low magnetic fields (typical conditions for cable applications), it has been possible to enhance 5 times the I_c of the pristine thin film by the use of pristine thick films. At larger magnetic fields (typical conditions for transformers and fault current limiters applications), thick nanocomposites are more effective, obtaining 17 times larger I_c than the pristine thin

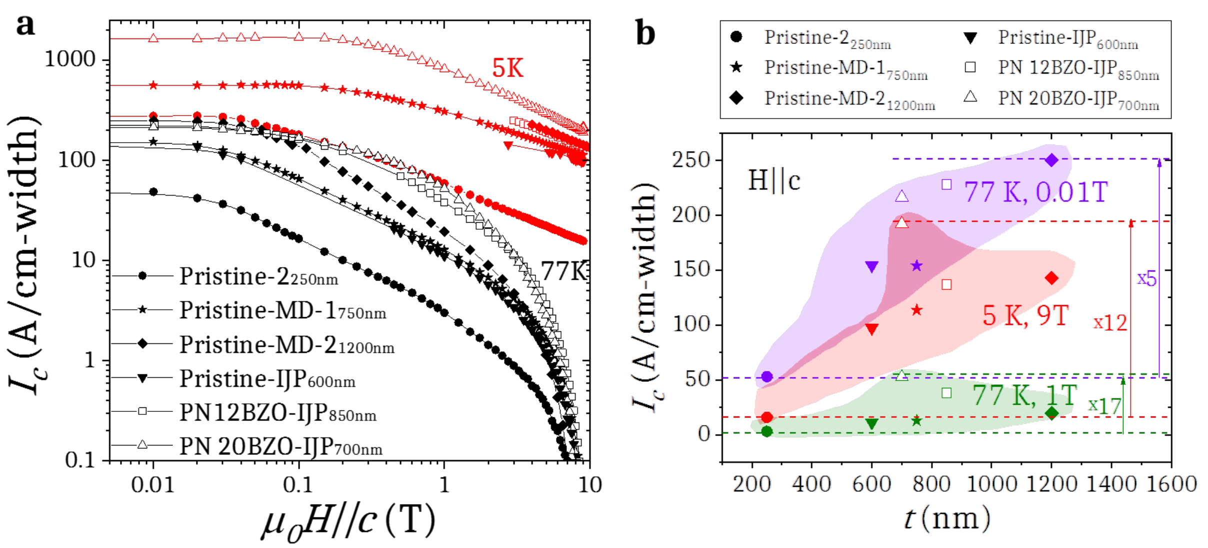

Figure 6.16: (a) magnetic field dependence of I_c for H||c at 77 K and 5 K for pristine and BZO pn-nanocomposites with different thickness and deposition techniques and (b) I_c as a function of thickness at the conditions of [77K,0.01T], [77K,1T] and [5K,9T] for H||c.

film. Finally, at low temperatures and high magnetic fields (typical for nuclear magnetic resonance and magnet applications), the I_c of the pristine thin film is multiplied by 12 with the use of the 20BZO-IJP nanocomposite.

6.1.4 Nanostrain and isotropic pinning in nanocomposites from preformed nanoparticles

The $H^*(\epsilon)$ and $H^*(\theta_T)$ relations obtained for ss-nanocomposites in sections 3.3.3 and 3.4.1 are proved in this section to evaluate if they can be extended to pn-nanocomposites, which would indicate that isotropic pinning is governed by the stacking fault induced nanostrained regions. Similarly, the analysis of pinning contributions and energy scales carried out in sections 4.3 and 4.4 is broadened to the study of a pn-nanocomposite at the end of this section.

$\mu_0 H^*$ is plotted versus nanostrain in figure 6.17 at 77 K, 50 K and 5 K for both H||c and H||ab, extending the analysis performed in figure 3.23. In general, the results obtained for pn-nanocomposites nicely overlap with the $\mu_0 H^*(\varepsilon)$ relations envisaged for ss-nanocomposites, implying that the empiric evidence of exponential trends gets more consistent and at the same time confirming that nanostrain governs the enlargement of the single vortex pinning regime in pn-nanocomposites.

The angular dependence of J_c and J_c^{iso} normalized by the J_c value for H||ab is plotted in figure 6.18 for several pn- and ss-nanocomposites and a pristine film at [77K,1T] and [65K,9T]. The corresponding isotropic contributions were obtained following the procedure described in section 3.3.1.

This plot illustrates that nanocomposites offer larger $J_c/J_c(90°)$ all through the angular range thanks to the boost of the isotropic contribution.

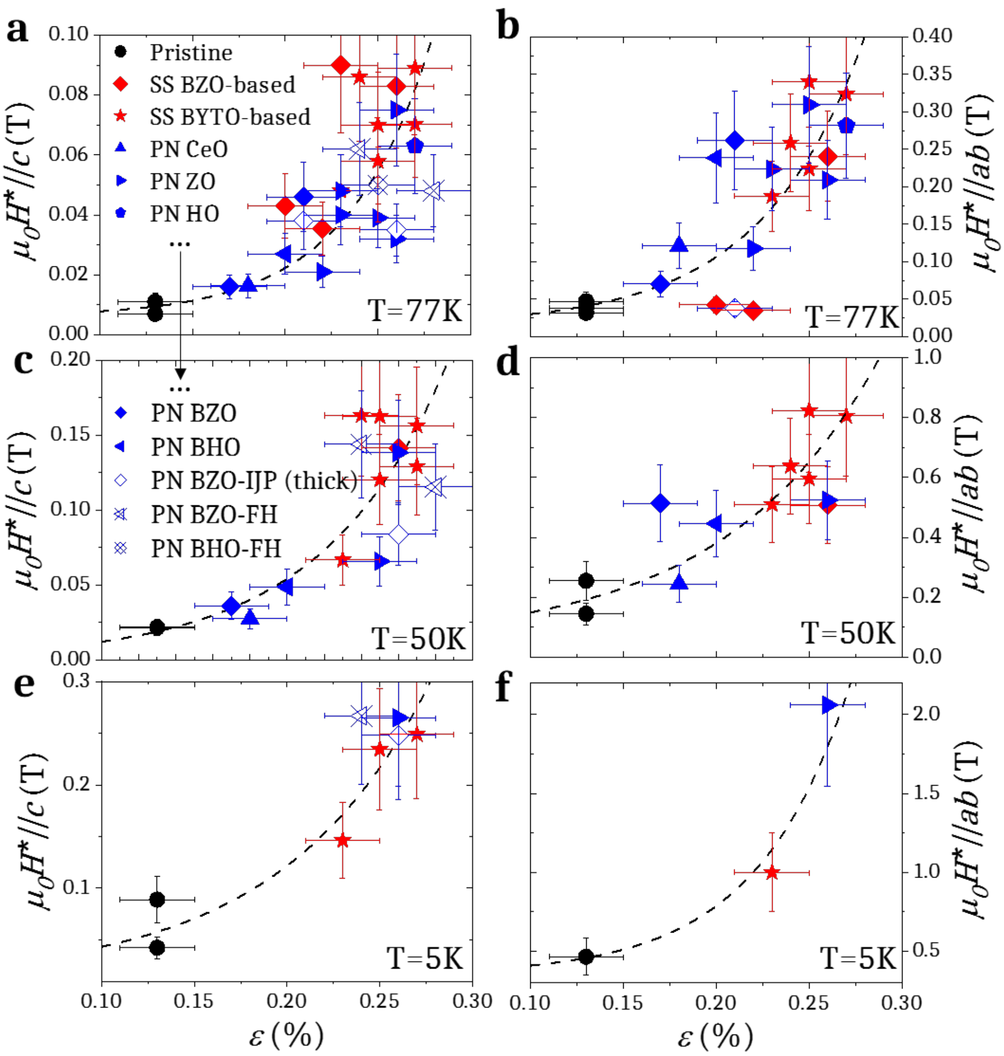

Figure 6.17: μ_0H* at (a-b) 77 K, (c-d) 50 K and (e-f) 5 K versus ε for pristine (black), ss-nanocomposites (red) and pn-nanocomposites (blue) for H||c (left) and H||ab (right). Exponential dashed curves are guides to the eye.

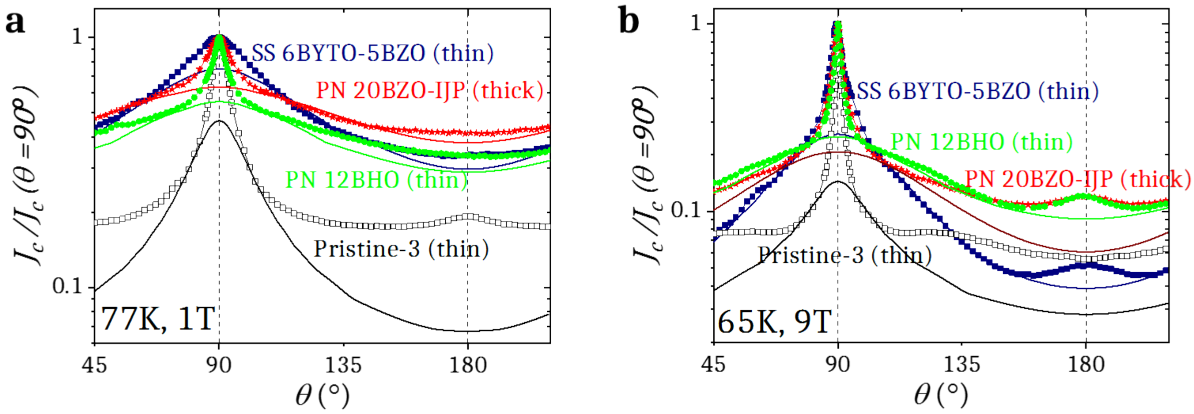

Figure 6.18: angular dependence of $J_c/J_c(90°)$ for Pristine-3, SS 6BYTO-5BZO, PN 12BHO and PN 20BZO-IJP at (a) 77 K, 1 T and (b) 65 K, 9 T. Solid lines correspond to the angular dependence of the isotropic contribution $J_c^{iso}/J_c(90°)$.

The ss-nanocomposite exhibits a wider $J_c(\theta)$ ab-peak, which implies larger $J_c/J_c(90°)$ values at the vicinity of H||ab, especially at [77K,1T]. However, the pinning performance near H||c is substantially reduced provoking smaller values than for the pristine at [65K,9T]. In contrast, pn-nanocomposites manage to combine both $J_c(\theta)$ peak widening and efficient c-axis pinning strength, yielding to the best angular results near H||c. The thin pn-nanocomposite reaches this good performance for H||c as a result of an improved isotropic pinning contribution, whereas the thick pn-nanocomposite does it by virtue of the combination of isotropic and anisotropic pinning contributions, as commented in the previous section.

From the analysis of the angular behaviour of J_c(9T) for several samples at 77 K and 50 K, the results for ss-nanocomposites shown in figure 3.26(c-e) of the trapping angle θ_T versus μ_0H^* are extended to pn-nanocomposites, shown in figure 6.19.

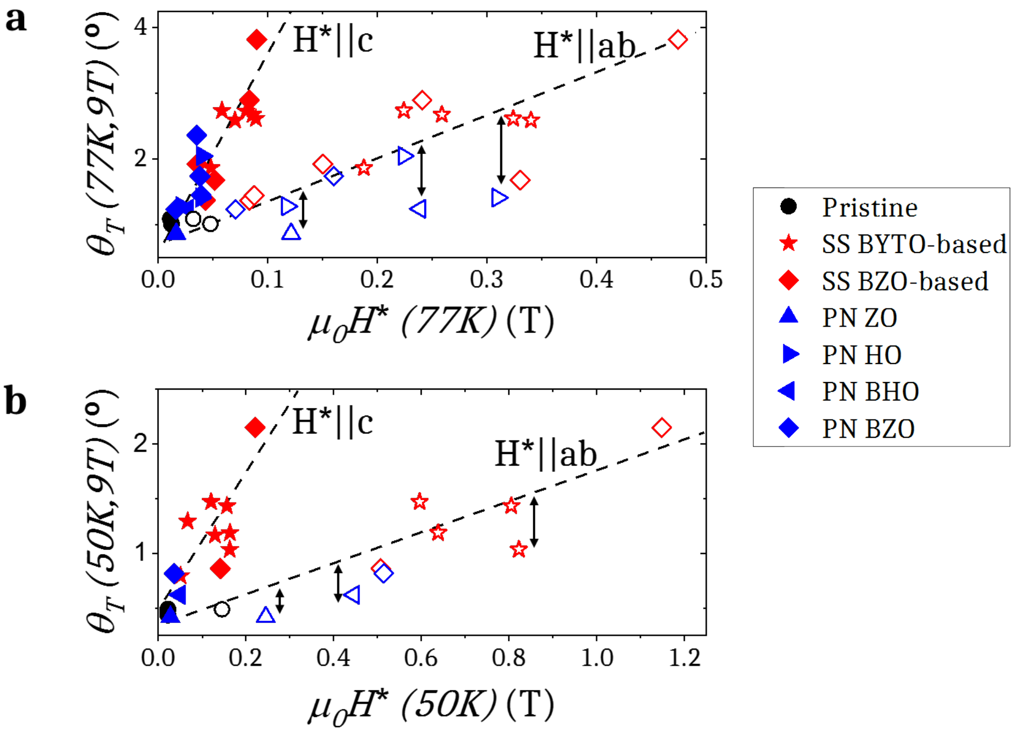

Figure 6.19: θ_T at 9 T as a function of μ_0H^* for pristine (black), ss-nanocomposites (red) and pn-nanocomposites (blue) at (a) 77 K and (b) 50 K. μ_0H^* was calculated for H||c (closed symbols) and H||ab (open symbols). Double-headed arrows indicate small deviations from the trend.

Again, the coincidence of the results for pn-nanocomposites with the trends obtained for ss-nanocomposites confirms the presence of the same pinning mechanisms for the enlargement of the single vortex pinning regime, region which has been related to the isotropic defects promoted by the appearance of stacking faults. Only some remarkable deviations are observed for μ_0H^* in the case of H||ab, where some nanocomposites show larger μ_0H^* values than the tendency.

As discussed in section 3.3.2 and observed in figures 3.19 and 3.20, μ_0H^* does not coincide with $\mu_0H^*_{iso}$ for nanocomposites up to 77 K for H||ab. This means that the arrangement of anisotropic defects, that may strongly vary from sample to sample taking into account the intricate competition between intrinsic pinning and stacking fault pinning (see for example the three different groups of nanocomposites identified in figure 5.13(b)), also play an important role in the enlargement of the single vortex pinning for H||ab. Therefore, μ_0H^* for H||ab does not strictly follow a simple correlation with the widening of θ_T.

Lastly, the temperature dependence of J_c has been evaluated for the sample PN 20BHO-FH, the thin pn-nanocomposite with very small nanoparticles and a very large density of short stacking faults, in order to extract the isotropic-weak, isotropic-strong and anisotropic-strong contributions, as well as the characteristic thermal pinning energies. The results are compared for H||c in figures 6.20 and 6.21 with Pristine-1 and the outstanding ss-nanocomposites SS 10BZO-5YO and SS 8BYTO, already shown in figures 4.8 and 4.10 in chapter 4.

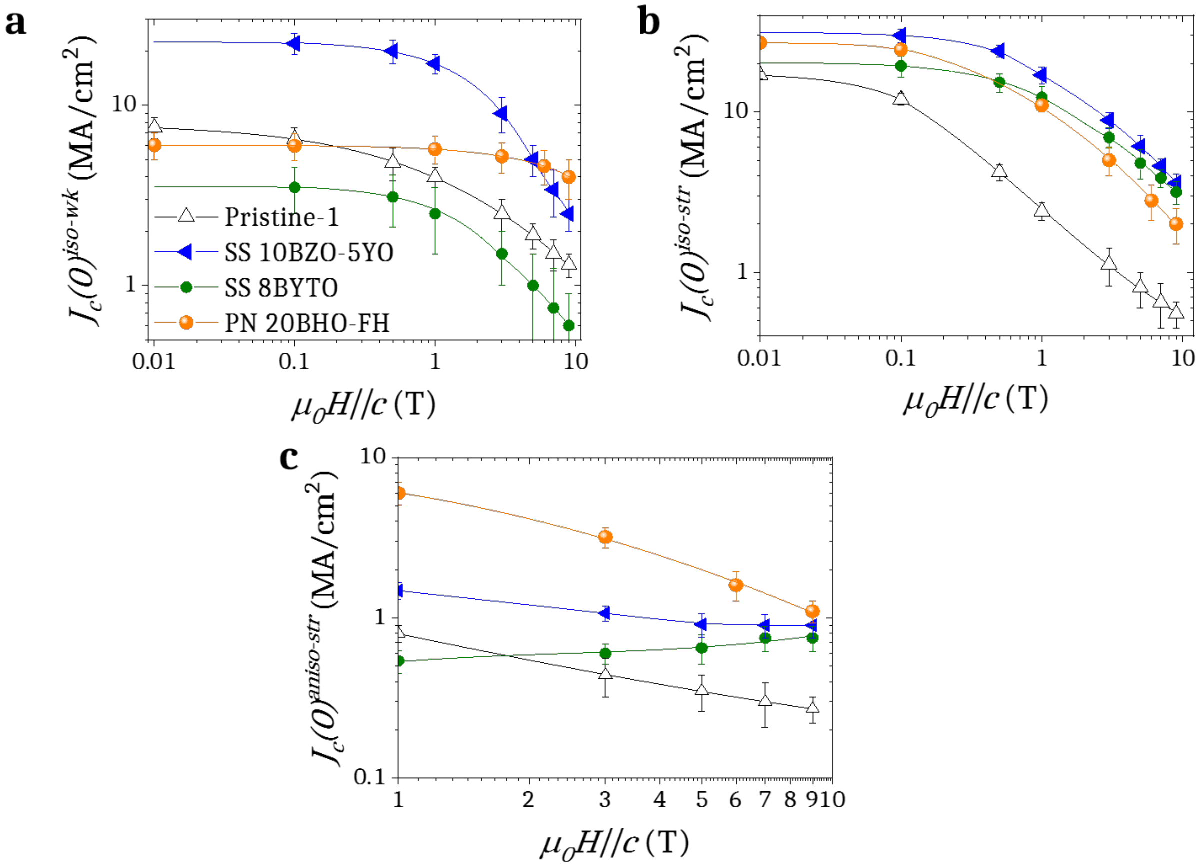

Figure 6.20: magnetic field dependence of the pinning contributions (a) J_c^{iso-wk}, (b) $J_c^{iso-str}$ and (c) $J_c^{aniso-str}$ at 0 K for Pristine-1, SS 10BZO-5YO, SS 8BYTO and PN 20BHO-FH films for H||c.

The self-field $J_c(0)^{iso-wk}$, ascribed to point defects, is similar for PN 20BHO-FH to the ones for SS 8BYTO and the pristine film at low magnetic fields, shown in figure 6.20(a). However, the magnetic field dependence $J_c(0)^{iso-wk}(H)$ for PN 20BHO-FH excels by an extraordinary $\mu_0H^*_{iso-wk}(0K)$ of 2.12 T, much larger than the ones for ss-nanocomposites ($\sim$ 0.4 T).

As observed in the STEM image in figure 6.6(b), the PN 20BHO-FH nanocomposite microstructure is distinguished by possessing a large density of short stacking faults. This shift of $\mu_0 H^*_{iso-wk}(0K)$ could be ascribed to the Cu-O vacancy clusters hosted in the stacking faults, which are smaller than the coherence length. However, more studies should be done to corroborate this relation. The characteristic pinning temperature for isotropic-weak T_0 in figure 6.21 displays no remarkable changes with respect to ss-nanocomposites.

What regards the isotropic-strong contribution in the PN 20BHO-FH nanocomposite shown in figure 6.20(b), it approaches the ones obtained for previously studied ss-nanocomposites. This indicates that the nanostrain induced by the partial dislocations surrounding stacking faults is very present in this pn-nanocomposite, in agreement with the short stacking faults observed in the STEM image in figure 6.6(b), also showing a very similar $T^*_{iso-str}$ to the one for SS 8BYTO nanocomposite in figure 6.21. This large isotropic-strong contribution could be also ascribed to the nanoparticles themselves, with a small size of 5 nm (which is already in the range of 2 times the coherence length).

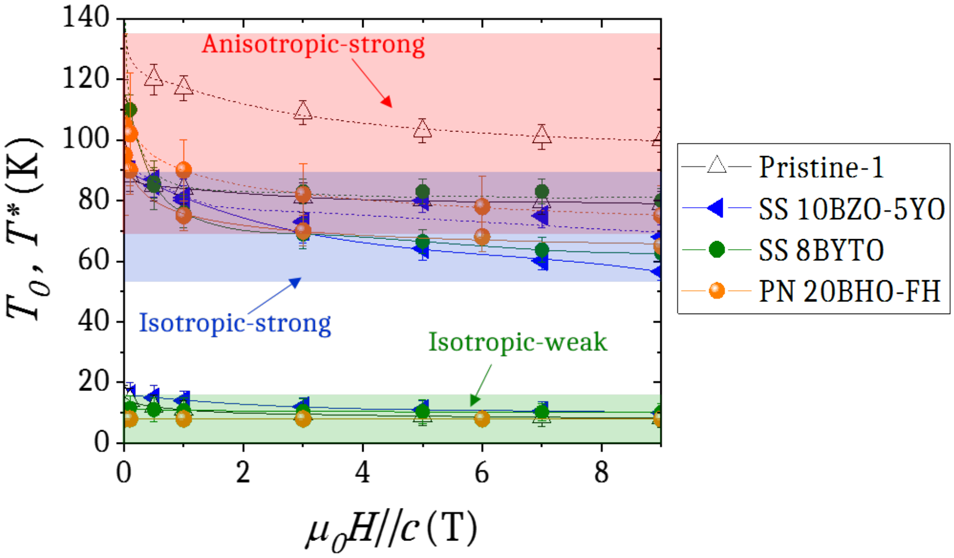

Figure 6.21: magnetic field dependence of T_0 (solid lines below), $T^*_{iso-str}$ (solid lines above) and $T^*_{aniso-str}$ (dashed lines) for Pristine-1, SS 10BZO-5YO, SS 8BYTO and PN 20BHO-FH films for H||c.

$T^*_{aniso-str}$ for PN 20BHO-FH shows neither any remarkable increase nor decrease with respect to ss-nanocomposites. However, the results of $J_c(0)^{aniso-str}$ in figure 6.20(c), attributed to the pinning performance of twin boundaries, exhibit the largest values along the entire studied magnetic field range whereas it shows a very strong decay at large magnetic fields, indicating that the density and configuration of twin boundaries has changed, possibly provoked by the advanced landscape of small nanoparticles and short stacking faults.

To summarize, the flash heated pn-nanocomposite shows similar pinning contributions to the best ss-nanocomposites, indicating that the main responsible sources of pinning (isotropic-strong) are the same, although it exhibits some modifications that seem to be related to the pinning landscape generated by the unique small size of nanoparticles. In particular, the increase of the $J_c(0)^{aniso-str}$ associated to the density of twin boundaries and the strong shift of $\mu_0 H^{*}_{iso-wk}$ illustrate remarkable modifications that still need to be further studied in order to enhance them and obtain higher pinning performance.

6.2 The performance of CSD nanocomposites at very high magnetic fields

REBCO CCs are conceived as very good candidates for the design of new coil architectures for several high magnetic field applications[125,206]. One of the main motivations for the development of profitable CCs is their potential use for high field magnets due to the compelling large critical currents under high magnetic fields[207,208].

Also the large H_{irr} of REBCO films allows them not only to improve the limited performance of Nb-Ti and Nb_3Sn magnets at 4.2 K, demonstrated by the progress in LTS-HTS hybrid magnets[208,209], but also to explore other operating conditions, as for example the development of a cryocooler-driven superconducting magnet technology capable to operate at 3-15 T in the 20-60 K temperature range[116,210].

Besides the technological and engineering challenge of growing such conductors in a long length scale, enhancement of J_c and H_{irr} and reduction of anisotropy of the superconducting material are strongly convenient for the development of cost-effective applications[116]. As commented in this thesis, the incorporation of nanoparticles in the YBCO matrix enhances the in-field performance and reduces the critical current anisotropy, indicating the special aptitude of YBCO nanocomposites for high field applications.

Furthermore, mixed pinning landscapes containing combinations of various types of disorder have been shown to be very effective at very high magnetic fields and a deep study is necessary to discern the most adequate pinning landscape for such operating conditions[125,211].

In this section, $J_c(H, \theta, T)$ dependences are studied at very high magnetic fields up to 35 T for a series of pristine and nanocomposite films of different thickness and processing conditions (a thin and a thick pristine, a thin flash heated pn-nanocomposite, a thick pn-nanocomposite and a ss-nanocomposite), which are distinctive films from tables 3.1, 6.1 and 6.2.

The electrical transport measurements have been carried out in a 35 T resistive solenoid magnet at the National High Magnetic Field Laboratory (NHMFL) facilities in Tallahassee (USA), whose experimental details are specified in section 2.3.4.2. The first experience in high magnetic fields and the initial trials were conducted during two previous stays in the high magnetic field facilities LNCMI-Grenoble.

6.2.1 Magnetic field dependence of J_c

Isothermal magnetic field dependent voltage-current curves were measured at different temperatures ranging 4.2-60 K from 6 T up to 35 T. The results of $J_c(H)$ and the subsequent calculation of $F_P(H)$ from equation 1.10 are shown in figure 6.22 for the thin and thick pristine and pn-nanocomposite samples. Note that the y-axis scale is the same for all J_c and F_P plots respectively.

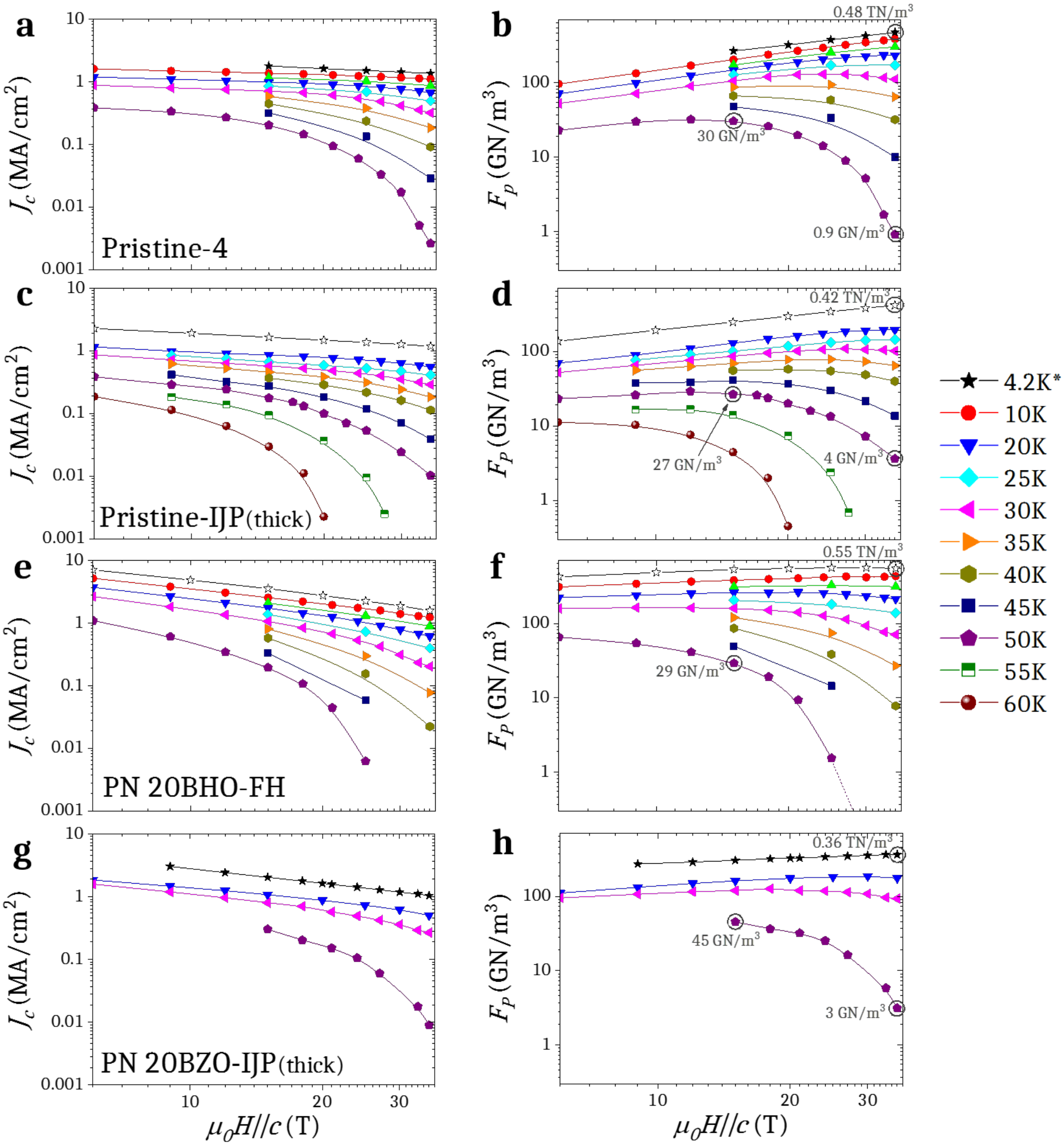

Figure 6.22: magnetic field dependence of (left) J_c and (right) F_P for H||c at temperatures ranging 4.2-60 K from 6 T up to 35 T for (a-b) Pristine-4, (c-d) Pristine-IJP, (e-f) PN 20BHO-FH and (g-h) PN 20BZO-IJP samples. *: 4.2 K data for Pristine-IJP and PN 20BHO-FH samples (open symbols) have been deduced from the fitting of equation 4.2.

There are several remarks that can be pointed form the comparison of the curves in the different samples. To begin with, nanocomposites show at the low temperature range (4.2-30K) clearly larger J_c up to ~ 15 T. However, given the fact that nanocomposites exhibit larger α values than pristine samples in agreement of a power law dominated by isotropic strong pinning centres characterized by a larger α^{iso} (see section 3.3.2), the J_c values above 15 T are similar for pristine and nanocomposite films. At higher temperatures, especially above 50 K, $J_c(H)$ curves are strongly influenced at very high fields by the strong decay ascribed to the $H_{irr}(T)$ line.

The F_P have been compared at three [T,μ_0H] conditions: [50K,15T], [50K,35T] and [5K,35T], each one interesting for different application purposes. At each particular condition, a different sample provides the best F_P values.

Taking into account the isotropic/anisotropic separation performed in section 3.3.2, the F_P at [50K,15T] is expected to be determined by the combination of isotropic and anisotropic contributions. The thick pn-nanocomposite, which has demonstrated to preserve a good balance of both contributions from the angular analysis in figure 6.15, is the sample exhibiting the largest value of 45 GN/m^3.

The F_P at [50K,35T] (in the vicinity of the irreversibility line) is expected to be mainly originated by the anisotropic pinning contribution of twin boundaries .The one for the thin pn-nanocomposite is estimated to fall further below 0.01 GN/m^3, whereas the pristine thin film displays a much larger pinning force of 0.9 GN/m^3. Thick pristine and nanocomposite films deposited by inkjet printing exhibit even larger pinning forces at these conditions of 4 and 3 GN/m^3 respectively, possibly related to the large irreversibility line obtained in thick inkjet printed pn-nanocomposite films, previously plotted in figure 6.15.

The magnetic field dependence of F_P is characterised by a monotonic increase up to a plateau at high fields which is consecutively followed by a decrease at very high fields. The lower is the temperature, the higher are the characteristic magnetic fields for each region.

At 4.2 K, the thin nanocomposite PN 20BHO-FH is the only one that reaches the plateau (the others still show the increasing $F_P(H)$ behaviour), but anyhow the one showing the largest pinning force at [4.2K,35T]: 0.55 TN/m^3, closer to remarkable values of 1.7 TN/m^3 obtained with self-assembled BZO nanorods[116]. The high performance of this pn-nanocomposite at low temperatures and high magnetic fields is in agreement with the analysis performed in figure 6.20, where it counts with large $J_c(0)$ values and a particularly large $\mu_0 H^*_{iso-wk}(0K)$, related to the unique stacking fault landscape originated by the small nanoparticles and presumably a high density of Cu-O vacancy clusters.

In figure 6.23, $J_c(H)$ curves at 4.2 and 30 K for the different samples are combined in the same graph, where the 4.2 K curve for a ss-nanocomposite is also included.

It is observed that although the PN 20BHO-FH nanocomposite is the film exhibiting the worst performance at 30 K and very high fields, the order is reversed at 4.2 K, showing the best performance of the studied films at the entire analysed magnetic field range. Only at larger magnetic fields than 35 T, a crossing is expected with respect to the values for the Pristine-4 sample. Such a crossing is on the other hand observed at 21 T and 31 T for PN 20BZO-IJP and SS 8BYTO-mod nanocomposites respectively.

At 30 K, the operating temperature for superconducting rotating machinery applications[116] and belonging to the temperature range aimed for applications with cryocooler

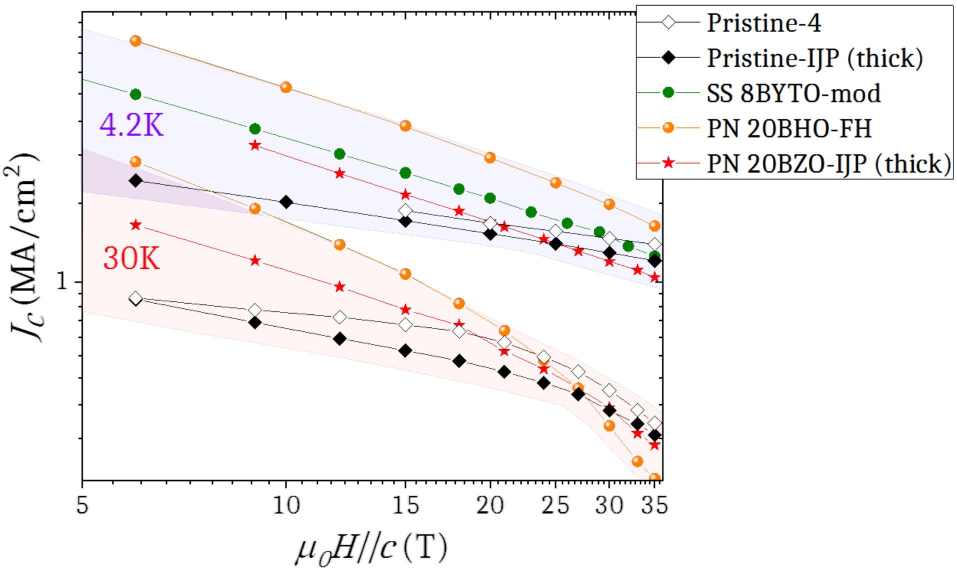

Figure 6.23: J_c(H) for H||c at 4.2 K (blue region) and 30 K (red region) for Pristine-4, Pristine-IJP, PN 20BHO-FH, PN 20BZO-IJP and SS 8BYTO-mod samples at very high magnetic fields.

technology (20-60 K), nanocomposites also offer substantially larger J_c values than pristine films in the magnetic field region of 5-20 T, strengthening the hypothesis that nanocomposites are very appropriate for the development of CCs for high field applications.

Although inkjet printed films do not offer best J_c values at very high fields as observed in figure 6.23, they indeed offer the best total critical current I_c values at 4.2 K, as depicted in figure 6.24, in comparison with the pristine thin film.

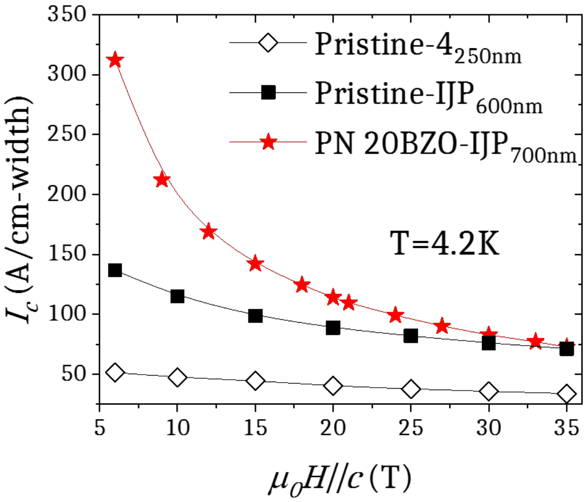

Figure 6.24: magnetic field dependence of I_c at 4.2 K for Pristine-4, Pristine-IJP and PN 20BZO-IJP for H||c from 6 up to 35 T.

The election of the thick nanocomposite sample is especially beneficial for the the design of CCs operating at intermediate magnetic fields (5-10 T) offering 6 and 2.5 times larger I_c values than the thin and thick pristine films respectively.

However, at very high magnetic fields, I_c values for both Pristine-IJP and PN 20BZO-IJP thick films coincide at $\sim$ 75 A/cm – width, only doubling the values of the pristine thin film. Anyhow, the performance of the thick nanocomposite has still room for improvement at these very high magnetic field conditions if the microstructure is further tuned in order to obtain a similar one to the thin flash heated pn-nanocomposite (PN 20BHO-FH), with small nanoparticles and a large density of short stacking faults.

6.2.2 Temperature dependence of J_c

The same $J_c(H)$ curves measured at different temperatures and showed in figure 6.22 for the four studied samples allow to evaluate the temperature dependence at each magnetic field in order to quantify the pinning contributions and energies present at very high magnetic films through the fitting of equation 4.2.

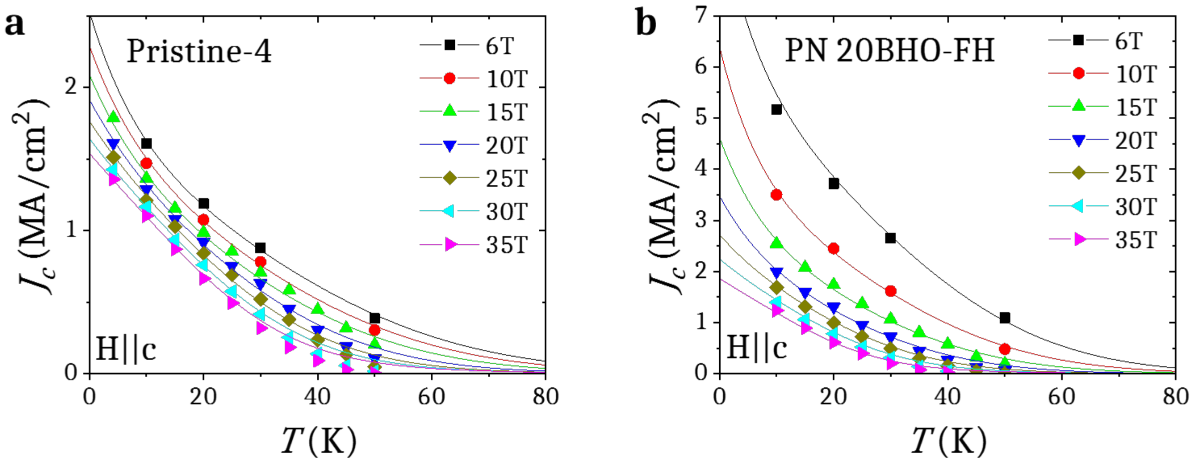

Figure 6.25: $J_c(T)$ dependence for Pristine-4 and PN 20BHO-FH samples at magnetic fields of 6, 10, 15, 20, 25, 30 and 35 T for H||c. Solid lines are the $J_c(T)$ fits to the equation 4.2.

The data is properly fitted by equation 4.2 as demonstrated for the cases of Pristine-4 and PN 20BHO-FH samples in figure 6.25, which also illustrates the acquirement of much larger J_c values for the pn-nanocomposite at intermediate fields.

With these fittings, it has been possible to extract the $J_c(0)^{iso-wk}$, $J_c(0)^{iso-str}$ and $J_c(0)^{aniso-str}$ contributions for the four samples. They are plotted in figure 6.26, where the previously obtained lower field contributions for Pristine-4 and PN 20BHO-FH are also included.

The first important remark of the analysis of the pinning contributions is the clear dominance at low temperatures of pn-nanocomposites in comparison to pristine films, showing in general larger $J_c(0)$ for all contributions. The PN 20BHO-FH nanocomposite film shows the largest isotropic-weak contributions at very high fields (see figure 6.26(a)), which is in fact related to the already commented large $\mu_0 H^*_{iso-wk}(0K)$ calculated from figure 6.20(a), possibly linked to a large amount of Cu-O vacancy clusters.

From the $J_c(0)^{iso-str}(H)$ curves plotted in figure 6.26(b), values are larger in pn-nanocomposites with very different α decay rates. The PN 20BHO-FH nanocomposite

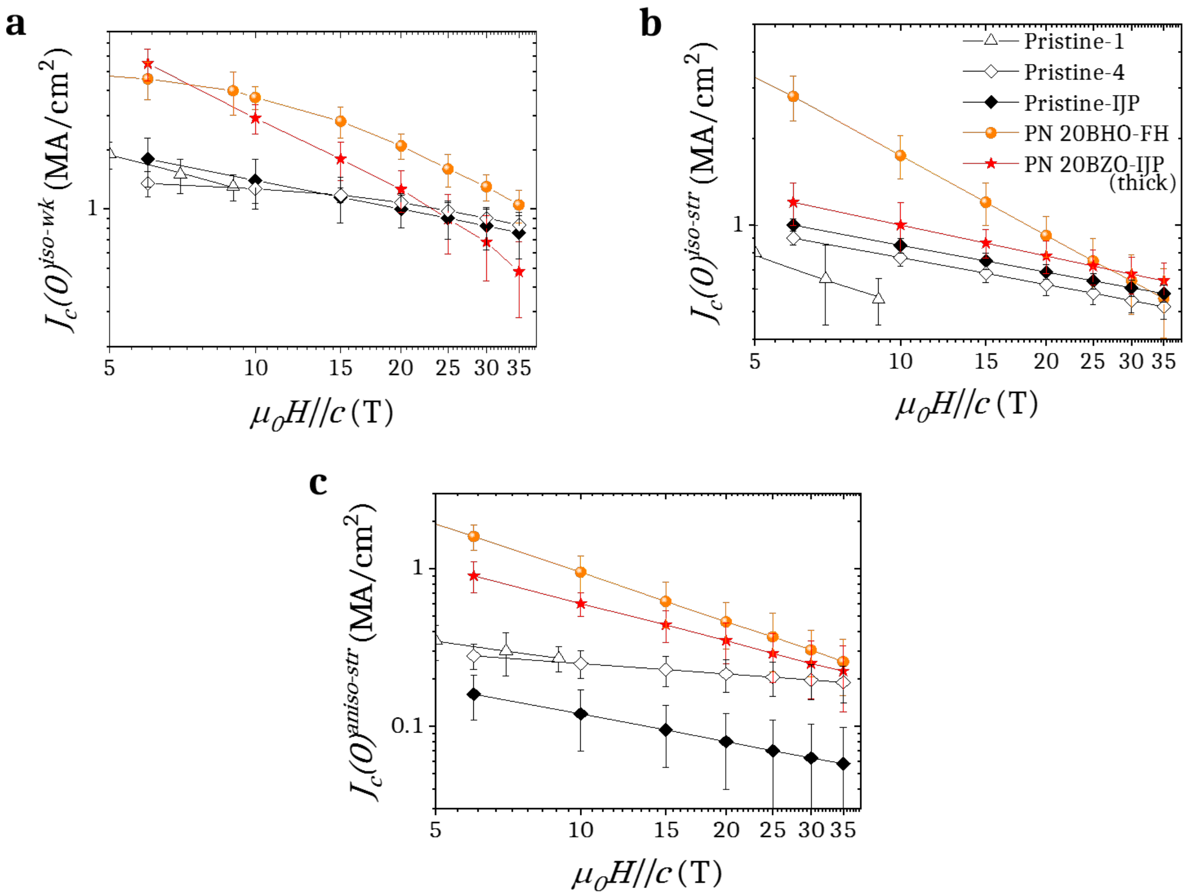

Figure 6.26: magnetic field dependence of the pinning contributions (a) J_c^{iso-wk}, (b) $J_c^{iso-str}$ and (c) $J_c^{aniso-str}$ at 0 K for Pristine-1, Pristine-4, Pristine-IJP, 20BHO-FH and PN 20BZO-IJP films for H||c at very high magnetic fields.

exhibits the largest values up to 25 T, given the fact that $J_c(0)^{iso-str}(H)$ decays faster with a larger α. This result, as observed in figure 6.20(b), is similar to those obtained for ss-nanocomposites, and it is an open question if this increase of isotropic-strong pinning density in this particular pn-nanocomposite is ascribed only to the high density of dislocations or also to the nanoparticles themselves, with a size of 5 nm. In contrast, the PN 20BZO-IJP nanocomposite behaves similarly to the pristine films with the increase of magnetic fields, displaying though the largest $J_c(0)^{iso-str}$ contribution at 35 T.

What regards the anisotropic-strong contribution (figure 6.26(c)), both pn-nanocomposites show larger values than pristine samples, which is attributed to a larger density of twin boundaries due to the reduction of the twin domain spacing. The $J_c(0)^{aniso-str}(H)$ dependence is similar for both pn-nanocomposites and unexpectedly also for the thick inkjet printed pristine film.

The obtained thermal pinning energies are plotted in figure 6.27, showing the evolution at very high magnetic fields. Interestingly, it is observed in general that T_0 tends to slightly increase whereas both anisotropic-strong and isotropic-strong T^* tend to decrease with increasing magnetic field. The performance at temperature region of 30-50 K at very high magnetic fields is therefore very influenced by the strong pinning characteristic temperatures.

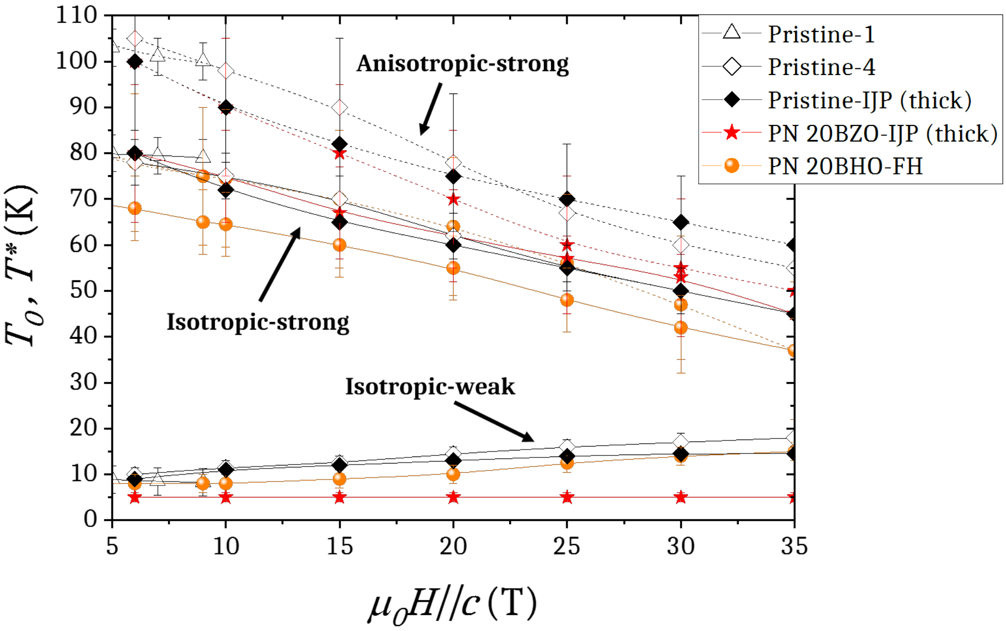

Figure 6.27: magnetic field dependence of $\mathrm{T_0}$ (solid lines below), $\mathrm{T^*_{iso-str}}$ (solid lines above) and $\mathrm{T^*_{aniso-str}}$ (dashed lines) for Pristine-1, Pristine-4, PN 20BZO-IJP and PN 20BHO-FH samples for H||c at very high magnetic fields.

The thick nanocomposite PN 20BZO-IJP exhibits larger $\mathrm{T^*_{iso-str}}$ and $\mathrm{T^*_{aniso-str}}$ than PN 20BHO-FH or ss-nanocomposites from figure 4.10. Actually, $\mathrm{T^*_{iso-str}}$ for PN 20BZO-IJP coincides with the one for the pristine films, indicating that the typology of the nanostrained regions has not been effectively modified, also manifested by the similar $\mathrm{J_c(0)^{iso-str}(H)}$ dependence in figure 6.26(b). $\mathrm{T^*_{aniso-str}}$ is also closer to the one for pristine films, indicating that the additional anisotropic pinning arising for H||c in the thick pn-nanocomposite at high temperatures, already observed in figures 6.14(b) and 6.15(b), is rather attributed to a regain in vertical coherence length of twin boundaries.

Comparing both thin and thick pristine films, it is observed a full coincidence of the $\mathrm{T^*_{iso-str}}$ but a considerable difference of $\mathrm{T^*_{aniso-str}}$, where the thick exhibits lower $\mathrm{T^*_{aniso-str}}$ at low fields and larger $\mathrm{T^*_{aniso-str}}$ at high fields. This result confirms the influence of the thickness or the deposition method on the coherence length of twin boundaries, already commented for thick nanocomposites. Further STEM analyses should be done in order to confirm the hypothesis that the twin boundary coherence is longer in thick films which yields to a gain in $\mathrm{T^*_{aniso-str}}$.

From the temperature fittings it is possible to acquire the $\mathrm{J_c(H,T,\theta)}$ 3D surface following the procedure developed in appendix A, in this case at very high magnetic fields. The surfaces are shown for Pristine-4 and PN 20BHO-FH in figure 6.28 for 5-60 K and 10-35 T temperature and magnetic field ranges.

It is visualized that the pn-nanocomposite displays larger critical current densities in a large H-T region, especially at low temperatures and intermediate fields. In contrast, at

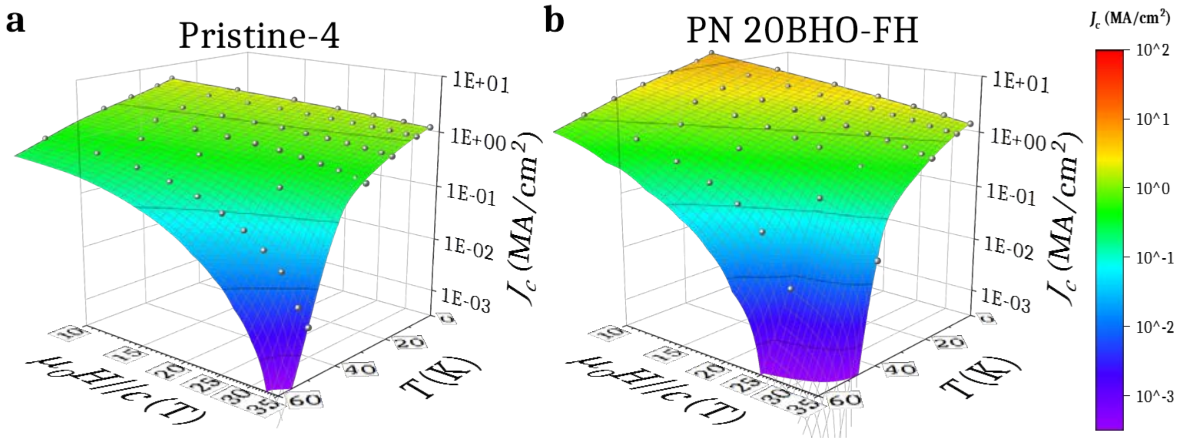

Figure 6.28: 3D $J_c(H,T)$ surface for (a) Pristine-4 and (b) PN 20BHO-FH at 5-60 K and 10-35 T temperature and magnetic field ranges for H||c .

high temperatures and large magnetic fields, the decay of J_c is more prominent in the thin pn-nanocomposite, characterised by a lower irreversibility line.

6.2.3 Magnetic field orientation dependence of J_c

Finally, the study of current-voltage curves at very high magnetic fields has been extended at magnetic field orientations different to H||c at the temperature of 20 K, covering an angular range of 180° centred at H||ab, for the specific magnetic fields of 15, 25 and 35 T. The angular $J_c(\theta)$ and $J_c^{iso}(\theta)$ results are plotted in figure 6.29(a) for Pristine-4, PN 20BHO-FH and PN 20BZO-IJP samples.

Firstly, it is observed that the ab peak is widened for nanocomposites, typical of a larger θ_T provided by the accommodation of vortices by stacking faults, in agreement with the results at lower fields in figure 3.26(a).

Secondly, J_c values are larger for both nanocomposites for all orientations at 15 T and only for PN 20BHO-FH at 25 T. These large angular values at 15 and 25 T are mainly provoked by a markedly strong isotropic contribution. At 35 T, isotropic contributions get weakened and the pristine film shows larger J_c near H||c than the two nanocomposites.

As observed in figure 6.23 at a similar temperature of 30 K, nanocomposite J_c(H||c) curves cross with the one for the pristine sample at magnetic fields of $\sim$ 20 T. Below this crossing magnetic field, nanocomposites offer higher performance throughout the angular range. In contrast, above the crossing field, the pristine film starts to exhibit larger J_c than nanocomposites in the vicinity of H||c, ascribed to the presence of anisotropic-strong pinning from twin boundaries, in agreement with a longer coherence along the c-axis.

Figure 6.29(b) shows the best collapses obtained with γ_{eff} values of 6, 2.5 and 2 for Pristine-4, PN 20BHO-FH and PN 20BZO-IJP samples respectively, which are comparable to the γ_{eff} obtained at lower fields shown in figures 3.16(a), 6.10 and 6.15(b) for similar or same samples. Thus, the γ_{eff} anisotropy remains constant at very intense magnetic

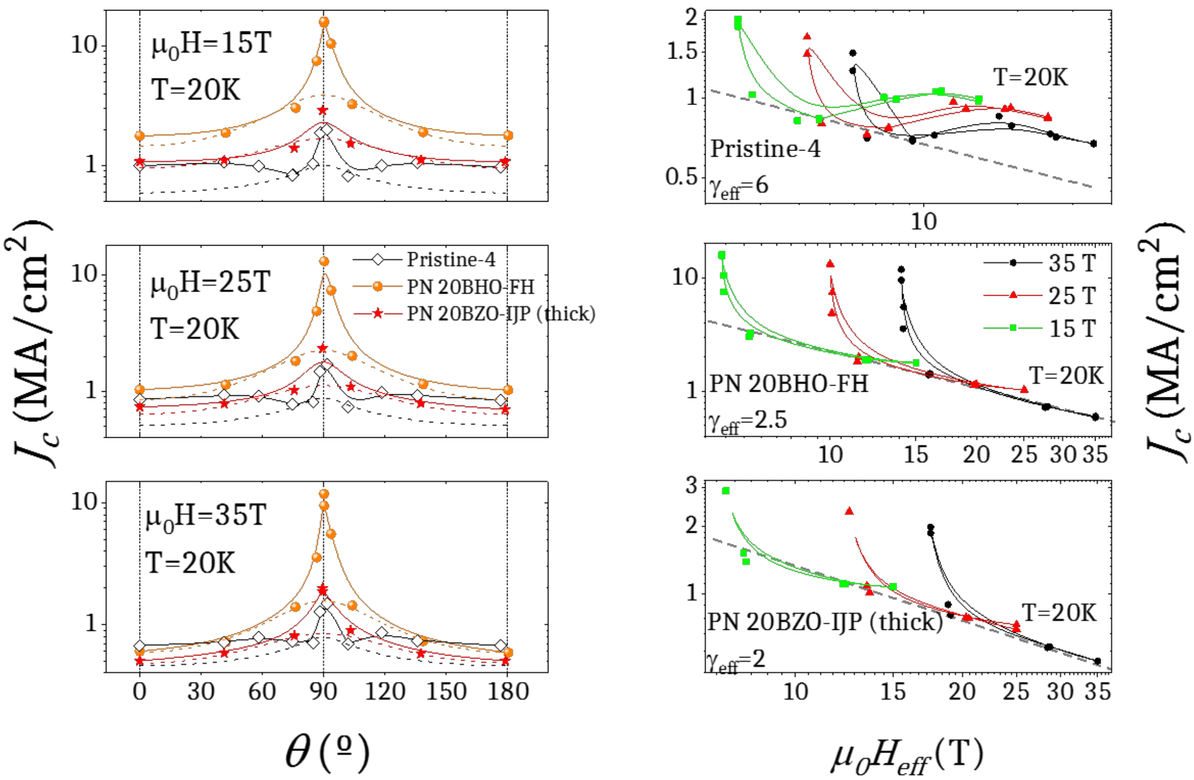

Figure 6.29: (a) $J_c(\theta)$ at 20 K for Pristine-4, PN 20BHO-FH and PN 20BZO-IJP samples at magnetic fields of 15, 25 and 35 T. Dashed lines correspond to the $J_c^{iso}(\theta)$ contributions, obtained from the collapses shown in (b) of J_c^{iso} versus $\mu_0 H_{eff}$ (dashed lines) plotted for each obtained γ_{eff}.

fields.

To summarize, it has been shown that the pinning performance of pn-nanocomposites is excellent at very high fields and very low temperatures (below 20 K), providing very large J_c values at any orientation thanks to the notable strength of both isotropic and anisotropic contributions for nanocomposites, especially for the flash heated pn-nanocomposite which exhibits a complete combination of defects: isotropic-strong, isotropic-weak and anisotropic-strong.

At higher temperatures (20-50 K), the influence of lower T^* values associated to segmented twin boundaries strongly affects the performance in nanocomposites and causes a $J_c(H)$ crossing of nanocomposites and pristine samples. The inkjet printed thick films (nanocomposites included) have been shown to preserve reasonably large T^* values and therefore be very good candidates at this temperature and magnetic field regions.

6.3 Conclusions

Despite the complexity given by the microstructural phenomena that has been addressed during the study of the growth process, compelling pn-nanocomposites were obtained with a smooth dependence with the magnetic field. The $BaZrO_3$ and $BaHfO_3$ preformed nanoparticles have been of particular interest, where the growth process can be controlled avoiding chemical reactivity and minimizing the coarsening of the nanoparticles, which leads to a better control of the final microstructure in the film.

Similarly to ss-nanocomposites, pn-nanocomposites include an enlargement of the single vortex pinning regime mainly dominated by isotropic-strong pinning defects induced by the generation of the stacking faults, concomitant with a reduction of the anisotropy and a widening of the $J_c(\theta)$ ab-peak. The previously found $H^*(\varepsilon)$ and $H^*(\theta_T)$ correlations are strengthened since the results follow the tendencies for pn-nanocomposites as well.

Among pn-nanocomposites, it is worth stressing the vortex pinning contributions coming from the $BaHfO_3$ nanocomposite grown by a flash heating thermal process, that generates a defect landscape which is rich in short stacking faults and small nanoparticles, which is ideal not only for the rise of the isotropic-strong contribution attributed to the partial dislocations but also for the enlargement of the magnetic field range where isotropic-weak pinning provides an excellent contribution.

The implementation of pn-nanocomposites to the growth of thick films by inkjet printing has been successful, strongly improving the I_c values under magnetic field obtained until now. Furthermore, thick pn-nanocomposites have shown an interesting gain of the anisotropic-strong contribution at high temperatures through the combination of a large density of twin boundaries and the recovery of the thermal pinning energy, associated to a long vertical coherence, enlarging H_{irr} for H||c and displaying good performances at high fields and high temperatures.

The electrical performance of CSD YBCO nanocomposites has been explored up to 35 T for first time. The results reveal the improved J_c values for nanocomposites with respect to the pristine near 4.2 K up to 35 T for H||c. This enhanced performance is mainly provided by the large isotropic pinning contribution coming from both isotropic-strong and isotropic-weak defects, that are also combined with significant anisotropic contributions.

At higher temperatures (20-50 K), closer to the anisotropic-strong pinning thermal energy $T^*_{aniso-str}$, the performance of nanocomposites is larger than the pristine up to a crossing given at high magnetic fields ($\sim$ 20 T), which can be shifted to larger fields by the use of thick nanocomposite films, presenting larger thermal pinning energies attributed to vertical coherent twin boundaries. At fields below this crossing, nanocomposites exhibit larger J_c values throughout the entire angular range.

To summarize, the most appealing option to obtain high critical currents at high magnetic fields is foreseen to be the use of thick films with a large vertical coherence of twin boundaries combined with a stacking fault defect landscape that promotes a large density of nanostrained regions and Cu-O vacancy clusters.

CHAPTER 7

GENERAL CONCLUSIONS

One of the main requirements for coated conductors is to be capable to transport very large currents under magnetic fields, which comprises the control of vortex pinning and vortex creep mechanisms and therefore a thorough understanding of the correlations between these mechanisms and the defect microstructure of the superconducting films.

This thesis has been devoted to the analysis of the underlying vortex pinning and vortex creep mechanisms in CSD-TFA YBCO nanocomposites from electrical transport measurements of J-E curves, from which it is possible determine the critical current density J_c and its time decay at different conditions of temperature and magnetic field intensity and orientation.

Firstly, a thoughtful study of pinning regimes has been realised in epitaxial nanocomposites formed by spontaneous segregated nanoparticles later extended to preformed nanoparticles nanocomposites, which has revealed the importance of the secondary defects induced by the incorporation of nanoparticles, which enhance the critical currents under high magnetic fields and reduce the anisotropic pinning behaviour provided by the layered structure of YBCO.

The combination of electrical transport measurements, XRD analysis and STEM observations has allowed us to detect correlations between nanostrain, the width of the angular J_c peak for H||ab and the relative volume of partial dislocations with the enlargement of the single vortex pinning regime for both H||c and H||ab, indicating that the main responsible defect of the in-field improvement of J_c are the isotropic nanosized strain regions located at the partial dislocations and surrounding the numerous stacking faults emerging from the incoherent interfaces between the nanoparticles and the YBCO matrix.

These nanostrained regions located at the partial dislocations have been associated to the isotropic-strong pinning contributions, which are particularly dominating the effects in nanocomposites with a large density of stacking faults and are especially effective at low, intermediate and high magnetic fields (∼0.01-10T) and up to intermediate temperatures (∼0-70 K).

Some nanocomposites also exhibit an enhancement of the isotropic-weak contribution, which is effective at temperatures below 20 K. This enhancement may be related to the Cu-O cluster vacancies hosted in the stacking faults, detected in STEM observations.

Besides the progress of isotropic pinning contributions encountered in the stacking-fault-rich defect landscape of CSD YBCO nanocomposites, anisotropic pinning contributions are also altered both at H||c and H||ab orientations in comparison to pristine YBCO films.

For H||c, the anisotropic strong pinning contribution associated to twin boundaries is reduced at high temperatures (above 60 K), causing a slight decrease of the irreversibility line, and enhanced at low temperatures (below 20 K). These changes are respectively related to the loss of vertical coherence of the twin boundary, indicated by the decrease of the anisotropic-strong pinning thermal energy $T^*_{\mathrm{aniso-str}}$ and to the increase of the density of defects, manifested by a larger $J_c(0)^{\mathrm{aniso-strong}}$.

STEM observations confirm that these changes are associated to a new arrangement of twin boundaries, which are denser due to the reduction of the twin domains spacing promoted by nanoparticles but on the other hand are less coherent along the c-axis by reason of the segmentation promoted by the already present high density of stacking faults.

Further investigations in thick pn-nanocomposites grown from inkjet printing deposition have shown that a large $T^*_{\mathrm{aniso-str}}$ can be obtained, associated to a recovery of the vertical coherence, and simultaneously maintain a large density of twin boundaries.

For H||ab, the anisotropic pinning performance is accomplished by the competition between intrinsic pinning and stacking fault pinning. In agreement with a wider pinning well than intrinsic pinning, the larger density of stacking faults increase the pinning thermal energy $T^*_{\mathrm{aniso-str}}$ and also widen the angular J_c peak arising at H||ab, exhibiting much larger trapping angles which saturate at larger magnetic fields.

The saturation of the trapping angle has been used to separate the dominance of intrinsic pinning and stacking fault pinning into two regions in the H-T diagram, which has been confirmed by a subsequent analysis of the flux creep implications of both kind of correlated pinning centres parallel to the ab-planes. Whereas stacking fault pinning dominates at low magnetic fields and high temperatures, intrinsic pinning dominates at large magnetic fields and low temperatures.

It has been shown that flux creep rates S can be originally obtained from electrical transport measurements by the relation between S and the J(E) power index n, derived from magnetic flux creep theories.

Although the creep rate values from electrical transport measurements should not be exchanged to the ones from inductive magnetic measurements, given the use of different time and electric field windows, results are in agreement with the dependences obtained by inductive methods and show only slightly larger creep rates, though of the same order of magnitude.

Creep evaluation from transport measurements has the advantage of being faster and that can be easily expanded to the study of the full angular range of the magnetic field orientation. With this approach, it has been possible to explore the temperature and magnetic field intensity and orientation dependences of the creep rate S, paying special attention to the results for H||ab, in order to evaluate the role that the emerging stacking faults play in vortex dynamics. Furthermore, the Blatter scaling approach has been applied for the angular analysis of S, allowing to separate S_{iso} and S_{aniso} contributions.

The creep analyses performed in nanocomposites with segregated nanoparticles indicate that the creep arising from the isotropic defects is reduced at low and intermediate magnetic fields at high temperatures.

Moreover, the anisotropic contributions coming from correlated defects at both H||c and H||ab, which can increase creep through double kink thermal excitations, are mostly precluded. In particular, three groups of nanocomposites have been identified with respectively low, intermediate and high densities of stacking faults, showing an increase of stacking fault pinning domination which increasingly precludes the vortex expansion through double kink excitations for H||ab (typical for a landscape dominated by intrinsic pinning).

After facing some microstructural complexities occurring during growth, novel nanocomposites from preformed nanoparticles have been successfully obtained with very similar electrical performance to the spontaneous segregated nanoparticles. In particular, the best results were obtained with non-reactive BZO and BHO preformed nanoparticles, which suffer a minimal coarsening during growth up to a final size of 10 nm.

Furthermore, high quality epitaxial 1 μm thick BZO nanocomposites from preformed nanoparticles have been grown by the use of inkjet printing deposition. These thick samples have shown to be particularly efficient at high temperatures and large magnetic fields for H||c, due to a recovery of the c-oriented twin boundary coherence.

The use of a flash heating in the growth process has allowed us to go beyond the standard situation with preformed nanoparticle nanocomposites, avoiding coarsening and obtaining final nanoparticles of 7 nm, whose landscape is very rich in short stacking faults and is thereby very convenient for the generation of larger relative volume of nanostrained regions, as demonstrated by an observed large isotropic-strong contribution. This particular microstructure is also favourable to the improvement of the magnetic field dependence of the isotropic-weak contribution, whose origin can be related to the Cu-O vacancies observed in the interior of stacking faults.

The study of the electrical performance of CSD YBCO pristine and nanocomposite films has been expanded to very high magnetic fields up to 35 T for first time. The performance of nanocomposites is excellent at very high magnetic fields and very low temperatures, surpassing those of pristine films and reaching a pinning force of 0.55 TN/m^3 at 4.2 K and 35 T.

At higher temperatures (20-50 K) and very high magnetic fields, there is a crossing of J_c values in nanocomposites with respect to the pristine films given by a reduced anisotropic strong pinning thermal energy associated to segmented twin boundaries, which decreases with increasing magnetic field (down to 40-50 K at 35 T).

The studies have shown that different defect landscapes are the best ones for different operating conditions: nanocomposites with very large densities of isotropic and anisotropic defects but with segmented twin boundaries show the best performances at very low temperatures and high and very high magnetic fields, whereas nanocomposites with intermediate defect densities and larger coherence of correlated defects show the best properties at intermediate temperatures and intermediate and high magnetic fields.

The most appealing defect landscape derived from these studies to obtain high critical currents at high fields and temperatures is foreseen to be the one generated in thick films with large vertical coherent twin boundaries combined with a stacking fault defect landscape that promotes a large density of nanostrained regions and Cu-O vacancy clusters.

Ideally, if nanostructure could be extremely well controlled, it would be worth to try to obtain a regular lattice (cubic, tetrahedral, octahedral,...) of strong isotropic pinning centres, which would provide strong pinning with large characteristic temperatures T* for many magnetic field orientations, combined with a concomitant network of randomly distributed isotropic pinning centres of different sizes (see figure 7.1(a)), which would help to provide additional pinning and smooth matching effects. However, the periodicity of the lattice would cause large flux creep rates, which could be avoided by breaking the periodicity through "defects" in the pinning centre lattice, as depicted in figure 7.1(b).

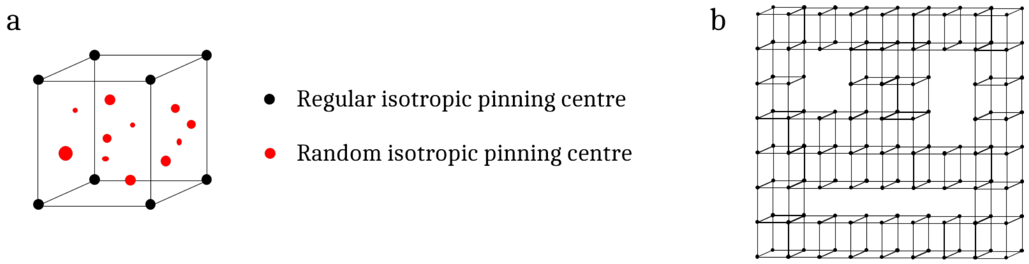

Figure 7.1: Ideal structure of a lattice of pinning centres. (a) Lattice unite cell and (b) "defects" in the lattice.

We suggest that further studies would be needed to ascertain some of the results here obtained. In particular, further investigations should be done to conclusively determine the origin of large densities of isotropic-weak defects and consequent improved magnetic field dependence of the isotropic-weak contribution in some films. On the other hand, the recovery of the pinning thermal energy in thick nanocomposites ascribed to the vertical coherence of twin boundaries is still not completely understood and should be complemented with further investigations in CSD YBCO nanocomposites.

Finally, we think that the analysis performed in this thesis should not be limited to the study of CSD nanocomposites but could be fairly extended to the study of other nanostructured YBCO films or even other layered superconductors. The attempt to measure magnetic relaxation from E-J curves is courageous but at the same time convincing which also motivates to expand the creep evaluation to other high temperature superconductors where vortex dynamics plays an important role. The results of both pinning and creep analysis serve as a path to design the best pinning landscape, which in turn, it has been demonstrated to be distinctive for particular magnetic field and temperature conditions.

APPENDIX A

GENERATION OF THE $J_C(T,H)$ SURFACE

The method used to obtain the 3D surface plot of $J_c(T,H)$ and H-T maps contributions as $J_c^{iso}/J_c(H,T)$ or $J_c^{wk}/J_c(H,T)$ is here explained, for the particular case of the sample 10BZO-5YO from figure 3.20.

$J_c(H)$ curves at different temperatures have been B-spline interpolated with a step size of 0.01 T in the x-axis. In this appendix, the procedure is shown for a step size of 0.5 T, for an easier distinction of the curves. The interpolation of the $J_c(H)$ curves in figure 3.20 yields to the temperature dependence of J_c plotted in figure A.1 for the different magnetic fields.

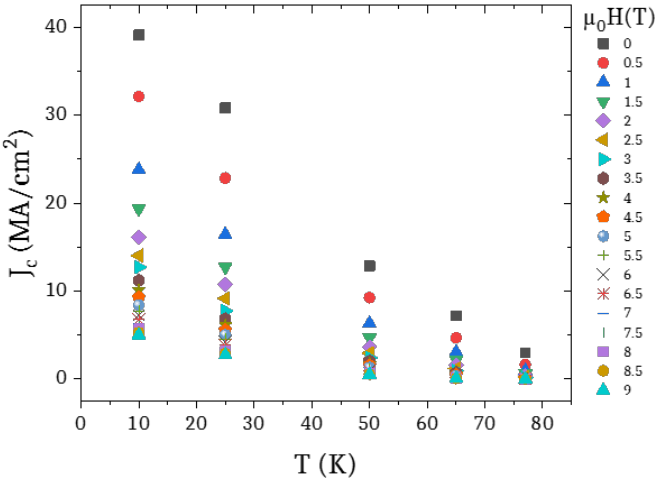

Figure A.1: J_c as a function of temperature for the interpolated points each 0.5 T from $J_c(H)$ curves for 10BZO-5YO at 77, 65, 50, 25 and 10 K.

Each $J_c(T)$ curve represented by the scattered points in the graph for each magnetic field are fitted following the direct sum of weak and strong pinning equations 3.1 and 3.2 (this means without considering interactions with each other):

$$J_c(T) = J_c^{wk}(T) + J_c^{str}(T) = J_c^{wk}(0)exp\left(-\frac{T}{T_0}\right) + J_c^{str}(0)exp\left[-3\left(\frac{T}{T^*}\right)^2\right] \tag{A.1}$$

For each magnetic field, the fitting involves 4 parameters to be found: J_c^{wk}, T_0, J_c^{str} and T^*. Evident bounds and initial fitting values $T_0 = 10$ K and $T^* = 75$ K have been used.

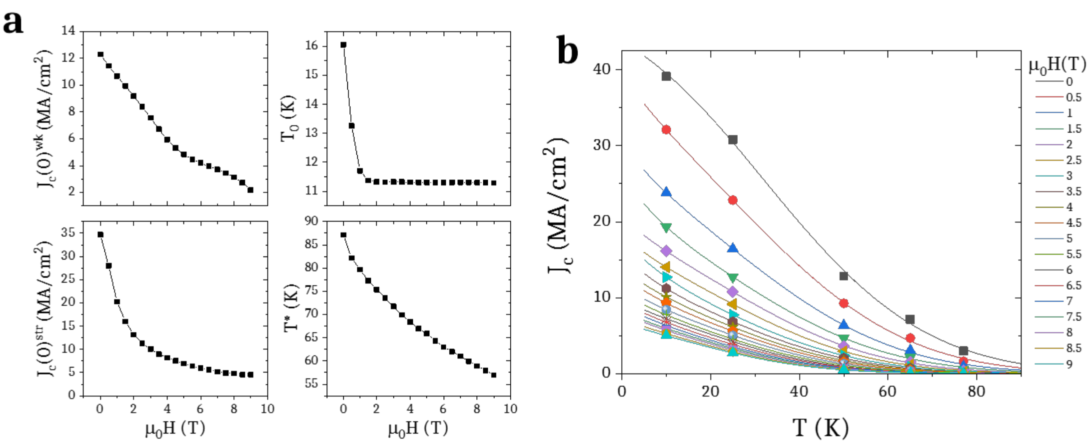

Figure A.2: results of the $J_c(T)$ fitting. (a) Magnetic field dependence of (left) J_c^{wk} and J_c^{str} and (right) the characteristic temperatures T_0 and T^*. (b) Temperature dependence of interpolated J_c, where solid lines correspond to the fitting of equation A.1 with the parameters from (a).

The resulting magnetic field dependence of the parameters J_c^{wk}, T_0, J_c^{str} and T^* and the fitting of $J_c(T)$ curves are shown in figure A.2(a). The data of the interpolated $J_c(H)$ curves fits well in figure A.2(b) the sum of weak and strong pinning equations.

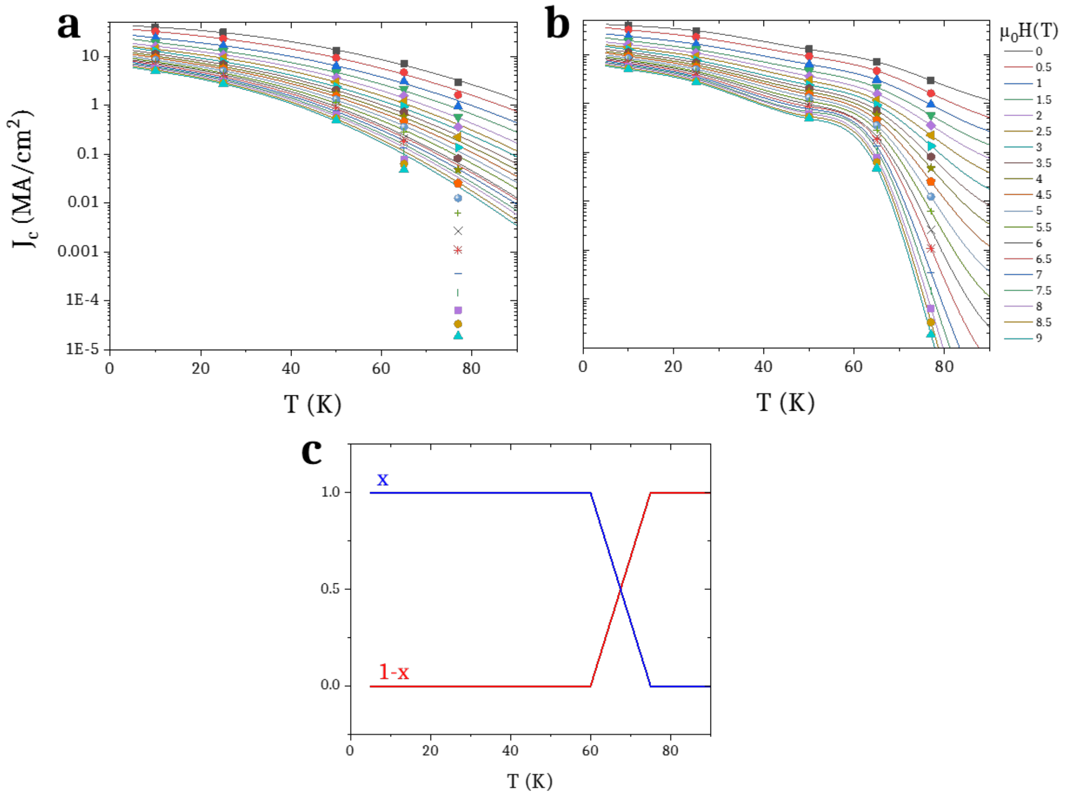

Figure A.3: log-lin temperature dependence of interpolated J_c with solid lines corresponding to (a) strong-weak equation and (b) log-lin B-spline function fittings. (c) Temperature dependence of the coefficient x and 1-x from equation A.2.

However, the fit fails to describe the $J_c(T)$ dependence at high temperatures when $J_c(T)$ is plotted in logarithmic scale as in figure A.3(a), in agreement with the high temperature limits foreseen for the applicability of these models[7,44].

Although it has no physical interpretation, the data can be well fitted with a B-spline polynomial function $J_c^{spl}(T)$ in the logarithmic scale of J_c, as observed in figure A.2(b). Therefore, in order to obtain a smooth final curve that describes well the behaviour also at high temperatures, the final $J_c(T)$ is obtained by a transition of both fittings following:

$$J_c(T) = x(J_c^{wk}(T) + J_c^{str}(T)) + (1 - x)J_c^{spl}(T) \tag{A.2}$$

Where x is a coefficient that defines the linear transition from one curve to the other, plotted in figure A.3(c), for a transition ranging from 60 K to 75 K. The final result for $J_c^{wk}(T,H)$, $J_c^{str}(T,H)$ and $J_c^{wk+str}(T,H)$ surfaces (obtained after the transition to the B-spline fitting) are plotted in figure A.4. From the division of these surfaces, the $J_c^{wk}/J_c(T,H)$ and $J_c^{str}/J_c(T,H)$ maps can be obtained. The same procedure can be applied for the $J_c^{iso}(H)$ curves. With that, ratios as $J_c^{iso}/J_c(T,H)$ or $J_c^{iso-str}/J_c(T,H)$ can be obtained as well, as in figures 3.21 or 4.13.

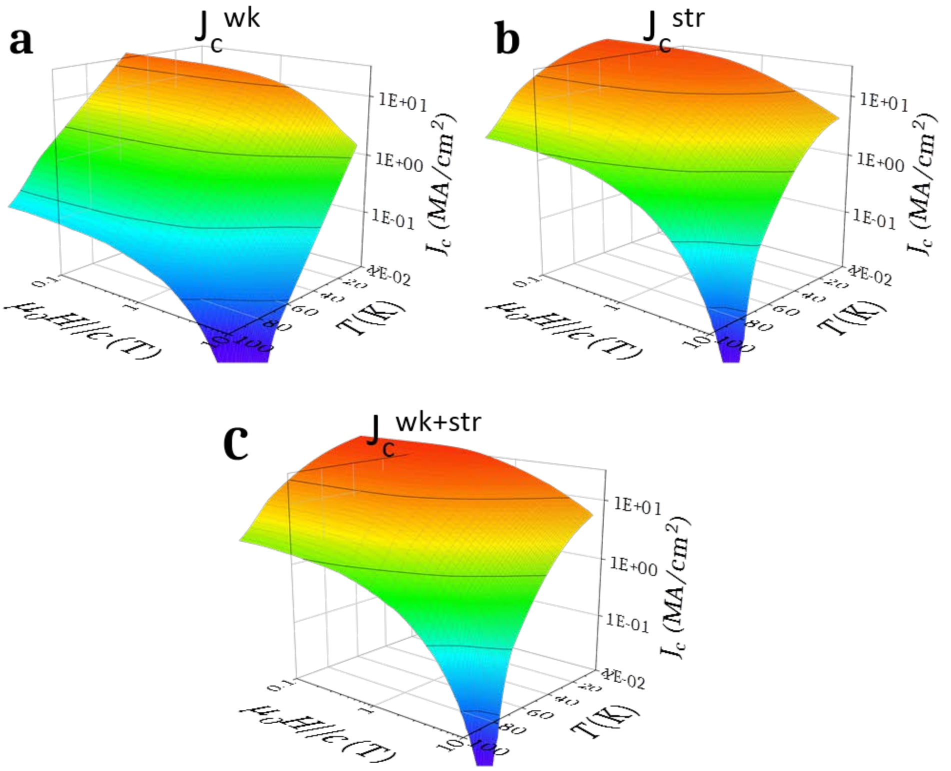

Figure A.4: final (a) $J_c^{wk}(T,H)$, (b) $J_c^{str}(T,H)$ and (c) $J_c^{wk+str}(T,H)$ surfaces after the linear transition to $J_c^{spl}(T,H)$ at high temperatures.

APPENDIX B

PARTIAL DISLOCATION RELATIVE VOLUME CALCULATION

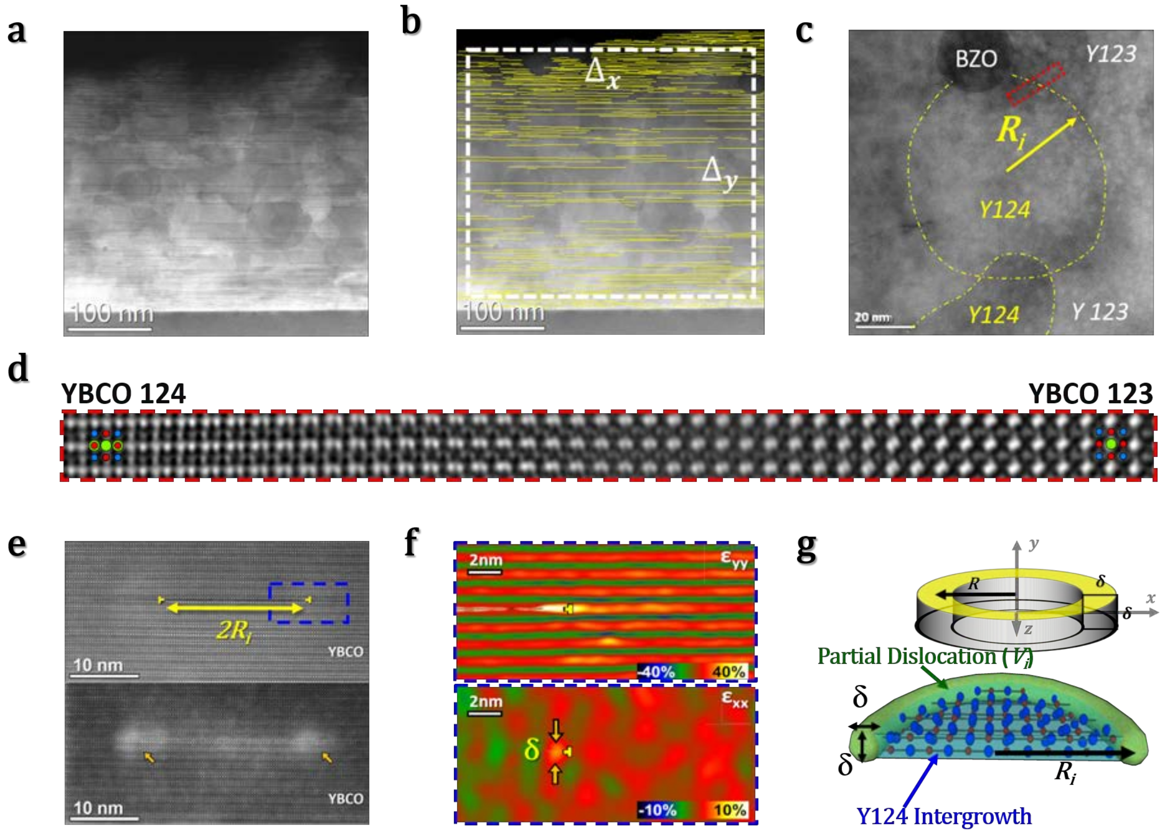

Figure B.1: STEM observation of stacking faults in YBCO nanocomposite films and schematic views of the defect. (a-b) Cross-sectional low magnification Z-contrast images of a 5%BZO-6%BYTO nanocomposite. In (b), stacking faults are marked with yellow stripes and the observed YBCO area $\Delta_x\Delta_y$ is delimited. (c) Plan view Z-contrast image of a 13%BZO nanocomposite. The boundaries of intergrowths are highlighted in yellow. (d) Plan view high resolution Z-contrast image of the red selected region in (c) and identification of Y124 and Y123 phases. (e) (above) Z-contrast and (below) LAADF images of an isolated stacking fault. Yellow symbols point to partial dislocations while the arrows to their associated strain fields. The blue selected region is studied in figure (f), that shows the GPA $\varepsilon_{\mathrm{yy}}$ (above) and $\varepsilon_{\mathrm{xx}}$ (below) deformation maps along the $\langle 001\rangle_{\mathrm{YBCO}}$ and $\langle 100\rangle_{\mathrm{YBCO}}$ directions, identifying a strained region with size $\delta \approx 0.8$nm. **g** (below) Schematic view of the partial dislocation and (above) approximation of the associated strain to a cylindrical disk shape.

From the observations performed by STEM in CSD YBCO films (see fig. B.1(a-f)), partial dislocations surrounding Y124-intergrowth planar defects (stacking faults) can be approximated to the shape of a cylindrical disk (see fig. B.1(g)). Therefore, the volume of each dislocation V_i can be approximated:

$$V_i = \pi \left(R_i + \delta/2\right)^2 \delta - \pi \left(R_i - \delta/2\right)^2 \delta = 2\pi R_i \delta^2 \tag{B.1}$$

where R_i is the radius of the stacking fault (for simplification, it is considered that the observed stacking faults are centred at the observation plane z=0) and δ is the size of the strained region caused by the dislocation, that is roughly 0.8 nm (see fig. B.1(f)). In order to calculate the volume density, we can divide the volume of the N dislocations found in the image by the total YBCO volume of the image, equivalent to the observed area $\Delta_x\Delta_y$ multiplied by the depth of observation Δ_z, estimated to be ~20 nm.

$$\rho_{dis} = \frac{\sum_i^N V_i}{\Delta_x \Delta_y \Delta_z} \tag{B.2}$$

However, in some cases, namely $(\Delta_z + \delta)/2 > R > (\Delta_z - \delta)/2$ and $R > (\Delta_z + \delta)/2$, part of the volume of the dislocation is out of the range of observation.In order to subtract this part of the volume, some trigonometric relations (in radians, from fig. B.2(a)) are taken into account.

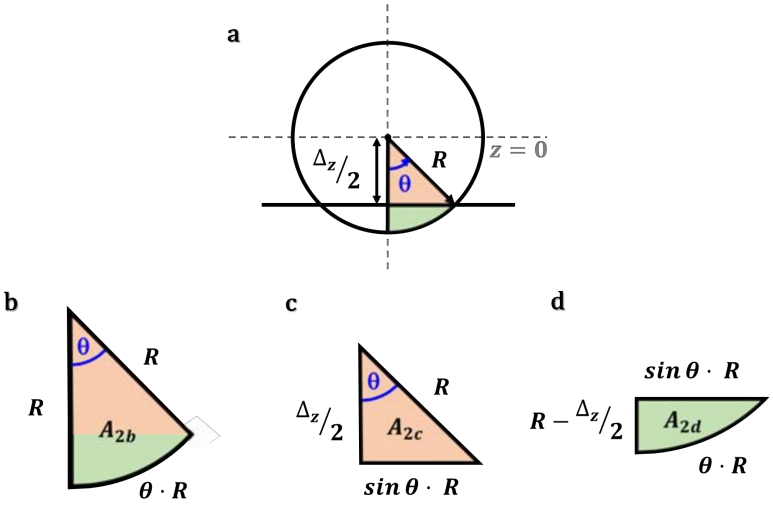

Figure B.2: trigonometric relations for a circle with radius R and a line $z = \Delta_z/2$. (a) Schematic plan view. (b) Circular sector with radius R, angle θ and area A_{2b}. (c) Right triangle with angle θ and area A_{2c}. (d) Resulting area A_{2d} after subtraction of A_{2c} from A_{2b}.

From fig. B.2(c), we obtain:

$$\cos\theta = \frac{\Delta_z}{2R} \tag{B.3}$$

$$\sin\theta = \sin(\arccos(\Delta_z/2R)) = \sqrt{1 - \left(\Delta_z/2R\right)^2} \tag{B.4}$$

Now, applying equations (B.3) and (B.4) to the calculation of areas A_{2b}, A_{2c}, and A_{2d} of the geometric shapes in fig. B.2(b-d):

$$A_{2b}(\boldsymbol{R}) = \frac{\theta R^2}{2} = \frac{\arccos(\Delta_z/2R)R^2}{2} \tag{B.5}$$

$$A_{2c}(\boldsymbol{R}) = \frac{\sin(\theta)R\Delta_z/2}{2} = \frac{\sqrt{1-(\Delta_z/2R)^2}\,R\Delta_z}{4} \tag{B.6}$$

$$A_{2d}(\boldsymbol{R}) = A_{2b}(\boldsymbol{R}) - A_{2c}(\boldsymbol{R}) = \frac{\arccos(\Delta_z/2R)R^2}{2} - \frac{\sqrt{1-(\Delta_z/2R)^2}\,R\Delta_z}{4} \tag{B.7}$$

With these areas, we are able to calculate the volume of the strain located in a dislocation V_i in each case.

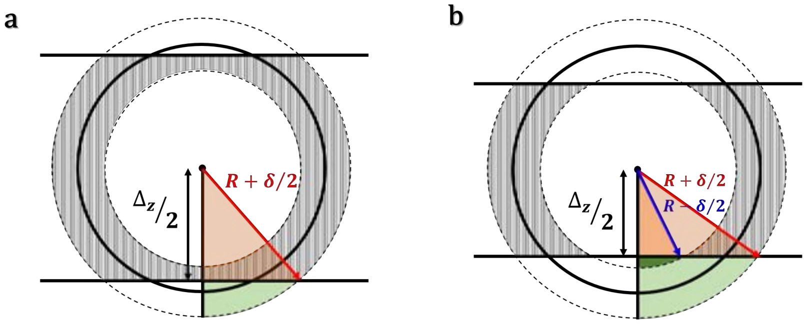

Figure B.3: schematic plan view of the circular dislocation and the observation depth limit Δ_z. (a) For the case $(\Delta_z+\delta)/2 > R > (\Delta_z-\delta)/2$. (b) For the case $R > (\Delta_z+\delta)/2$.

For $(\Delta_z+\delta)/2 > R > (\Delta_z-\delta)/2$ (see fig. B.3(a)), the volume of the striped region is:

$$\begin{aligned} V_i = 2\pi R_i\delta^2 - 4\delta A_{2d}(\boldsymbol{R_i+\delta/2}) = \\ = 2\pi R_i\delta^2 - \delta\left(R_i+\delta/2\right)\left[\left(R_i+\delta/2\right)2\arccos\left(\Delta_z/2(R_i+\delta/2)\right) - \Delta_z\sqrt{1-\left(\Delta_z/2(R_i+\delta/2)\right)^2}\right] \end{aligned} \tag{B.8}$$

For $R > (\Delta_z+\delta)/2$ (see fig. B.3(b)), the volume of the striped region is:

$$\begin{aligned} V_i = 2\pi R_i\delta^2 - 4\delta A_{2d}(\boldsymbol{R_i+\delta/2}) + 4\delta A_{2d}(\boldsymbol{R_i-\delta/2}) = \\ = 2\pi R_i\delta^2 - \delta\left(R_i+\delta/2\right)\left[\left(R_i+\delta/2\right)2\arccos\left(\Delta_z/2(R_i+\delta/2)\right) - \Delta_z\sqrt{1-\left(\Delta_z/2(R_i+\delta/2)\right)^2}\right] + \\ +\delta\left(R_i-\delta/2\right)\left[\left(R_i-\delta/2\right)2\arccos\left(\Delta_z/2(R_i-\delta/2)\right) - \Delta_z\sqrt{1-\left(\Delta_z/2(R_i-\delta/2)\right)^2}\right] \end{aligned} \tag{B.9}$$

In summary:

$$V_i(R_i) =$$

$$= \begin{cases} 2\pi R_i \delta^2 & \text{for } R_i < \frac{(\Delta_z-\delta)}{2} \\ 2\pi R_i\delta^2 - \\ -\delta\left(R_i+\frac{\delta}{2}\right)\left[\left(R_i+\frac{\delta}{2}\right)2\arccos\left(\frac{\Delta_z}{2(R_i+\frac{\delta}{2})}\right)-\Delta_z\sqrt{1-\left(\frac{\Delta_z}{2(R_i+\frac{\delta}{2})}\right)^2}\right] & \text{for } \frac{(\Delta_z+\delta)}{2} > R_i > \frac{(\Delta_z-\delta)}{2} \\ 2\pi R_i\delta^2 - \\ -\delta\left(R_i+\frac{\delta}{2}\right)\left[\left(R_i+\frac{\delta}{2}\right)2\arccos\left(\frac{\Delta_z}{2(R_i+\frac{\delta}{2})}\right)-\Delta_z\sqrt{1-\left(\frac{\Delta_z}{2(R_i+\frac{\delta}{2})}\right)^2}\right]+ & \text{for } R_i > \frac{(\Delta_z+\delta)}{2} \\ +\delta\left(R_i-\frac{\delta}{2}\right)\left[\left(R_i-\frac{\delta}{2}\right)2\arccos\left(\frac{\Delta_z}{2(R_i-\frac{\delta}{2})}\right)-\Delta_z\sqrt{1-\left(\frac{\Delta_z}{2(R_i-\frac{\delta}{2})}\right)^2}\right] \end{cases} \tag{B.10}$$

The $V_i(\boldsymbol{R_i})$ dependence is plotted in fig. B.4 for the three different ranges of R_i for each case.

Finally, the expression used for the calculation of ρ_{dis} is:

$$\rho_{dis} = \frac{\sum_i^{R_i<\frac{(\Delta_z-\delta)}{2}} V_i + \sum_i^{\frac{(\Delta_z+\delta)}{2}>R_i>\frac{(\Delta_z-\delta)}{2}} V_i + \sum_i^{R_i>\frac{(\Delta_z+\delta)}{2}} V_i}{\Delta_x\Delta_y\Delta_z} \tag{B.11}$$

Where V_i corresponds to each case developed in equation (B.10).

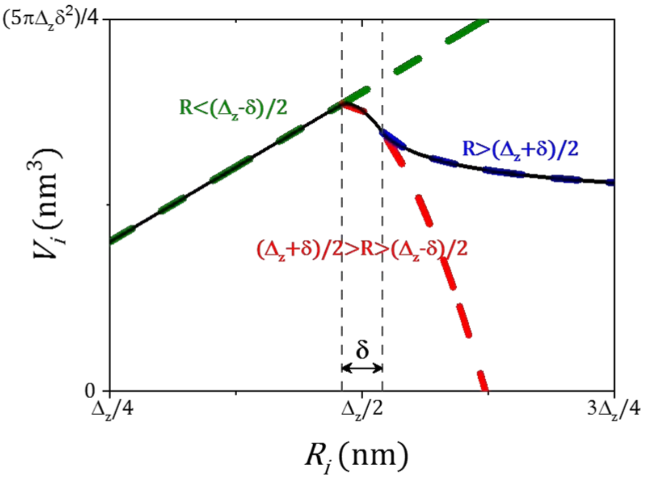

Figure B.4: volume V_i as a function of the stacking fault radius R_i. The dashed lines correspond to the volume of each of the cases from equation (B.10). The solid line corresponds to the combined V_i.

REFERENCES

[1] J Ortoli, S Klein. La superconductividad, historia y leyendas. *Salvat Editores S. A.*, 1993.

[2] J De Nobel and P Lindenfeld. The Discovery of Superconductivity. *Physics Today, 49(9), pages 40-42*, 1996. `https://doi.org/10.1063/1.881517`

[3] R De Bruyn Outober. Heike Kamerlingh Onnes's Discovery of Superconductivity. *Scientific American, pages 98-103*, 1997. `https://ilorentz.org/history/cold/Bruyn_Ouboter_SciAM.pdf`

[4] D Van Delft and P Kes. The discovery of superconductivity. *Physics Today, 63(9), pages 38-43*, 2010. `https://doi.org/10.1063/1.3490499`

[5] M Tinkham. Introduction to superconductivity. *Dover Publications*, 1996.

[6] W Meissner and R Ochsenfeld. Ein neuer Effekt bei Eintritt der Supraleitfähigkeit. *Die Naturwissenschaften, 21(44), pages 787-788*, 1933. `https://doi.org/10.1007/BF01504252`

[7] G Blatter, M V Feigel'man, V B Geshkenbein, A I Larkin, and V M Vinokur. Vortices in high-temperature superconductors. *Reviews of Modern Physics, 66(4), pages 1125-1388*, 1994. `https://doi.org/10.1103/RevModPhys.66.1125`

[8] J M Lock, A B Pippard, and D Shoenberg. Superconductivity of tin isotopes. *Mathematical Proceedings of the Cambridge Philosophical Society, 47(4), pages 811-819*, 1951. `https://doi.org/10.1017/S0305004100027250`

[9] B Serin, C A Reynolds, and C Lohman. The isotope effect in superconductivity. II. Tin and lead. *Physical Review, 86(2), pages 162-164*, 1952. `https://doi.org/10.1103/PhysRev.86.162`

[10] E Maxwell. Superconductivity of the Isotopes of Tin. *Physical Review, 86(2), pages 235-242*, 1952. `https://doi.org/10.1103/PhysRev.86.235`

[11] J Bardeen, L N Cooper, and J R Schrieffer. Microscopic Theory of Superconductivity. *Physical Review, 106, pages 162-164*, 1957. `https://doi.org/10.1103/PhysRev.106.162`

[12] E H Brandt. The flux-line lattice in superconductors. *Reports on Progress in Physics, 58, pages 1465-1594*, 1995. `https://doi.org/10.1088/0034-4885/58/11/003`

[13] P J Ray. Structural investigation of $\mathrm{La_{2-x}Sr_xCuO_{4+y}}$ - Following staging as a function of temperature. *Master thesis*, 2015. `https://figshare.com/articles/Structural_investigation_of_La_2_x_Sr_x_CuO_4_y_Following_staging_as_a_function_of_temperature/2075680/2`

[14] P C Canfield. Still alluring and hard to predict at 100. *Nature Materials, 10, pages 259-261*, 2011. `https://doi.org/10.1038/nmat2990`

[15] P H Rogalla, H Kes. 100 years of superconductivity. *Taylor and Francis Group*, 2012.

[16] U Essmann and E Träuble. The Direct Observation of Individual Flux Lines in type II superconductors. *Physics Letters, 24(10), pages 526-527*, 1967. `https://doi.org/10.1016/0375-9601(67)90819-5`

[17] J R Waldram. Superconductivity of metals and cuprates. *Institute of Physics Publishing*, 1996.

[18] C P Bean. Magnetization of hard superconductors. *Physical Review Letters, 8(6), pages 250-253*, 1962. `https://doi.org/10.1103/PhysRevLett.8.250`

[19] D X Chen and R B Goldfarb. Kim model for magnetization of type-II superconductors. *Journal of Applied Physics, 66(6), pages 2489-2500*, 1989. `https://doi.org/10.1103/PhysRevLett.8.250`

[20] A Sanchez and C Navau. Magnetic properties of finite superconducting cylinders. I. Uniform applied field. *Physical Review B, 64(214506), pages 1-10*, 2001. `https://doi.org/10.1103/PhysRevB.64.214506`

[21] F C Moon. Superconducting Levitation. *Wiley-Interscience Publication*, 1994.

[22] J G Bednorz and K A Müller. Possible Hight Tc Superconductivity in the Ba-La-Cu-O System. *Zeitschrift für Physik B - Condensed Matter, 64(2), pages 189-193*, 1986. `https://doi.org/10.1007/BF01303701`

[23] A Gurevich. To use or not to use cool superconductors? *Nature materials, 10, pages 255-9*, 2011. `https://doi.org/10.1038/nmat2991`

[24] K Isawa, T Higuchi, T Machi, A Tokiwa-Yamamoto, S Adachi, M Murakami, and H Yamauchi. Irreversibility line for a Pb-doped Hg-Ba-Ca-Cu-O superconductor. *Applied Physics Letters, 64(10), pages 1301-1303*, 1994. `https://doi.org/10.1063/1.111941`

[25] J Kumar, D Sharma, P K Ahluwalia, and V P S Awana. Enhanced superconducting performance of melt quenched $Bi_2Sr_2CaCu_2O_8$ (Bi-2212) superconductor. *Materials Chemistry and Physics, 139(2-3), pages 681-688*, 2013. `https://doi.org/10.1016/j.matchemphys.2013.02.016`

[26] T P Sheahen. Introduction to High-Temperature Superconductivity. *Plenum Press, New York*, 1994.

[27] J L Tallon, C Bernhard, H Shaked, R L Hitterman, and J D Jorgensen. Generic superconducting phase behavior in high-T_c cuprates: T_c variation with hole concentration in $YBa_2Cu_3O_{7-\delta}$. *Physical Review B, 51(18), pages 12911-12914*, 1995. `https://doi.org/10.1103/PhysRevB.51.12911`

[28] E F Talantsev, N M Strickland, S C Wimbush, J G Storey, J L Tallon, and N J Long. Hole doping dependence of critical current density in $YBa_2Cu_3O_{7-\delta}$ conductors. *Applied Physics Letters, 104(242601), pages 1-4*, 2014. `http://dx.doi.org/10.1063/1.4883483`

[29] V Breit, P Schweiss, R Hauff, H Wühl, H Claus, H Rietschel, A Erb, and G Müller-Vogt. Evidence for chain superconductivity in near-stoichiometric $YBa_2Cu_3O_x$ single crystals. *Physical Review B, 52(22), pages R15727-R15730*, 1995. `https://doi.org/10.1103/PhysRevB.52.R15727`

[30] M A Beno, L Soderholm, D W Capone, D G Hinks, J D Jorgensen, J D Grace, Ivan K Schuller, C U Segre, and K Zhang. Structure of the single-phase high-temperature superconductor $YBa_2Cu_3O_{7-\delta}$. *Applied Physics Letters*, 51(1), pages 57-59, 1987. `http://dx.doi.org/10.1063/1.98886`

[31] A Xu, J Jaroszynski, F Kametani, and D Larbalestier. Broad temperature range study of J_c and H_{irr} anisotropy in $YBa_2Cu_3O_x$ thin films containing either Y_2O_3 nanoparticles or stacking faults. *Applied Physics Letters*, 106(5), 2015. `https://doi.org/10.1063/1.4907891`

[32] E Bartolomé, F Vallés, V Rouco, N Pompeo, F F Balakirev, B Maiorov, L Civale, T Puig, X Obradors and E Silva. Intrinsic anisotropy versus effective pinning anisotropy in $YBa_2Cu_3O_7$ thin films and nanocomposites. *Submitted*, 2019.

[33] M Tachiki and S Takahashi. Strong vortex pinning intrinsic in high-T_c oxide superconductors. *Solid State Communications, 70(3), pages 291-295*, 1989. `https://doi.org/10.1016/0038-1098(89)90330-X`

[34] B Maiorov, A Kursumovic, L Stan, H Zhou, H Wang, L Civale, R Feenstra, and J L MacManus-Driscoll. Vortex pinning landscape in $YBa_2Cu_3O_7$ films grown by hybrid liquid phase epitaxy. *Superconductor Science and Technology, 20(9), pages S223-S229*, 2007. `https://doi.org/10.1088/0953-2048/20/9/S17`

[35] T Puig, J Gutiérrez, A Pomar, A Llordés, J Gázquez, S Ricart, F Sandiumenge, and X Obradors. Vortex pinning in chemical solution nanostructured YBCO films. *Superconductor Science and Technology, 21(034008), pages 1-12*, 2008. `https://doi.org/10.1088/0953-2048/21/3/034008`

[36] B Maiorov, S A Baily, H Zhou, O Ugurlu, J A Kennison, P C Dowden, T G Holesinger, S R Foltyn, and L Civale. Synergetic combination of different types of defect to optimize pinning landscape using $BaZrO_3$-doped $YBa_2Cu_3O_7$. *Nature materials, 8(5), pages 398-404*, 2009. `https://doi.org/10.1038/nmat2408`

[37] M Miura, B Maiorov, S A Baily, N Haberkorn, J O Willis, K Marken, T Izumi, Y Shiohara, and L Civale. Mixed pinning landscape in nanoparticle-introduced $YGdBa_2Cu_3O_y$ films grown by metal organic deposition. *Physical Review B, 83(184519), pages 1-8*, 2011. `https://doi.org/10.1103/PhysRevB.83.184519`

[38] K Matsumoto, T Horide, A K Jha, P Mele, Y Yoshida, and S Awaji. Irreversibility Fields and Critical Current Densities in Strongly Pinned $YBa_2Cu_3O_{7-x}$ Films With Artificial Pinning Centers. *IEEE Transactions on Applied Superconductivity, 25(3), pages 1-6*, 2015. `https://doi.org/10.1109/TASC.2015.2396358`

[39] N Haberkorn, Jeehoon Kim, S Suárez, Jae-hun Lee, and S H Moon. Influence of random point defects introduced by proton irradiation on the flux creep rates and magnetic field dependence of the critical current density J_c of co-evaporated $GdBa_2Cu_3O_{7-\delta}$ coated conductors. *Superconductor Science and Tech-*

nology, 28(125007), pages 1-6, 2015. `https://doi.org/10.1088/0953-2048/28/12/125007`

[40] A Palau, F Vallès, V Rouco, M Coll, Z Li, C Pop, B Mundet, J Gàzquez, R Guzman, J Gutierrez, X Obradors, and T Puig. Disentangling vortex pinning landscape in chemical solution deposited superconducting $\mathrm{YBa_2Cu_3O_{7-x}}$ films and nanocomposites. *Superconductor Science and Technology, 31(034004), pages 1-12*, 2018. `https://doi.org/10.1088/1361-6668/aaa65e`

[41] D S Fisher, M P A Fisher, and D A Huse. Thermal Fluctuations, quenched disorder, phase transitions, and transport in type-II superconductors. *Physical Review B, 43(1), pages 130-159*, 1991. `https://doi.org/10.1103/PhysRevB.43.130`

[42] M P A Fisher. Vortex-glass superconductivity: A possible new phase in bulk high-$\mathrm{T_c}$ oxides. *Physical Review Letters, 62(12), pages 1415-1418*, 1989. `https://doi.org/10.1103/PhysRevLett.62.1415`

[43] C Dekker, W Eidelloth, and R H Koch. Measurement of the Exponent μ in the Low-Temperature Phase of $\mathrm{YBa_2Cu_3O_{7-\delta}}$ Films in a Magnetic Field: Direct Evidence for a Vortex-Glass Phase. *Physical Review Letters, 68(22), pages 3347-3350*, 1992. `https://doi.org/10.1103/PhysRevLett.68.3347`

[44] D R Nelson and V M Vinokur. Boson localization and correlated pinning of superconducting vortex arrays. *Physical Review B, 48(17), pages 60-97*, 1993. `https://doi.org/10.1103/PhysRevB.48.13060`

[45] W Jiang, N C Yeh, D S Reed, U Kriplani, D A Beam, M Konczykowski, T A Tombrello, and F Holtzberg. Evidence of a Bose-glass transition in superconducting $\mathrm{YBa_2Cu_3O_7}$ single crystals with columnar defects. *Physical Review Letters, 72(4), pages 550-553*, 1994. `https://doi.org/10.1103/PhysRevLett.72.550`

[46] P W Anderson. Theory of flux creep in hard superconductors. *Physical Review Letters, 9(7), pages 309-311*, 1962. `https://doi.org/10.1103/PhysRevLett.9.309`

[47] P W Anderson and Y B Kim. Hard Superconductivity : Theory of the Motion of Abrikosov Flux Lines. *Reviews of Modern Physics, 36, pages 39-43*, 1964. `https://doi.org/10.1103/RevModPhys.36.39`

[48] Y Yeshurun, A P Malozemoff, and A Shaulov. Magnetic relaxation in high-temperature superconductors. *Reviews of Modern Physics, 68(3), pages 911-949*, 1996. `https://doi.org/10.1103/RevModPhys.68.911`

[49] J D Hettinger, A G Swanson, W J Skocpol, J S Brooks, J M Graybeal, P M Mankiewich, R E Howard, B L Straughn, and E G Burkhardt. Flux Creep and High-Field Critical Currents in Epitaxial Thin Films of $\mathrm{YBa_2Cu_3O_7}$. *Physical Review Letters, 62(17), pages 2044-2047*, 1989. `https://doi.org/10.1103/PhysRevLett.62.2044`

[50] E Zeldov, N M Amer, G Koren, A Gupta, M W McElfresh, and R J Gambino. Flux creep characteristics in high-temperature superconductors. *Applied Physics Letters, 56(7), pages 680-682*, 1990. `https://doi.org/10.1063/1.103310`

[51] M P Paranthaman and Teruo Izumi. High-Performance YBCO-Coated Superconductor Wires. *MRS Bulletin, 29(8), pages 533-541*, 2004. `https://doi.org/10.1557/mrs2004.159`

[52] X Obradors, T Puig, A Pomar, F Sandiumenge, N Mestres, M Coll, A Cavallaro, N Romà, J Gázquez, J C González, O Castaño, J Gutierrez, A Palau, K Zalamova, S Morlens, A Hassini, M Gibert, S Ricart, J M Moretó, S Piñol, D Isfort, and J Bock. Progress towards all-chemical superconducting $YBa_2Cu_3O_7$-coated conductors. *Superconductor Science and Technology, 19(3), pages S13-S26*, 2006. `https://doi.org/10.1088/0953-2048/19/3/003`

[53] M W Rupich, X Li, C Thieme, S Sathyamurthy, S Fleshler, D Tucker, E Thompson, J Schreiber, J Lynch, D Buczek, K Demoranville, J Inch, P Cedrone, and J Slack. Advances in second generation high temperature superconducting wire manufacturing and R&D at American Superconductor Corporation. *Superconductor Science and Technology, 23(014015), pages 1-9*, 2010. `https://doi.org/10.1088/0953-2048/23/1/014015`

[54] Y Shiohara, M Yoshizumi, Y Takagi, and T Izumi. Future prospects of high T_c superconductors-coated conductors and their applications. *Physica C: Superconductivity and its Applications, 484, pages 1-5*, 2013. `https://doi.org/10.1016/j.physc.2012.03.058`

[55] V Selvamanickam, Y Chen, T Shi, Y Liu, N D Khatri, J Liu, Y Yao, X Xiong, C Lei, S Soloveichik, E Galstyan, and G Majkic. Enhanced critical currents in $(Gd, Y)Ba_2Cu_3O_x$ superconducting tapes with high levels of Zr addition. *Superconductor Science and Technology, 26(035006), pages 1-9*, 2013. `https://doi.org/10.1088/0953-2048/26/3/035006`

[56] X Obradors and T Puig. Coated conductors for power applications: materials challenges. *Superconductor Science and Technology, 27(044003), pages 1-17*, 2014. `https://doi.org/10.1088/0953-2048/27/4/044003`

[57] D Larbalestier, A Gurevich, D M Feldmann, and A Polyanskii. High-T_c superconducting materials for electric power applications. *Nature, 414, pages 368-377*, 2001. `https://doi.org/10.1038/35104654`

[58] N Newman, B F Cole, S M Garrison K Char and R C Taber. Double Gun Off-Axis Sputtering of Large Area $YBa_2Cu_3O_{7-\delta}$ Superconducting Films for Microwave Applications. *IEEE Transactions on Magnetics, 27(2), pages 1276-1279*, 1991. `https://doi.org/10.1109/20.133417`

[59] M Lorenz, H Hochmuth, D Natusch, H Börner, G Lippold, K Kreher, and W Schmitz. Large-area double-side pulsed laser deposition of $YBa_2Cu_3O_{7-x}$ thin films on 3-in. sapphire wafers. *Applied Physics Letters, 68(23), pages 3332-3334*, 1996. `https://doi.org/10.1063/1.116048`

[60] R K Singh and D Kumar. Pulsed laser deposition and characterization of high-T_c $YBa_2Cu_3O_{7-x}$ superconducting thin films. *Materials Science and Engineering: R: Reports, 22(4), pages 113-185*, 1998. `https://doi.org/10.1016/S0927-796X(97)00019-3`

[61] H M Christen, D F Lee, F A List, S W Cook, K J Leonard, L Heatherly, P M Martin, M Paranthaman, A Goyal, and C M Rouleau. Pulsed electron deposition of fluorine-based precursors for $YBa_2Cu_3O_{7-x}$-coated conductors. *Superconductor Science and Technology, 18(9), pages 1168-1175*, 2005. `https://doi.org/10.1088/0953-2048/18/9/004`

[62] H J Scheel, C Klemenz, F K Reinhart, H P Lang, and H J Güntherodt. Monosteps on extremely flat $YBa_2Cu_3O_{7-x}$ surfaces grown by liquid-phase epitaxy. *Applied Physics Letters, 65(7), pages 901-903*, 1994. `https://doi.org/10.1063/1.112195`

[63] I M Watson. Metal-Organic CVD of the High-Tc Superconductor YBa2Cu3O7-δ. *Chemical Vapor Deposition, 3(1), pages 9-26*, 1997. `https://doi.org/10.1002/cvde.19970030102`

[64] R W Schwartz, T Schneller, and R Waser. Chemical solution deposition of electronic oxide films. *Comptes Rendus Chimie, 7(5), pages 433-461*, 2004. `https://doi.org/10.1016/j.crci.2004.01.007`

[65] X Obradors, T Puig, S Ricart, M Coll, J Gazquez, A Palau, and X Granados. Growth, nanostructure and vortex pinning in superconducting $YBa_2Cu_3O_7$ thin films based on trifluoroacetate solutions. *Superconductor Science and Technology, 25(123001), pages 1-32*, 2012. `https://doi.org/10.1088/0953-2048/25/12/123001`

[66] X Obradors, T Puig, Z Li, C Pop, B Mundet, N Chamorro, F Vallés, M Coll, S Ricart, B Vallejo, F Pino, A Palau, J Gázquez, J Ros, and A Usoskin. Epitaxial $YBa_2Cu_3O_{7-x}$ nanocomposite films and coated conductors from $BaMO_3$ (M=Zr,Hf) colloidal solutions. *Superconductor Science and Technology, 31(044001), pages 1-16*, 2018. `https://doi.org/10.1088/1361-6668/aaaad7`

[67] A Gupta, R Jagannathan, E I Cooper, E A Giess, J I Landman, and B W Hussey. Superconducting oxide films with high transition temperature prepared from metal trifluoroacetate precursors. *Applied Physics Letters, 52(24), pages 2077-2079*, 1988. `https://doi.org/10.1063/1.99752`

[68] N Roma, S Morlens, S Ricart, K Zalamova, J M Moreto, A Pomar, T Puig, and X Obradors. Acid anhydrides: A simple route to highly pure organometallic solutions for superconducting films. *Superconductor Science and Technology*, 19(6), pages 521-527, 2006. `https://doi.org/10.1088/0953-2048/19/6/019`

[69] A A Armenio, A Augieri, L Ciontea, G Contini, I Davoli, M Di Giovannantonio, V Galluzzi, A Mancini, A Rufoloni and T Petrisor. Structural and chemical evolution of propionate based metal-organic precursors for superconducting YBCO epitaxial film growth. *Superconductor Science and Technology, 24(115008)*, 2011. `https://doi.org/10.1088/0953-2048/24/11/115008`

[70] Y Chen, C Wu, G Zhao, and C You. An advanced low-fluorine solution route for fabrication of high-performance YBCO superconducting films. *Superconductor Science and Technology, 25(062001), pages 1-5*, 2012. `https://doi.org/10.1088/0953-2048/25/6/062001`

[71] X Palmer, C Pop, H Eloussifi, B Villarejo, P Roura, J Farjas, A Calleja, A Palau, X Obradors, T Puig, and S Ricart. Solution design for low-fluorine trifluoroacetate

route to $YBa_2Cu_3O_7$ films. *Superconductor Science and Technology, 29(024002), pages 1-11*, 2016. `https://doi.org/10.1088/0953-2048/29/2/024002`

[72] C Pop, B Villarejo, F Pino, B Mundet, S Ricart, T Puig, and X Obradors. Growth of all-chemical high critical current $YBa_2Cu_3O_{7-\delta}$ thick films and coated conductors. *Superconductor Science and Technology, 32(015004), pages 1-18*, 2019. `https://doi.org/10.1088/1361-6668/aaea4e`

[73] L Soler. Liquid-assisted ultrafast growth of superconducting films derived from chemical solutions. *PhD thesis*, 2019.

[74] Z Li. Growth and Characterization of Nanocomposite $YBa_2Cu_3O_{7-\delta}$–$BaMO_3$ (M=Zr,Hf) Nanocomposite Colloidal Solutions. *PhD thesis*, 2018. `http://hdl.handle.net/10803/663979`

[75] A Llordés, A Palau, J Gázquez, M Coll, R Vlad, A Pomar, J Arbiol, R Guzmán, S Ye, V Rouco, F Sandiumenge, S Ricart, T Puig, M Varela, D Chateigner, J Vanacken, J Gutiérrez, V Moshchalkov, G Deutscher, C Magen, and X Obradors. Nanoscale strain-induced pair suppression as a vortex-pinning mechanism in high-temperature superconductors. *Nature Materials, 11, pages 329-336*, 2012. `https://doi.org/10.1038/nmat3247`

[76] M Coll, R Guzman, P Garcés, J Gazquez, V Rouco, A Palau, S Ye, C Magen, H Suo, H Castro, T Puig, and X Obradors. Size-controlled spontaneously segregated Ba_2YTaO_6 nanoparticles in $YBa_2Cu_3O_7$ nanocomposites obtained by chemical solution deposition. *Superconductor Science and Technology, 27(044008), pages 1-9*, 2014. `https://doi.org/10.1088/0953-2048/27/4/044008`

[77] P Cayado. *Multifunctional nanostructured superconductors by chemical routes: towards high current conductors. PhD thesis*, 2016. `http://hdl.handle.net/10803/384856`

[78] P Cayado, K De Keukeleere, A Garzón, L Perez-Mirabet, A Meledin, J De Roo, F Vallés, B Mundet, H Rijckaert, G Pollefeyt, M Coll, S Ricart, A Palau, J Gázquez, J Ros, G Van Tendeloo, I Van Driessche, T Puig, and X Obradors. Epitaxial $YBa_2Cu_3O_{7-x}$ nanocomposite thin films from colloidal solutions. *Superconductor Science and Technology, 28(124007), pages 1-18*, 2015. `https://doi.org/10.1088/0953-2048/28/12/124007`

[79] K De Keukeleere, P Cayado, A Meledin, F Vallès, J De Roo, H Rijckaert, G Pollefeyt, E Bruneel, A Palau, M Coll, S Ricart, G Van Tendeloo, T Puig, X Obradors, and I Van Driessche. Superconducting $YBa_2Cu_3O_{7-\delta}$ Nanocomposites Using Preformed ZrO_2 Nanocrystals: Growth Mechanisms and Vortex Pinning Properties. *Advanced Electronic Materials, 2(10), pages 1-9*, 2016. `https://doi.org/10.1002/aelm.201600161`

[80] F Sánchez, C Ocal, and J Fontcuberta. Tailored surfaces of perovskite oxide substrates for conducted growth of thin films. *Chemical Society Reviews, 43(7), pages 2272-2285*, 2014. `http://doi.org/10.1039/C3CS60434A`

[81] M Vilardell, X Granados, S Ricart, I V Driessche, T Puig, and X Obradors. Flexible manufacturing of functional ceramic coatings by inkjet printing. *Thin Solid Films, 548, pages 489-497*, 2013. `https://doi.org/10.1016/j.tsf.2013.09.012`

[82] B Villarejo. *Synthesis of defect free* $YBa_2Cu_3O_{7-x}$ *films over 1µm by CSD using Inkjet Printing. PhD thesis*, 2018. `http://hdl.handle.net/10803/664222`

[83] A Llordés, K Zalamova, S Ricart, A Pomar, T Puig, A Hardy, M K Van Bael, and X Obradors. Evolution of Metal-Trifluoroacetate Precursors in the Thermal Decomposition toward High-Performance $YBa_2Cu_3O_7$ Superconducting Films. *Chemistry of Materials, 22(5), pages 1686-1694*, 2010. `https://doi.org/10.1021/cm903080k`

[84] E D Specht, C J Sparks, A G Dhere, J Brynestad, O B Cavin, D M Kroeger, and H A Oye. Effect of oxygen pressure on the orthorhombic-tetragonal transition in the high-temperature superconductor $YBa_2Cu_3O_x$. *Physical Review B, 37(13), pages 7426-7434*, 1988. `https://doi.org/10.1103/PhysRevB.37.7426`

[85] C J Jou and J Washburn. Formation of coherent twins in $YBa_2Cu_3O_{7-\delta}$ superconductors. *J. Mater. Res, 4(4), pages 795-801*, 1989. `https://doi.org/10.1557/JMR.1989.0795`

[86] K Zalamova, A Pomar, A Palau, T Puig, and X Obradors. Intermediate phase evolution in YBCO thin films grown by the TFA process. *Superconductor Science and Technology, 23(014012), pages 1-11*, 2010. `https://doi.org/10.1088/0953-2048/23/1/014012`

[87] David S. Ginley David A. Cardwell. Handbook of Superconducting Materials. *IOP Publishing Ltd*, 2003.

[88] J W Ekin, T M Larson, N F Bergren, A J Nelson, A B Swartzlander, L L Kazmerski, A J Panson, and B A Blankenship. High T_c superconductor/noble-metal contacts with surface resistivities in the 10^{-10} Ω cm^2 range. *Applied Physics Letters, 52(21), pages 1819-1821*, 1988. `https://doi.org/10.1063/1.99725`

[89] A Stangl. Oxygen kinetics and charge doping for high critical current YBCO films. *PhD thesis*, 2019.

[90] W H Bragg and W L Bragg. The Reflection of X-rays by Crystals. *Proceedings of the Royal Society of London, 88, pages 428-438*, 1913. `https://doi.org/10.1098/rspa.1913.0040`

[91] B Tlili. Caractérisation de films durs multicouches élaborés par pulvérisation magnétron. Influence des conditions d'élaboration sur leurs propriétés. *PhD thesis*, 2010. `https://pastel.archives-ouvertes.fr/pastel-00573968`

[92] G K Williamson and W H Hall. X-Ray Line Broadening from Filed Aluminium and Wolfram. *Acta metallurgica, 1(1), pages 22-31*, 1953. `https://doi.org/10.1016/0001-6160(53)90006-6`

[93] R C Jaklevic, J Lambe, A H Silver, and J E Mercereau. Quantum Interference Effects in Josephson Tunneling. *Physical Review Letters, 12(7), pages 159-160*, 1964. `https://doi.org/10.1103/PhysRevLett.12.159`

[94] S Murase, K Itoh, H Wada, K Noto, Y Kimura, Y Tanaka, and K Osamura. Critical temperature measurement method of composite superconductors. *Physica C: Superconductivity, 357-360, Part 2, pages 1197-1200*, 2001. `https://doi.org/10.1016/S0921-4534(01)00483-X`

[95] M J Hÿtch, E Snoeck, and R Kilaas. Quantitative measurement of displacement and strain fields from HREM micrographs. *Ultramicroscopy, 74(3), pages 131-146*, 1998. `https://doi.org/10.1016/S0304-3991(98)00035-7`

[96] R Guzmán. *In-depth investigation of the origin, evolution and interaction of structural defects in YBCO nanocomposite thin films. PhD thesis*, 2013. `http://hdl.handle.net/10803/129295`

[97] B Mundet. *Atomic-scale characterization of structural distortions in perovskite oxide thin films. PhD thesis*, 2018. `http://hdl.handle.net/10803/664357`

[98] J Gutiérrez, T Puig, and X Obradors. Anisotropy and strength of vortex pinning centers in $YBa_2Cu_3O_{7-\delta}$ coated conductors. *Applied Physics Letters, 90(162514), pages 1-3*, 2007. `https://doi.org/10.1063/1.2728757`

[99] A Sanchez, C Navau, N Del-Valle, D Chen, and J R Clem. Self-fields in thin superconducting tapes: Implications for the thickness effect in coated conductors. *Applied Physics Letters, 96(072510), pages 1-3*, 2010. `https://doi.org/10.1063/1.3315893`

[100] E. F. Talantsev and J. L. Tallon. Universal self-field critical current for thin-film superconductors. *Nature Communications, 6(7820), pages 1-8*, 2015. `https://doi.org/10.1038/ncomms8820`

[101] L Krusin-Elbaum, L Civale, G Blatter, A D Marwick, F Holtzberg, and C Feild. Bose-Glass melting in YBaCuO crystals with correlated disorder. *Physical Review Letters, 72(12), pages 1914-1917*, 1994. `https://doi.org/10.1103/PhysRevLett.72.1914`

[102] L Krusin-Elbaum, L Civale, J R Thompson, and C Feild. Accommodation of vortices to columnar defects: Evidence for large entropic reduction of vortex localization. *Physical Review B, 53(17), pages 744-750*, 1996. `https://doi.org/10.1103/PhysRevB.53.11744`

[103] L Civale. Vortex pinning and creep in high-temperature superconductors with columnar defects. *Superconductor Science and Technology, 10(7A), pages A11-A28*, 1997. `https://doi.org/10.1088/0953-2048/10/7A/003`

[104] W Kwok, U Welp, A Glatz, A E Koshelev, K J Kihlstrom, and G W Crabtree. Vortices in high-performance high-temperature superconductors. *Reports on Progress in Physics, 79(116501), pages 1-39*, 2016. `https://doi.org/10.1088/0034-4885/79/11/116501`

[105] B Dam, J M Huijbregtse, F C Klaassen, R C F van der Geest, G Doornbos, J H Rector, A M Testa, S Freisem, J C Martinez, B Stäuble-Pümpin, and R Griessen. Origin of high critical currents in $YBa_2Cu_3O_{7-\delta}$ superconducting thin films. *Nature, 399, pages 439-442*, 1999. `https://doi.org/10.1038/20880`

[106] C J van der Beek, M Konczykowski, A Abal'oshev, I Abal'osheva, P Gierlowski, S J Lewandowski, M V Indenbom, and S Barbanera. Strong pinning in high-temperature superconducting films. *Physical Review B, 66(024523), pages 1-10*, 2002. `https://doi.org/10.1103/PhysRevB.66.024523`

[107] A O Ijaduola, J R Thompson, R Feenstra, D K Christen, A A Gapud, and X Song. Critical currents of ex situ $YBa_2Cu_3O_{7-\delta}$ thin films on rolling assisted biaxially textured substrates: Thickness, field, and temperature dependencies. *Physical Review B, 73(134502), pages 1-9*, 2006. `https://doi.org/10.1103/PhysRevB.73.134502`

[108] F C Klaassen, G Doornbos, J M Huijbregtse, R C F van der Geest, B Dam, and R Griessen. Vortex pinning by natural linear defects in thin films of $YBa_2Cu_3O_{7-\delta}$. *Physical Review B, 64(184523), pages 1-20*, 2001. `https://doi.org/10.1103/PhysRevB.64.184523`

[109] B Maiorov, H Wang, S R Foltyn, Y Li, R DePaula, L Stan, P N Arendt, and L Civale. Influence of naturally grown nanoparticles at the buffer layer in the flux pinning in $YBa_2Cu_3O_7$ coated conductors. *Superconductor Science and Technology, 19(9), pages 891-895*, 2006. `https://doi.org/10.1088/0953-2048/19/9/001`

[110] S R Foltyn, L Civale, J L Macmanus-Driscoll, Q X Jia, B Maiorov, H Wang, and M Maley. Materials science challenges for high-temperature superconducting wire. *Nature materials, 6, pages 631-642*, 2007. `https://doi.org/10.1038/nmat1989`

[111] D M Feldmann, O Ugurlu, B Maiorov, L Stan, T G Holesinger, L Civale, S R Foltyn, and Q X Jia. Influence of growth temperature on critical current and magnetic flux pinning structures in $YBa_2Cu_3O_{7-x}$. *Applied Physics Letters, 91(162501), pages 1-3*, 2007. `https://doi.org/10.1063/1.2799875`

[112] K Matsumoto and P Mele. Artificial pinning center technology to enhance vortex pinning in YBCO coated conductors. *Superconductor Science and Technology, 23(014001), pages 1-12*, 2010. `https://doi.org/10.1088/0953-2048/23/1/014001`

[113] V Braccini, a Xu, J Jaroszynski, Y Xin, D C Larbalestier, Y Chen, G Carota, J Dackow, I Kesgin, Y Yao, A Guevara, T Shi, and V Selvamanickam. Properties of recent IBAD–MOCVD coated conductors relevant to their high field, low temperature magnet use. *Superconductor Science and Technology, 24(035001), pages 1-9*, 2011. `https://doi.org/10.1088/0953-2048/24/3/035001`

[114] J L MacManus-Driscoll, S R Foltyn, Q X Jia, H Wang, A Serquis, L Civale, B Maiorov, M E Hawley, M P Maley, and D E Peterson. Strongly enhanced current densities in superconducting coated conductors of $YBa_2Cu_3O_{7-x} + BaZrO_3$. *Nature materials, 3, pages 439-443*, 2004. `https://doi.org/10.1038/nmat1156`

[115] A Xu, V Braccini, J Jaroszynski, Y Xin, and D C Larbalestier. Role of weak uncorrelated pinning introduced by $BaZrO_3$ nanorods at low-temperature in $(Y, Gd)Ba_2Cu_3O_x$ thin films. *Physical Review B, 86(115416), pages 1-9*, 2012. `https://doi.org/10.1103/PhysRevB.86.115416`

[116] A Xu, L Delgado, N Khatri, Y Liu, V Selvamanickam, D Abraimov, J Jaroszynski, F Kametani, and D C Larbalestier. Strongly enhanced vortex pinning from 4 to 77 K in magnetic fields up to 31 T in 15 mol.% Zr-added (Gd,Y)-Ba-Cu-O superconducting tapes. *APL Materials, 2(046111), pages 1-8*, 2014. `https://doi.org/10.1063/1.4872060`

[117] A Goyal, S Kang, K J Leonard, P M Martin, A A Gapud, M Varela, M Paranthaman, A O Ijaduola, E D Specht, J R Thompson, D K Christen, S J Pennycook,

and F A List. Irradiation-free, columnar defects comprised of self-assembled nanodots and nanorods resulting in strongly enhanced flux-pinning in $YBa_2Cu_3O_{7-\delta}$ films. *Superconductor Science and Technology, 18(11), pages 1533-1538*, 2005. `https://doi.org/10.1088/0953-2048/18/11/021`

[118] T Aytug, M Paranthaman, K J Leonard, S Kang, P M Martin, L Heatherly, A Goyal, A O Ijaduola, J R Thompson, D K Christen, R Meng, I Rusakova, and C W Chu. Analysis of flux pinning in $YBa_2Cu_3O_{7-\delta}$ films by nanoparticle-modified substrate surfaces. *Physical Review B, 74(184505), pages 1-8*, 2006. `https://doi.org/10.1103/PhysRevB.74.184505`

[119] Y L Zuev, D K Christen, S H Wee, A Goyal, and S W Cook. Near-isotropic performance of intrinsically anisotropic high-temperature superconducting tapes due to self-assembled nanostructures. *Applied Physics Letters, 93(172512), pages 1-3*, 2008. `https://doi.org/10.1063/1.3009286`

[120] G Blatter, V B Geshkenbein, and A I Larkin. From Isotropic to Anisotropic Superconductors: A Scaling Approach. *Physical Review Letters, 68(6), pages 875-878*, 1992. `https://doi.org/10.1103/PhysRevLett.68.875`

[121] K Iida, J Hänisch, T Thersleff, F Kurth, M Kidszun, S Haindl, R Hühne, L Schultz, and B Holzapfel. Scaling behavior of the critical current in clean epitaxial $Ba(Fe_{1-x}Co_x)_2As_2$ thin films. *Physical Review B, 81(100507), pages 1-4*, 2010. `https://doi.org/10.1103/PhysRevB.81.100507`

[122] H Yamasaki, K Ohki, I Yamaguchi, M Sohma, W Kondo, H Matsui, T Manabe, and T Kumagai. Strong flux pinning due to dislocations associated with stacking faults in $YBa_2Cu_3O_{7-\delta}$ thin films prepared by fluorine-free metal organic deposition. *Superconductor Science and Technology, 23(105004), pages 1-9*, 2010. `https://doi.org/10.1088/0953-2048/23/10/105004`

[123] Víctor Rouco. Controlling Vortex Pinning and Dynamics of Nanostructured YBCO Thin Films Grown by Chemical Solution Deposition. *PhD thesis*, 2014. `http://hdl.handle.net/10803/133329`

[124] V Mishev, M Zehetmayer, D X Fischer, M Nakajima, H Eisaki, and M Eisterer. Interaction of vortices in anisotropic superconductors with isotropic defects. *Superconductor Science and Technology, 28(102001), pages 1-9*, 2015. `https://doi.org/10.1088/0953-2048/28/10/102001`

[125] M Miura, B Maiorov, F F Balakirev, T Kato, M Sato, Y Takagi, T Izumi, and L Civale. Upward shift of the vortex solid phase in high-temperature-superconducting wires through high density nanoparticle addition. *Scientific Reports, 6(20436), pages 1-9*, 2016. `https://doi.org/10.1038/srep20436`

[126] J Gutiérrez, A Llordés, J Gázquez, M Gibert, N Romà, S Ricart, A Pomar, F Sandiumenge, N Mestres, T Puig, and X Obradors. Strong isotropic flux pinning in solution-derived $YBa_2Cu_3O_{7-x}$ nanocomposite superconductor films. *Nature Materials, 6, pages 367-373*, 2007. `https://doi.org/10.1038/nmat1893`

[127] Z Chen, D M Feldmann, X Song, S I Kim, A Gurevich, J L Reeves, Y Y Xie, V Selvamanickam, and D C Larbalestier. Three-dimensional vortex pinning by nano-precipitates in a Sm-doped $YBa_2Cu_3O_{7-x}$ coated conductor. *Superconductor*

Science and Technology, 20(9), pages S205-S210, 2007. `https://doi.org/10.1088/0953-2048/20/9/S14`

[128] C Tarantini, J Jaroszynski, F Kametani, Y L Zuev, A Gurevich, Y Chen, V Selvamanickam, D C Larbalestier, and D K Christen. Anisotropy of the irreversibility field for Zr-doped $(\mathrm{Y,Gd})\mathrm{Ba_2Cu_3O_{7-x}}$ thin films up to 45 T. *Physical Review B, 84(224514), pages 1-8*, 2011. `https://doi.org/10.1103/PhysRevB.84.224514`

[129] A Palau, J H Durrell, J L MacManus-Driscoll, S Harrington, T Puig, F Sandiumenge, X Obradors, and M G Blamire. Crossover between Channeling and Pinning at Twin Boundaries in $\mathrm{YBa_2Cu_3O_7}$ Thin Films. *Physical Review Letters, 97(257002), pages 1-4*, 2006. `https://doi.org/10.1103/PhysRevLett.97.257002`

[130] V Rouco, A Palau, R Guzman, J Gazquez, M Coll, X Obradors, and T Puig. Role of twin boundaries on vortex pinning of CSD YBCO nanocomposites. *Superconductor Science and Technology, 27(125009), pages 1-7*, 2014. `https://doi.org/10.1088/0953-2048/27/12/125009`

[131] L Civale, B Maiorov, J L MacManus-Driscoll, H Wang, T G Holesinger, S R Foltyn, A Serquis, and P N Arendt. Identification of intrinsic ab-plane pinning in $\mathrm{YBa_2Cu_3O_7}$ thin films and coated conductors. *IEEE Transactions on Applied Superconductivity, 15(2), pages 2808-2811*, 2005. `https://doi.org/10.1109/TASC.2005.848218`

[132] J Gazquez, M Coll, N Roma, F Sandiumenge, T Puig, and X Obradors. Structural defects in trifluoroacetate derived $\mathrm{YBa_2Cu_3O_7}$ thin films. *Superconductor Science and Technology*, 25(065009), pages 1-8, 2012. `https://doi.org/10.1088/0953-2048/25/6/065009`

[133] R Guzman, J Gazquez, B Mundet, M Coll, X Obradors, and T Puig. Probing localized strain in solution-derived $(\mathrm{Y,Gd})\mathrm{Ba_2Cu_3O_{7-\delta}}$ nanocomposite thin films. *Physical Review Materials, 1(024801), pages 1-7*, 2017. `https://doi.org/10.1103/PhysRevMaterials.1.024801`

[134] P Marsh, R M Fleming, M L Mandich, A M DeSantolo, J Kwo, M Hong, and L J Martinez-Miranda. Crystal Structure of the 80 K superconductor $\mathrm{YBa_2Cu_4O_8}$. *Nature, 334, pages 141-143*, 1988. `https://doi.org/10.1038/334141a0`

[135] J Gazquez, R Guzman, R Mishra, E Bartolomé, J Salafranca, C Magén, M Varela, M Coll, S M Valvidares, P Gargiani, E Pellegrin, J Herrero-Martin, S J Pennycook, S T Pantelides, T Puig, and X Obradors. Emerging Diluted Ferromagnetism in High-$\mathrm{T_c}$ Superconductors Driven by Point Defect Clusters. *Advanced Science, 3(1500295), pages 1-8*, 2016. `https://doi.org/10.1002/advs.201500295`

[136] E F Talantsev, S C Wimbush, N M Strickland, J A Xia, P D' Souza, J G Storey, J L Tallon, B Ingham, R Knibbe, and N J Long. Oxygen Deficiency , Stacking Faults and Calcium Substitution in MOD YBCO Coated Conductors. *IEEE Transactions on Applied Superconductivity*, 23(3), pages 1-5, 2013. `https://doi.org/10.1109/TASC.2012.2233843`

[137] M Coll, S Ye, V Rouco, A Palau, R Guzman, J Gazquez, J Arbiol, H Suo, T Puig, and X Obradors. Solution-derived $\mathrm{YBa_2Cu_3O_7}$ nanocomposite films with

a Ba_2YTaO_6 secondary phase for improved superconducting properties. *Superconductor Science and Technology, 26(015001), pages 1-8*, 2013. `https://doi.org/10.1088/0953-2048/26/1/015001`

[138] Y Zhu, M Suenaga, J Tafto, and D O Welch. Variable nature of twin boundaries in $YBa_2Cu_3O_{7-\delta}$ and its alloys. *Physical Review B, 44(6), pages 2871-2874*, 1991. `https://doi.org/10.1103/PhysRevB.44.2871`

[139] R Guzman, J Gazquez, V Rouco, A Palau, C Magen, M Varela, J Arbiol, X Obradors, and T Puig. Strain-driven broken twin boundary coherence in $YBa_2Cu_3O_{7-\delta}$ nanocomposite thin films. *Applied Physics Letters, 102(081906), pages 1-5*, 2013. `https://doi.org/10.1063/1.4793749`

[140] L Civale, A D Marwick, T K Worthington, M A Kirk, J R Thompson, L Krusin-Elbaum, Y Sun, J R Clem and F Holtzberg Vortex Confinement by Columnar Defects in YBCO Crystals. *Physical Review Letters, 67(5), pages 648-651*, 1991. `https://doi.org/10.1103/PhysRevLett.67.648`

[141] T Matsushita. Flux pinning in superconducting 123 materials. *Superconductor Science and Technology, 13(6), pages 730-737*, 2000. `https://doi.org/10.1088/0953-2048/13/6/320`

[142] T Haugan, P N Barnes, R Wheeler, F Meisenkothen, and M Sumption. Addition of nanoparticle dispersions to enhance flux pinning of the $YBa_2Cu_3O_{7-x}$ superconductor. *Nature, 430, pages 867-870*, 2004. `https://doi.org/10.1038/nature02792`

[143] H Wang, A Serquis, B Maiorov, L Civale, Q X Jia, P N Arendt, S R Foltyn, J L MacManus-Driscoll, and X Zhang. Microstructure and transport properties of Y-rich $YBa_2Cu_3O_{7-\delta}$ thin films. *Journal of Applied Physics, 100(053904), pages 1-5*, 2006. `https://doi.org/10.1063/1.2337262`

[144] M Sieger, J Hänisch, P Pahlke, M Sparing, U Gaitzsch, K Iida, R Nast, E Reich, L Schultz, B Holzapfel, and R Hühne. $BaHfO_3$-Doped Thick $YBa_2Cu_3O_{7-\delta}$ Films on Highly Alloyed Textured Ni-W Tapes. *IEEE Transactions on Applied Superconductivity, 25(3), pages 1-4*, 2015. `https://doi.org/10.1109/TASC.2014.2372903`

[145] A Palau, E Bartolomé, A Llordés, T Puig, and X Obradors. Isotropic and anisotropic pinning in TFA-grown $YBa_2Cu_3O_{7-x}$ films with $BaZrO_3$ nanoparticles. *Superconductor Science and Technology, 24(125010), pages 1-6*, 2011. `https://doi.org/10.1088/0953-2048/24/12/125010`

[146] M Erbe, J Hänisch, R Hühne, T Freudenberg, A Kirchner, L Molina-Luna, C Damm, G Van Tendeloo, S Kaskel, L Schultz, and B Holzapfel. $BaHfO_3$ artificial pinning centres in TFA-MOD-derived YBCO and GdBCO thin films. *Superconductor Science and Technology, 28(114002), pages 1-13*, 2015. `https://doi.org/10.1088/0953-2048/28/11/114002`

[147] S Kang, A Goyal, J Li, A A Gapud, P M Martin, L Heatherly, J R Thompson, D K Christen, F A List, M Paranthaman, and D F Lee. High-Performance High-T_c Superconducting Wires. *Science, 311(5769), pages 1911-1914*, 2006. `https://doi.org/10.1126/science.1124872`

[148] L Opherden, M Sieger, P Pahlke, R Hühne, L Schultz, A Meledin, G Van Tendeloo, R Nast, B Holzapfel, M Bianchetti, J.L. MacManus-Driscoll, and J Hänisch. Large pinning forces and matching effects in $YBa_2Cu_3O_{7-\delta}$ thin films with $Ba_2Y(Nb/Ta)O_6$ nano-precipitates. *Scientific Reports, 6(21188), pages 1-10*, 2016. `https://doi.org/10.1038/srep21188`

[149] V Rouco, E Bartolomé, A Palau, M Coll, X Obradors, and T Puig. Nanostrain induced pinning in $YBa_2Cu_3O_{7-x}$ nanocomposites even close to the irreversibility line. *Superconductor Science and Technology, 25(122001), pages 1-4*, 2012. `https://doi.org/10.1088/0953-2048/25/12/122001`

[150] L Lei, L Liu, X Wang, S Wang, J Jia, G Zhao, C Wu, L Jin, C Li and P Zhang. Strongly improved current-carrying capacity induced by nanoscale lattice strains in $YBa_2Cu_3O_{7-\delta}$–$Ba_{0.7}$Sr0.3TiO3 composite films derived from chemical solution deposition. *Journal of Materials Chemistry C, 4, pages 1392-1397*, 2016. `https://doi.org/10.1039/c5tc02952j`

[151] T G Holesinger, L Civale, B Maiorov, D M Feldmann, J Y Coulter, D J Miller, V A Maroni, Z Chen, D C Larbalestier, R Feenstra, X Li, Y Huang, T Kodenkandath, W Zhang, M W Rupich, and A P Malozemoff. Progress in Nanoengineered Microstructures for Tunable High-Current, High-Temperature Superconducting Wires. *Advanced Materials, 20(3), pages 391-407*, 2008. https://doi.org/10.1002/adma.200700919

[152] G Deutscher and P G De Gennes. A spatial interpretation of emerging superconductivity in lightly doped cuprates. *Comptes Rendus Physique, 8(7-8), pages 937-941*, 2007. `https://doi.org/10.1016/j.crhy.2007.08.004`

[153] G Deutscher. Origin of weak-link behavior of grain boundaries in superconducting cuprates and pnictides. *Applied Physics Letters, 96(122502), pages 1-3*, 2010. `https://doi.org/10.1063/1.3367723`

[154] W K Kwok, U Welp, V M Vinokur, S Fleshler, J Downey, and G W Crabtree. Direct Observation of Intrinsic Pinning by Layered Structure in Single-Crystal $YBa_2Cu_3O_{7-\delta}$. *Physical Review Letters, 67(3), pages 390-393*, 1991. `https://doi.org/10.1103/PhysRevLett.67.390`

[155] L Civale, B Maiorov, A Serquis, S R Foltyn, Q X Jia, P N Arendt, H Wang, J. O Willis, J Y Coulter, T G Holesinger, J L MacManus-Driscoll, M W Rupich, W Zhang, and X Li. Influence of crystalline texture on vortex pinning near the ab-plane in $YBa_2Cu_3O_7$ thin films and coated conductors. *Physica C, 412-414, pages 976-982*, 2004. `https://doi.org/10.1016/j.physc.2003.12.076`

[156] J Gutiérrez, B Maiorov, T Puig, J Gázquez, N Romà, H Wang, F Sandiumenge, and X Obradors. The role of stacking faults in the critical current density of MOD films through a thickness dependence study. *Superconductor Science and Technology, 22(015022), pages 1-4*, 2009. `https://doi.org/10.1088/0953-2048/22/1/015022`

[157] T Horide, T Murayama, K Takata, K Matsumoto, P Mele, Y Yoshida, Y Ichino, and S Awaji. Variation of c-axis correlation on vortex pinning by ab-plane

non-superconducting layers in $YBa_2Cu_3O_7$ films. *Journal of Applied Physics, 114(073903), pages 1-7*, 2013. `https://doi.org/10.1063/1.4818518`

[158] K Iida, J Hänisch, E Reich, F Kurth, R Hühne, L Schultz, B Holzapfel, A Ichinose, M Hanawa, I Tsukada, M Schulze, S Aswartham, S Wurmehl, and B Büchner. Intrinsic pinning and the critical current scaling of clean epitaxial Fe(Se,Te) thin films. *Physical Review B, 87(104510), pages 1-6*, 2013. `https://doi.org/10.1103/PhysRevB.87.104510`

[159] C Tarantini, K Iida, J Hänisch, F Kurth, J Jaroszynski, N Sumiya, M Chihara, T Hatano, H Ikuta, S Schmidt, P Seidel, B Holzapfel, and D C Larbalestier. Intrinsic and extrinsic pinning in NdFeAs(O,F): vortex trapping and lock-in by the layered structure. *Scientific Reports, 6(36047), pages 1-9*, 2016. `https://doi.org/10.1038/srep36047`

[160] W K Kwok, S Fleshler, U Welp, V M Vinokur, J Downey, G W Crabtree, and M M Miller. Vortex Lattice Melting in Untwinned and Twinned Single Crystals of $YBa_2Cu_3O_{7-\delta}$. *Physical Review Letters, 69(23), pages 3370-3373*, 1992. `https://doi.org/10.1103/PhysRevLett.69.3370`

[161] T Puig, F Galante, E M González, J L Vicent, B Martínez and X Obradors. Vortex liquid entanglement in twinned $YBa_2Cu_3O_7/Y_2BaCuO_5$ composite superconductors. *Physical Review B, 60(18), pages 13099-13106*, 1999. `https://doi.org/10.1103/PhysRevB.60.13099`

[162] J Figueras, T Puig, X Obradors, W K Kwok, L Paulius, G W Crabtree, and G Deutscher. The loss of vortex line tension sets an upper limit to the irreversibility line in $YBa_2Cu_3O_7$. *Nature Physics, 2, pages 402-407*, 2006. `https://doi.org/10.1038/nphys311`

[163] Ö Polat, J W Sinclair, Y L Zuev, J R Thompson, D K Christen, S W Cook, D Kumar, Y Chen, and V Selvamanickam. Thickness dependence of magnetic relaxation and E-J characteristics in superconducting (Gd-Y)-Ba-Cu-O films with strong vortex pinning. *Physical Review B, 84, pages 1-13*, 2011. `https://doi.org/10.1103/PhysRevB.84.024519`

[164] E Mezzetti, R Gerbaldo, G Ghigo, L Gozzelino, B Minetti, C Camerlingo, A Monaco, G Cuttone and A Rovelli. Control of the critical current density in $YBa_2Cu_3O_{7-\delta}$ films by means of intergrain and intragrain correlated defects. *Physical Review B, 60(10), pages 7623-7630*, 1999. `https://doi.org/10.1103/PhysRevB.60.7623`

[165] E. Mezzetti, A Chiodoni, R Gerbaldo, G Ghigo, L Gozzelino, B Minetti, C Camerlingo, and A Monaco. Probing of current-tailoring mechanisms in $YBa_2Cu_3O_{7-\delta}$ films by means of heavy ion irradiation. *Physica C, 332(1-4), pages 115-121*, 2000. `https://doi.org/10.1016/S0921-4534(00)00008-3`

[166] L Civale, B Maiorov, A Serquis, J O Willis, J Y Coulter, H Wang, Q X Jia, P N Arendt, J L MacManus-Driscoll, M P Maley, and S R Foltyn. Angular-dependent vortex pinning mechanisms in $YBa_2Cu_3O_7$ coated conductors and thin films. *Applied Physics Letters, 84(12), pages 2121-2123*, 2004. `https://doi.org/10.1063/1.1655707`

[167] J Gutiérrez. Vortex pinning and critical currents in $YBa_2Cu_3O_{7-x}$ MOD-TFA thin films and Coated Conductors. *PhD thesis*, 2008.

[168] S Awaji, K Watanabe, and N Kobayashi. Crossover from intrinsic to extrinsic pinning for YBa2Cu3O7 Films. *Cryogenics, 39(7), pages 569-577*, 1999. `https://doi.org/10.1016/S0011-2275(99)00079-X`

[169] M V Feigel'man and V M Vinokur. Thermal fluctuations of vortex lines, pinning, and creep in high-T_c superconductors. *Physical Review B, 41(13), pages 8986-8990*, 1990. `https://doi.org/10.1103/PhysRevB.41.8986`

[170] L Civale, A D Marwick, M W McElfresh, T K Worthington, A P Malozemoff, F H Holtzberg, J R Thompson, and M A Kirk. Defect Independence of the Irreversibility Line in Proton-Irradiated Y-Ba-Cu-0 Crystals. *Physical Review Letters, 65(9), pages 1164-1167*, 1990. `https://doi.org/10.1103/PhysRevB.41.8986`

[171] J Z Sun, C B Eom, B Lairson, J C Bravman, and T H Geballe. Magnetic relaxation, current-voltage characteristics, and possible dissipation mechanisms for high-T_c superconducting thin films of Y-Ba-Cu-O. *Physical Review B, 43(4), pages 3002-3008*, 1991. `https://doi.org/10.1103/PhysRevB.43.3002`

[172] H Yamasaki and Y Mawatari. Current–voltage characteristics and flux creep in melt-textured $YBa_2Cu_3O_{7-\delta}$. *Superconductor Science and Technology, 13(2), pages 202-208*, 2000. `https://doi.org/10.1088/0953-2048/13/2/315`

[173] J R Thompson, Ö Polat, D K Christen, D Kumar, P M Martin, and J W Sinclair. Wide-range characterization of current conduction in high-T_c coated conductors. *Applied Physics Letters, 93(042506), 1-3*, 2008. `https://doi.org/10.1063/1.2964195`

[174] D Niebieskikwiat, L Civale, C A Balseiro, and G Nieva. Nonglassy relaxation by double kinks in $YBa_2Cu_3O_{7-\delta}$ with columnar defects. *Physical Review B, 61(10), pages 7135-7141*, 2000. `https://doi.org/10.1103/PhysRevB.61.7135`

[175] D Niebieskikwiat, A Silhanek, L Civale, G Nieva, P Levy, and L Krusin-Elbaum. Suppression of matching field effects by splay and pinning energy dispersion in $YBa_2Cu_3O_7$. *Physical Review B, 63(144504), pages 1-5*, 2001. `https://doi.org/10.1103/PhysRevB.63.144504`

[176] T Hwa, P Le-Doussal, D R Nelson, and V M Vinokur. Flux Pinning and Forced Vortex Entanglement by Splayed Columnar Defects. *Physical Review Letters, 71(21), pages 3545-3548*, 1993. `https://doi.org/10.1103/PhysRevLett.71.3545`

[177] L Civale, L Krusin-Elbaum, J R Thompson, R Wheeler, A D Marwick, M A Kirk, Y R Sun, F Holtzberg, and C Feild. Reducing vortex motion in $YBa_2Cu_3O_7$ crystals with splay in columnar defects. *Physical Review B, 50(6), pages 4102-4105*, 1994. `https://doi.org/10.1103/PhysRevB.50.4102`

[178] J R Thompson, L Krusin-Elbaum, L Civale, G Blatter, and C Feild. Superfast Vortex Creep in $YBa_2Cu_3O_{7-\delta}$ Crystals with Columnar Defects: Evidence for Variable-Range Vortex Hopping. *Physical Review Letters, 78(16), pages 3181-3184*, 1997. `https://doi.org/10.1103/PhysRevLett.78.3181`

[179] L Miu Vortex depinning temperature in $YBa_2Cu_3O_7$ films with $BaZrO_3$ nanorods. *Physical Review B, 85(104519), pages 1-5*, 2012. `https://doi.org/10.1103/PhysRevB.85.104519`

[180] S Awaji, R Ishihara, K Watanabe, K Shikimachi, N Hirano, and S Nagaya. Anisotropy of the Critical Current Density and Intrinsic Pinning Behaviors of $YBa_2Cu_3O_y$ Coated Conductors. *Applied Physics Express, 4(013101), pages 1-3*, 2011. `https://doi.org/10.1143/APEX.4.013101`

[181] K Iida, J Hänisch, C Tarantini, F Kurth, J Jaroszynski, S Ueda, M Naito, A Ichinose, I Tsukada, E Reich, V Grinenko, L Schultz, and B Holzapfel. Oxypnictide SmFeAs(O,F) superconductor: a candidate for high-field magnet applications. *Scientific reports, 3(2139), pages 1-5*, 2013. `https://doi.org/10.1038/srep02139`

[182] S Eley, M Miura, B Maiorov, and L Civale. Universal lower limit on vortex creep in superconductors. *Nature Materials, 16, pages 409-413*, 2017. `https://doi.org/10.1038/nmat4840`

[183] S Eley, M Leroux, M W Rupich, D J Miller, H Sheng, P M Niraula, A Kayani, U Welp, W K Kwok, and L Civale. Decoupling and tuning competing effects of different types of defects on flux creep in irradiated $YBa_2Cu_3O_{7-\delta}$. *Superconductor Science and Technology, 30(015010), pages 1-22*, 2016. `https://doi.org/10.1088/0953-2048/30/1/015010`

[184] L Civale, G Pasquini, P Levy, G Nieva, D Casa, and H Lanza. Time relaxation of persistent currents in $YBa_2Cu_3O_{7-x}$ crystals with columnar defects. *Physica C, 263(1-4), pages 389-395*, 1996. `https://doi.org/10.1016/0921-4534(95)00782-2`

[185] L Miu, P Mele, A Crisan, A Ionescu, and D Miu. Evolution of vortex dynamics in $YBa_2Cu_3O_7$ films with nanorods by adding nanoparticles. *Physica C, 500, pages 40-43*, 2014. `https://doi.org/10.1016/j.physc.2014.03.002`

[186] N Haberkorn, M Miura, J Baca, B Maiorov, I Usov, P Dowden, S R. Foltyn, T G Holesinger, J O Willis, K R Marken, T Izumi, Y Shiohara, and L Civale. High-temperature change of the creep rate in $YBa_2Cu_3O_{7-\delta}$ films with different pinning landscapes. *Physical Review B, 85(174504), pages 1-7*, 2012. `https://doi.org/10.1103/PhysRevB.85.174504`

[187] V Rouco, E Bartolomé, B Maiorov, A Palau, L Civale, X Obradors, and T Puig. Vortex creep in TFA–YBCO nanocomposite films. *Superconductor Science and Technology, 27(115008), pages 1-7*, 2014. `https://doi.org/10.1088/0953-2048/27/11/115008`

[188] F Vallès, A Palau, V Rouco, B Mundet, X Obradors, and T Puig. Angular flux creep contributions in $YBa_2Cu_3O_{7-\delta}$ nanocomposites from electrical transport measurements. *Scientific Reports*, 8(5924), pages 1-7, 2018. `https://doi.org/10.1038/s41598-018-24392-1`

[189] N Pompeo, A Augieri, K Torokhtii, V Galluzzi, G Celentano, and E Silva. Vortex matter dynamics in $YBa_2Cu_3O_{7-x}$ with $BaZrO_3$ nanocolumns as revealed by dc and high-frequency experiments: role of anisotropy and directional pinning. *Ap-*

plied Physics Letters, 106(022603), pages 1-4, 2013. `https://doi.org/10.1063/1.4813405`

[190] F Martinez-Julian, S Ricart, A Pomar, M Coll, P Abelian, F Sandiumenge, M J Casanove, X Obradors, T Puig, I Pastoriza-Santos, and L M Liz-Marzán. Chemical Solution Approaches to $YBa_2Cu_3O_{7-\delta}$-Au Nanocomposite Superconducting Thin Films. *Journal of Nanoscience and Nanotechnology, 11(4), pages 3245–3255*, 2011. `https://doi.org/10.1166/jnn.2011.3762`

[191] I Bretos, T Schneller, M Falter, M Bäcker, E Hollmann, R Wördenweber, L Molina-Luna, G Van Tendeloo, and O Eibl. Solution-derived $YBa_2Cu_3O_{7-\delta}$ (YBCO) superconducting films with $BaZrO_3$ (BZO) nanodots based on reverse micelle stabilized nanoparticles. *Journal of Materials Chemistry C, 3(16), pages 3971-3979*, 2015. `http://doi.org/10.1039/C4TC02543A`

[192] S K Brar and M Verma. Measurement of nanoparticles by light-scattering techniques. *Trends in Analytical Chemistry, 30(1), pages 4-17*, 2011. `https://doi.org/10.1016/j.trac.2010.08.008`

[193] M Coll, J Gázquez, R Hühne, B Holzapfel, Y Morilla, J García-López, A Pomar, F Sandiumenge, T Puig, and X Obradors. All chemical $YBa_2Cu_3O_7$ superconducting multilayers: Critical role of CeO_2 cap layer flatness. *Journal of Materials Research, 24(4), pages 1446-1455*, 2009. `https://doi.org/10.1557/jmr.2009.0160`

[194] D R Uhlmann, B Chalmers, and K A Jackson. Interaction between particles and a solid-liquid interface. *Journal of Applied Physics, 35(10), pages 2986-2993*, 1964. `https://doi.org/10.1063/1.1713142`

[195] J Pötschke and V Rogge. On the behaviour of foreign particles at an advancing solid-liquid interface. *Journal of Crystal Growth, 94(3), pages 726-738*, 1989. `https://doi.org/10.1016/0022-0248(89)90097-3`

[196] Y Yamada, K Takahashi, H Kobayashi, M Konishi, T Watanabe, A Ibi, T Muroga, S Miyata, T Kato, T Hirayama, and Y Shiohara. Epitaxial nanostructure and defects effective for pinning in $Y(RE)Ba_2Cu_3O_{7-x}$ coated conductors. *Applied Physics Letters, 87(132502), pages 1-3*, 2005. `https://doi.org/10.1063/1.2061874`

[197] J S Matsuda, Y Tokunaga, K Nakaoka, R Teranishi, Y Aoki, H Fuji, A Yajima, Y Yamada, T Izumi, and Y Shiohara. Transmission electron microscopic studies on crystallization of $YBa_2Cu_3O_{7-y}$ films deposited by advanced TFA-MOD method. *Physica C: Superconductivity and its Applications, 426-431(Part 2), pages 1051-1055*, 2005. `https://doi.org/10.1016/j.physc.2005.01.086`

[198] D E Wesolowski and M J Cima. Large-area quantification of $BaCeO_3$ formation during processing of metalorganic-deposition-derived YBCO films. *Journal of Materials Research, 22(4), pages 1077-1081*, 2007. `https://doi.org/10.1557/jmr.2007.0125`

[199] Z Li, M Coll, B Mundet, N Chamorro, F Valles, A Palau, J Gazquez, S Ricart, T Puig, and X Obradors. Control of nanostructure and pinning properties in solution deposited $Y(RE)Ba_2Cu_3O_{7-x}$ nanocomposites with preformed perovskite nanoparticles. *Scientific Reports, Accepted*, 2019.

[200] S Engel, T Thersleff, R Hühne, L Schultz, B Holzapfel, Enhanced flux pinning in $Y(RE)Ba_2Cu_3O_7$ layers by the formation of nanosized $BaHfO_3$ precipitates using the chemical deposition method. *Applied Physics Letters, 90(102505), pages 1-3*, 2007. `https://doi.org/10.1063/1.2711761`

[201] M Miura, M Yoshizumi, T Izumi, and Y Shiohara. Formation mechanism of $BaZrO_3$ nanoparticles in $Y_{1-x}Sm_xBa_2Cu_3O_y$-coated conductors derived from trifluoroacetate metal-organic deposition. *Superconductor Science and Technology*, 23(1), pages 1-5, 2010. `https://doi.org/10.1088/0953-2048/23/1/014013`

[202] S R Foltyn, H Wang, L Civale, Q X Jia, P N Arendt, B Maiorov, Y Li, M P Maley, and J L MacManus-Driscoll. Overcoming the barrier to 1000 A/cm width superconducting coatings. *Applied Physics Letters, 87(162505), pages 1-3*, 2005. `https://doi.org/10.1063/1.2106021`

[203] J L MacManus-Driscoll, A Kursumovic, B Maiorov, L Civale, Q X Jia, S R Foltyn and H Wang. $YBa_2Cu_3O_7$ Coated Conductor Grown by Hybrid Liquid Phase Epitaxy. *IEEE Transactions on Applied Superconductivity, 17(2), pages 2537-2541*, 2007. `https://doi.org/10.1109/TASC.2007.898171`

[204] M Dürrschnabel, Z Aabdin, M Bauer, R Semerad, W Prusseit and O Eibl. $DyBa_2Cu_3O_{7-x}$ superconducting coated conductors with critical currents exceeding 1000 A cm^{-1}. *Superconductor Science and Technology, 25(104007), pages 1-4*, 2012. `https://doi.org/10.1088/0953-2048/25/10/105007`

[205] J Lee, H Lee, J Lee, S Choi, S Yoo, and S Moon. RCE-DR, a novel process for coated conductor fabrication with high performance. *Superconductor Science and Technology, 27(044018), pages 1-6*, 2014. `https://doi.org/10.1088/0953-2048/27/4/044018`

[206] U P Trociewitz, M Dalban-Canassy, M Hannion, D K Hilton, J Jaroszynski, P Noyes, Y Viouchkov, H W Weijers, and D C Larbalestier. 35.4 T field generated using a layer-wound superconducting coil made of $(RE)Ba_2Cu_3O_{7-x}$ (RE = rare earth) coated conductor. *Applied Physics Letters, 99(202506), pages 1-3*, 2011. `https://doi.org/10.1063/1.3662963`

[207] Y Shiohara, T Taneda and M Yoshizumi. Overview of Materials and Power Applications of Coated Conductors Project Overview of Materials and Power Applications of Coated Conductors Project. *Japanese Journal of Applied Physics, 51(010007), pages 1-16*, 2012. `https://doi.org/10.1143/JJAP.51.010007`

[208] H W Weijers, U P Trociewitz, W D Markiewicz, J Jiang, D Myers, E E Hellstrom, A Xu, J Jaroszynski, P Noyes, Y Viouchkov, and D C Larbalestier. High Field Magnets With HTS Conductors. *IEEE Transactions on Applied Superconductivity, 20(3), pages 576-582*, 2010. `https://doi.org/10.1109/TASC.2010.2043080`

[209] H W Weijers, W D Markiewicz, A V Gavrilin, A J Voran, Y L Viouchkov, S R Gundlach, P D Noyes, D V Abraimov, H Bai, S T Hannahs, and T P Murphy. Progress in the Development and Construction of a 32-T Superconducting Magnet. *IEEE Transactions on Applied Superconductivity, 26(4), pages 1-7*, 2016. `https://doi.org/10.1109/TASC.2016.2517022`

[210] D C Larbalestier, J Jiang, U P Trociewitz, F Kametani, C Scheuerlein, M Matras, P Chen, N C Craig, P J Lee, and E E Hellstrom. Isotropic round-wire multifilament cuprate superconductor for generation of magnetic fields above 30 T. *Nature materials, 13, pages 375-381*, 2014. `https://doi.org/10.1038/nmat3887`

[211] M Miura, B Maiorov, T Kato, T Shimode, K Wada, S Adachi, and K Tanabe. Strongly enhanced flux pinning in one-step deposition of $BaFe_2(As_{0.66}P_{0.33})_2$ superconductor films with uniformly dispersed $BaZrO_3$ nanoparticles. *Nature communications, 4(2499), pages 1-7*, 2013. `https://doi.org/10.1038/ncomms3499`

NOMENCLATURE

α	$J_c(H)$ power law index
ΔT_c	Transition width
γ	Intrinsic anisotropy
γ_{eff}	Effective anisotropy
ε	Nanostrain
λ	Magnetic penetration depth
μ_0	Magnetic permeability of vacuum
ϕ_0	Magnetic flux quantum
ψ	Superconducting coherence length
ρ_{dis}	Partial dislocation relative volume
θ	Magnetic field orientation
θ_T	Trapping critical angle
ξ	Coherence length
aniso	Anisotropic
a-s	Anisotropic-strong
BHO	$BaHfO_3$
BYTO	Ba_2YTaO_6
BZO	$BaZrO_3$
CC	Coated conductor
CSD	Chemical solution deposition
d_{SF}	Stacking fault length
F_P	Pinning force
FH	Flash heating
H||ab	Magnetic field parallel to the ab-planes
H||c	Magnetic field parallel to the c-axis
H^*	Crossover magnetic field (single vortex pinning / vortex-vortex interactions)
H_Φ	Matching magnetic field
H_{c2}	Upper critical magnetic field

H_{cr1}	Lower crossover magnetic field (stacking fault pinning / intrinsic pinning)
H_{cr2}	Upper crossover magnetic field (stacking fault pinning / intrinsic pinning)
H_{eff}	Effective magnetic field
H_{irr}	Irreversibility magnetic field
I_c	Critical current
IJP	Inkjet printing
iso	Isotropic
i-w	Isotropic-weak
i-s	Isotropic-strong
J_c	Critical current density
MD	Multideposition
n	E(J) power law index
pn or PN	Preformed nanoparticles
YBCO	$YBa_2Cu_3O_{7-x}$
Y123	$YBa_2Cu_3O_y$ phase
Y124	$YBa_2Cu_4O_y$ phase
T_0	Characteristic weak pinning temperature
T^*	Characteristic strong pinning temperature
T_c	Critical temperature
T_{irr}	Irreversibility temperature
S	Flux creep rate
S_{ind}	Inductive flux creep rate
sf	Self field
ss or SS	Spontaneous segregated (nanoparticles)
STEM	Scanning transmission electron microscopy
str	Strong
t	Thickness
TFA	Trifluoroacetate
wk	Weak
XRD	X-ray diffraction